CNWRA 95-016

EVALUATION OF ABAQUS AS A COMPLIANCE DETERMINATION COMPUTER CODE

Prepared for

Nuclear Regulatory Commission
Contract NRC-02-93-005

Prepared by

Center for Nuclear Waste Regulatory Analyses
San Antonio, Texas

August 1995

CNWRA 95-016

EVALUATION OF ABAQUS AS A COMPLIANCE DETERMINATION COMPUTER CODE

Prepared for

Nuclear Regulatory Commission
Contract NRC-02-93-005

Prepared by

Goodluck I. Ofoegbu
Amitava Ghosh
Mikko P. Ahola
Sui-Min Hsiung
Asadul H. Chowdhury

Center for Nuclear Waste Regulatory Analyses
San Antonio, Texas

August 1995

PREVIOUS REPORTS IN SERIES

Number	Name	Date Issued
CNWRA 93-005	Evaluation of Coupled Computer Codes for Compliance Determination	June 1993
NUREG/CR-6021	A Literature Review of Coupled Thermal-Hydrologic-Mechanical-Chemical Processes Pertinent to the Proposed High-Level Nuclear Waste Repository at Yucca Mountain	July 1993
CNWRA 94-001	Evaluation of Computer Codes for Compliance Determination—Phase II	January 1994
CNWRA 95-011	Compliance Determination Computer Codes for Preclosure Safety Assessments	June 1995

ABSTRACT

This report presents the results of a study to evaluate the computer code ABAQUS conducted at the Center for Nuclear Waste Regulatory Analyses for the Nuclear Regulatory Commission. The purpose of the evaluation was to determine if the code would be suitable as a compliance-determination computer code for the anticipated license application for a proposed high-level nuclear waste repository at Yucca Mountain, Nevada. Such a code would be used to assess the impact of the key technical uncertainty related to thermal-mechanical effects on near-field fluid flow and, in turn, on the capability of the proposed repository to provide effective isolation of the proposed types and quantities of radioactive waste. Therefore, the code was evaluated with respect to its capabilities to model coupled thermal, mechanical, and hydrologic processes in a fractured rock mass.

The code was used to solve individual mechanical, thermal, and hydrological problems, as well as coupled problems, such as those involving thermal-mechanical, thermal-hydrological, mechanical-hydrological, and thermal-mechanical-hydrological (TMH) processes. The performance of the code was assessed by comparing the calculated results with those calculated using available analytical solutions or other computer codes, and, for one problem, with field test results. Modeling fractures as discrete entities was emphasized in all problems. The options available in ABAQUS for discrete-fracture modeling make use of either interface elements, which simulate fractures as block-to-block contact, or thin solid elements, in which a fracture is modeled as a thin-layer solid with direction-dependent properties.

The code was judged to possess the capability to model the thermal-mechanical responses of fractured rock. On the other hand, because the interface elements cannot model fracture intersections, only the thin solid elements may be used to model fracture networks. The code also possesses the capability to model conduction-dominated heat flow through fractured rock. It was also found to have the capability to model the isothermal flow of water through rock matrix and fractures, under water-saturated and unsaturated conditions; the thin solid elements performed satisfactorily, whereas the interface elements did not. Thus, the thin solid elements were found to be more suitable than the interface elements for calculating the effects of mechanical deformation on fracture permeability.

The code did not perform satisfactorily for modeling thermal effects on moisture flow under unsaturated conditions. The reason for its unsatisfactory performance in such problems is that it does not make provisions for the simultaneous flow of two fluid phases, such as water and vapor. As a result, it is unable to model the drying effects of evaporation and gas expansion.

Based on the study, it is recommended that ABAQUS be used to conduct a study of the effects of thermal-mechanical deformation on rock-mass permeability, under conditions similar to those anticipated for the proposed Yucca Mountain repository. For this purpose, ABAQUS would be used in conjuction with a separate thermal-hydrological code (such as CTOUGH) through the exchange of input and output. If the results of such a study should indicate that thermal-hydrological analyses have to be coupled with mechanical analyses in order to account satisfactorily for thermal-mechanical effects on fluid flow, then ABAQUS should be adapted as a stand-alone code for conducting coupled TMH analyses. The modifications necessary to improve the capabilities of the code for conducting such analyses are discussed in the report. Otherwise, the use of ABAQUS in TMH modeling would be limited to the computation of permeabilities that would be applied as input into a separate thermal-hydrological analysis code.

CONTENTS

CONTENTS (Cont'd)

CONTENTS (Cont'd)

CONTENTS

FIGURES

FIGURES (Cont'd)

FIGURES (Cont'd)

FIGURES (Cont'd)

Figure | Page

FIGURES (Cont'd)

FIGURES (Cont'd)

TABLES

ACKNOWLEDGMENTS

This report was prepared to document work performed by the Center for Nuclear Waste Regulatory Analyses (CNWRA) for the Nuclear Regulatory Commission (NRC) under Contract No. NRC-02-93-005. The activities reported here were performed on behalf of the NRC Office of Nuclear Material Safety and Safeguards (NMSS), Division of Waste Management (DWM). The report is an independent product of the CNWRA and does not necessarily reflect the views or regulatory position of the NRC.

Valuable technical assistance was provided at various stages of the project by R.T. Green, G. Rice, S. Stothoff, V. Kapoor, P.K. Nair, R.G. Baca, and B. Sagar. The technical and programmatic reviews of the report were performed by W.C. Patrick, S. Stothoff, P.C. Lichtner, and B. Sagar; and the editorial review by J.W. Pryor and C. Gray. Secretarial assistance was provided by R. Sanchez and Y. Lozano.

QUALITY OF DATA

There is no CNWRA-generated original data contained in this report. Sources for other data should be consulted for determining the level of quality for those data.

SOFTWARE QUALITY ASSURANCE

The finite element code ABAQUS, the mesh-generation code PATRAN-3, and the integrated finite difference code CTOUGH, which were used for some of the analyses contained in this report, have not yet been placed under configuration control in accordance with the CNWRA software quality-assurance procedure (TOP-018, Development and Control of Scientific and Engineering Software). Once it is decided that ABAQUS and PATRAN-3 will be used for compliance determination, these codes will be controlled following the procedures of TOP-018. CTOUGH, which is a modified version of VTOUGH (currently under configuration control at CNWRA) will also be controlled once its updating is completed.

The distinct element code UDEC and the finite difference code BREATH, which were used for some of the analyses contained in this report, are controlled under the CNWRA software quality-assurance procedure (TOP–018, Development and Control of Scientific and Engineering Software).

EXECUTIVE SUMMARY

This report presents the results of a study conducted at the Center for Nuclear Waste Regulatory Analyses for the Nuclear Regulatory Commission (NRC). The purpose of the study is to evaluate the finite element code ABAQUS as a possible computer code for conducting analyses related to the review of the license application that may be submitted by the U.S. Department of Energy (DOE) to construct and operate a repository for high-level nuclear waste (HLW). The site at Yucca Mountain, Nevada, is currently being investigated for this purpose. If the code is found suitable, it would be used by NRC staff to conduct analyses related to the evaluation of DOE compliance with NRC regulations on the design of the proposed repository. Specifically, the code would be used to evaluate possible effects of the key technical uncertainty related to thermal-mechanical effects on near-field fluid flow, and, in turn, on the capabilities of the proposed repository to provide effective isolation of the proposed types and quantities of radioactive materials. Such analyses would consider the responses of the host rock mass and groundwater system to the imposed thermal loads and superimposed seismic disturbances. Therefore, the code was evaluated for its capabilities to model coupled thermal, mechanical, and hydrological processes in a fractured rock mass.

The computer code was used to simulate a set of benchmark problems and one field-test problem involving (i) individual thermal, mechanical, and hydrological processes; (ii) coupled thermal-mechanical (TM), thermal-hydrological (TH), and mechanical-hydrological processes; and (iii) coupled thermal-mechanical-hydrological (TMH) processes. The performance of the code was judged by comparing its calculated responses with those calculated using either the analytical solutions for the same problems, or a different computer code, or both, and for one problem with field test results. In all the problems, emphasis was placed on modeling fractures as geometrically discrete entities. The procedures available in ABAQUS for such modeling of fractures make use of either interface elements, in which a fracture is modeled as a contact between two solid blocks, or solid elements, in which a fracture is modeled as a thin zone of material having different properties than the surrounding rock.

ABAQUS was judged to possess the capabilities to model the mechanical responses of fractured rock to changes induced by excavation, thermal loading, and seismic disturbance. On the other hand, because the interface elements cannot model fracture intersections satisfactorily, only the thin-solid representation may be used to model fracture networks. Results of numerical experiments indicate that the aspect ratio of such thin solids should be greater than about 250 for them to model the mechanical response of rock fractures satisfactorily. ABAQUS was also judged to possess the capability to model conduction-dominated heat flow through fractured rock. The code also has the capability to model the isothermal flow of water through rock matrix and fractures under both water-saturated and unsaturated states; the thin solid element model of fractures performed satisfactorily, whereas the interface-element model did not. Thus, the thin solid elements were found to be more suitable than the interface elements for simulating the effects of mechanical deformation on the hydraulic conductivity of fractured rock.

For modeling thermal effects on water flow, ABAQUS was found to be satisfactory for simulating water-saturated conditions, but not satisfactory for unsaturated conditions. The unsatisfactory performance of the code for unsaturated media arises from the fact that it does not model the simultaneous flow of two fluid phases (such as water and vapor). As a result, it is unable to predict drying effects caused by gas expansion and the evaporation of water.

Based on these studies, it is recommended that ABAQUS be adapted for use as a compliance determination computer code. The modifications required in the code for this purpose will be effected in up to three steps as follows: First, the code should be adapted as a companion code for TMH analyses, along with a TH code (such as CTOUGH). For this purpose, ABAQUS would be used for the computation

of thermal-mechanical effects on rock-mass permeability, and its link with the TH code would be developed through the exchange of input and output. Although modeling tools are currently available in ABAQUS to enable its use as such a companion TMH code, its capabilities for conducting such analyses need to be enhanced by implementing a material model in the code that makes provisions for strain-dependent friction and dilation angles for solid elements. The adequacy of this approach to TMH modeling (i.e., the use of separate TM and TH analysis codes) can be investigated through a series of numerical experiments, to determine whether TH analyses should be fully coupled with mechanical analyses, or whether mechanical effects on permeability can be computed separately and applied as input into TH models.

If the results of such a study should indicate that thermally induced mechanical effects on fluid flow can be simulated satisfactorily through separate TM and TH analyses, then the use of ABAQUS in TMH modeling would be limited to the computation of permeabilities that would be applied as input into a separate TH analysis code. Otherwise, a second step of modification would be considered to adapt ABAQUS as a stand-alone code for coupled TMH analyses. In order to use the code for such analyses under situations for which the effects of vapor flow may be ignored, it would have to be modified to make provisions for deformation-dependent permeabilities for solid elements. A third step of modifications would be necessary in order to use the code under situations for which the effects of vapor flow cannot be ignored. To be used for such situations, ABAQUS would have to be modified to accept temperature-dependent volumetric sources in its fluid-flow model, and a separate code would have to be developed to express the effects of vapor flow in terms of source-strength distributions.

1 INTRODUCTION

The Nuclear Regulatory Commission (NRC) is required to review a license application from the U.S. Department of Energy (DOE) to construct and operate a proposed repository for high-level radioactive waste (HLW) at Yucca Mountain (YM), Nevada, if the YM site is found to be suitable. The YM area consists of a thick sequence of Tertiary volcanic deposits (bedded and pyroclastic ash-flow tuffs), overlain by thin layers of Quaternary alluvium, and underlain by Paleozoic sedimentary rocks (U.S. Department of Energy, 1988; Young et al., 1992). The volcanic rocks are generally fractured, with the fracture density being highest in the welded tuffs; there are also numerous steeply dipping faults, some of which cut through both the volcanics and the underlying sedimentary (mostly carbonate) rocks. The proposed repository location is at a depth of about 350 m below the crest of YM and 50–100 m below the surrounding alluvium-filled washes, in the welded and densely fractured Topopah Spring member of the Paintbrush tuff. The groundwater table is at about 225 m below the proposed repository horizon, and there may also be perched-water zones at higher elevations (Klavetter and Peters, 1986).

The key issues to be considered in the license application include whether a mined geologic repository at the proposed location will provide effective long-term waste isolation from the accessible environment and whether short-term and retrievability objectives will be met as specified in 10 CFR Part 60. For example, a specific requirement for construction authorization (10 CFR 60.31) is that there be reasonable assurance that the types and quantities of radioactive materials described in the application can be received, possessed, and disposed of in a geologic repository operations area (GROA) of the design proposed without unreasonable risk to the health and safety of the public. This requirement emphasizes the design of the GROA, considering the natural and engineered characteristics of both the surface and underground facilities and the host rock mass. In assessing the GROA design, consideration will be given to the predicted thermal and thermal-mechanical responses of the rock mass and groundwater system. Therefore, it is necessary to understand the uncertainties associated with the response of the fractured rock mass and groundwater system to thermal loading, and the impact of such responses to the performance of the engineered barrier and total systems.

Two key technical uncertainties (KTUs) have been identified that relate to the effects of the imposed thermal loads and possible superimposed seismic disturbances on: (i) the stability of the emplacement drifts and integrity of the engineered barrier system (EBS), and (ii) the mechanical-hydrological response of the rock mass surrounding the EBS. These KTUs focus on two issues, namely, (i) the flow of water within the near-field area of the repository, either toward or away from the waste packages (WPs); and (ii) the stability of the repository openings.

1.1 WATER FLOW WITHIN THE NEAR FIELD

The emplacement of radioactive waste in the repository is expected to cause significant perturbations within a zone of the host rock mass, involving coupled thermal, mechanical, hydrological, and chemical (TMHC) processes (Manteufel et al., 1993; Ghosh et al., 1993, 1994; Lichtner, 1995). The rock-mass zone within which such perturbations may occur will be referred to hereafter as the near field. Heat generated by the WPs may induce sufficient temperature rise within sections of the near field to cause the evaporation of pore water. The flow of water vapor away from the WPs and its condensation in cooler areas may lead to the formation of a dry zone around the WPs and perched water zones at some distance away (cf. Buscheck and Nitao, 1993). Water from the perched (condensate) zones or other sources may flow to the WPs at a later time, when the available water flux is able to overcome the evaporation rate. Whether or not the rate of evaporation is overcome by the water flux depends on several factors, such as the thermal characteristics of the WPs, the permeability of the rock mass within the near field, and the amount of water available to feed the flux.

Among these factors, the permeability of the rock mass is likely to be affected most by the TMHC processes. The unresolved issues related to rock-mass permeability include the following:

(i) The contributions of rock-matrix and fracture permeability to the distribution of water flux within the near-field.

(ii) Significant changes in rock-mass permeability may occur as a result of rock deformations induced by excavation, temperature changes, or seismic excitation.

(iii) The precipitation of minerals on fracture walls and the dissolution of existing fracture-wall minerals may also cause significant changes in rock-mass permeability.

Because the magnitude and distribution of permeability within the near field is likely to vary with time under the influence of a series of complicated processes, the temporal and spatial distributions of water flux are likely to be evaluated using the results of numerical analyses. Some of the issues that need to be considered in selecting the methods and computer codes for conducting such analyses are described briefly in the following paragraphs.

1.1.1 Role and Modeling of Matrix-Fracture Interaction

The possibility of water flow between rock fractures and matrix is important in the numerical modeling of water flow through an unsaturated, fractured porous medium. It has been suggested (cf. Buscheck and Nitao, 1993) that matrix imbibition may reduce fracture flux enough to promote the development of a dry zone around the WP and may significantly increase the length of time during which such a zone would remain dry. Analytical results presented by Nitao (1991) strengthen the intuitive belief that the effect of matrix imbibition on fracture flow depends on factors such as the matrix porosity, permeability, and capillary pressure.

The flow of water in a variably saturated, fractured porous medium can be modeled either by considering the fractures as geometrically distinct entities, or by smearing the effects of the fractures and the matrix to produce a composite continuum. The second approach, referred to as the equivalent continuum model (ECM), is attractive because it does not require explicit modeling of the geometrical details of the fracture distribution. As a result, the ECM has been used frequently; for example, see Klavetter and Peters (1986), Buscheck and Nitao (1993), and other works cited in Kapoor (1994). One of the modeling issues to be resolved is whether the ECM can be used to predict satisfactorily the distribution of water flux within the near-field. A code that has both discrete-fracture and ECM capabilities may be used to investigate the acceptability of certain results calculated using the ECM.

1.1.2 Mechanical Effects on Rock-Mass Permeability

Rock-mass deformations within the near-field may occur as a result of excavation, temperature changes, or seismic disturbance. It has been demonstrated that a large proportion of the rock deformation in a densely fractured rock mass consists of the opening, closure, and shear displacement of fractures (e.g., Kana et al., 1991; Hsiung et al., 1992). Such deformations cause changes in fracture aperture, which may translate into significant changes in rock-mass permeability. The key unresolved question related to such permeability changes is whether their magnitudes are large enough to warrant consideration of mechanical effects on permeability in the hydrological analysis of the proposed repository. Also, if the magnitudes of the permeability changes are considered significant, it is necessary to determine their spatial and temporal distributions.

Based on previous underground rock-engineering experience (cf. Hoek and Brown, 1980), it is expected that deformations associated with stress changes induced by the repository openings will occur within a few years following construction and will be limited to a distance of a few equivalent tunnel-diameters around each opening. However, the zone of mechanical deformation around the repository openings may increase with time because of the possibility of rock-strength deterioration due to creep and chemical alteration of fracture walls. It may be difficult to establish the spatial distribution and temporal rate of such strength changes, but their effects on repository-opening stability and rock-mass permeability may be bounded through numerical modeling, using a range of possible deterioration rates.

Thermally induced deformations are related to the expansion of rock and pore fluid. The expansion of solid rock may cause rock fractures to close or open, depending mainly on the spatial distribution of temperature changes and thermal expansivity. Two of the thermal goals established by the DOE for the YM repository (Saterlie and Thomson, 1994) consist of limits on the magnitude and rate of thermally induced ground heave. The rationale for the limits is that ground heave may be accompanied by increase in fracture aperture, the impact of which may be reduced by limiting the magnitude and rate of heave. The possibility has also been raised of the development of excess pore pressure due to the expansion of pore fluids. Where the rock-matrix permeability is very small, as is the case for the YM repository area, the excess pore pressure may not dissipate quickly. Laboratory data presented by Althaus et al. (1994) for water-saturated rock suggest that such pressure increase may cause the re-opening and growth of microcracks, which in turn may cause the rock-matrix permeability to increase. The occurrence of such thermally induced microcracking in unsaturated rock and its significance to rock-matrix permeability may be investigated through numerical modeling. Furthermore, numerical modeling may be used to investigate the temporal and spatial distributions of thermally induced fracture-aperture changes and to bound their effects on rock-mass permeability.

Seismically induced deformations related to earthquakes or possible nuclear weapons tests in the vicinity may also cause changes in fracture aperture. Potential sources of earthquakes include regional faults such as the Death Valley-Furnace Creek and Bare Mountain Faults, subregional faults such as the Solitario Canyon, Bow Ridge, and Paintbrush Canyon Faults, and locally important faults such as the Ghost Dance and Sundance Faults (cf. Young et al., 1992; Scott, 1990; Spengler et al., 1994). There are examples of observed seismically induced hydrologic changes that have been attributed to large-scale changes in rock-mass permeability (cf. Rojstaczer and Wolf, 1992; Ofoegbu et al., 1994). It has been demonstrated that, although the deformations due to an individual small-magnitude earthquake may be negligible, the cumulative deformations due to successive (small or large) earthquakes can be quite large

(Hsiung et al., 1992). The effects of such cumulative deformations on the magnitudes and distribution of rock-mass permeability can be evaluated through numerical modeling.

1.1.3 Geochemical Effects on Rock-Mass Permeability

The geochemical effects on rock-mass permeability are expected to be related mainly to the dissolution and precipitation of minerals on fracture walls (cf. Lin and Daily, 1989; de Marsily, 1987). Both processes are likely to be affected by temperature; furthermore, they may be affected by the prevailing values of fracture aperture. No tool is currently available for fully coupled modeling of thermomechanical interactions with geochemical processes; however, it may be possible to evaluate such interactions through the exchange of input and output parameters between geochemical-hydrological and thermomechanical models.

1.2 STABILITY OF REPOSITORY OPENINGS

There are concerns for both the short- and long-term stability of the underground openings (emplacement drifts, and service tunnels, shafts, and ramps) within the GROA. The concern for short-term stability relates to the worker-safety requirements [10 CFR 60.131(b)(9)], and especially the waste-retrievability requirement defined in 10 CFR 60.111(b): The GROA shall be designed to preserve the option of waste retrieval throughout the period during which wastes are being emplaced and, thereafter, until the completion of a performance confirmation program and NRC review of the information obtained from such a program. The extent to which the stability of the openings may affect compliance with the retrievability requirements will depend on the specific methods of retrieval proposed in the GROA design.

The concern for stability beyond permanent closure of the repository relates to the effects of rock movements on the integrity of the WPs and on water flow within the near-field. The issue of water flow relates to the possibility of changes in rock mass permeability as a result of rock deformation, which was discussed in Section 1.1.2. The concern for WP integrity arises because surface flaws such as dents may develop on the WPs as a result of impact by rock blocks. Such flaws may become sites for localized corrosion, which is important in the prediction of WP lifetime. The probability of such impacts occurring, and the magnitude of their effects on the WPs depends on factors such as the ambient stress field (including thermally induced stress), the orientations and density of fractures, shear resistance of fracture surfaces, and the magnitude and frequency of seismically induced forces. The possibility of rock-strength deterioration due to chemical alteration of fracture walls, which was mentioned in Section 1.1.2, may also be important in evaluating the postclosure stability of the repository openings, as well as the probability of significant block impacts on the WPs.

The evaluation of both the short- and long-term stability of the repository openings requires the capability to resolve the contributions of rock stress (including thermal stress), network of fractures, seismicity, and progressive strength deterioration. Such capability can most likely be achieved through numerical modeling.

1.3 EVALUATION OF COMPUTER CODES

A study was undertaken by the Center for Nuclear Waste Regulatory Analyses (CNWRA) to select a computer code, or combination of computer codes, for the evaluation of DOE compliance with

NRC regulations on thermal loads, for the proposed YM repository. Such codes are expected to be used for the verification of repository-design calculations, related to KTUs in the areas of repository-opening stability and near-field water flow. The codes should have the capabilities to model the following:

(i) Individual mechanical, thermal, and hydrological processes in a fractured rock mass;

(ii) The mechanical, thermal, and hydrological responses of rock fractures;

(iii) Coupled thermal-mechanical (TM), thermal-hydrological (TH), mechanical-hydrological (MH), and thermal-mechanical-hydrological (TMH) processes in a fractured rock mass; and

(iv) Seismic loading superimposed on mechanical and thermal loads.

In addition, there should be provisions for user-modifications of such codes, either through the availability of the source codes to the user or through built-in user interfaces. The user-modification requirement was included to enable the implementation of specific changes considered necessary and feasible to improve the capabilities of a selected code.

An examination of 15 computer codes with reference to these requirements was conducted, using information available in their users' manuals and other publications (Ghosh et al., 1993). Based on the examination, the distinct element code UDEC (ITASCA Consulting Group, Inc., 1993) and the finite element code ABAQUS (Hibbitt, Karlsson and Sorensen, Inc., 1994) were selected for further evaluation.

The TMH modeling capabilities of UDEC were evaluated (Brady et al., 1990; Hsiung et al., 1994a; Ahola et al., 1992; 1993) under the Seismic Rock Mechanics Research Project (Ghosh et al., 1995). The performance of the code in modeling the mechanical response of fractured rock under both static and dynamic loading was evaluated with respect to four benchmark problems and a series of laboratory measurements. In addition, the code was evaluated against one MH and two TMH problems under the international cooperative project DECOVALEX (DEvelopment of COupled models and their VALidation against EXperiments in nuclear waste isolation). Also, the capabilities of ABAQUS in modeling mechanical processes were evaluated (Ghosh et al., 1994), with respect to the same set of four benchmark problems, as well as two additional problems involving intersecting fractures.

It was determined that the distinct element code UDEC is well suited for the mechanical analyses of rock-mass problems involving large numbers of intersecting fractures. For such cases, it may often be necessary to model explicitly the interactions of the individual rock blocks formed by the fracture network. The internal logic of UDEC was set up for such analyses. On the other hand, because UDEC does not incorporate any mechanisms for modeling fluid flow through rock matrix, it is not suitable for solving hydrological problems in situations for which fracture-matrix interactions may be important. It was, therefore, recommended (Ghosh et al., 1994; Hsiung and Chowdhury, 1991) that UDEC and its three-dimensional (3D) counterpart 3DEC be adopted for the analyses of repository-opening stability problems in which the mechanical response of a fracture network under thermal and mechanical (including seismic) loading is emphasized.

Considering the information available in the ABAQUS users' manuals, it was believed that ABAQUS would be better suited for those TMH problems for which hydrological coupling cannot be ignored. Because the previous evaluation of ABAQUS (Ghosh et al., 1994) examined only the mechanical-processes modeling capabilities of the code, it was recommended that additional evaluation of the code be conducted to examine more aspects of its TMH-modeling capabilities.

1.4 OBJECTIVES

The objectives of the evaluation of ABAQUS are (i) to determine whether the code is suitable for conducting analyses related to KTUs involving TMH coupled processes; and, (ii) if the code is determined to be suitable, to identify modifications to the code that might enhance its TMH-modeling capabilities. The suitability of the code was examined by evaluating its capability to solve selected problems associated with fractured rock mass, each involving one of the following:

(i) Individual mechanical, thermal, and hydrological processes

(ii) Coupled TM, TH, and MH processes

(iii) Coupled TMH processes

A brief description of each of the problems will now be presented. Detailed descriptions of the problems, their method of solution, and the evaluation strategy applied to each problem are presented in subsequent chapters.

1.5 SCOPE

The information presented in this report covers all the work done by the CNWRA on the evaluation of ABAQUS. The part of the work dealing with the code's mechanical-processes modeling capabilities will only be summarized, because the details have been presented elsewhere (Ghosh et al., 1994). Also, the part of the ABAQUS-evaluation work that was done under the DECOVALEX project, which has been discussed in detail in a separate report (Ahola et al., 1994), will only be presented briefly. Therefore, a good fraction of the report will be devoted to a discussion of the ABAQUS-evaluation work done during the 1994 and 1995 fiscal years.

1.5.1 Mechanical Problems

The mechanical problems have been described in detail by Ghosh et al. (1994) and are summarized in Chapter 2. The ABAQUS analyses conducted in this category were performed using Versions 5.2 and 5.3 of the code.

1.5.2 Thermal Problem

One problem was solved in this category. It examined the flow of heat and development of thermal stresses and deformations in a thick-walled cylinder with incomplete annular cracks. Special attention was given modeling heat flow across cracks using interface elements. The response of the elements was examined under two extreme cases of thermal conductivity. The problem is discussed in

Chapter 3. The ABAQUS analyses conducted in this category were performed using Version 5.3 of the code.

1.5.3 Hydrological Problems

Two hydrological problems were solved, dealing with the flow of water in unsaturated rock mass. The first problem examined matrix flow only, whereas the second examined fracture-matrix interactions. In both cases, water was made available at the top of an unsaturated rock column, and the progress of the wetting front was monitored as a function of time. The two problems are presented in Chapter 4. The ABAQUS analyses conducted in this category were performed using Versions 5.3 and 5.4 of the code.

1.5.4 Thermal-Mechanical Problems

Two cases of a heated drift in a fractured rock mass were examined under this category. In one case the drift was intersected by three sets of fractures and was considered to lie in the interior of a rectangular array of horizontal drifts. In the other case, the drift was intersected at its crown by a single vertical fracture; it was considered to lie in the middle of a linear array of horizontal drifts, so its interaction with the ground surface was included in the analyses. In both cases, the drift wall was subjected to a prescribed temperature history, to simulate the thermal load due to emplaced waste, and the distributions of stresses and fracture aperture were monitored. The first problem was solved in two dimensions, whereas the second was solved in both two and three dimensions. Both problems are discussed in Chapter 5. The ABAQUS analyses conducted in this category were performed using Versions 5.3 and 5.4 of the code.

1.5.5 Thermal-Hydrological Problems

One problem was solved in this category. It examined the development and dissipation of excess pore-water pressure in a rock medium surrounding a cylindrical heat source. Two cases of the problem were solved, one for a saturated medium and the other for unsaturated conditions. Both are discussed in Chapter 6. The ABAQUS analyses conducted in this category were performed using Version 5.4 of the code.

1.5.6 Mechanical-Hydrological Problem

The one problem solved in this category was developed to parallel a laboratory experiment being conducted at the CNWRA under the DECOVALEX project. It considers the flow of water through a single fracture, with emphasis on the effects of mechanical loading on the permeability of the fracture. The problem is discussed in Chapter 7. Because the laboratory experiment is still at the initial stages, no laboratory data was available for comparison with the calculated results. Such comparison will be performed in connection with a future numerical-model investigation of mechanical effects on rock-mass permeability. The ABAQUS analyses conducted in this category were performed using Version 5.4 of the code.

1.5.7 Thermal-Mechanical-Hydrological Problem

One problem was solved in this category. It examined the numerical modeling of an experiment conducted in Japan under the DECOVALEX project, to evaluate the EBS for the current Japanese radioactive waste disposal concept. The problem examines the development of stresses and water-saturation changes in a bentonitic barrier around a heat source. It is discussed in Chapter 8. The ABAQUS analyses conducted in this category were performed using Version 5.3 of the code.

2 MECHANICAL PROBLEMS

Five sets of mechanical problems were analyzed using ABAQUS in order to examine its modeling of the mechanical processes that may occur in a fractured rock mass. Four of the problem sets are benchmark problems used to evaluate the distinct element code UDEC (Brady et al., 1990). ABAQUS was evaluated by comparing the ABAQUS-calculated responses with the analytical solutions, as well as with solutions obtained using UDEC. Detailed descriptions of the problems and the results have been provided in a previous report (Ghosh et al., 1994).

2.1 CYCLIC LOADING OF SPECIMEN WITH EMBEDDED CRACK

The problem domain consists of a rectangular rock block containing a closed crack that is inclined at an angle α to the direction of loading (Figure 2-1). The rock is assumed to be linearly elastic, homogeneous, and isotropic in the uncracked state. The specimen is fixed at its base, and a downward displacement u_a is applied at its top, thereby causing inelastic slip on the crack surface. The applied displacement is gradually reduced to zero after reaching a specified maximum value.

An analytical model of the problem, developed by Olsson (1982) and Brady et al. (1985), is illustrated in Figure 2-2. The elastic stiffness of the rock specimen parallel to its long dimension is represented by a spring of stiffness k, whereas the elastic stiffness parallel to the crack is represented by K_s. The stress-displacement relation for the specimen based on this model is illustrated in Figure 2-3. The stress-displacement relation consists of three distinct segments, as follows:

(i) A loading segment, OA, which involves elastic deformation of the intact rock and inelastic slip along the crack;

(ii) An initial unloading segment, AB, where the crack does not slip and the measured deformation is the true elastic deformation of the rock; and

(iii) A final unloading segment, BO, which represents elastic deformation of the rock block and inelastic slip of the crack.

Analytical expressions for the slopes of the three segments are given in Ghosh et al. (1994), in terms of the Young's modulus, E, of intact rock, the normal and shear stiffnesses of the crack, K_n and K_s, respectively, the dimensions of the block and embedded crack, and the angle of inclination of the crack.

2.1.1 Numerical Model Results

The rock block specimen was modeled using ABAQUS and UDEC for the set of parameters given in Table 2-1. The results obtained using the two codes, and the analytical solution based on the conceptual model, are shown in Table 2-2 and Figure 2-4.

There is no simple and completely rigorous analytical solution to the problem of an elastic body with an internal slipping crack. The analytical solution ignores the stress concentration near the crack tips. The results illustrated in Figure 2-4 and Table 2-2 show that both ABAQUS and UDEC can model the hysteresis observed in cyclic loading of a slipping crack in a rock specimen. The results agree well with the analytical model; however, the results will agree less closely as the length of the slipping crack increases with respect to the width of the specimen. Such deviation is expected because the conceptual model assumes uniform distribution of normal stress on the crack, and the elastic bridges and stress

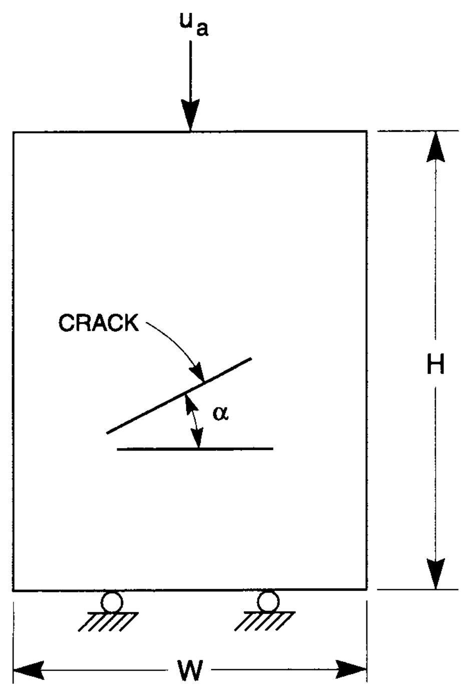

Figure 2-1. Problem geometry for rock specimen with an embedded crack

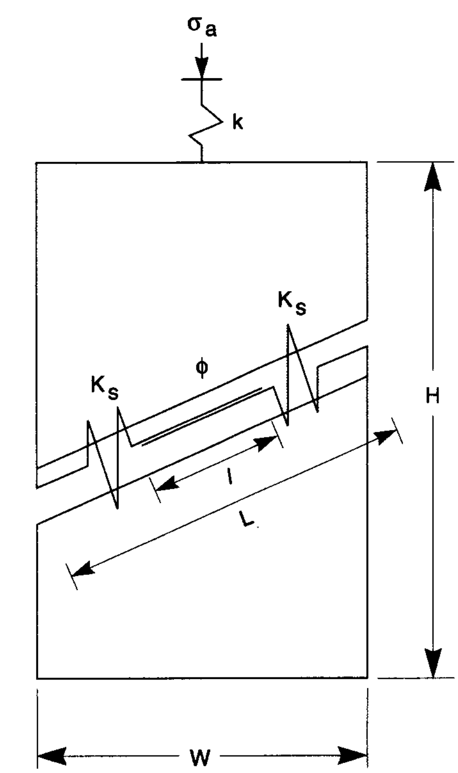

Figure 2-2. Conceptual model of an elastic specimen with an embedded crack (after Brady et al., 1985)

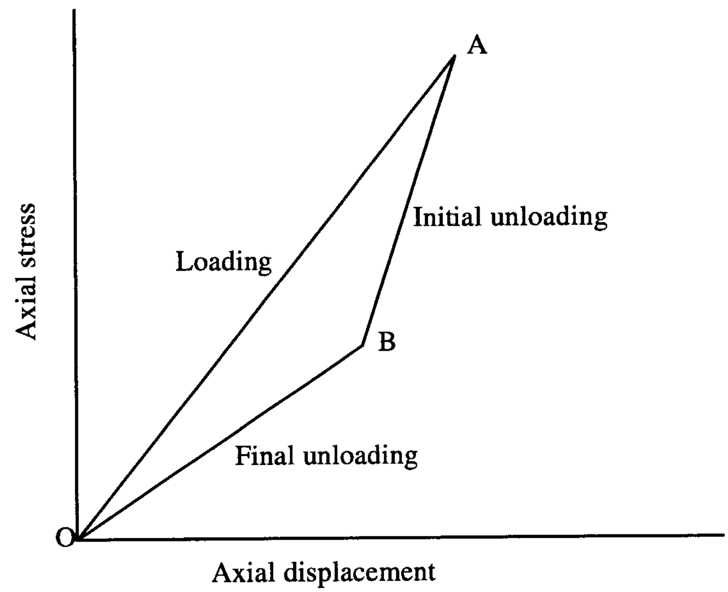

Figure 2-3. Stress-displacement relationship for an elastic specimen with an embedded crack subjected to a uniaxial load cycle (after Olsson, 1982)

Table 2-1. Material and model parameters for elastic specimen with embedded crack

Material and Model Parameters	Value
Height, H	2 m
Width, W	1 m
Crack inclination, α	45°
Crack length, l	0.54 m
Young's modulus, E	88.9 GPa
Poisson's ratio, ν	0.26
Crack normal stiffness, K_n	220 GPa/m
Crack shear stiffness, K_s	220 GPa/m
Crack friction angle	16°

concentrations become more significant as the length of the elastic bridge between the crack and the specimen boundary decreases.

ABAQUS is somewhat stiffer, whereas UDEC is slightly softer than the analytical solution. This difference in stiffness probably is due to the fundamental difference in the solution process. ABAQUS is a displacement-based finite element code. As the displacement is interpolated from element to element, it is expected that the model will be somewhat stiffer than the actual structure. Use of triangular elements to model the fracture might also have contributed to the deviation from the analytical solution. Conversely, UDEC is energy or force based. Consequently, it produces a somewhat softer model of the structure.

Table 2-2. Comparison of ABAQUS and UDEC results with those based on the conceptual model

Segment	Conceptual Model	ABAQUS Model		UDEC Model	
	Stiffness (GPa/m)	Stiffness (GPa/m)	Percent Error	Stiffness (GPa/m)	Percent Error
Loading OA	36.28	42.69	−17.7	36.04	+0.66
Unloading AB	38.89	44.84	−15.3	38.91	−0.05
Unloading BO	34.42	41.18	−19.6	34.14	+0.81

2.2 CIRCULAR EXCAVATION IN INFINITE MEDIUM, WITH HORIZONTAL JOINT NEAR THE CROWN

A circular opening of radius 5 m is excavated in an infinite, homogeneous, isotropic, and elastic medium. The geometry of the problem is illustrated in Figure 2-5. A horizontal weakness plane (joint) of infinite extent intersects the excavation at an elevation of 4.33 m above the horizontal centerline. The point of intersection of the weakness plane with the excavation wall is at an angle of 60° counterclockwise from the x-axis. The *in situ* stress field is hydrostatic and equal to 24 MPa. The problem was solved using ABAQUS and UDEC for the set of parameters given in Table 2-3.

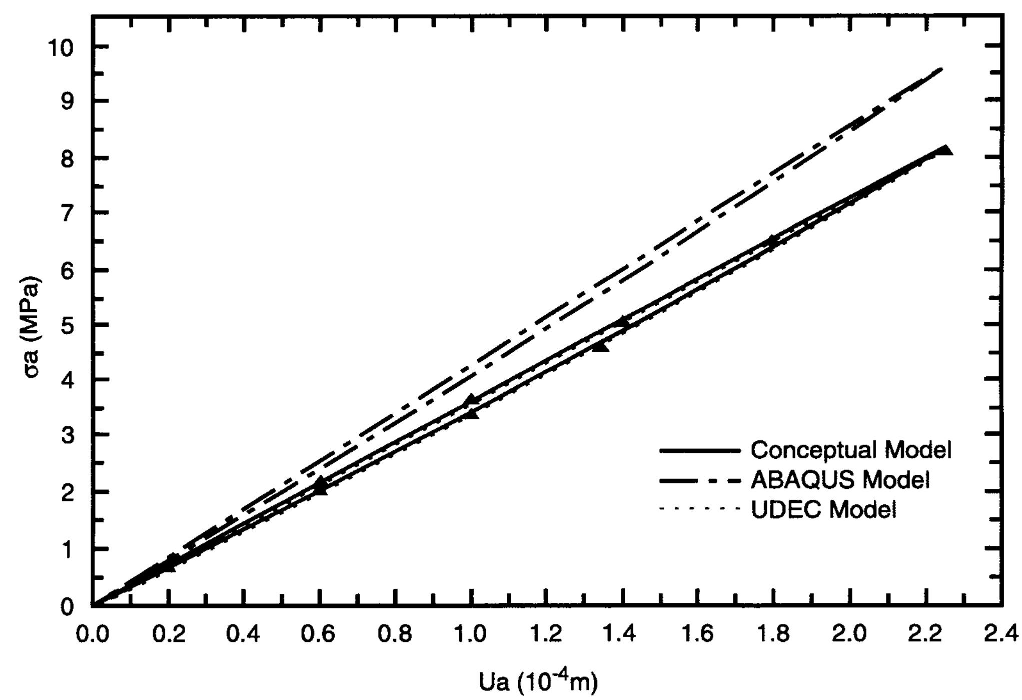

Figure 2-4. Comparison of ABAQUS and UDEC results with the analytical solution

The calculated stress components normal and tangential to the weakness plane are plotted in Figure 2-6. The stresses are normalized by dividing with the *in situ* hydrostatic stress. The results calculated using the two codes are satisfactorily close. They also compare well with results based on the Kirsch solutions for stresses around circular openings (cf. Brady and Brown, 1985; Ghosh et al., 1994).

Table 2-3. Material parameters for circular excavation with near-crown horizontal joint

Parameter	Value
Density	10 kg/m^3
Shear modulus	35 GPa
Bulk modulus	60 GPa
Normal stiffness of joint	200 GPa/m
Shear stiffness of joint	200 GPa/m
Cohesion for joint	0
Friction angle for joint	16.3°

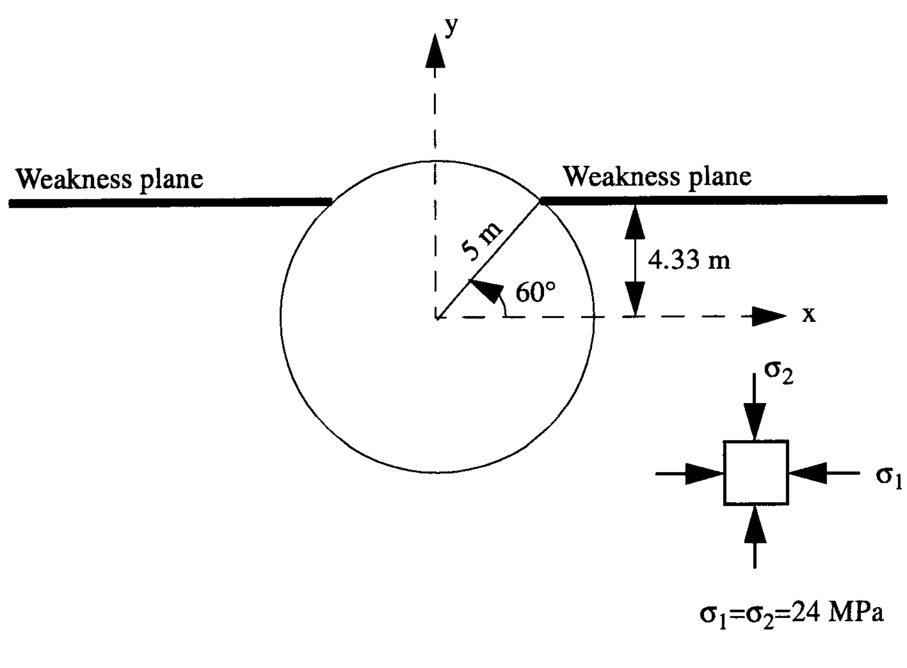

Figure 2-5. Problem geometry for circular excavation with horizontal joint near its crown

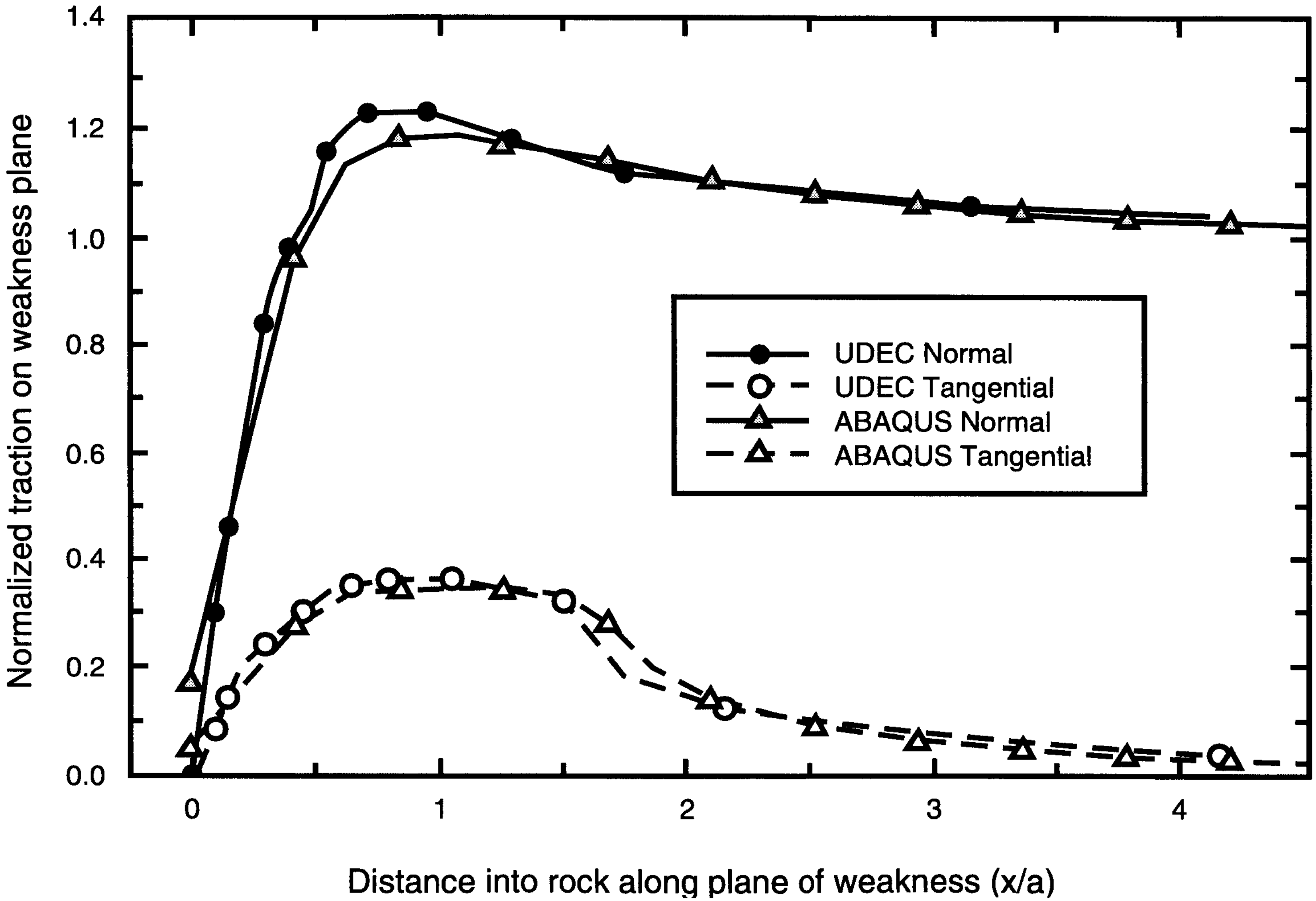

Figure 2-6. Normalized shear and normal stresses on the weakness plane, calculated using ABAQUS and UDEC

2.3 SLIP ON A JOINT INDUCED BY HARMONIC SHEAR WAVE

This problem deals with the dynamic response of a planar discontinuity subjected to a normally incident plane harmonic shear wave. The geometry of the problem is illustrated in Figure 2-7. It consists of a rock discontinuity of infinite extent that lies within an infinite, homogeneous, isotropic, and elastic rock mass. The shear strength of the discontinuity surface is characterized by zero friction angle and nonzero cohesion, which implies a constant shear strength (independent of normal stress). As a result, the discontinuity will slip if the transient shear stress induced by the shear wave equals or exceeds the cohesion. If slip occurs, the energy of the incident wave is partitioned between reflected and transmitted waves and absorption at the interface. The problem was analyzed using UDEC (Brady et al., 1990) and ABAQUS for the set of material parameters in Table 2-4.

Table 2-4. Material parameters for wave propagation in an elastic medium with a single horizontal discontinuity

Parameter	Value
Density	2.65 kg/m^3
Shear modulus	10 GPa
Bulk modulus	16.667 GPa
Normal stiffness of discontinuity	10 GPa/m
Shear stiffness of discontinuity	10 GPa/m
Friction angle for discontinuity	0
Cohesion for discontinuity	0.25, 0.5, 0.75, and 5 MPa

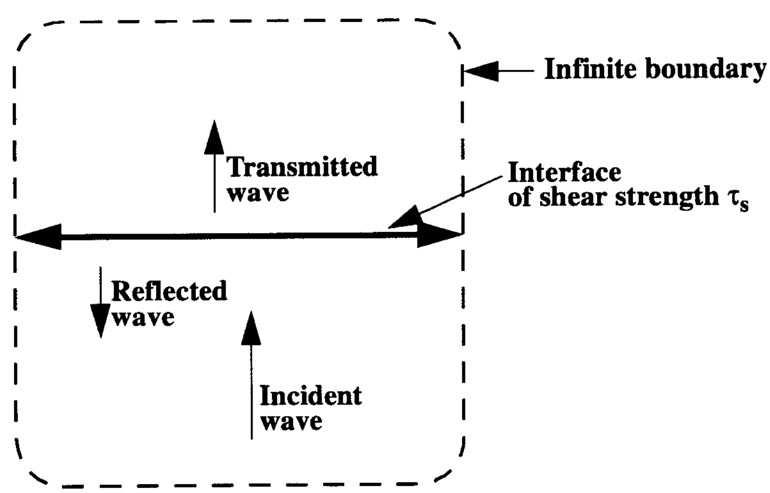

Figure 2-7. Problem geometry for wave propagation in an elastic medium with a single horizontal discontinuity

2.3.1 ABAQUS Model

The model used for the ABAQUS analyses of the problem (Ghosh et al., 1994) includes the following features:

(i) The top and bottom boundaries of the model were modeled using infinite elements. In dynamic analyses, such elements are intended to prevent the reflection of energy at the boundary, thereby simulating the energy-absorbing character of an infinite domain.

(ii) The standard constitutive model available to interface elements in ABAQUS is based on purely frictional shear strength (i.e., $\tau=\mu\sigma_n$, where τ is the shear strength, μ is the friction coefficient, and σ_n is the interface normal stress). An alternative constitutive model based on a purely cohesive shear strength (i.e., $\tau=c$, where c is the cohesion) was implemented for the elements, using the FRIC user-subroutine interface.

(iii) Because ABAQUS does not provide any direct way of applying external shear stress on the surfaces of solid elements, the input sinusoidal shear was applied indirectly through beam elements. Axial force was applied along beam elements attached to (and coincident with) one side of a row of solid continuum elements. The stiffness of the beam elements was set to a small value relative to that of the solid elements to ensure that the beams do not significantly add to the stiffness of the medium at the location of such elements.

2.3.2 Results

Figures 2-8 and 2-9 show typical results obtained for the problem. Points A and B in the figures refer to observation points at 195 m below and above the discontinuity, respectively. The two figures show the history of shear stress at points A and B in response to a horizontal shear stress wave of amplitude 1 MPa, originating at a depth of 200 m below the discontinuity.

Figure 2-8 is for the case of 5-MPa cohesion for the discontinuity. The applied shear stress is insufficient to cause slip; therefore, the medium should respond elastically. The two codes (ABAQUS and UDEC) gave identical results for this case. The shear-stress-wave traces calculated for the two points have peak amplitudes of 1 MPa separated by a time increment equal to the wave transmission time between the points. These identical results indicate that the elastic waves were transmitted perfectly through the rock-interface models in the two codes. The results in this figure are also interpreted to indicate that the infinite elements performed well in this analysis. Waves reflected from the top and bottom boundaries (at 300 m above and below the discontinuity) would have reached the observation points with a phase shift of about 0.1 s, and the effect of the reflected wave would have been clearly noticeable in Figure 2-8. The fact that there was no such effect means that waves hitting the boundary were perfectly transmitted. The infinite elements in ABAQUS are expected to be 100 percent effective when the infinite/finite boundary is normal to the direction of wave propagation; this expectation is confirmed in this analysis.

Figure 2-9 is for the case of 0.5-MPa cohesion for the discontinuity and is typical of cases for which the shear strength (cohesion) of the discontinuity is less than the applied shear stress. For such cases, the peak of the transmitted wave should be truncated at a value equal to the cohesion. The observed response at point B shows a truncation at 0.5 MPa, which is in agreement with the expected response. Both ABAQUS and UDEC predicted the response correctly (Ghosh et al., 1994). Also, the shear stress history at a point below the discontinuity should show a peak of 1.0 MPa due to energy transmitted directly from the

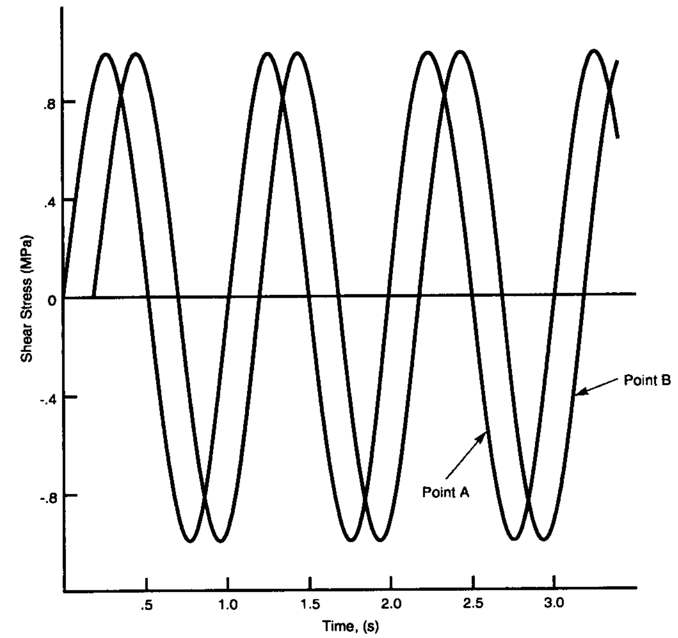

Figure 2-8. History of shear stress at the observation points for the case of 5-MPa cohesion for the discontinuity (Points A and B are 195 m below and above the discontinuity, respectively)

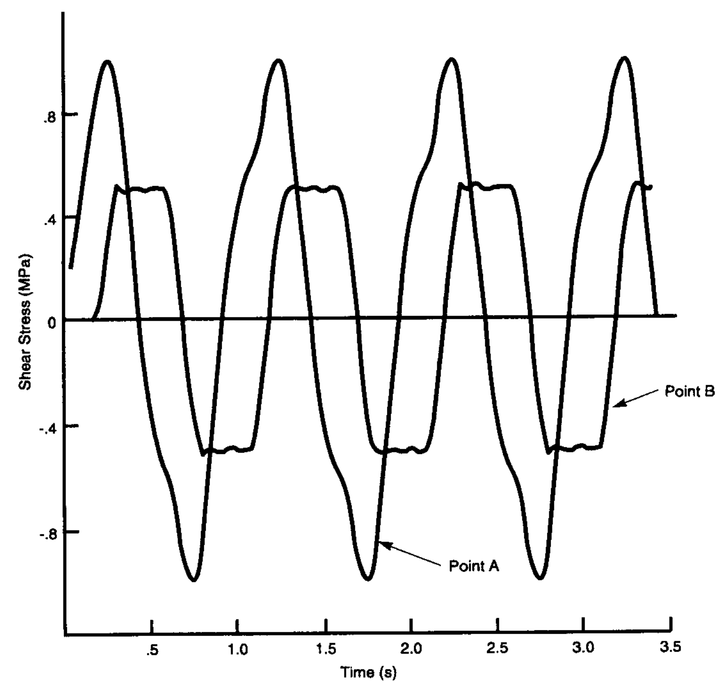

Figure 2-9. History of shear stress at the observation points for the case of 0.5-MPa cohesion for the discontinuity (Points A and B are 195 m below and above the discontinuity, respectively)

source and a secondary peak due to energy reflected from the slipping interface. The secondary peak should become more pronounced as the shear strength of the interface decreases (i.e., as the fraction of reflected energy increases). Again, both ABAQUS and UDEC predicted this aspect of the response correctly.

2.4 LINE SOURCE OF DYNAMIC ENERGY CLOSE TO A DISCONTINUITY IN AN INFINITE MEDIUM

This problem deals with the dynamic behavior of a single discontinuity under explosive loading. The geometry of the problem is illustrated in Figure 2-10. It consists of a horizontal discontinuity of infinite lateral extent embedded in an elastic medium. An impulsive dynamic load is applied along an infinite horizontal line that is normal to the discontinuity, and at an elevation *h* above it. A closed-form solution for the problem, which gives the magnitude of slip as a function of time, was derived by Day (1985) as a special symmetric condition for the general problem of slip on a discontinuity due to a dynamic point source (Salvado and Minster, 1980). The problem was solved using ABAQUS, and the calculated response was compared with those obtained using UDEC and the analytical solution (Brady et al., 1990; Ghosh et al., 1994). The problem was selected to examine the capabilities of ABAQUS to simulate: (i) the dynamic response of a rock discontinuity under impulsive loading, (ii) high-frequency dynamic waves emanating from a buried explosive, and (iii) nonreflecting boundary conditions. The problem was solved for the set of parameters in Table 2-5.

Table 2-5. Material and geometrical parameters for the analysis of a dynamic line-load close to a discontinuity

Parameter	Value
Elevation of line load above discontinuity, *h*	10 m
Density	1 kg/m^3
Shear modulus of medium material	100 Pa
Bulk modulus of medium material	166.67 Pa
Compressional wave velocity	17.32 m/s
Shear wave velocity	10.0 m/s
Shear strength of discontinuity	0

The responses calculated using ABAQUS, UDEC, and the analytical solution are shown in Figure 2-11, in terms of the history of slip on the discontinuity at a horizontal distance of 10 m from the line source. In the figure, dimensionless slip refers to the ratio $4h\rho c^2(\Delta u)/m_o$ and dimensionless time is the ratio tc/h, where h=10 m is the elevation of the line source above the discontinuity, ρ=1 kg/m^3 is the density of the medium, c=10 m/s is the shear wave velocity for the medium, Δu is the slip in meter, m_o=1 N is the source strength, and t is the time in seconds. As the figure shows, there is satisfactory agreement among the three solutions.

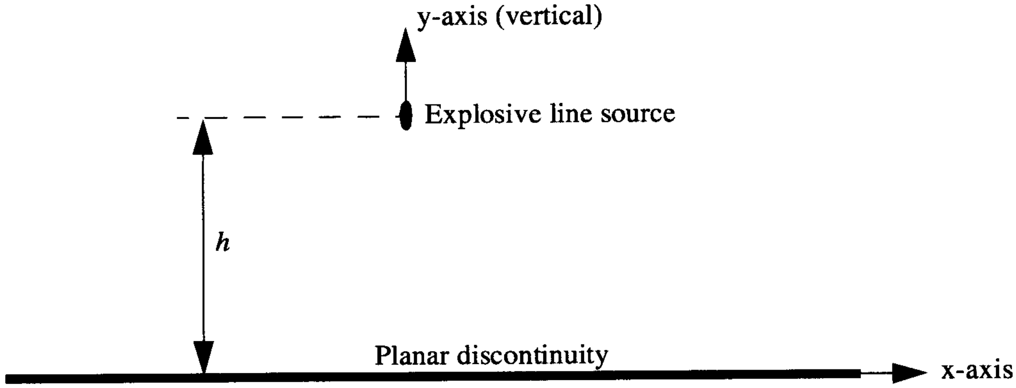

Figure 2-10. Problem geometry for dynamic line load close to a discontinuity

2.5 INTERSECTING JOINTS

Two problems were solved to investigate the response of the ABAQUS interface elements for modeling intersecting rock discontinuities. Because the geometry of the two problems and the results obtained are similar, only one of them is described in this report. The two problems are described in detail by Ghosh et al. (1994). The geometry of one of the problems is illustrated in Figure 2-12. It consists of four rock blocks arranged to give two orthogonal fractures. The blocks were restrained as shown in the figure: that is, B1 at the base, B2 at the top and right edges, and B3 at the left edge. The contacts between the blocks were modeled using interface elements.

An x-displacement of 19.4 cm was applied on the left edge of block B4 followed by an equal amount of y-displacement on the bottom edge. The shape of the model at the end of the displacement application is shown in Figure 2-13. The applied displacement caused blocks B4 and B1 to move 19.4 cm in the x-direction, and B4 and B3 an equal amount in the y-direction. As a result, block B4 penetrated into B2 by a diagonal distance of about 27.4 cm. That is, the corner-to-corner contact between blocks B4 and B2 was not simulated correctly by the interface elements.

The developers of ABAQUS[1] explained that the result of the analysis is expected, because there is no communication in the model between B4 and B2. All four blocks participate in the model as separate entities. Block B4 communicates with B1 and B3 through the interface elements; blocks B1 and B2 communicate the same way, as do blocks B2 and B3. There is no such connection between B2 and B4. The results of this problem led to the conclusion that the ABAQUS interface elements should not be used to model fractures that intersect within the problem domain.

1. Telephone conversation between the authors and representatives of Hibbit, Karlsson, and Sorensen, Inc.

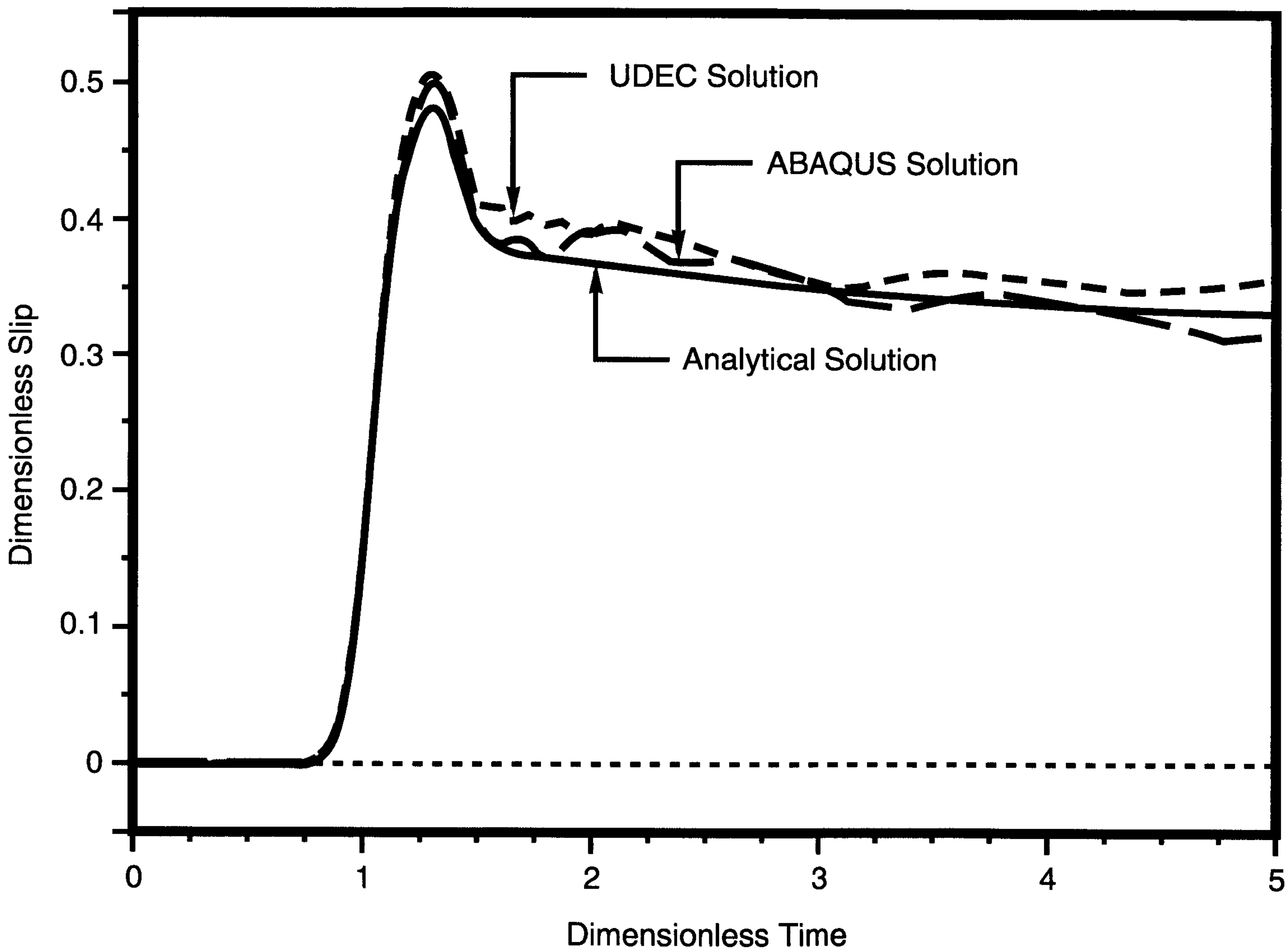

Figure 2-11. History of slip on the discontinuity at 10 m horizontally from the line source

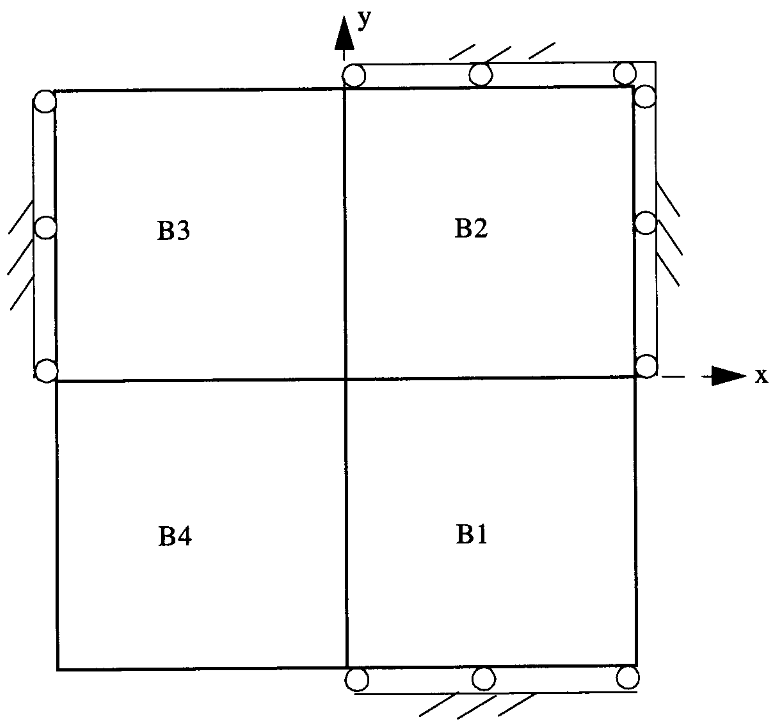

Figure 2-12. Problem geometry for intersecting joints

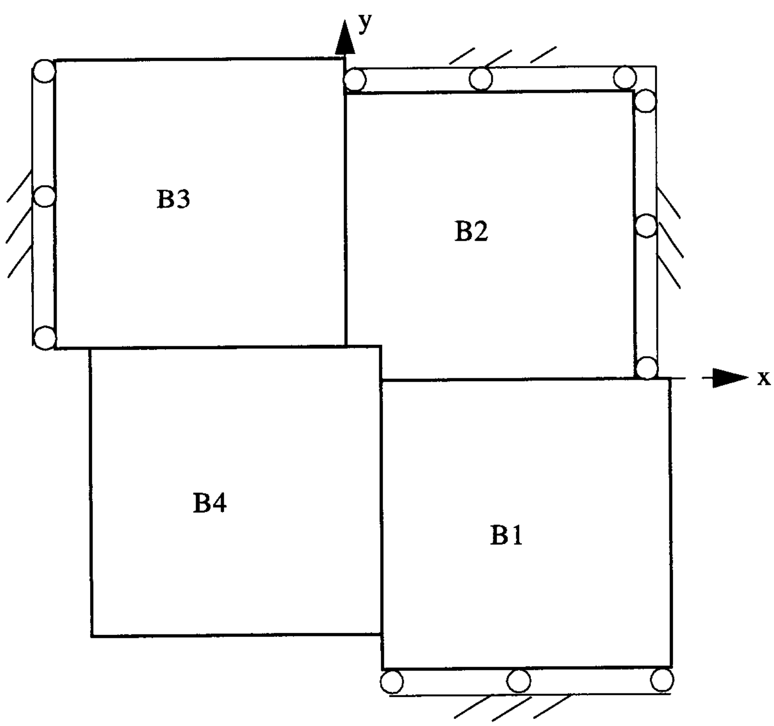

Figure 2-13. Final arrangement of the blocks after the application of displacements

2.6 CONCLUSIONS

In this chapter, the computer code ABAQUS was evaluated with respect to its capabilities to model the mechanical response of rock fractures, under both static and dynamic loading. Rock fractures were modeled using interface elements in all the problems solved. The code was evaluated by comparing its calculated responses with those calculated using the distinct element code UDEC, as well as with the analytical solutions for the same problems where analytical solutions are available. The code was judged to have performed satisfactorily for all cases of nonintersecting fractures. The interface elements did not perform satisfactorily in modeling intersecting fractures.

3 THERMAL PROBLEMS: HEAT FLOW IN A THICK-WALLED CYLINDER WITH ANNULAR CRACK

The problems solved under this category were selected to examine the modeling of heat flow across fractures using the ABAQUS interface elements. The interface elements are provided in ABAQUS for modeling discontinuities in solid bodies, such as rock joints, bedding planes, and faults. They are provided with the capabilities to model the mechanical, thermal, and hydrological effects of such discontinuities.

There is little evidence in the literature regarding the effect of discontinuities on the thermal response of a rock mass. Lin et al. (1991) reported experimental data that suggested that fractures may reduce the effective thermal conductivity of a rock mass, in the direction normal to the fractures. On the other hand, they concluded that the overall effect of fractures on heat flow is very small. It is expected that the effect of discontinuities on the thermal performance of a rock mass will vary, depending on such things as the aperture, orientation, and filling. Therefore, it is likely that the decision regarding the significance of their effect may be made by analyzing specific cases. The purpose of this problem set is to determine if the ABAQUS interface elements may be suitable for such analyses.

3.1 PROBLEM GEOMETRY AND MATERIAL PROPERTIES

The problems consider heat flow and thermal stress development within a thick-walled cylinder of internal and external radii a and b, respectively. The temperature on the interior surface, that is at $r=a$ (where r is the radial distance from the axis of the cylinder), is fixed at T_a; at the exterior surface, that is at $r=b$, it is fixed at T_b. A cross section normal to the axis of the cylinder is shown in Figure 3-1. As the figure shows, the specific dimensions for this problem are a=4.5 m and b=50 m. The cylinder has two incomplete annular cracks at r=9 m; one crack extends from θ=−45° to θ=45°, and the other from θ=135° to θ=225°, where θ is the angle measured counter-clockwise from the right-extending horizontal radius, as shown in the figure. Both cracks had an initial aperture of 2 mm. The interior and exterior temperature settings are T_a=300 °C and T_b=25 °C. An initial temperature of 25 °C, corresponding to the zero-strain state, was applied everywhere. The material of the cylinder is assumed to be similar to the Topopah Spring welded tuff, and the parameters were assigned values taken from the Reference Information Base (RIB), Version 4.4 (cf. Hardy et al., 1993), as shown in Table 3-1.

Table 3-1. Material property specifications for the problem of heated cylinder with annular crack

Property, Symbol, and Unit	Value
Young's modulus, E (MPa)	3.27×10^4
Poisson's ratio, ν	0.25
Coefficient of linear expansion, α (K^{-1})	8.5×10^{-6}
Thermal conductivity, k_θ [MJ/(m·s·K)]	2.1×10^{-6}
Specific heat capacity, C_v [MJ/(m^3·K)]	2.2
Density, ρ (kg/m^3)	2.0×10^3

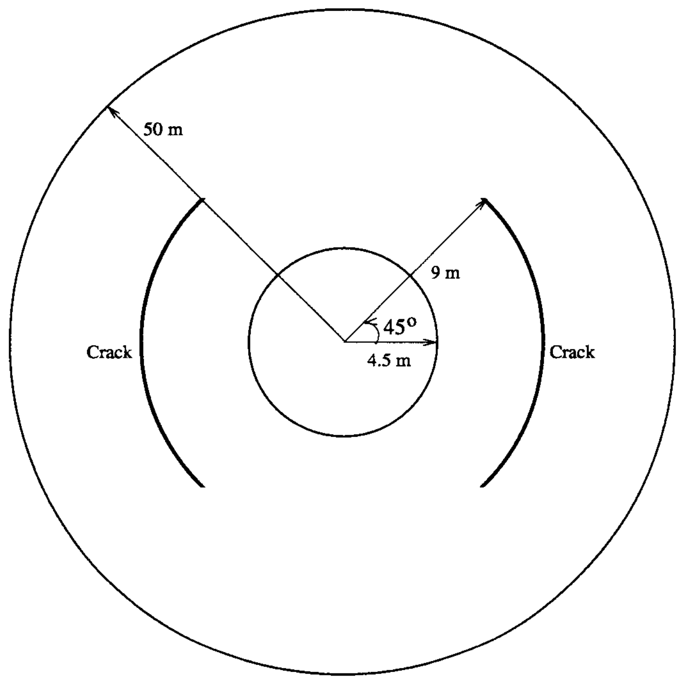

Figure 3-1. Problem geometry for thick-walled cylinder with annular crack

3.2 EVALUATION STRATEGY

The authors are not aware of any available analytical solution for the cracked-cylinder problem illustrated in Figure 3-1. On the other hand, analytical solutions are available for the uncracked thick-walled cylinder, both for temperature distributions and thermally induced mechanical response. Therefore, the performance of ABAQUS with respect to this problem set was evaluated qualitatively, by comparing the ABAQUS-predicted response for the cracked cylinder with the analytically predicted response for the uncracked cylinder.

ABAQUS models heat conduction across the interface elements using a user-specified property referred to as gap conductance. If the value of gap conductance is assigned in such a way as to give the interface elements the same thermal conductivity as the surrounding solid elements, then the temperature distribution calculated for the cracked cylinder should be the same as that of the uncracked cylinder. On the other hand, the temperature distribution for the cracked cylinder for the case of zero gap conductance should show clear evidence of heat flowing around the cracks instead of across them.

Therefore, three problems were solved, as follows:

(i) The problem of steady-state heat flow in the uncracked cylinder was solved analytically for the temperature distribution and thermally induced stresses and displacements.

(ii) The problem of steady-state heat flow in the cracked cylinder, with the crack space assigned the same thermal conductivity as the intact rock, was solved using ABAQUS, for the temperature distribution and thermally induced stresses and displacements. The cracks for this case will be referred to hereafter as fully conducting cracks. The solution for this problem should be the same as for the first one.

(iii) The problem of transient and steady-state heat flow in the cracked cylinder, with the crack space assigned zero thermal conductivity, was solved using ABAQUS, for the temperature distribution and thermally induced stresses and displacements. The cracks for this case will be referred to hereafter as perfectly insulating cracks.

3.3 ANALYTICAL SOLUTION

The steady-state analytical solution for the temperature, T, for the case of the uncracked cylinder, is given by the following equation (Carslaw and Jaeger, 1959):

$$T = \frac{1}{\log(b/a)}\left[T_a \log\left(\frac{b}{r}\right) + T_b \log\left(\frac{r}{a}\right)\right] \tag{3-1}$$

As Eq. (3-1) shows, the only geometrical variable that influences the temperature is the radial distance, r; therefore, temperature contours for this case should form concentric rings around the inner surface of the cylinder. The corresponding analytical solutions for stresses and displacement are given by the following equations (Boley and Weiner, 1960):

$$\sigma_{rr} = \frac{\alpha E}{r^2}\left[\frac{r^2 - a^2}{b^2 - a^2}\int_a^b Tr dr - \int_a^r Tr' dr'\right] \tag{3-2}$$

$$\sigma_{\theta\theta} = \frac{\alpha E}{r^2}\left[\frac{r^2 + a^2}{b^2 - a^2}\int_a^b Tr dr + \int_a^r Tr' dr' - Tr^2\right] \tag{3-3}$$

$$u_r = \frac{\alpha}{r}\left[(1+\nu)\int_a^r Tr' dr' + \frac{(1-\nu)r^2 + (1+\nu)a^2}{b^2 - a^2}\int_a^b Tr dr\right] \tag{3-4}$$

where σ_{rr}, $\sigma_{\theta\theta}$, and u_r are the radial stress, circumferential stress, and radial displacement, respectively. The previous equations, Eqs. (3-2) through (3-4), are for plane-stress conditions. In order to obtain the corresponding solutions for plane strain, the parameters E, α, and ν, are replaced with E_1, α_1, and ν_1, respectively; where

$$E_1 = \frac{E}{1-\nu^2}; \quad \nu_1 = \frac{\nu}{1-\nu}; \quad \alpha_1 = \alpha(1+\nu) \tag{3-5}$$

Equations (3-2) through (3-4) give the thermally induced mechanical response due to an arbitrary temperature distribution, T. The specific equations for the mechanical response due to the temperature distribution specified in Eq. (3-1) were obtained by substituting that equation into Eqs. (3-2) through (3-4). The integral expressions in the resulting equations were evaluated using *Mathematica* (Wolfram, 1991), which gave the following expressions:

$$\int_a^b Trdr = \frac{1}{4\log\left(\frac{b}{a}\right)}\left(b^2\left[T_a - T_b + 2T_b\log\left(\frac{b}{a}\right)\right] - a^2\left[T_a - T_b + 2T_a\log\left(\frac{b}{a}\right)\right]\right) \tag{3-6}$$

$$\begin{aligned}\int_a^r Tr'dr' &= \frac{-a^2}{4\log\left(\frac{b}{a}\right)}\left[T_a - T_b + 2T_a\log\left(\frac{b}{a}\right)\right] \\ &+ \frac{r^2}{4\log\left(\frac{b}{a}\right)}\left[2\left(T_a - T_b\right)\log\left(\frac{b}{r}\right) + T_a - T_b + 2T_b\log\left(\frac{b}{a}\right)\right]\end{aligned} \tag{3-7}$$

Eqs. (3-6) and (3-7) were substituted into Eqs. (3-2) through (3-4) to obtain the expressions for σ_{rr}, $\sigma_{\theta\theta}$, and u_r

3.4 ABAQUS MODEL

There are two possible methods for solving TM problems using ABAQUS. The first is the fully coupled analysis, which is recommended for problems that include mechanical-to-thermal coupling. For example, if it is necessary to account for the effect of changes in fracture aperture on thermal conductivity or the effect of heat generation due to frictional sliding, then the fully coupled approach will be adopted. The second method relies on sequential coupling in order to account for thermal effects on mechanical response. This method is appropriate for problems in which mechanical changes have no effect on heat flow. For example, sequential coupling would be appropriate for analyzing the TM response of a fractured rock if it can be assumed that the effect of fractures on heat flow does not depend on the fracture aperture. In that case, the heat flow analysis and thermal stress analysis can be run separately, using the temperature distribution obtained from the heat flow analysis as input to the thermal stress analysis. ABAQUS provides an interface for using the results of a heat flow analysis in a subsequent mechanical analysis, without any user-manipulation of the heat flow results.

The sequential-coupling method was used in these studies. Because the thermal conductivity of the crack space was assigned either a zero value or a value equal to that of intact rock, it was not dependent on the crack aperture. That is, the problems in this set did not include any mechanical effects on thermal response. As a result, each analysis was conducted in two phases, namely, a heat conduction analysis to obtain the temperature distribution, and a mechanical analysis using the temperature distribution as input.

3.4.1 Thermal Analysis Model

The problem geometry illustrated in Figure 3-1 was selected to permit the use of quarter-symmetry. The problem is symmetrical about the horizontal and vertical lines that pass through the center of the two circles in the figure. Therefore, only the region of the problem bounded by these two lines, which represents one-quarter of the problem, need be analyzed. The finite element discretization of this region is shown in Figure 3-2.

The mesh consists of 1,488 four-noded quadrilateral elements, for modeling intact rock; and 12 four-noded interface elements for the crack. The appropriate elements of these categories for heat conduction analysis are named DC2D4 (solid elements) and DINTER2 (interface elements).

3.4.1.1 Boundary and Initial Conditions

Boundary conditions consist of fixed temperature values at the two circular boundaries (300 °C on the inner circle and 25 °C on the outer circle), and zero heat flux (symmetry condition) normal to the horizontal and vertical boundaries of the model. The initial temperature was set to 25 °C at every node.

3.4.1.2 Material Property Definitions

The material properties required for the solid elements are the thermal conductivity, density, and heat capacity per unit mass (equal to C_v/ρ); these properties were defined as specified in Table 3-1. Heat flow normal to the interface elements is controlled by the gap conductance, μ, which is defined through the equation

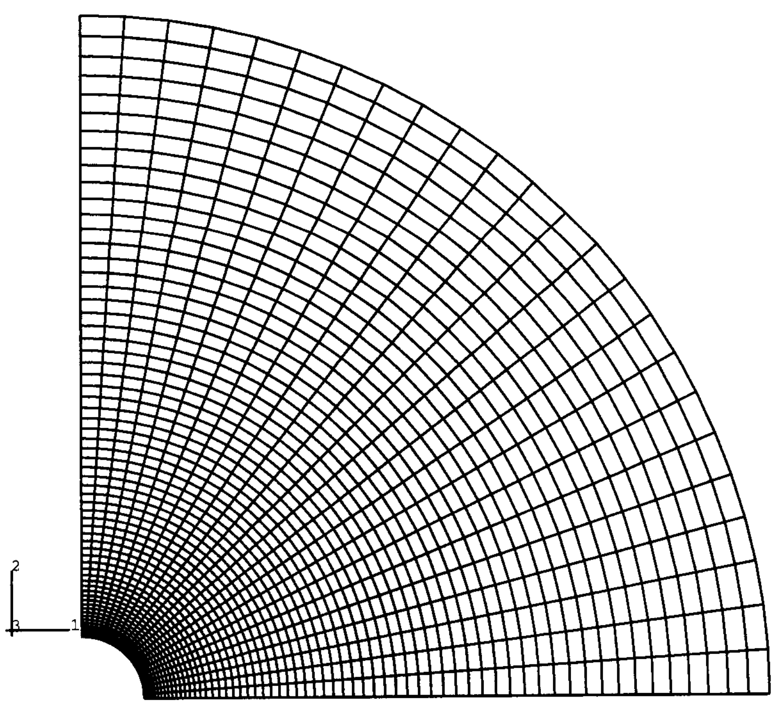

Figure 3-2. Two-dimensional finite-element discretization of the cracked thick-walled cylinder

$$q = \mu(\theta_A - \theta_B) \tag{3-8}$$

where q is the heat flux (quantity of heat per unit time per unit area) in the normal direction of the interface element, θ_A is the temperature at point A on one surface of the element, and θ_B is the temperature at point B on the opposite surface (the line AB is normal to the element surface). ABAQUS requires the user to specify the value of μ as a function of crack aperture or normal pressure. It was specified as a constant in these studies. In order to assign the crack space the same thermal conductivity as the intact rock, the value of μ was calculated as follows:

$$\mu = \frac{k_\theta}{d} \tag{3-9}$$

where d is the crack aperture. The value of d was fixed at 2 mm during the heat flow analysis, which implies a value of 1.05×10^{-3} MJ/(m^2·s·K) for μ.

3.4.1.3 Loading Procedure

Each of the steady-state analyses was conducted in one step, during which the fixed boundary temperatures were applied instantaneously in a "*HEAT TRANSFER, STEADY STATE" procedure. The transient analysis was conducted in five steps, to generate the temperature distributions at the end of 1 hr, 1 d, 100 d, 1 yr (i.e., 365 d), and 10 yr. The fixed boundary temperatures were applied instantaneously during the first step of the transient analysis. The values of temperature at all nodal points were stored in a file at the end of each analysis step, using the "*NODE FILE" command. This file constitutes the interface between the heat-transfer and mechanical analyses in a sequentially coupled thermomechanical analysis in ABAQUS. It is necessary that node numbers in the thermal and mechanical models refer to the same nodal points, in order that the information in the temperature file be transferred correctly to the mechanical model.

3.4.2 Mechanical Analysis Model

The same finite element mesh (shown in Figure 3-2) was used for both the mechanical and thermal analyses. The nodal point numbers are the same for both analyses, and all elements are four-noded quadrilaterals. On the other hand, whereas the DC2D4 and DINTER2 elements were used for the thermal analyses, the mechanical analyses required CPE4 and INTER2 elements for the intact solid and cracks, respectively.

3.4.2.1 Boundary and Initial Conditions

The only user-specified mechanical boundary conditions in this problem arise from symmetry, and consist of no vertical displacement along the horizontal boundary and no horizontal displacement along the vertical boundary. The initial conditions are a temperature of 25 °C and zero stress and strain everywhere.

3.4.2.2 Material Property Definitions

The required material parameters are the Young's modulus, Poisson's ratio, and coefficient of linear expansion for the solid. These parameters were assigned the values specified in Table 3-1.

3.4.2.3 Loading Procedure

Mechanical analyses were performed for the steady-state temperature distributions only, and each of the analyses was conducted in a single-step *STATIC procedure, during which the temperature distribution was introduced using the *TEMPERATURE command. No mechanical analysis was performed for the transient temperature distributions, because the transient heat-transfer analyses were performed only to ensure that the long-term temperature distribution obtained for the case of the perfectly insulating crack is consistent with the steady-state temperature distribution obtained for the same case.

3.5 RESULTS

3.5.1 Temperature Distributions

Temperature distributions are presented in this section to compare the ABAQUS solutions for the cases of fully conducting and perfectly insulating cracks with the analytical solution for the case of the uncracked solid. Figure 3-3 shows the temperature contours calculated using ABAQUS for the case of fully conducting cracks. Values of temperature in the figure are in °C. The dark dotted line in the figure marks the location of the crack. As the figure shows, the cracks in this case have no effect on the temperature distribution; the temperature contours form concentric rings around the inner surface of the cylinder, which is the same result given by the analytical solution presented in Section 3.3.

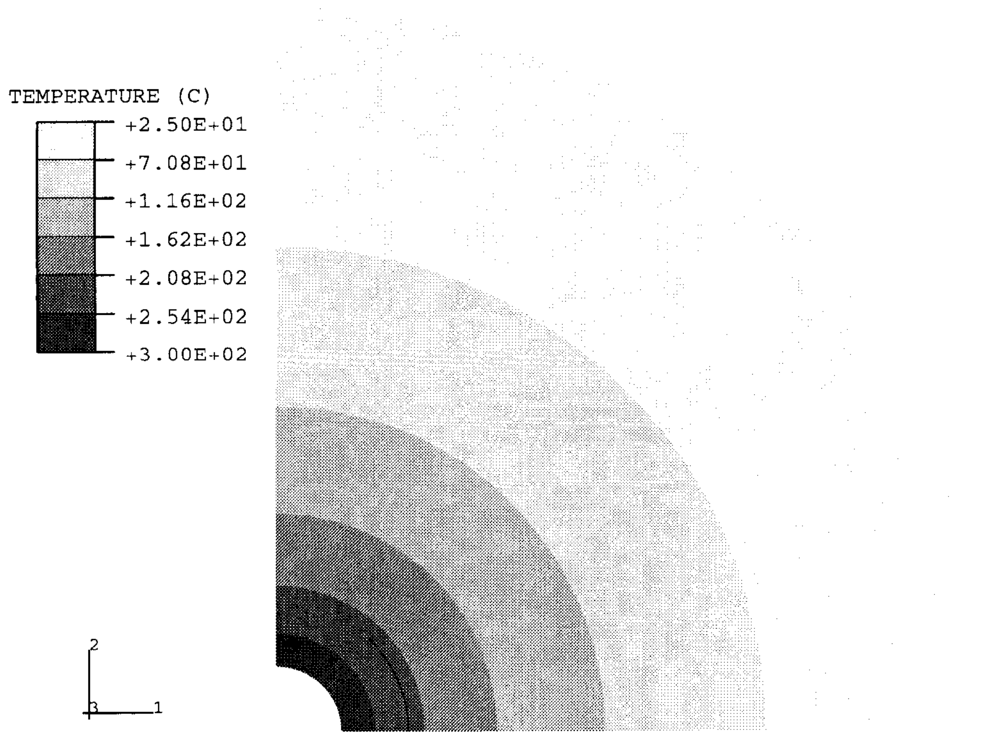

Figure 3-3. Temperature contours calculated using ABAQUS for the case of fully conducting cracks

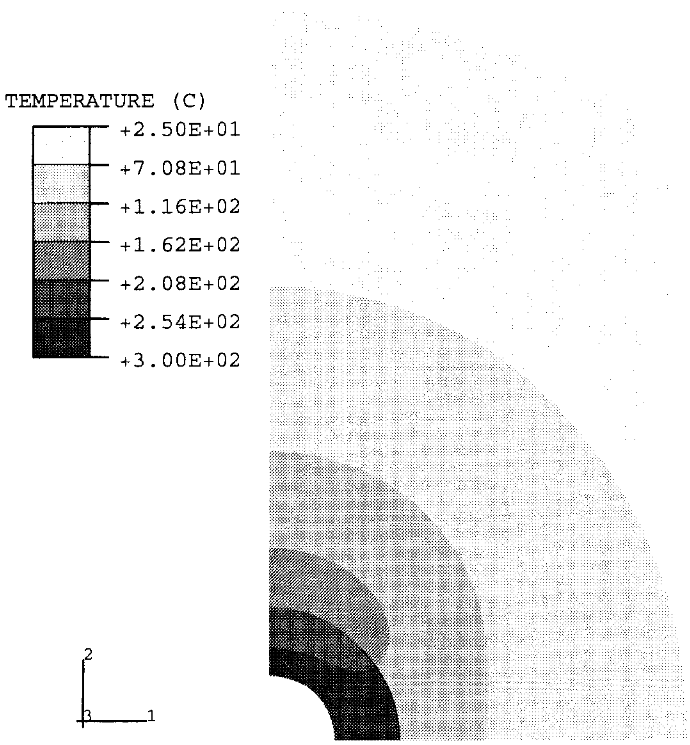

Figure 3-4. Temperature contours calculated using ABAQUS for the case of perfectly insulating cracks

The temperature contours for the case of perfectly insulating cracks are presented in Figure 3-4. As the figure shows, the only difference between the contours for this case and those for the case of the fully conducting cracks is that the contours for this case are normal to the crack surface in the immediate vicinity of the crack. The direction of heat flow is normal to the temperature contours. Therefore, the shape of the contours in Figure 3-4 implies the flow of heat around the cracks, which is the expected effect of perfectly insulating cracks.

The steady-state radial profiles of temperature are given in Figure 3-5, for both the ABAQUS solution for the case of fully conducting cracks (which is independent of the angle θ as Figure 3-3 shows) and the analytical solution for the uncracked solid. The figure illustrates excellent agreement between the two solutions.

The steady-state temperature profiles calculated using ABAQUS for the case of perfectly insulating cracks are presented in Figure 3-6, along with the steady-state analytical solution for the uncracked solid. The radial temperature profile for the case of perfectly insulating cracks varies with the angle θ, because the cracks cause the effective thermal conductivity of the cylinder to be anisotropic. Therefore, temperature profiles are given in Figure 3-6 for three radii, along $\theta=0°$ (i.e, horizontal radius), 45°, and 90° (i.e., vertical radius), respectively. The figure shows that the effect of the crack on the temperature distribution is strongest along the horizontal radius and weakest along the vertical radius, which is consistent with the expected response, considering the location of the cracks shown in Figure 3-1.

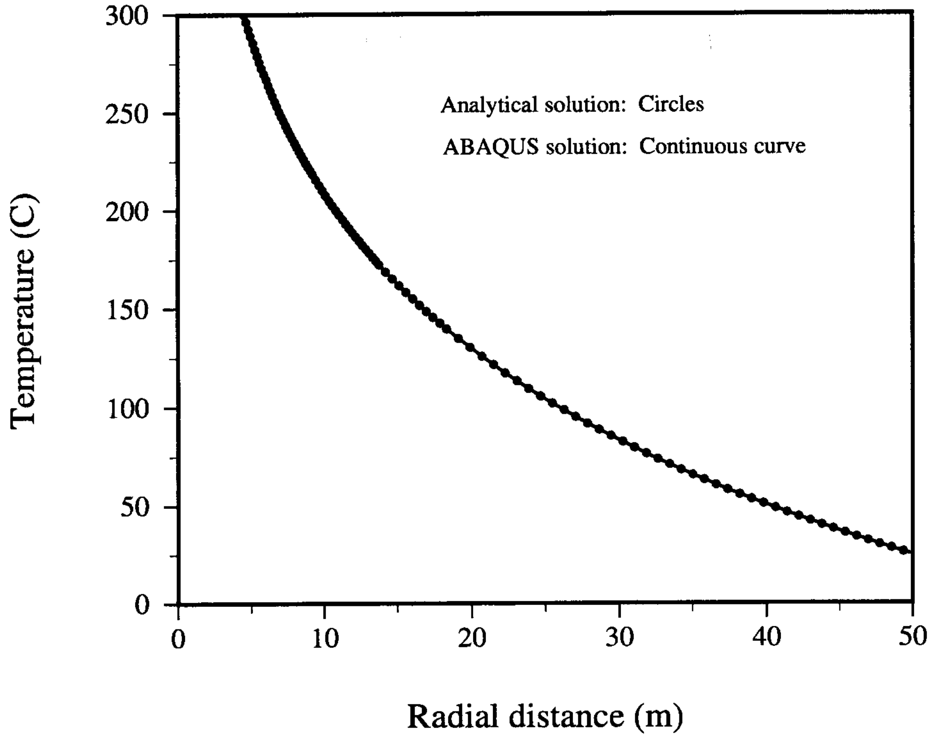

Figure 3-5. Steady-state temperature profiles based on the ABAQUS solution for the case of fully conducting cracks and the analytical solution for the uncracked solid

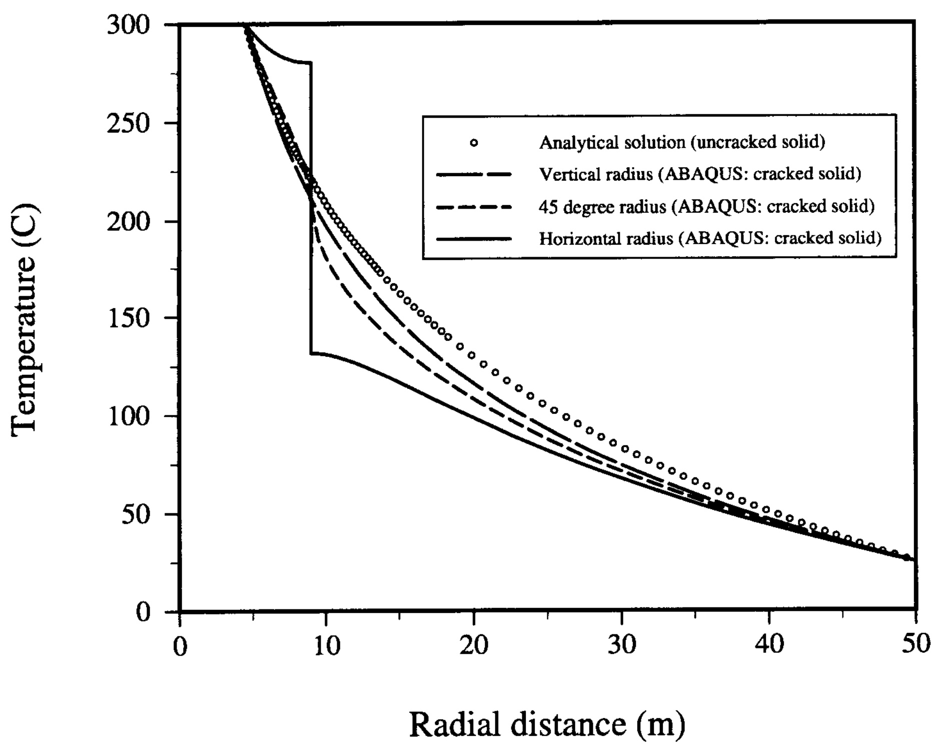

Figure 3-6. Steady-state temperature profiles based on the ABAQUS solution for the case of perfectly insulating cracks and the analytical solution for the uncracked solid

The radial temperature profiles based on the transient analysis of the case of perfectly insulating cracks are presented in Figure 3-7 for the end of 100 d and Figure 3-8 for the end of 10 yr. The steady-state analytical solution for the uncracked solid is also shown in the figures. These figures illustrate that the transient solutions calculated using the code progress with time towards long-term solutions that are similar to the corresponding steady-state solutions.

3.5.2 Stresses and Displacements: Case of the Uncracked Solid

The thermally induced stresses and displacements for the uncracked thick-walled cylinder are included here as a base case. The stresses and displacements for the cracked cylinder deviate from the base case because of the thermal or mechanical effects (or both) of the cracks. Therefore, it was decided to determine the level of agreement between the analytical and ABAQUS solutions for the base case before proceeding with the other cases.

The radial profile of radial displacement, u_r, is presented in Figure 3-9. Radial displacements directed outward from the axis of the cylinder were considered positive. Therefore, the figure shows that the uncracked cylinder would expand by an amount ranging from about 2.5 mm at its inside surface to about 30 mm at the outside surface. Radial profiles of the associated stresses, σ_{rr} (radial stress) and $\sigma_{\theta\theta}$ (circumferential stress), are given in Figure 3-10, which shows that the radial stress is compressive everywhere, whereas the circumferential stress is compressive near the inner surface of the cylinder and tensile near its outer surface. Both figures show excellent agreement between the analytical and ABAQUS solutions for the base case.

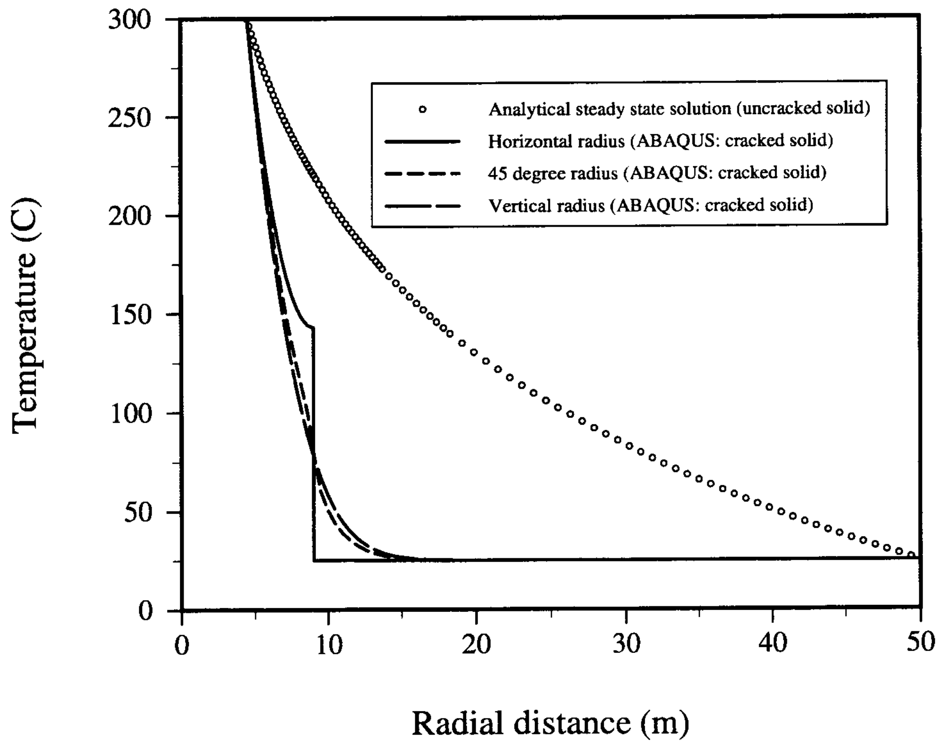

Figure 3-7. Temperature profiles for the end of 100 d, based on the ABAQUS transient analyses for the case of perfectly insulating cracks

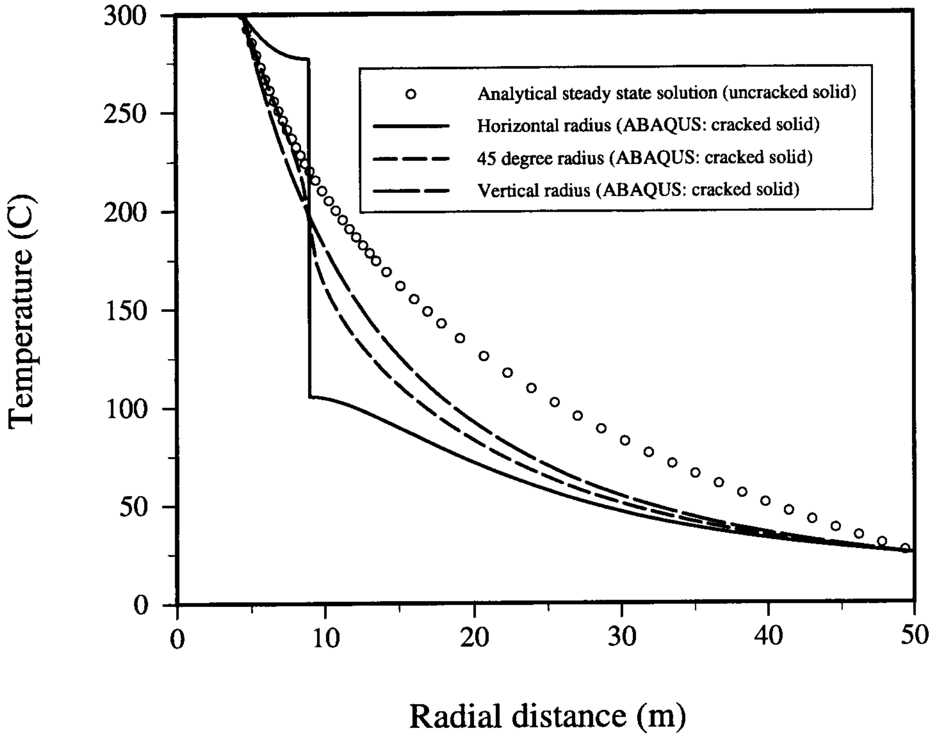

Figure 3-8. Temperature profiles for the end of 10 yr, based on the ABAQUS transient analyses for the case of perfectly insulating cracks

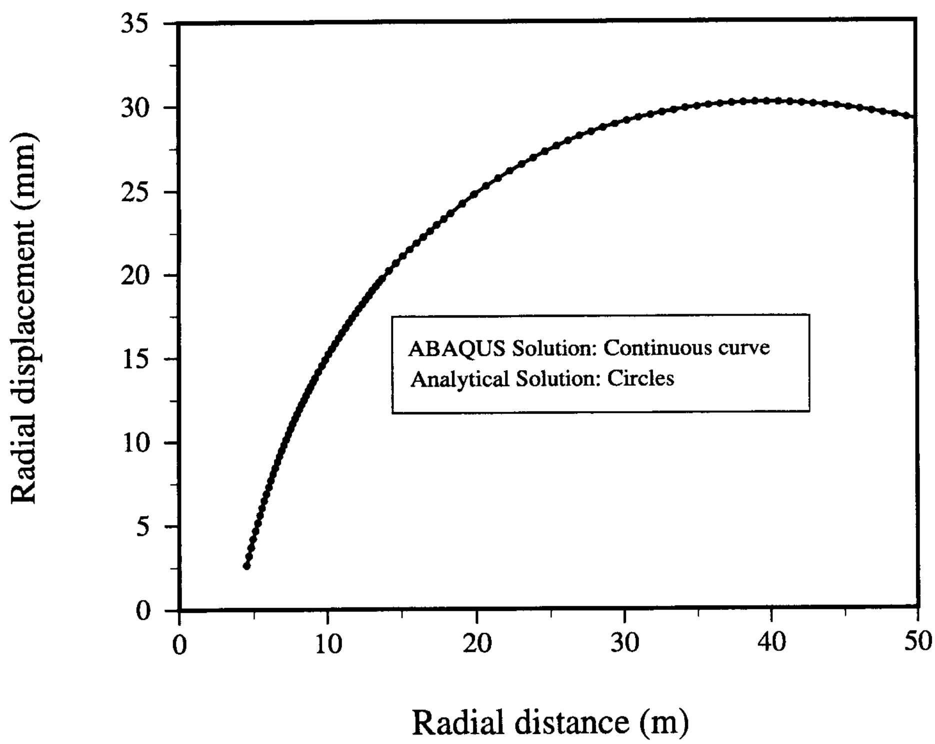

Figure 3-9. Radial displacement profiles for the case of the uncracked solid

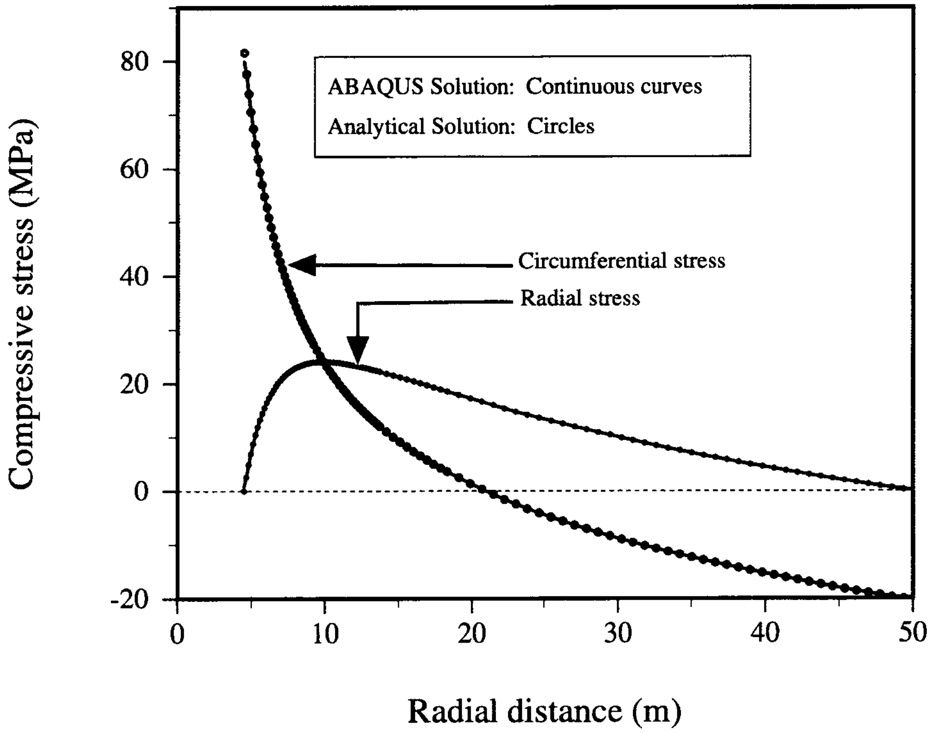

Figure 3-10. Profiles of radial and circumferential stresses for the case of the uncracked solid

3.5.3 Stresses and Displacements: Case of Fully Conducting Cracks

Although the cracks have no effect on the temperature distribution for this case (see Figure 3-3, for example), they are expected to affect the distribution of stresses and displacements. Because the cracks are oriented normal to the direction of expansion, they are expected to close, and their closure would cause the stresses and displacements in the crack vicinity to deviate from the analytical solution for the uncracked solid.

Because of the crack-induced stiffness-anisotropy, the mechanical response varies with the angle θ. As a result, the profiles of displacements and stresses are presented along three radii, namely, the $\theta=0°$ (horizontal), $\theta=45°$, and $\theta=90°$ (vertical) radii. The radial displacement profiles are presented in Figure 3-11. As the figure shows, the displacement profile along the horizontal radius deviates most from the analytical solution. Along this radius, the displacement of points on the near side of the crack (on the side of the crack closer to the inner surface of the cylinder) is larger than the displacement of corresponding points in the uncracked solid. A displacement discontinuity of about 2 mm magnitude occurs at the crack location, the near surface of the crack having been displaced about 2 mm more than the far surface. The magnitude of this discontinuity is the same as the initial aperture of the crack.

The stresses associated with these displacements are plotted in Figures 3-12 through 3-14. Generally, the magnitudes of compressive stress close to the crack on its near side are smaller than the magnitudes calculated using the analytical solution for the uncracked solid. The smaller value of compressive stress for the cracked solid is consistent with the fact that the displacements on the near side

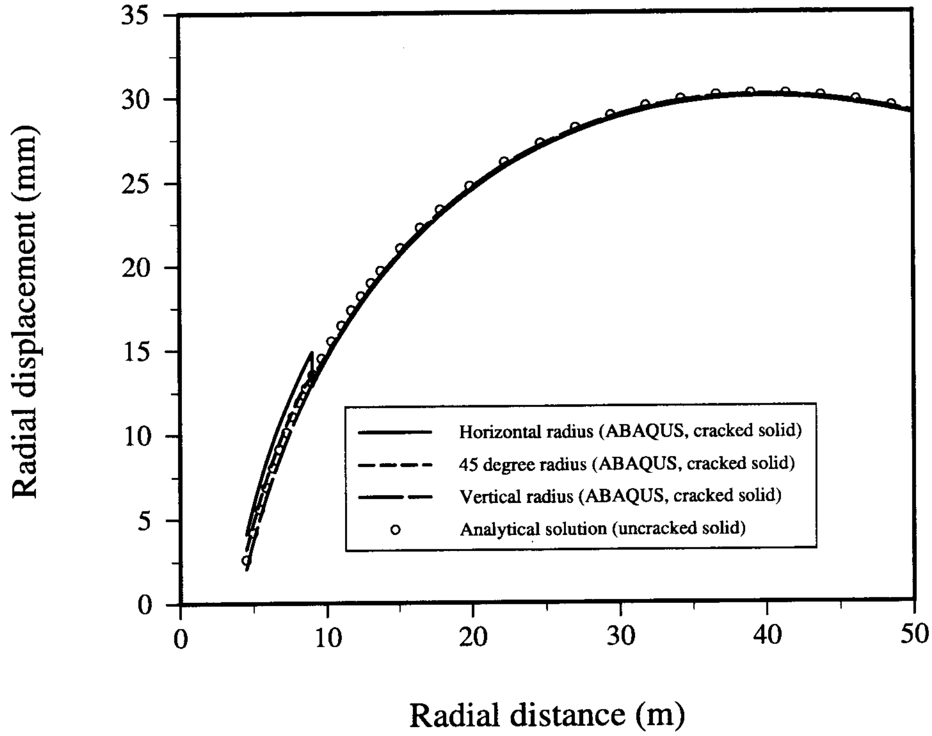

Figure 3-11. Radial displacement profiles for the case of fully conducting cracks

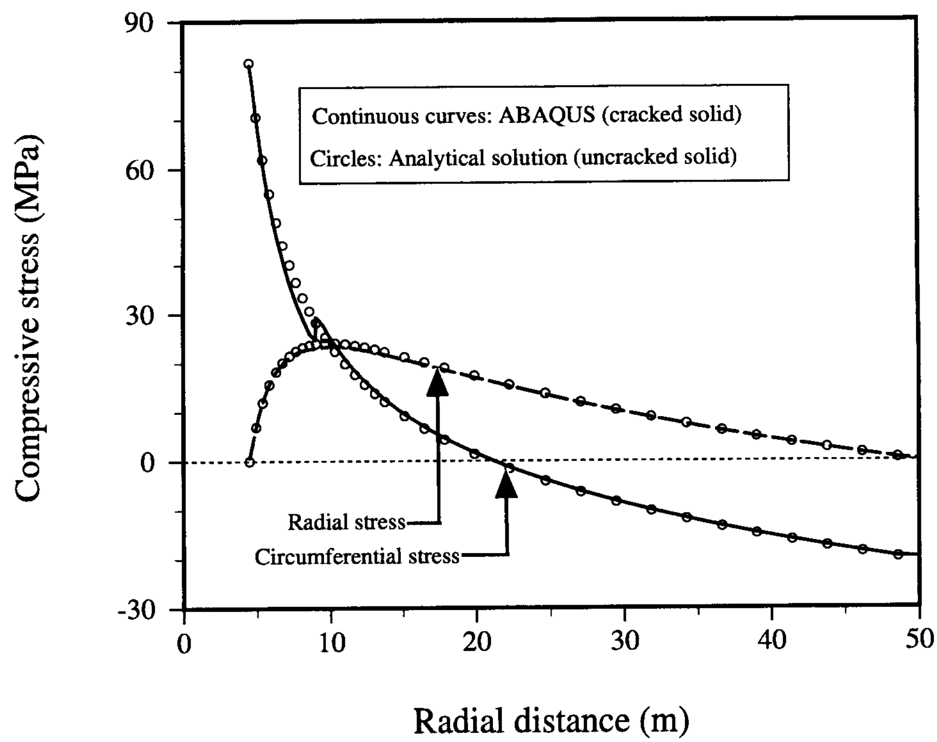

Figure 3-12. Stress profiles along the horizontal radius for the case of fully conducting cracks

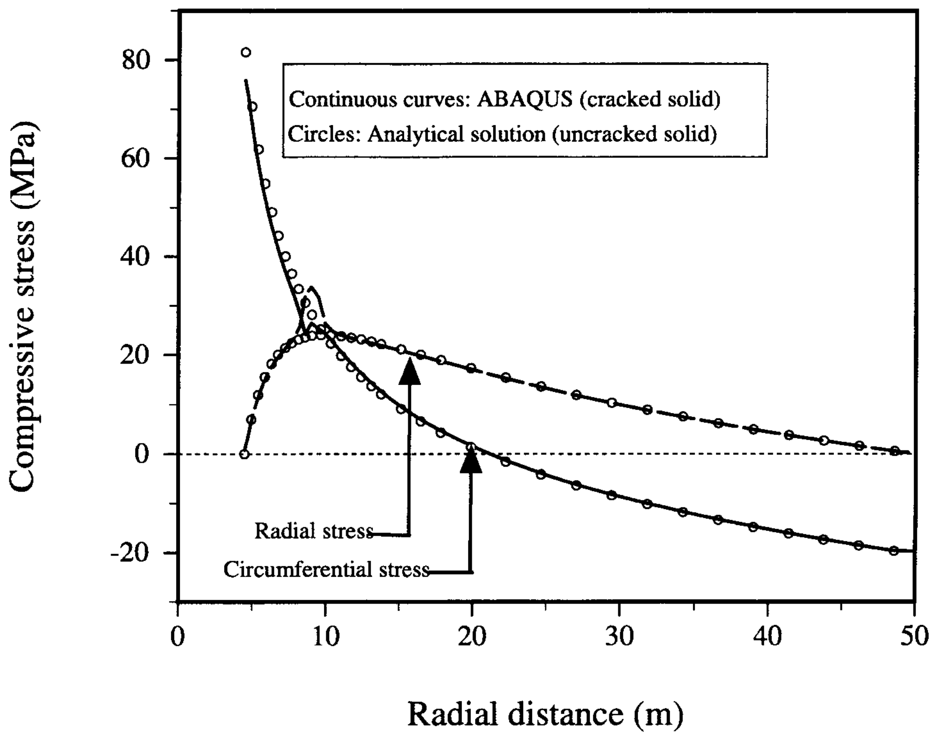

Figure 3-13. Stress profiles along the 45° radius for the case of fully conducting cracks

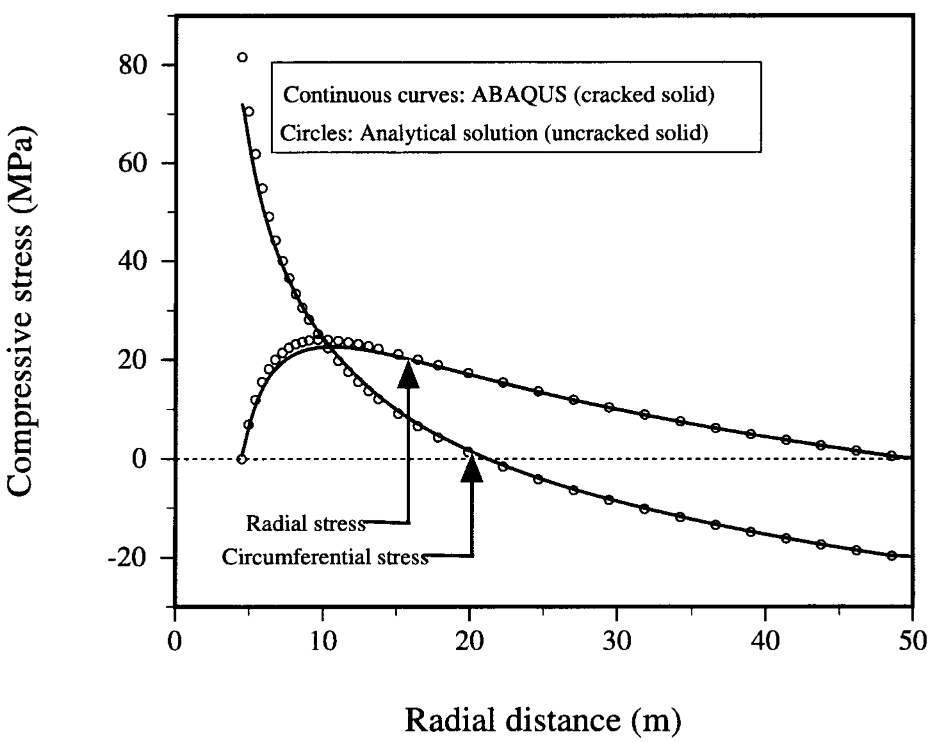

Figure 3-14. Stress profiles along the vertical radius for the case of fully conducting cracks

of the crack are larger than the displacements at corresponding points in the uncracked solid. The 45° radius passes through the crack tip (see Figure 3-1) and, as a result, stress concentration at the crack tip causes larger-than-normal compressive stress in the vicinity of the point of intersection of the radius with the crack.

3.5.4 Stresses and Displacements: Case of Perfectly Insulating Cracks

The stresses and displacements for the case of the perfectly insulating crack deviate from the analytical solution for the uncracked solid, because of both the thermal and mechanical effects of the crack (unlike the case discussed in Section 3.5.3, in which the deviations in mechanical response are due to the mechanical effects only). As was illustrated in Figure 3-4, the cracks act as thermal barriers, such that values of temperature are lower on the far side of a crack and higher on its near side when compared with the temperatures calculated at corresponding points in the uncracked solid. The mechanical effect of this thermal barrier consists of smaller magnitudes of compressive stress close to the crack on its far side, when compared with the compressive stress at corresponding points in the uncracked solid. This mechanical effect is superimposed on the effect of crack closure that was examined in Section 3.5.3.

Figure 3-15 shows the radial displacement profiles along the horizontal, 45°, and vertical radii; the analytical solution for the uncracked solid is also shown in the figure. The figure shows that the cylinder with perfectly insulating cracks would undergo less expansion than the uncracked cylinder. The smaller expansion occurs because a large volume of the solid in the cracked cylinder is exposed to lower temperatures than would occur at corresponding points in the uncracked cylinder (compare Figures 3-3 and 3-4, for example). Displacements on the near side of the crack along the horizontal radius are larger than the displacements at corresponding points in the uncracked cylinder because of the effect of crack closure, which was discussed in Section 3.5.3.

The profiles of radial and circumferential stresses are presented in Figures 3-16 through 3-18 that show that stress magnitudes in the cracked cylinder (for the case of perfectly insulating cracks) are generally smaller than those at corresponding locations in the uncracked cylinder. The largest difference between the stress profiles for the cracked and uncracked cylinders occurs in the values of circumferential stress close to the crack on its far side. Generally, the effects of the crack are most pronounced near the horizontal radius and least pronounced near the vertical radius. This distribution of the effects is consistent with the locations of the cracks shown in Figure 3-1.

3.6 CONCLUSIONS

The computer code ABAQUS was evaluated in this chapter with respect to its capabilities to model the flow of heat and associated thermally induced stresses and deformations in a fractured rock. Special attention was given to the effect of fractures on heat conduction, considering both perfectly insulating fractures and fully conducting fractures. The performance of ABAQUS was found to be satisfactory, having been evaluated as follows:

(i) The ABAQUS solutions for the case of fully conducting fractures were compared with the analytical solutions for intact rock.

(ii) The ABAQUS solutions for the case of perfectly insulating fractures were evaluated qualitatively by considering the nature of their deviation from the analytical solutions for intact rock.

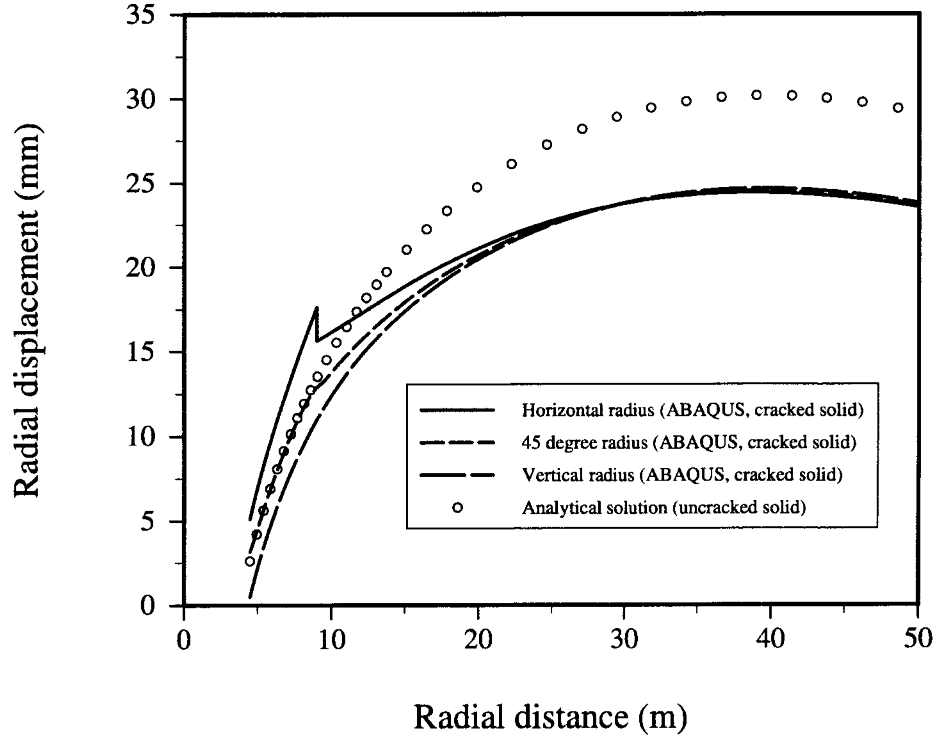

Figure 3-15. Radial displacement profiles for the case of perfectly insulating cracks

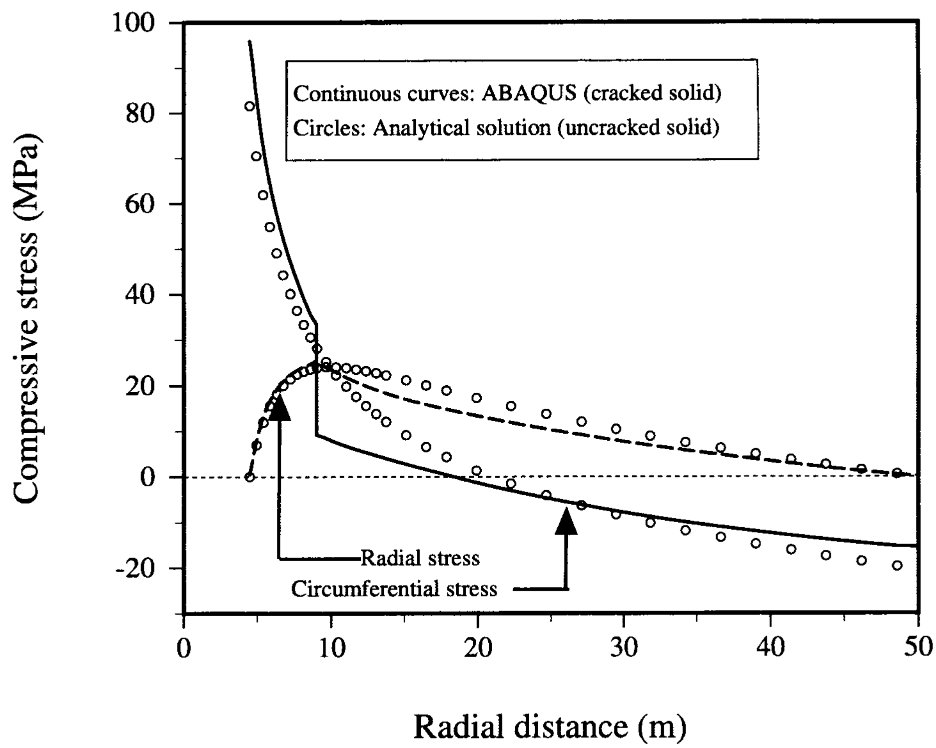

Figure 3-16. Stress profiles along the horizontal radius for the case of perfectly insulating cracks

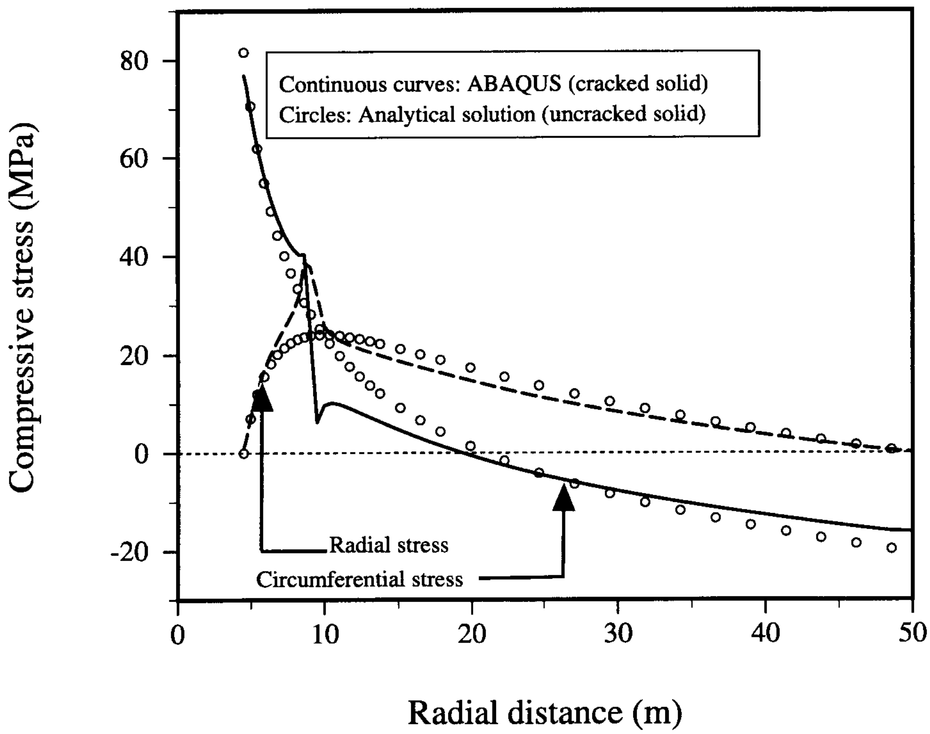

Figure 3-17. Stress profiles along the 45° radius for the case of perfectly insulating cracks

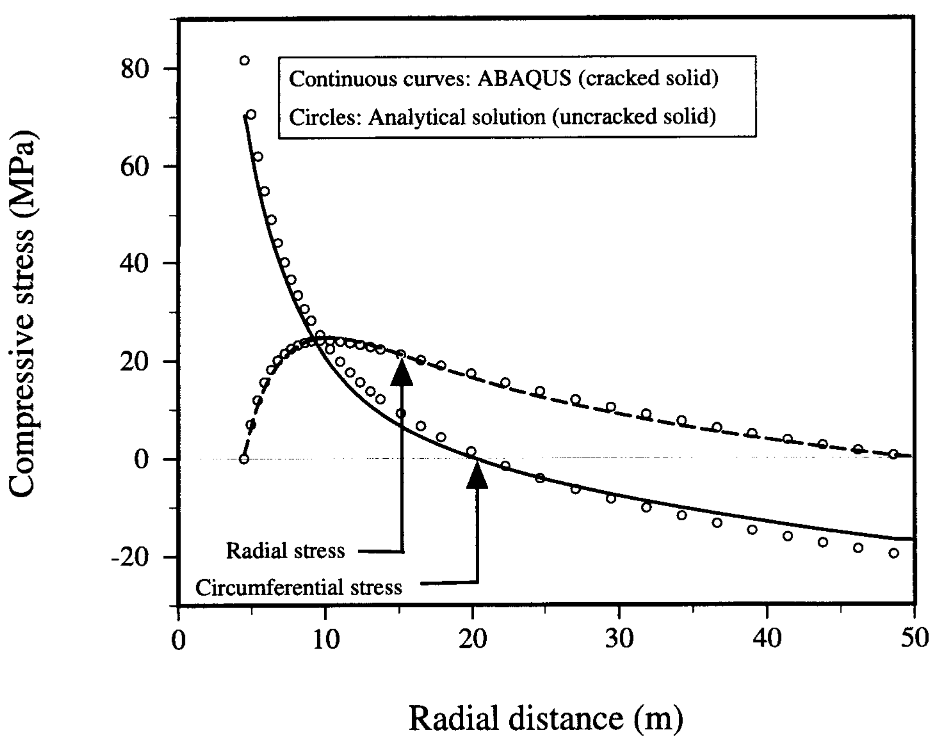

Figure 3-18. Stress profiles along the vertical radius for the case of perfectly insulating cracks

4 HYDROLOGICAL PROBLEMS

Two sets of hydrological problems were solved to evaluate the modeling capabilities of ABAQUS for the flow of water through a fractured rock mass. The problem in both sets consisted of introducing water at the top of a column of rock and monitoring the progress of the wetting front as a function of time. The rock mass was initially unsaturated (i.e., less than 100 percent of the available pore space is occupied by water) in every case. The first problem set examined matrix flow only, whereas the second examined flow through both fracture and matrix.

4.1 TRANSIENT INFILTRATION: FLOW THROUGH MATRIX

The phenomenon modeled in this problem set consists of the vertically downward infiltration of water through unsaturated porous rock. A similar problem solved in the ABAQUS Example Manual considers the one-dimensional (1D) wicking test, in which the absorption of a fluid takes place against the gravity load caused by the weight of the fluid. In such a test, fluid is made available to the material at the base of a column, and the material absorbs as much fluid as the weight of the rising fluid permits. At steady state, the pore pressure gradient must equal the unit weight of the fluid. Although satisfactory results were obtained for this problem using ABAQUS, the performance of the code in modeling the flow of water through unsaturated rock matrix cannot be evaluated based on the problem alone, because the range of conditions (suction head gradient, hydraulic conductivity, etc.) covered by the problem is quite small. The problems in this set were selected to extend the range of test conditions.

4.1.1 Problem Definition

In this problem, a steady supply of water is applied everywhere on a horizontal ground surface. The rock mass below the surface is homogeneous and isotropic. The initial degree of saturation is the same everywhere. Under these conditions, water flows vertically downward, and the rate of flow does not vary laterally. The problem is therefore 1D.

The flow of water under such conditions is governed by the following equation:

$$\frac{\partial}{\partial t}(\phi\rho S) + \rho\frac{\partial q_z}{\partial z} = 0 \tag{4-1}$$

where t stands for time, ϕ is the porosity of the medium, ρ is the density of water, z is the vertical coordinate (positive upward), q_z is the vertical flux of water, and S is the saturation ($S = v_w/v_v$, where v_w is the volume of water and v_v is the volume of pore space). The water flux q_z is governed by Darcy's law, which gives the equation

$$q_z = -\frac{\kappa_e}{\mu}\left(\frac{\partial p}{\partial z} - \rho g_z\right) \tag{4-2}$$

where κ_e is the effective permeability of the medium (m^2), μ is the dynamic viscosity of water (Pa·s), p is the water pressure (Pa), and g_z is the z-component of gravitational acceleration (m/s^2).

The substitution of Eq. (4-2) into Eq. (4-1) gives one equation with the two unknown field variables S and p. The additional equation needed to solve this equation is obtained from the constitutive law that governs the development of suction (i.e., negative pore-water pressure) in unsaturated porous media. This law defines the relationship between suction and saturation. The relationship depends on the microstructure of the porous medium and its interactions with water and air. It is very difficult to describe these interactions mathematically; therefore, mathematical formulations of the constitutive law are usually based on functional generalizations of empirical data, or on mathematical relations based on idealized models (such as a capillary tube, spheres of constant radius, or a bundle of parallel circular rods), or both. For example, the van Genuchten (1980) function expresses the relationship in terms of the following equation:

$$S_e = \frac{1}{[1 + (-\beta h)^n]^m} \tag{4-3}$$

where S_e is the effective saturation, defined as

$$S_e = \frac{S - S_r}{1 - S_r} \tag{4-4}$$

h is the pressure head (m), related to the water pressure through the equation

$$h = \frac{p}{\gamma_w} \tag{4-5}$$

and $\gamma_w = \rho g_z$ is the unit weight of water (N/m^3). The material parameters β, n, and S_r in Eqs. (4-3) and (4-4) are evaluated using laboratory test data, and $m = 1 - 1/n$.

Because the water permeability of an unsaturated porous medium depends on the distribution of water in the pore spaces, its value varies with the value of saturation. Its relationship with saturation is given in terms of functional generalizations of empirical data. Two such functions were used in the work described in this report, namely, the Gardner (1958) function and the Mualem-van Genuchten function (van Genuchten et al., 1991). These functions define the effective permeability (κ_e) as the product of two parameters, as follows:

$$\kappa_e = \kappa \kappa_r \tag{4-6}$$

where κ is the intrinsic permeability of the medium, which depends only on the properties of the porous medium, and κ_r is the relative permeability. The values of κ_r vary from 0 for a porous medium containing no mobile water, to 1 for a saturated porous medium. Therefore, the effective permeability for a saturated porous medium is numerically equal to the intrinsic permeability. The Gardner function defines relative permeability as an exponential function of pressure head, as follows:

$$\kappa_r = e^{\alpha h} \tag{4-7}$$

where α is an empirical parameter. On the other hand, the Mualem-van Genuchten function defines it as a function of saturation, as follows:

$$\kappa_r = S_e^{\iota}\left[1 - (1 - S_e^{1/m})^m\right]^2 \tag{4-8}$$

where ι is the pore-connectivity parameter, usually assigned a value of 0.5 for soils (cf. van Genuchten et al., 1991); it was assigned a zero value for both the ABAQUS and CTOUGH analyses in this study.

The hydraulic conductivity, K (m s^{-1}), is related to the effective permeability, κ_e, through the following equation:

$$K = \frac{\gamma_w \kappa_e}{\mu} \tag{4-9}$$

4.1.1.1 Material Properties

Two groups of material properties were used for the study, as is shown in Table 4-1. The first group represents a material with hydraulic properties similar to the Topopah Spring welded tuff (Bagtzoglou and Muller, 1994); the second represents a higher permeability material, referred to hereafter as Material #2 (Ababou and Bagtzoglou, 1993).

The properties of water were set as follows: ρ=1,000 kg·m^{-3} and μ=8.95 × 10^{-4} Pa·s; the value of gravitational acceleration was set to 10 m·s^{-2} (vertically downward).

Table 4-1. Material and model parameter specifications for transient-infiltration problem

Material and Model Parameters	Value for Topopah Spring Welded Tuff	Value for Material #2
Height of rock column (m)	1.0	3.0
Pressure head at the (saturated) top surface (m)	0.0	0.0
Pressure head at the base (m)	−1,000	−2.5
Initial saturation everywhere	0.274	0.288
Initial pressure head everywhere (m)	−1,000	−2.5
Saturated hydraulic conductivity (m·s^{-1})	6.693×10^{-12}	1.625×10^{-5}
Porosity	0.0925	0.3
Gardner permeability parameter, α (m^{-1})	0.0177	7.3
Residual saturation, S_r	0.0724	0.1833
van Genuchten parameter, β (m^{-1})	0.0072	2.9227
van Genuchten parameter, n	1.7664	2.0304

4.1.1.2 Boundary and Initial Conditions

The initial condition for suction head in each rock column was set to a value of 1,000 m for the Topopah Spring material and 2.5 m for the higher permeability material. The initial values of saturation corresponding to these values of suction head were calculated using Eq. (4-3) and the appropriate material parameters from Table 4-1. The values of suction head at the base and at the top surface of each column were held constant.

4.1.1.3 Evaluation Strategy

The problem was solved for the two groups of material properties using ABAQUS and the integrated finite difference code CTOUGH (Lichtner, 1994; Nitao, 1989). Each of the codes was used to generate solutions in terms of the depth profiles of pressure and saturation for selected values of time, including a time long enough to give the code's best estimate of the steady-state solution. The Gardner permeability formulation [Eq. (4-7)] is not implemented in CTOUGH; therefore, CTOUGH solutions were obtained using only the Mualem-van Genuchten permeability formulation [Eq. (4-8)]. On the other hand, because ABAQUS uses table lookup to describe both the h versus S and κ_r versus S functions, it was possible to obtain the solutions using both permeability formulations, hence giving two sets of ABAQUS solutions for each material property group.

The steady-state solution for the problem was also obtained analytically, using the Gardner permeability formulation. The solution, in terms of suction head ψ ($\psi=-h$), is given by the following equation (Kapoor, 1994):

$$\psi(\zeta) = \psi(0) - \frac{1}{\alpha}\ln\left[1 - \frac{(1-e^{\alpha[\psi(0)-\psi(H)]})}{(1-e^{\alpha H})}(1-e^{\alpha\zeta})\right] \qquad (4\text{-}10)$$

where ζ is the depth below surface; $\zeta=0$ at $z=0$, and $\zeta=H$ at $z=-H$, where H is the height of each rock column and $z = 0$ at the top surface of the column.

Having obtained these solutions, the performance of ABAQUS was evaluated as follows:

(i) By comparing the CTOUGH and ABAQUS solutions for the case of the Mualem-van Genuchten permeability formulation

(ii) By comparing the ABAQUS steady-state solutions with the analytical solution for the case of the Gardner permeability formulation

4.1.2 ABAQUS Models

Two ABAQUS models were prepared for the vertical infiltration problem set, one for the Topopah Spring material, and the other for the higher permeability material. Each model consisted of 100 CPE8RP elements stacked as shown in Figure 4-1. The designation CPE8RP stands for eight-noded quadrilateral plane-strain elements with reduced order of integration and pore-pressure modeling capability (Hibbitt, Karlsson & Sorensen, Inc., 1994). The width of the elements was selected to obtain squares, which resulted in a width of 0.01 m for the Topopah Spring model and 0.03 m for the other. The shape of elements would usually not be the only concern in setting element sizes; however, because this problem is one-dimensional, the width assigned to the elements is not very important. It was necessary to solve the vertical infiltration problem as a purely hydrological one, in order to compare ABAQUS results with those of CTOUGH, since the latter does not account for mechanical effects. Therefore, all vertical and horizontal displacements were constrained to zero to preclude mechanical deformation.

4.1.2.1 Material Property Definitions

The moisture retention and relative permeability behavior were defined in terms of tables of values of p versus S and κ_r versus S, using the *SORPTION and *PERMEABILITY commands, respectively. The p versus S values were calculated using Eq. (4-3), whereas the κ_r versus S values were calculated using either Eq. (4-7) or Eq. (4-8), depending on which permeability model was being used in the analysis. ABAQUS requires that both the imbibition and drainage parts of the moisture retention behavior be defined. On the other hand, because no drainage was expected to occur in the models (saturation was expected to either increase or remain the same everywhere), it was not necessary to specify the drainage response accurately. Therefore, the drainage data were obtained using the imbibition data in Table 4-1 with a slightly larger value of residual saturation, S_r. The drainage data were obtained with S_r=0.0832 for the Topopah Spring material, and S_r=0.217 for the higher permeability material. Each of the tables of values was defined using 500 points. A preliminary analysis conducted using 50 points gave very poor results. Although a table with less than 500 points, say 200, might have been adequate, this possibility was not investigated.

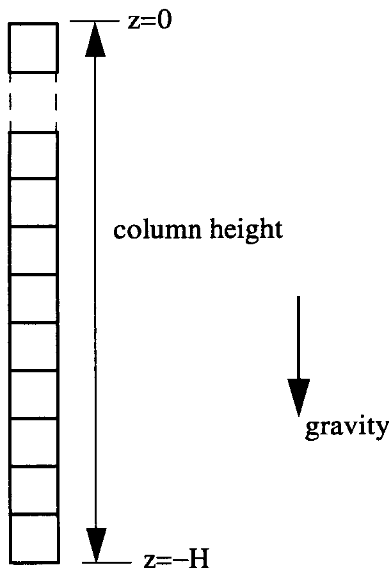

Figure 4-1. Schematic illustration of finite element mesh for Problem Set 1

4.1.2.2 Loading Procedure

Each analysis was conducted in eight steps. During the first step, gravity loading was turned on using the GRAV option of the *DLOAD command in a "*SOILS, CONSOLIDATION" procedure; the pore pressure at the base of the column was constrained to its initial value, whereas the pore pressure at the top was constrained to zero value, using the *BOUNDARY command. This step lasted for 1 s. The reason for such a short-duration step was to establish the required boundary and initial conditions (presented in Section 4.1.1.2) without significant water flow. It is also possible to start such an analysis from an initial no-flow state by prescribing an initial pore pressure distribution with an upward gradient equal to the unit weight of water, but such an initial condition would redefine the problem. Therefore, it was decided to allow some amount of flow during the initial step, but make it insignificant by running the step for a negligible amount of time.

Each of Steps 2 through 8 consisted of a "*SOILS, CONSOLIDATION" procedure with no change in boundary conditions. The steps were run to generate the distributions of pore pressure and saturation at the end of 1, 5, 10, 50, 100, 500, and 1,000 d, respectively, for the Topopah Spring material and at the end of 0.005, 0.05, 0.1, 0.15, 0.25, 0.5, and 1 d, respectively, for the higher permeability material. The analysis in Steps 2 through 8 could have been accomplished in one step. However, it was necessary to divide it into seven steps, in order to have results saved at specific times and only at those times.

4.1.3 CTOUGH Models

Two CTOUGH models were set up, each consisting of 100 cells, stacked vertically to form a one-dimensional model, such as is shown in Figure 4-1. Each of the 98 middle cells had a cross-sectional area of 10^{-4} m^2 and a length of 0.01 m (i.e., a volume of 10^{-6} m^3 per cell), for the Topopah Spring model; for the higher permeability material, each cell had a cross-sectional area of 9.0×10^{-4} m^2 and a length of 0.03 m (i.e., a volume of 2.7×10^{-5} m^3 per cell). Each of the two end cells in each model was assigned a volume of 10^{50} m^3. The two large end cells were necessary in each case to simulate fixed-pore-pressure boundary conditions. This type of boundary condition is not directly supported in CTOUGH, but can be achieved by letting water flow into what essentially is an infinite volume. Hence, the initial values of pore pressure and saturation in those cells (which were assigned to satisfy the boundary conditions specified in Section 4.1.1.2) remained essentially unchanged during the simulation period.

4.1.4 Results

4.1.4.1 ABAQUS Results Versus CTOUGH Results

The pressure head and saturation profiles obtained using ABAQUS and CTOUGH are compared in Figures 4-2 through 4-5. The figures demonstrate good agreement between the predictions of the two codes. Based on the difference between the locations of corresponding solid lines (ABAQUS profiles) and broken lines (CTOUGH profiles) in the figures, it can be concluded that the rate of infiltration predicted using CTOUGH is higher than the rate predicted using ABAQUS, but the difference between the two rates is very small. The humps at the low-saturation end of the ABAQUS saturation profiles are caused by the discontinuity at the corresponding end of the pore-pressure profiles. In the ABAQUS formulation of the solution procedure, the governing equation [such as Eq. (4-1)] is solved in terms of pore pressure, p, and the saturation increment ΔS is computed as follows:

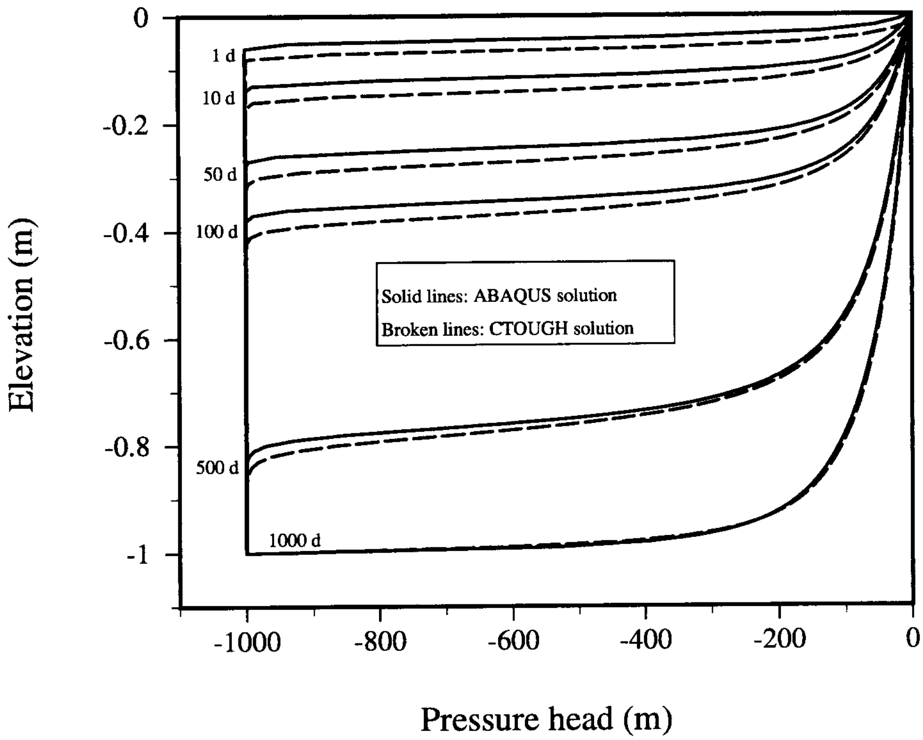

Figure 4-2. Pressure head profiles: Topopah Spring welded tuff with Mualem-van Genuchten permeability formulation

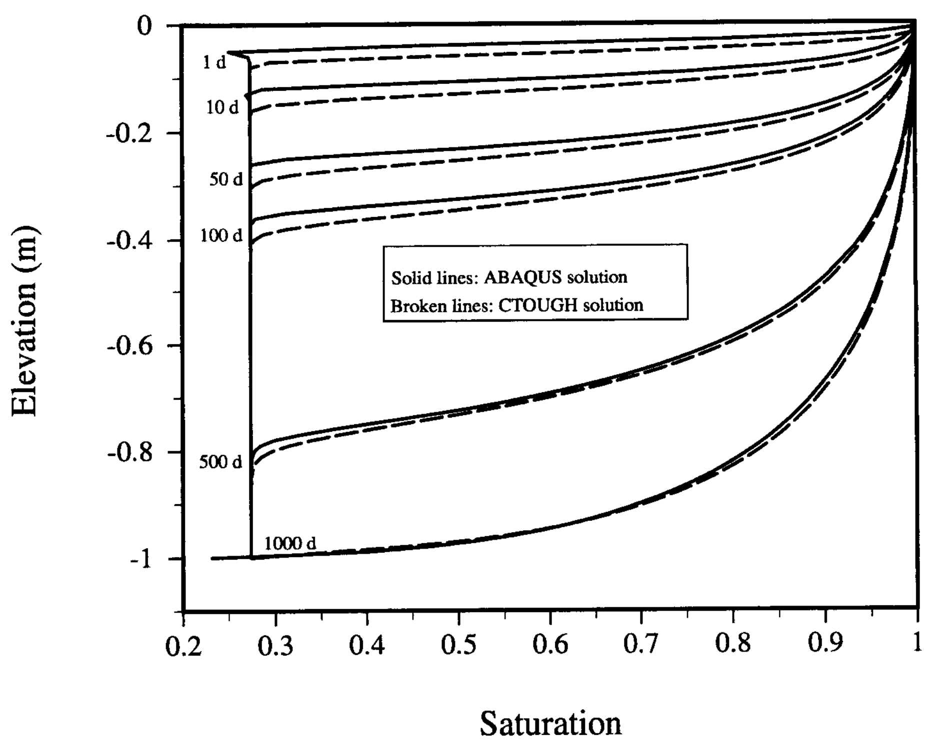

Figure 4-3. Saturation profiles: Topopah Spring welded tuff with Mualem-van Genuchten permeability formulation

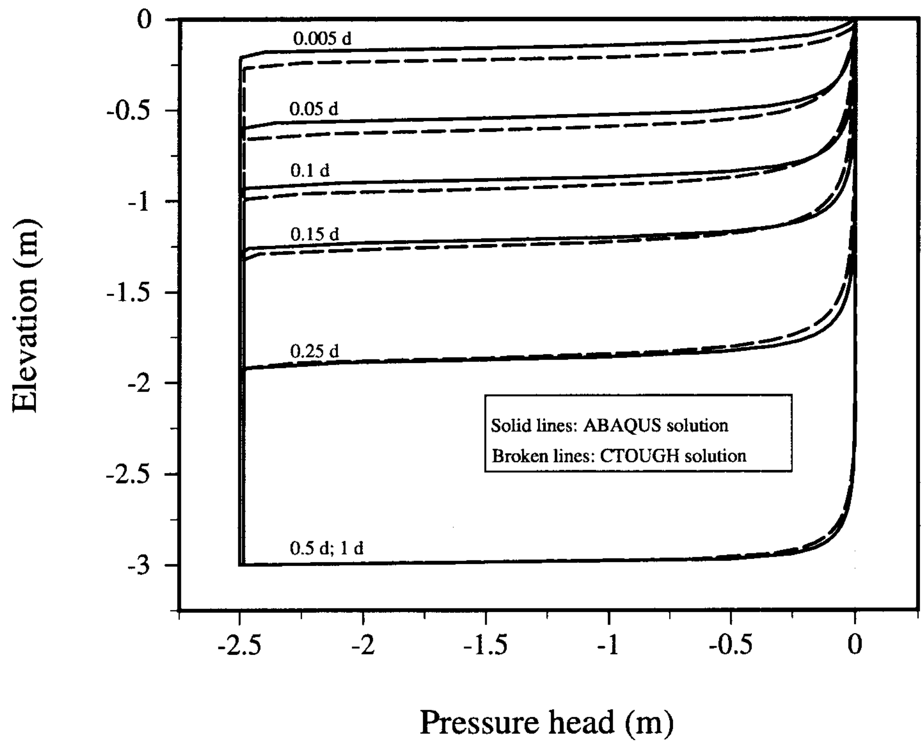

Figure 4-4. Pressure head profiles: Higher permeability material with Mualem-van Genuchten permeability formulation

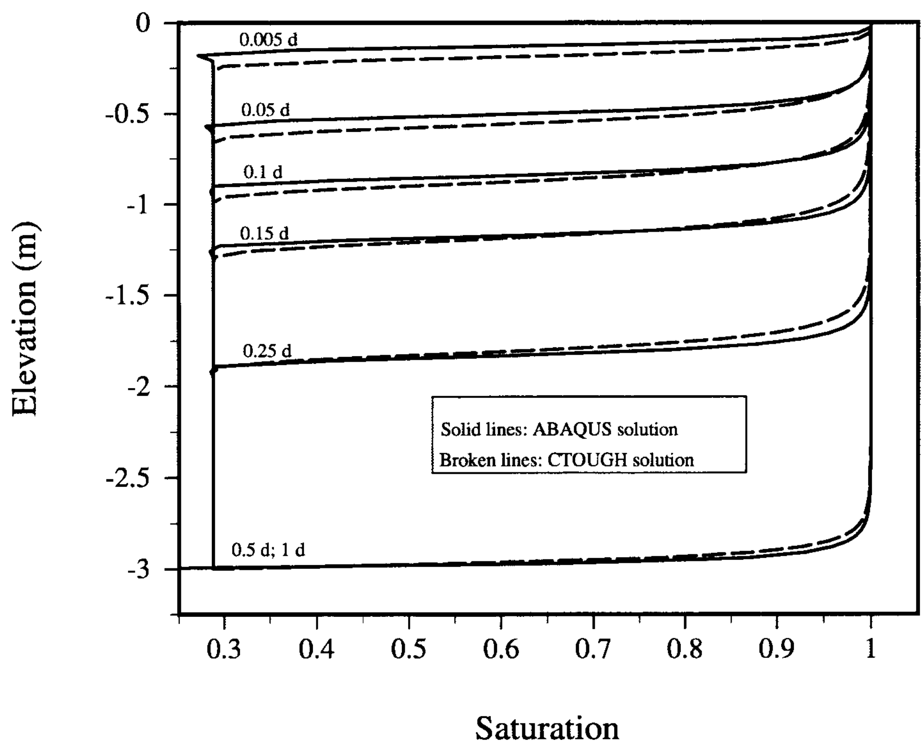

Figure 4-5. Saturation profiles: Higher permeability material with Mualem-van Genuchten permeability formulation

$$\Delta S = \frac{\partial f}{\partial p}\Delta p = \frac{\partial f}{\partial p}\frac{\partial p}{\partial t}\Delta t \tag{4-11}$$

where f is the S versus p function, such as given in Eq. (4-3). The derivative $\partial p/\partial t$ may give inaccurate results if the shape of the curve $p(t)$ changes rapidly, as may occur at the wetting front. On the other hand, as the figures show, its effect on the ABAQUS-predicted values of saturation is negligible.

The histories of wetting front elevations calculated for the two problems are plotted in Figures 4-6 and 4-7, where the wetting front is defined as the boundary between the part of the rock at initial saturation and the part for which values of saturation are larger than the initial value. The figures further illustrate the small difference in the infiltration rates predicted using the two codes.

4.1.4.2 ABAQUS Results Versus the Analytical Solution

The ABAQUS-predicted profiles of pressure head and saturation, for the cases in which the Gardner permeability formulation [Eq. (4-7)] was used, are compared with the steady-state analytical solution [Eq. (4-10)] through the plots in Figures 4-8 through 4-11. As these figures show, the ABAQUS-predicted profiles approach the analytical steady-state solution as time increases. This relationship is consistent with the expected response.

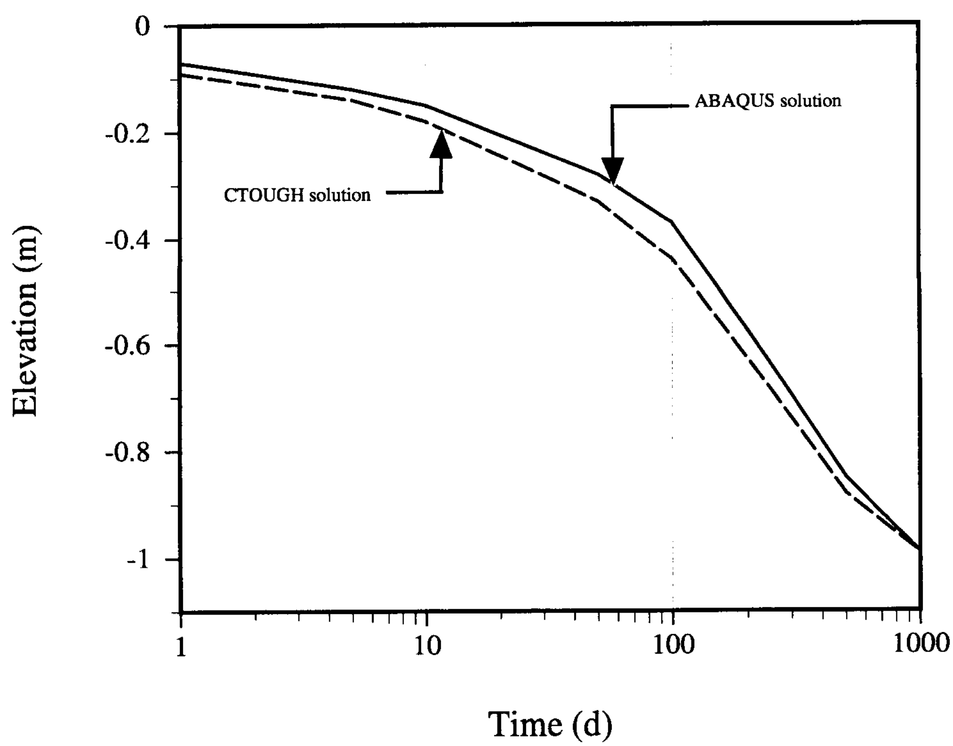

Figure 4-6. History of wetting front elevations: Topopah Spring welded tuff with Mualem-van Genuchten permeability formulation

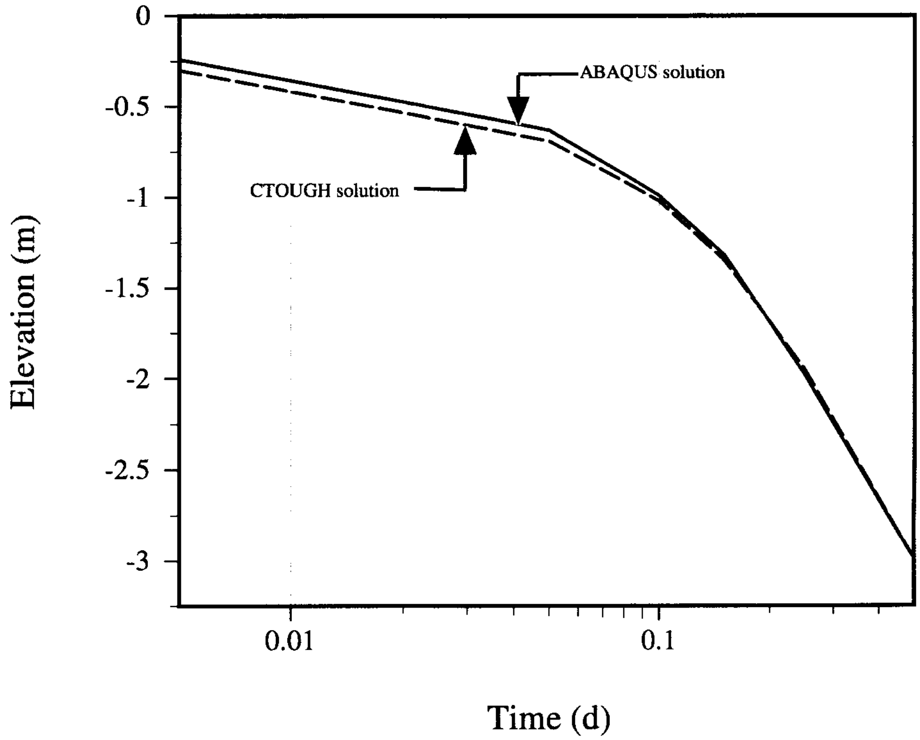

Figure 4-7. History of wetting front elevations: Higher permeability material with Mualem-van Genuchten permeability formulation

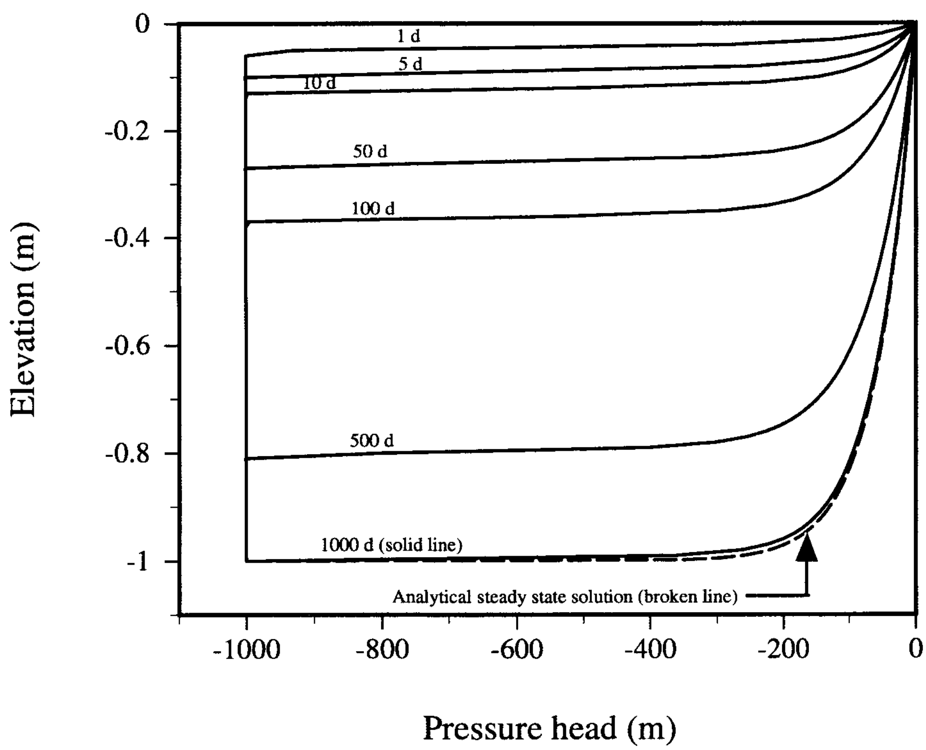

Figure 4-8. Pressure head profiles: Topopah Spring welded tuff with Gardner permeability formulation

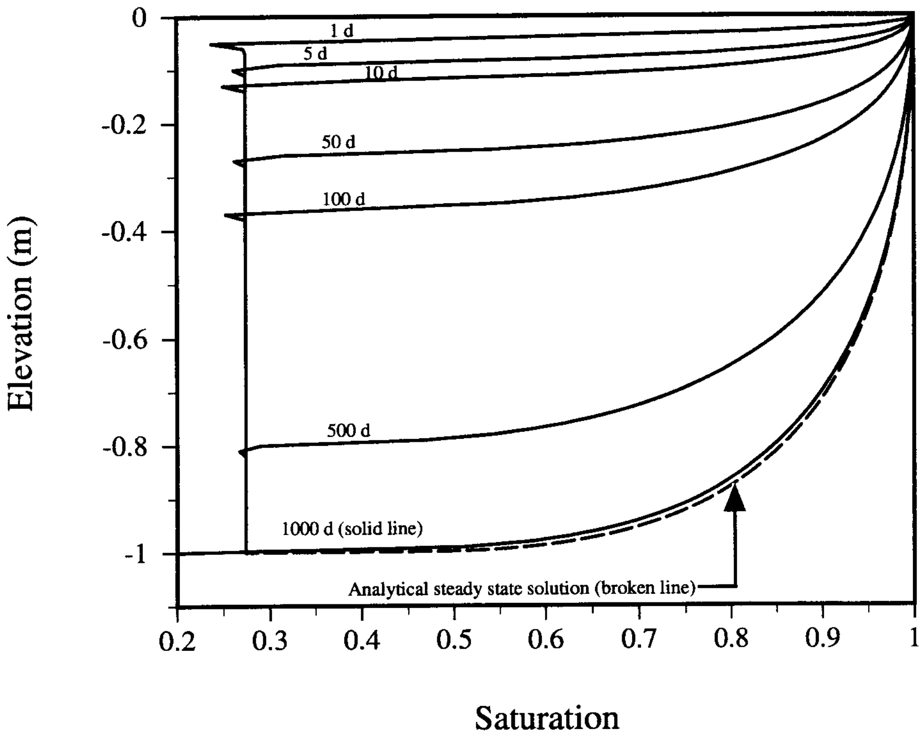

Figure 4-9. Saturation profiles: Topopah Spring welded tuff with Gardner permeability formulation

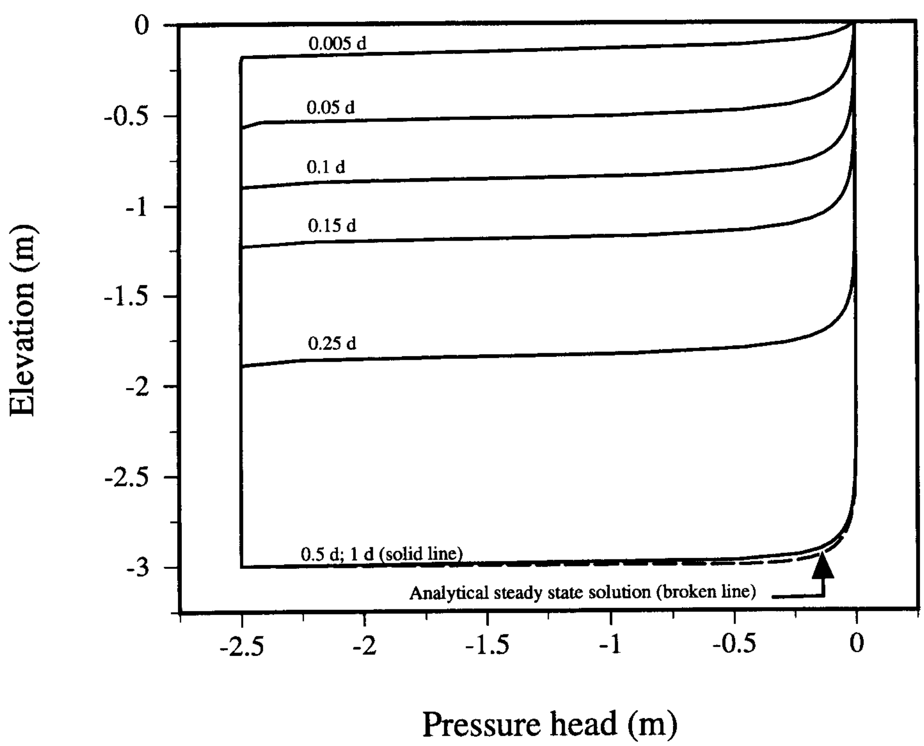

Figure 4-10. Pressure head profiles: Higher permeability material with Gardner permeability formulation

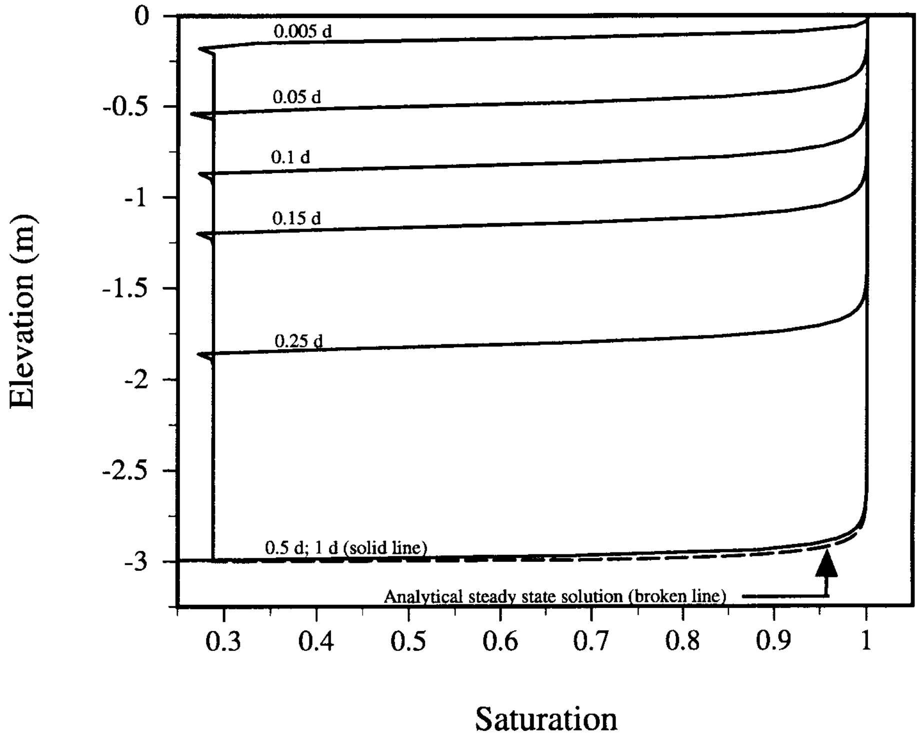

Figure 4-11. Saturation profiles: Higher permeability material with Gardner permeability formulation

4.2 TRANSIENT INFILTRATION: MATRIX-FRACTURE INTERACTIONS

The problems in this set examine the tools available in ABAQUS for modeling the flow of water through fractures in unsaturated rock. The geometry of the problem is illustrated in Figure 4-12. A steady downward water flux is applied at the top of a vertical fracture and the advance of water in the fracture and absorption into the matrix are monitored.

The governing equations for the problem are the same as given in Section 4.1.1, with Eq. (4-1) modified to include a term for the gradient of horizontal flux. The values of the material parameters are the same as in Table 4-1; the properties of water are density, ρ=1,000 kg/m^3, and dynamic viscosity, $\mu=10^{-3}$ Pa·s; and the gravitational acceleration is 10 m·s^{-2} (vertically downward).

The initial conditions for the problem are the same as presented in Section 4.1.1.2. The boundary conditions consist of pressure head fixed at the initial value on the bottom and vertical boundaries of the domain, and no vertical flux on the top boundary. A constant downward flux was applied at the top surface of the fracture.

4.2.1 ABAQUS Model Using Interface Elements

The first ABAQUS model of the fracture-flow problem is based on modeling the fracture using interface elements. Because the ABAQUS interface elements have no provision for the external input of fluid flux, the geometry of the problem was modified as illustrated in Figure 4-13. The part of the seal zone on the left and right of the funnel zone was modeled using CPE8R elements, which do not have

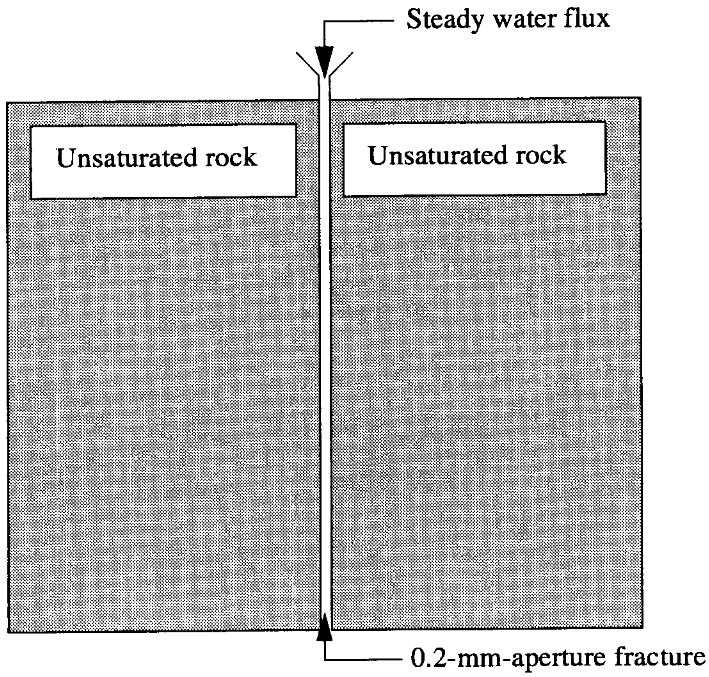

Figure 4-12. Problem geometry for the study of matrix-fracture flow interactions

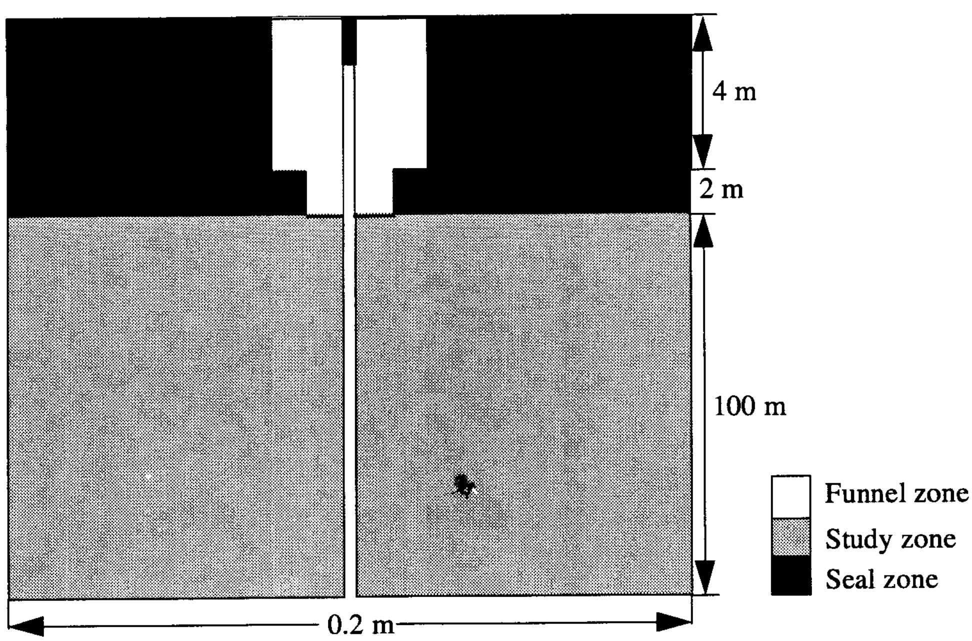

Figure 4-13. Schematic illustration of the geometrical model used for the matrix-fracture interactions problem, with fracture modeled using interface elements

fluid-conducting capabilities. Also, the seal zone at the top of the fracture was modeled with interface elements that were not assigned tangential fluid-conducting capability. The base of the funnel zone was sealed (using no-flux boundary condition) to prevent direct water flow from the funnel zone to the study zone. This arrangement ensured that the only way water could flow into the study zone was through the fracture. The finite element mesh is shown in Figure 4-14.

The study and funnel zones were modeled using CPE8RP, and the fracture with INTER3P, elements. The funnel and study zones were assigned the porosity and moisture-retention properties of the Topopah Spring welded tuff (Table 4-1). The values of saturated hydraulic conductivity were assigned as 6.693×10^{-12} and 6.693×10^{-4} m/s for the study and funnel zones, respectively. The tangential conductivity of the fracture elements (except those that constitute part of the seal zone) was assigned a value equivalent to a hydraulic conductivity of 0.033 m/s using the "*GAP FLOW" command.

The boundary conditions are: fixed pressure head of −1,000 m at all exterior boundaries of the study zone and zero normal flux at the base of the funnel zone. The same initial condition (saturation of 0.274 and pressure head of −1,000 m) was applied in both funnel and study zones. The analysis was conducted in two steps: The first was a *GEOSTATIC step in which gravity was turned on and the initial and boundary conditions were established; the step lasted for one second. The second step was a "*SOILS, CONSOLIDATION" step during which a constant vertically downward flux of 6.693×10^{-4} m/s was applied on the top surface of the funnel zone over a period of 6,000 s.

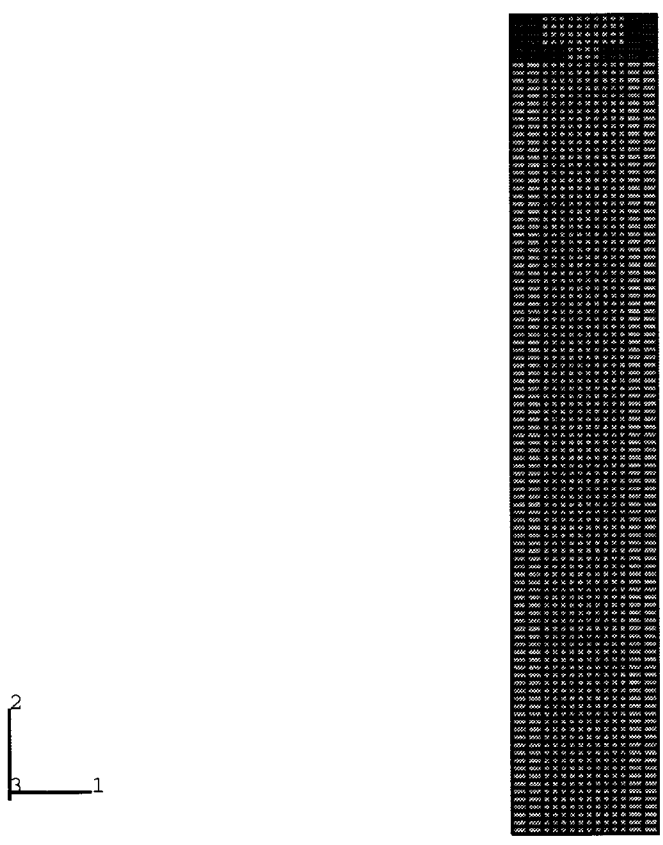

Figure 4-14. Finite-element mesh used for the matrix-fracture interactions problem, with fracture modeled as interface elements (vertical scale reduced 100 times)

4.2.2 ABAQUS Results Using Interface Elements

The pore-pressure distribution is shown in Figure 4-15 for the condition at the end of 6,000 s of steady downward water flux on the top surface of the funnel zone. The seal-zone elements are not included in the figure. It should be noted that the vertical scale is reduced 100 times in the figure. Whereas the width of the model is only 0.2 m, the height of the study zone (i.e., up to the base of the funnel zone) is 100 m. The pore-pressure distribution shown in the figure is consistent with the concentration of flow in the fracture with little matrix imbibition. Such distribution of flow is consistent with analytical results obtained for inclined surfaces on unsaturated low-permeability materials using a thin-film flow model (Kapoor, 1994).

An important piece of information required from analyses such as this is the rate of advance of the wetting front along the fracture wall. This information may be obtained from pore-pressure or saturation profiles, such as are given in Figures 4-2 through 4-5, or in terms of history plots of either pore pressure or saturation at specific points. The pore-pressure histories obtained at eight points along the left fracture wall are shown in Figure 4-16. The figure suggests that an instantaneous pore-pressure increase occurred along the entire length of the fracture following the application of water flux at the top of the funnel zone. Thereafter, the pore pressure increased progressively at every point, the rate of increase being largest at the fracture top and smallest at its base. The pore-pressure histories at points near the base of the fracture were examined and found to follow the same pattern as those shown in Figure 4-16.

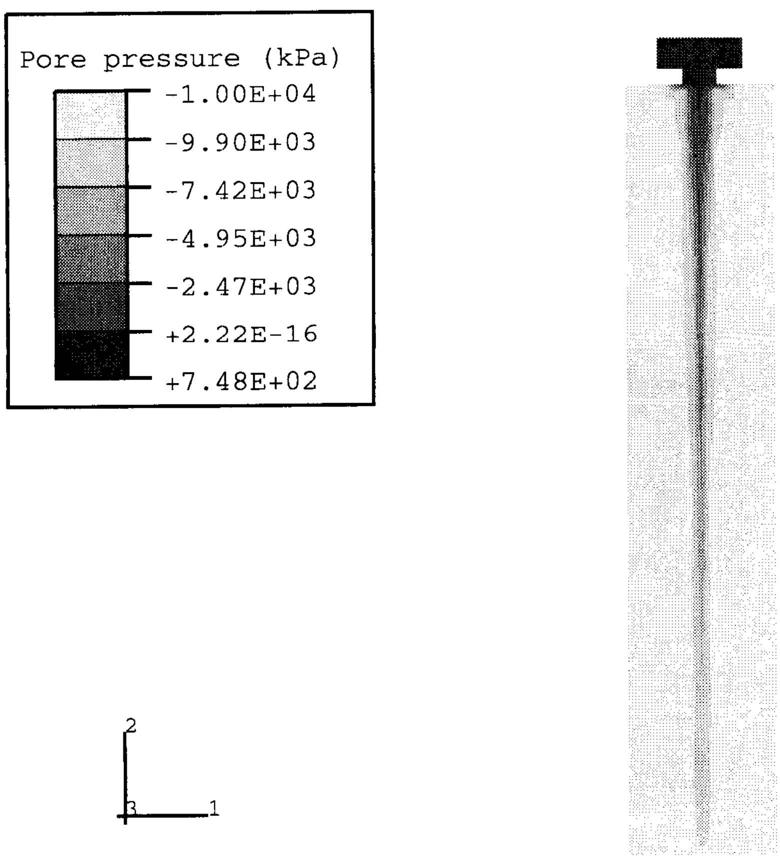

Figure 4-15. Pore-pressure distribution at the end of 6,000 s, using the ABAQUS interface-element model of fracture flow, in Topopah Spring welded tuff (vertical scale reduced 100 times)

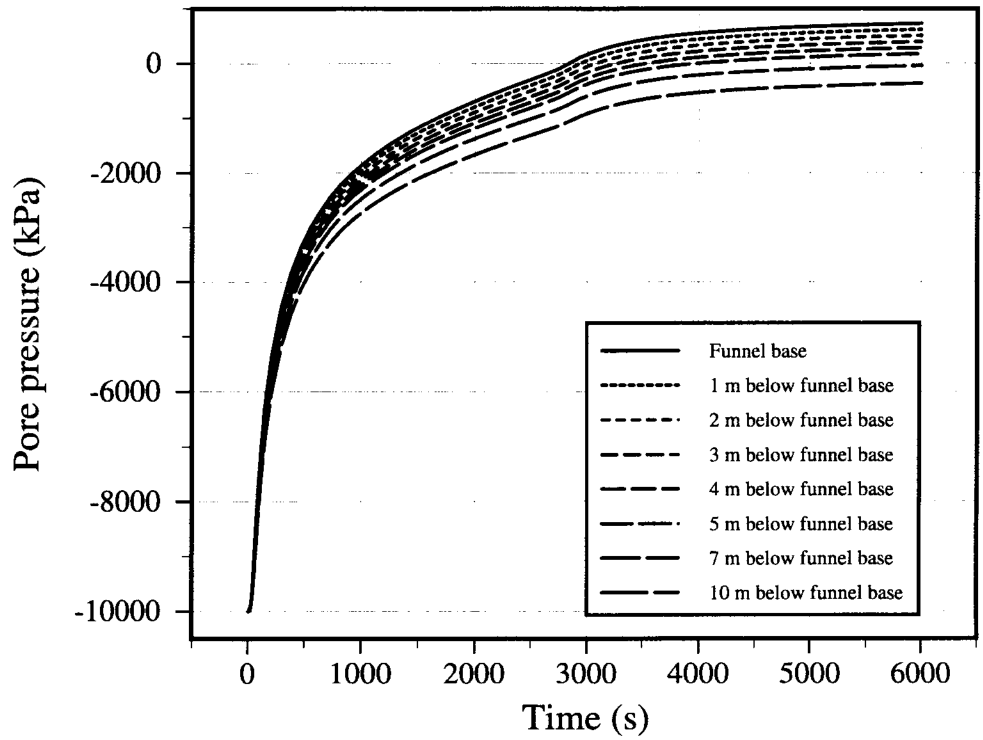

Figure 4-16. Pore-pressure histories along the fracture wall, using the ABAQUS interface-element model of fracture flow, in Topopah Spring welded tuff

The instantaneous pore-pressure increase that is predicted to occur at the same time everywhere along the fracture is not correct. The wetting front should advance down the fracture at a finite velocity. That is, the first occurrence of pore-pressure increase at a given elevation on the fracture should lag behind the occurrence at any other higher elevation by a nonzero amount of time. This miscalculation of the pore-pressure response along the fracture may be related to the ABAQUS implementation of fluid-flow constitutive relations for the interface elements. As was discussed in Section 4.1.1, the flow of water in unsaturated media is governed by two sets of constitutive laws: one defines the relationship between fluxes and pressure gradients [such as Eq. (4-2)], and the other defines the moisture-retention behavior [such as Eq. (4-3)]. Only the flux-vs-pressure-gradient relation is implemented for the interface elements in ABAQUS, with an additional restriction that the values of pressure be the same at pairs of opposite nodes. This implementation of the fluid-flow constitutive model for the interface elements is adequate for the analysis of saturated flow (for which the moisture-retention behavior is not required because saturation is permanently equal to unity); but, as the results in Figure 4-16 show, it is not appropriate for the analysis of unsaturated flow.

On the other hand, any of the ABAQUS solid elements with fluid-flow capabilities may be used as thin-layer elements to simulate fracture flow, provided that appropriate values are assigned to the geometry and material properties of such element. This approach to modeling fracture flow was tested and is described next.

4.2.3 ABAQUS Model Using Thin Solid Elements

The use of thin solid elements to model rock fractures is more readily justified when the fractures are filled. In such cases, the properties of the thin solid can be assigned values similar to those of the fracture filling. On the other hand, when there are no fracture fillings the justification for using the thin solid elements and the assignment of their property values depend on the type of phenomena being modeled. The behavior of such elements in mechanical-processes modeling was examined by Sharma and Desai (1992), who suggested empirical criteria for selecting values of length-to-thickness ratio for the elements. They demonstrated that results computed using the elements agreed satisfactorily with the measured mechanical responses of fractures in concrete. A key problem with using the thin solid elements to model water flow through fractures in unsaturated rock is how to assign appropriate moisture-retention behaviors to such elements. The moisture-retention response of an unfilled fracture is likely to depend on the fracture aperture (similar to the effect of cross-sectional radius on the capillarity of a tube) and on the properties of the fracture-wall rock.

Because of the lack of measured data on unsaturated fracture flow, assumptions are often made for the values for the moisture-retention parameters, such as S_r, β, and n in Table 4-1 (cf. Bagtzoglou and Muller, 1994). The moisture-retention behavior implied by such assumed parameters should satisfy the following: (i) the magnitude of suction head developed in the fracture should be orders of magnitude smaller than that of the rock matrix; and (ii) the change in saturation between the residual value (S_r) and full saturation should occur over a small change in pressure head. The second requirement implies a moisture-retention curve for which the gradient of pressure head with respect to saturation is nearly zero. The curves assumed in this study for fractures in Topopah Spring welded tuff are shown in Figure 4-17. The parameters are: S_r=0.274 and n=5.0 for the two fracture curves, and β=1.0 and 0.1 for fracture zones 1

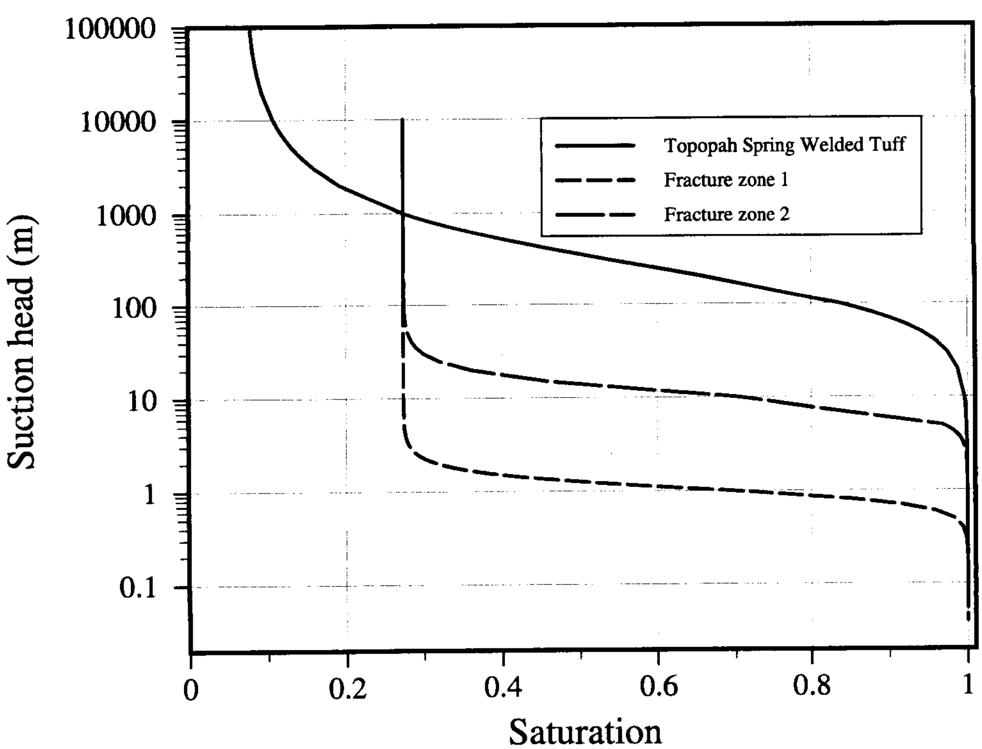

Figure 4-17. A moisture-retention curve for Topopah Spring welded tuff, showing behaviors assumed for fractures in the same rock

and 2, respectively. The fractures were assigned high values of S_r (equal to the value of initial saturation for the rock matrix) to avoid numerical problems which occur when two contacting materials are assigned widely different values of initial saturation. The parameters for fracture zone 2 were used for the study. Serious numerical problems occurred with the fracture-zone-1 curve.

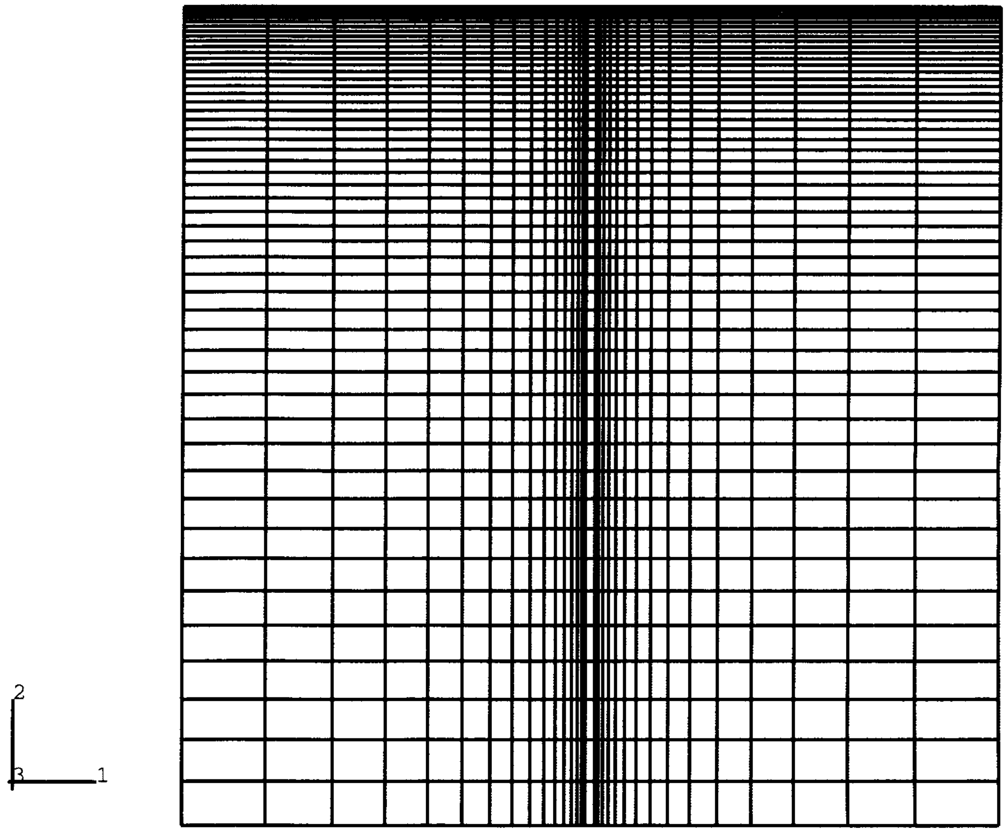

Figure 4-18. Finite-element mesh used for the matrix-fracture interactions problem, with fracture modeled as thin solid elements (vertical scale reduced 100 times)

The finite element mesh used for the problem, with the fracture modeled using thin solid elements, is shown in Figure 4-18. Both the rock matrix and fracture were modeled using CPE8RP elements. Unlike the interface elements used previously, the solid elements permit the external input of fluid flux. Therefore, all the material zones above the study zone in Figure 4-13 are not necessary for the current model so they were eliminated. Also, experience gained from the previous model showed that the test could be run with a much smaller fracture height. As a result, the height of the study zone was reduced to 20 m (from the 100 m used in the previous model). The width of the model is 0.2 m. The width of the thin solid elements (used to model the fracture) was chosen as e/ϕ (where e=0.2 mm is the fracture aperture and ϕ=0.0925 is the porosity of the thin solid) to provide an amount of pore volume equal to the fracture volume. Thus, the thin solid (equivalent fracture) elements, which occupy the center of the mesh, are each 2.2 mm wide. The height and width of the rest of the elements were graded as shown in the mesh.

The boundary conditions are: fixed pressure head of −1,000 m at the base of the model and on the two vertical exterior boundaries; and zero normal flux at the top of the model, except for the fracture elements. An initial saturation of 0.274 and pressure head of −1,000 m were applied everywhere. The saturated hydraulic conductivity for the fracture elements was set to 0.033 m/s (equal to the equivalent conductivity of a 0.2-mm-aperture fracture) vertically and 6.693×10^{-12} m/s (the same as that of the rock matrix) horizontally.

The analysis was conducted in three steps: The first was a *GEOSTATIC step, in which gravity was turned on and the initial and boundary conditions were established: the step lasted for 1 s. The second was a "*SOILS, CONSOLIDATION" step, during which the water flux at the top of the top fracture element was ramped up from 0 to 0.033 m/s (vertically downward) over a period of 10 s. The third step was the same as the second, except that the input flux at the top fracture element was held constant at 0.033 m/s over a period of 55 s.

4.2.4 ABAQUS Results Using Thin Solid Elements

The pore-pressure distribution at the end of the 66-s simulation time is shown in Figure 4-19. It should be noted that the vertical scale in the figure is reduced 100 times (the model is 20 m high and 0.2 m wide). As the results show, the model used in this study predicts that water flow occurs mainly through the fracture, with little matrix imbibition. A similar behavior was predicted using the interface elements, as was shown in Figure 4-15. Therefore, the results in Figure 4-19 strengthen the belief that thin solid elements can be used to match the performance of the interface elements with respect to the concentration of flow in the simulated fracture.

The histories of pore pressure on the fracture wall and saturation along the middle of the fracture are given in Figures 4-20 and 4-21, respectively. As the first figure shows, the pore pressure at a point on the fracture wall remains essentially unchanged at the initial value until a certain time at which it increases rapidly to a value near zero. The second figure shows that the saturation at a point changes in the same manner as the pore pressure, except that saturation increases at a slower rate than pore pressure. The calculated pore-pressure or saturation histories can be used to monitor the progress of the wetting front along the fracture, where "wetting front" is defined as the boundary between materials at the initial

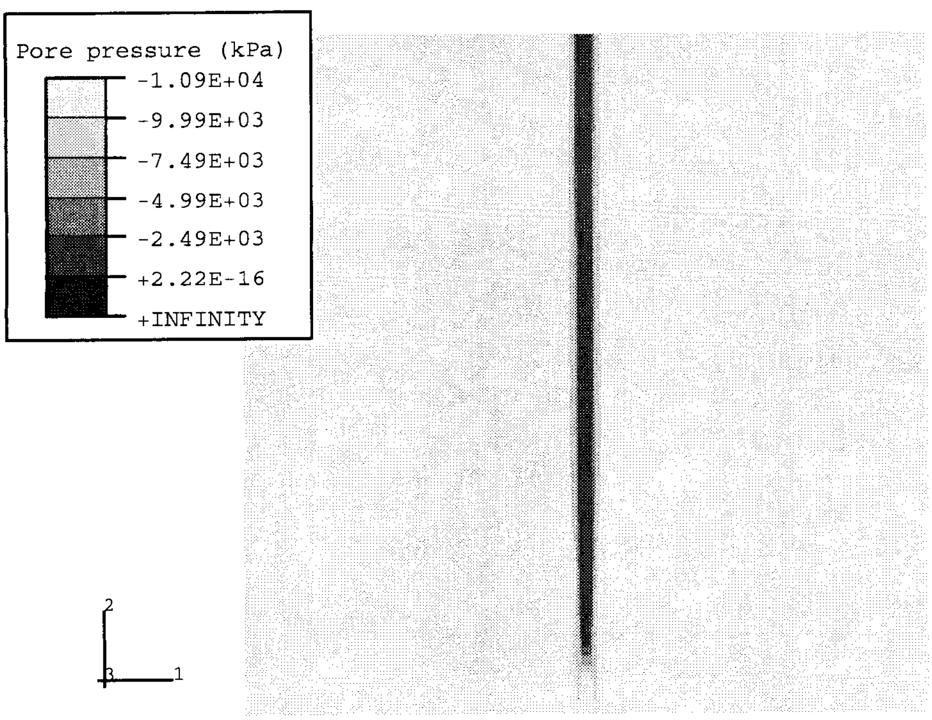

Figure 4-19. Pore-pressure distribution at the end of 66 s, using the ABAQUS thin-solid-element model of fracture flow, in Topopah Spring welded tuff (vertical scale reduced 100 times)

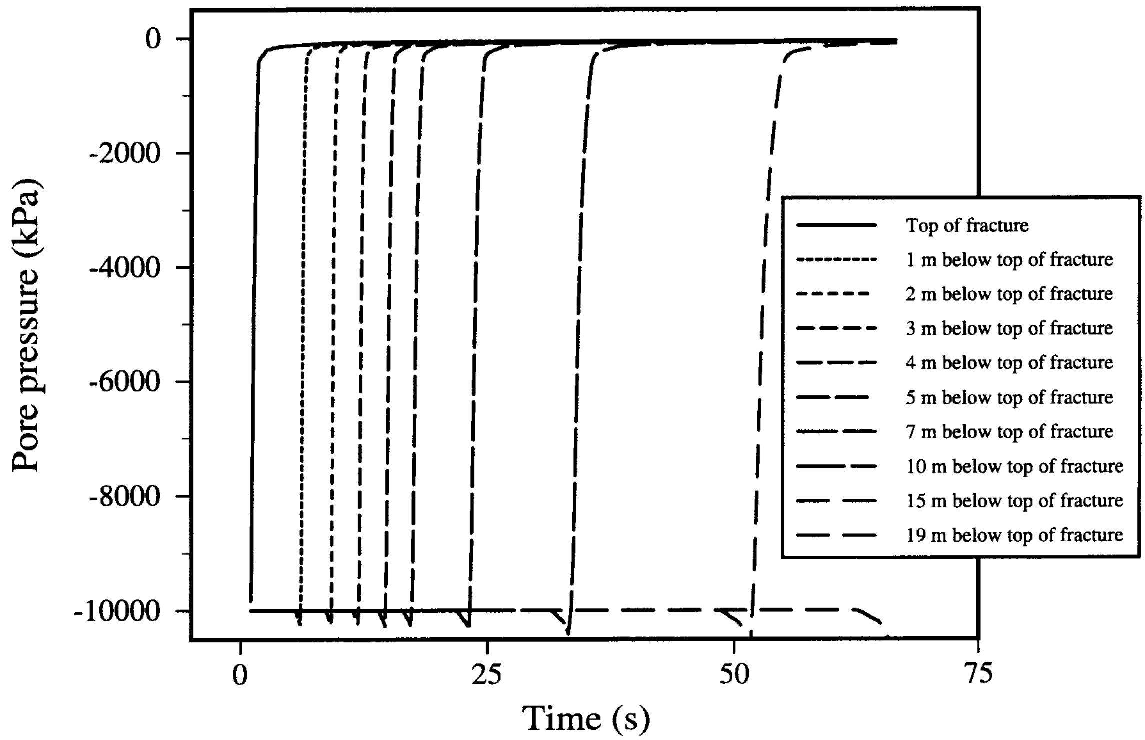

Figure 4-20. Pore-pressure histories along a vertical fracture in Topopah Spring welded tuff, calculated using the ABAQUS thin-solid-element model

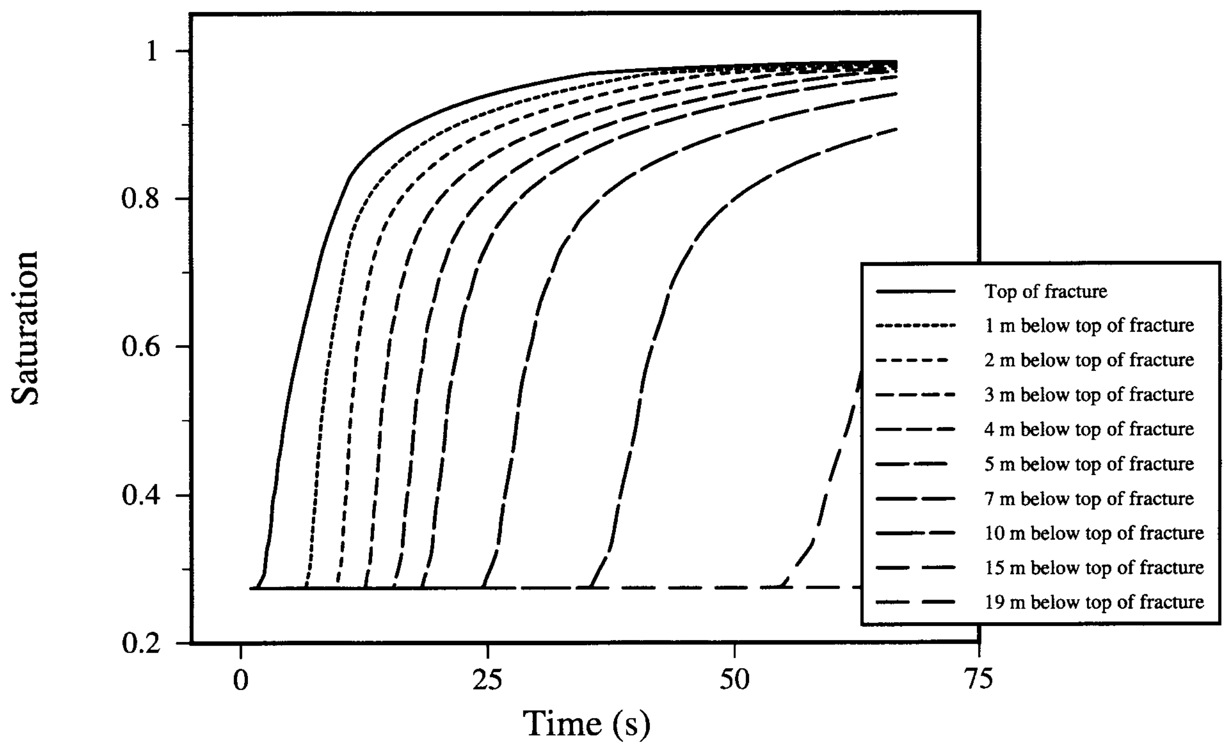

Figure 4-21. Saturation histories along a vertical fracture in Topopah Spring welded tuff, calculated using the ABAQUS thin-solid-element model

saturation (or pore pressure) and those for which the value of saturation (or pore pressure) has increased above the initial value. The results calculated using the interface elements, which were presented in Figure 4-16, do not yield information on the progress of the wetting front. As a result, the thin-solid elements are considered to be better suited for fracture-flow analyses than are the interface elements (using the current implementation of the interface elements in ABAQUS).

4.2.5 CTOUGH Model Using Thin Solid Elements

The finite difference code CTOUGH was also used to solve the same problem. As with the ABAQUS model, the fracture in the CTOUGH model was simulated using thin solid elements. The values of the material parameters are the same as were used in the ABAQUS analysis. The boundary conditions and value of initial saturation were also the same as were applied in ABAQUS. On the other hand, CTOUGH does not permit user-specification of the initial pore pressure; instead, it uses the specified values of initial saturation to compute the initial pore pressure. This method of setting the initial pore pressure created a problem for the fracture elements, for which the initial saturation is very close to the residual saturation. The code calculated an initial pore pressure of about −1,300 kPa, corresponding to an initial suction head of about 130 m instead of the required 1,000 m. However, the initial suction head of 130 m in the fracture elements was considered a satisfactory starting value for the problem, considering the shape of the moisture-retention curve for the fracture (Figure 4-17) between suction-head values of 100 and 1,000 m.

The histories of pore pressure and saturation calculated using CTOUGH are presented in Figures 4-22 and 4-23, respectively. The results presented in these figures agree generally with the corresponding ABAQUS-calculated results presented in Figures 4-20 and 4-21, but the following differences occur:

(i) The rate of wetting-front advance calculated using ABAQUS is faster than the CTOUGH-calculated rate. As Figure 4-20 shows, the wetting-front would be placed at a depth of about 15 m in 50 s, based on the ABAQUS calculations; on the other hand, CTOUGH would place it at a depth of less than 7 m in 50 s.

(ii) Both the rate of saturation increase and the ultimate value of saturation predicted at a given depth using ABAQUS are larger than the corresponding values predicted using CTOUGH (Compare Figures 4-21 and 4-23).

The differences between the ABAQUS and CTOUGH results imply differences in the amount of water-loss by matrix imbibition predicted by the two codes. The rate of matrix imbibition implied by the CTOUGH results is larger than the rate implied by the ABAQUS results. The difference between the imbibition rates is illustrated further in the next section using wetting-front arrival time plots.

4.2.6 Comparison of Wetting-Front Advance Rates

The wetting-front advance histories computed using different models of the same fracture-flow problem are plotted in Figure 4-24. The different models are:

(i) Analytical solution for a 1D model assuming fully filled fracture with constant flux of 0.033 m/s at the top

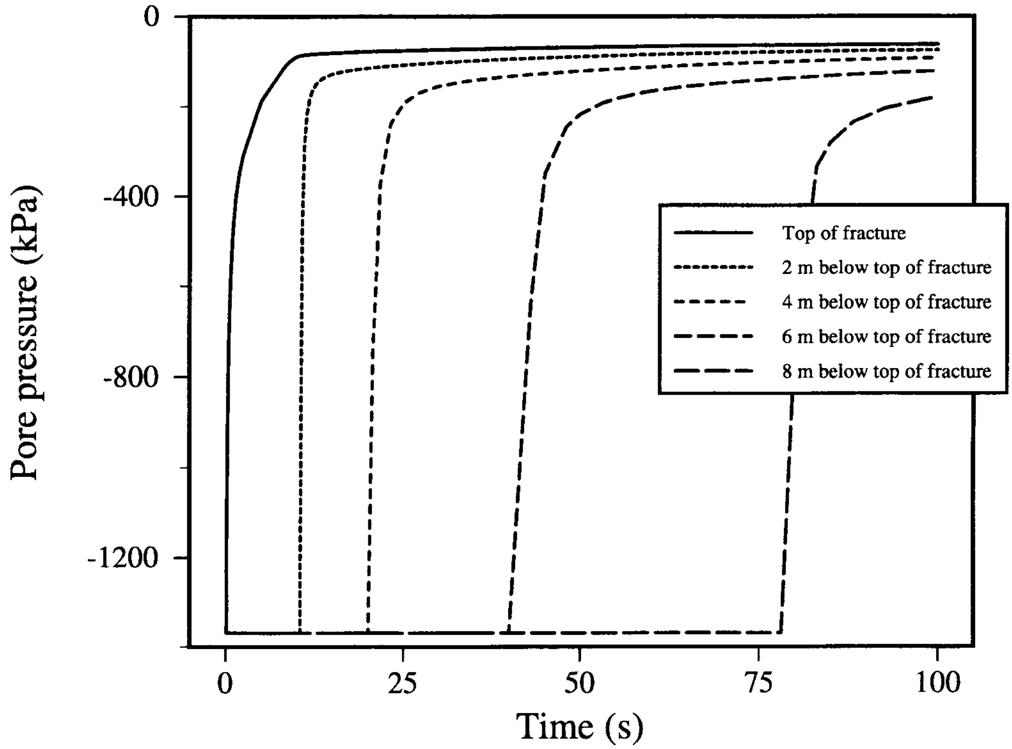

Figure 4-22. Pore-pressure histories along a vertical fracture in Topopah Spring welded tuff, calculated using the CTOUGH model

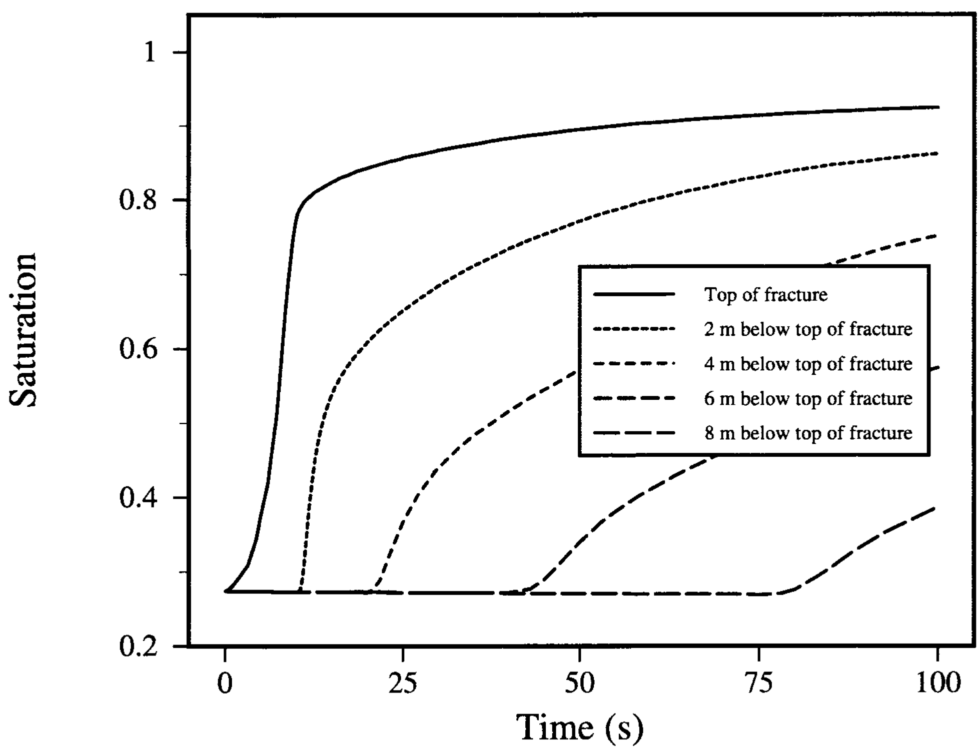

Figure 4-23. Saturation histories along a vertical fracture in Topopah Spring welded tuff, calculated using the CTOUGH model

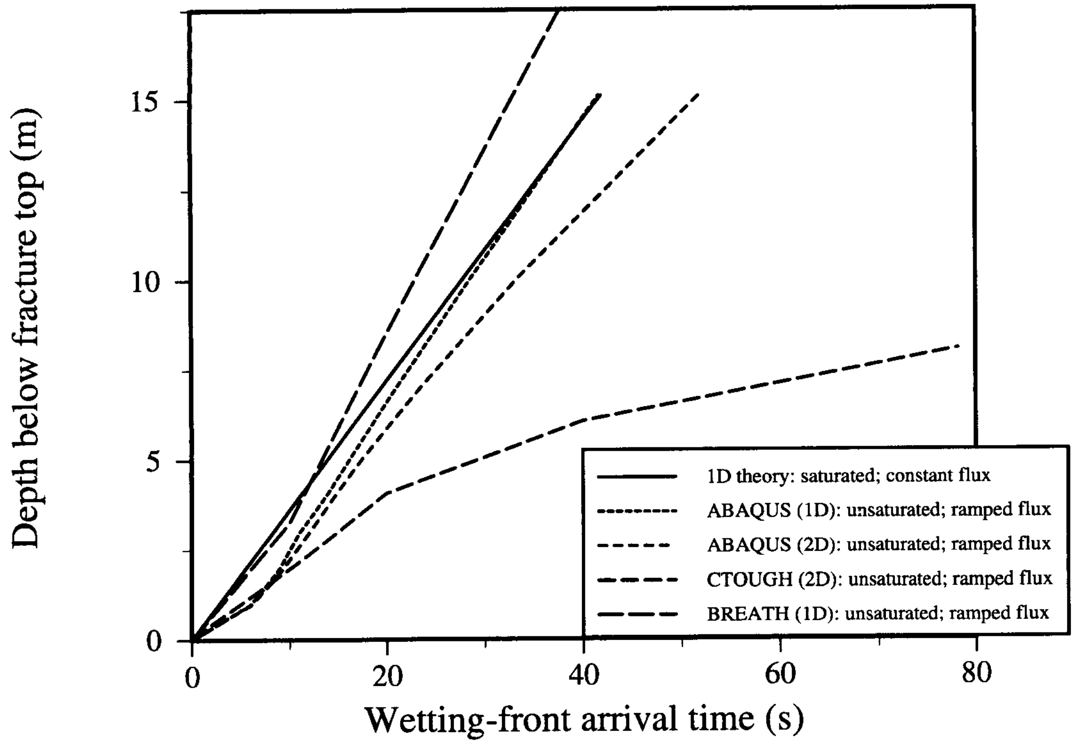

Figure 4-24. Histories of wetting-front advance along a vertical fracture in Topopah Spring welded tuff, calculated using different models

(ii) For a 1D thin-solid model of the unsaturated fracture with flux ramped from 0 to 0.033 m/s in 10 s, and held constant thereafter; the solution was obtained using the computer code BREATH (Stothoff, 1995)

(iii) For a 1D thin-solid model of the unsaturated fracture with flux ramped as described in item (ii); the solution was obtained using ABAQUS

(iv) The ABAQUS two-dimensional (2D) model described previously

(v) The CTOUGH 2D model

The velocity of the wetting front based on a 1D model is equal to $q/(\phi S)$, where q is the applied flux, ϕ=0.0925 is the porosity, and S is the saturation. For the saturated case with constant flux, this gives a velocity of 0.357 m/s, corresponding to the solid line in Figure 4-24. For the 1D unsaturated cases with ramped flux, the wetting-front velocity should be small initially because of the small value of q; thereafter, the velocity should increase and approach a limiting value that depends on the limiting saturation distribution. Both the BREATH and ABAQUS 1D solutions follow this behavior, except that the BREATH-calculated initial velocity is larger than that of ABAQUS. This difference may be explained by the fact that the ABAQUS 1D solution was actually computed using the 2D model described earlier, with the saturated conductivity of the rock matrix reduced to 6.693×10^{-20} m/s from the 6.693×10^{-12} m/s used in the 2D model.

The wetting-front velocity calculated using a 2D model should be smaller than the 1D velocities; furthermore, the 2D-model velocity should decrease progressively because of increasing matrix imbibition. Both the ABAQUS and CTOUGH 2D results follow this behavior. However, the CTOUGH velocities are smaller than those of ABAQUS, which implies a larger rate of matrix imbibition in the CTOUGH model than in the ABAQUS models.

4.2.7 ABAQUS Analyses for Material #2

A similar fracture-flow problem was solved for a fracture in a rock with the material #2 property set (see Table 4-1). The problem was solved using the finite element mesh presented in Figure 4-18, except for the following changes:

(i) The width of the model was increased to 2.0 m to accommodate the faster rate of matrix imbibition in material #2; the height remained unchanged at 20 m

(ii) The width of the (thin-solid) fracture elements was changed to 0.667 mm, to represent a 0.2-mm-aperture fracture with 0.3-porosity solid elements

The moisture-retention curves for the rock matrix and the assumed curves for the fracture are given in Figure 4-25. The parameters for the fracture curves are: S_r=0.285 and n=3.0 for the two curves, and β=7.5 and 100 for fracture zones 3 and 4, respectively.

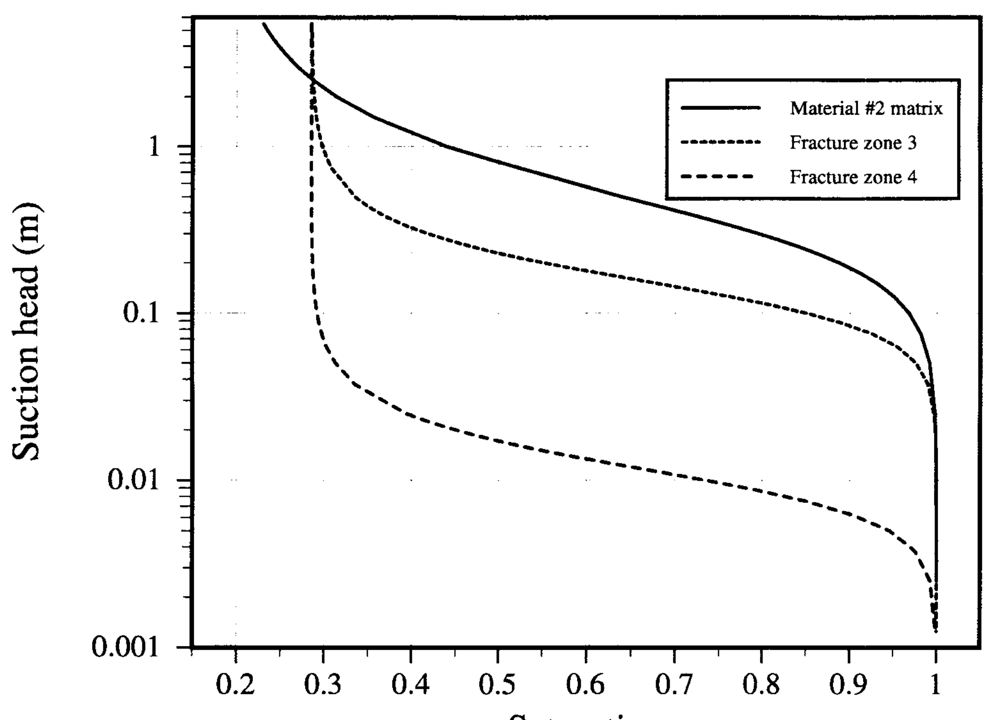

Figure 4-25. Moisture-retention curve for material #2 showing behaviors assumed for fractures in the rock

The initial conditions were set as defined for material #2 in Table 4-1, that is, a saturation of 0.288 and pressure head of −2.5 m everywhere. The boundary conditions are: fixed pressure head of −2.5 m at the base of the model and on the two vertical exterior boundaries; and zero normal flux at the top of the model, except for the fracture elements. The saturated hydraulic conductivity for the fracture elements was set to 0.033 m/s (equal to the equivalent conductivity of a 0.2-mm-aperture fracture) vertically and 1.625×10^{-5} m/s (the same as that of the rock matrix) horizontally.

The analysis was conducted in two steps: a *GEOSTATIC step, during which gravity was turned on and the initial and boundary conditions were established, followed by a "*SOILS, CONSOLIDATION" step, during which a constant downward water flux of 0.033 m/s was applied on the top surface of the top fracture element. The first step lasted for 1 s while the second was for 2 hr.

Two analyses were conducted using this model. The rock-matrix properties were the same for both cases. On the other hand, the fracture elements were assigned the moisture-retention parameters for fracture zone 3 in one case (FZ3 case), and those of fracture zone 4 in the other (FZ4 case). As Figure 4-25 shows, the values of pore pressure developed in the wet zone of the fracture would be higher with the fracture zone 4 properties than with fracture zone 3 properties, which implies that the fracture-to-matrix pressure gradient would be higher for the FZ4 analysis case than for the FZ3 case. As a result, the rate of matrix imbibition is likely to be larger, and that of downward wetting-front advance likely to be smaller, in the FZ4 case than in the FZ3 case.

The pore-pressure distributions at the end of 2 hr are given in Figures 4-26 and 4-27 for the FZ3 and FZ4 analysis cases, respectively. The figures show the top 2 m of the model (recall that the model is 2 m wide). The histories of wetting-front advance down the fracture for both analysis cases are plotted in Figure 4-28, which also shows the analytical solution for the 1D saturated fracture model. The following observations are made, considering the results presented in these figures:

(i) The rates of downward wetting-front advance calculated using ABAQUS are much larger for a fracture in Topopah Spring welded tuff than for a fracture in material #2. The wetting front advanced a maximum of about 1.8 m in 2 hr for a fracture in material #2; on the other hand, it advanced about 19 m in 60 s for a fracture in Topopah Spring welded tuff.

(ii) Based on theoretical considerations, it is expected that the rate of matrix imbibition should be larger for a fracture in material #2 modeled using fracture zone 4 properties than for one with fracture zone 3 properties (Figure 4-25). The ABAQUS-calculated results for analysis cases FZ3 and FZ4, which are shown in Figures 4-26 through 4-28, are consistent with this expectation.

4.3 CONCLUSIONS

The computer code ABAQUS was evaluated in this chapter with respect to its capabilities to model the flow of water through an unsaturated fractured rock mass. The problems solved examined the flow of water through rock matrix alone, as well as through both fractures and rock matrix, including the effects of matrix imbibition on fracture flow. The performance of the code was evaluated as follows:

(i) Solutions obtained using ABAQUS were compared with those obtained using two other computer codes [CTOUGH (Lichtner, 1994), which is a modified version of V-TOUGH (Nitao, 1989), and BREATH (Stothoff, 1995)]

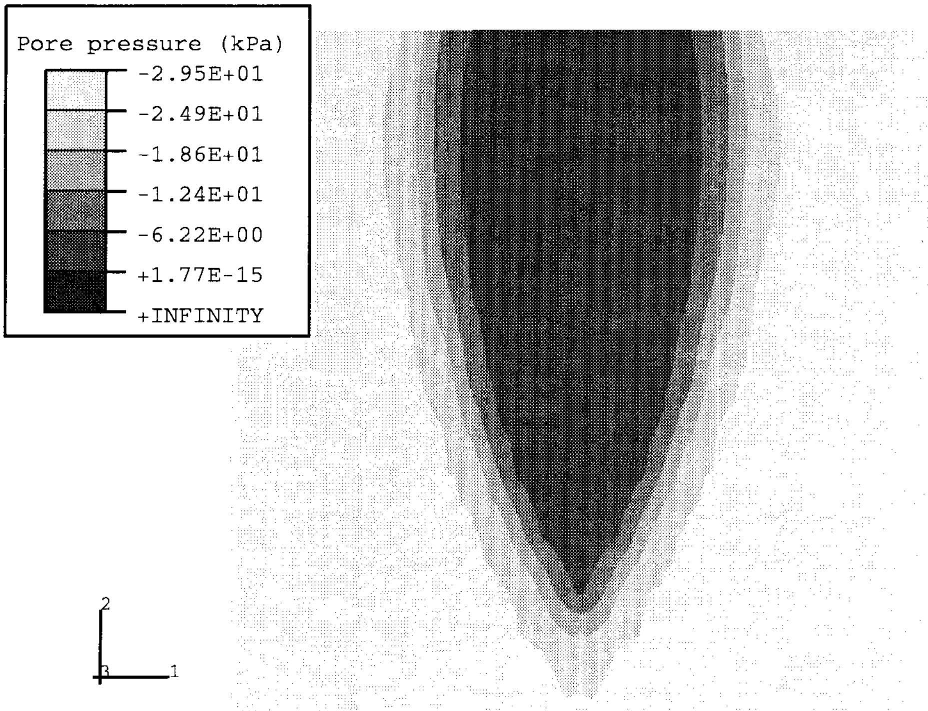

Figure 4-26. Pore-pressure distribution at the end of 2 hr, calculated using ABAQUS for FZ3 analysis case. Only the top 2 m section of the model is shown (model width = 2 m).

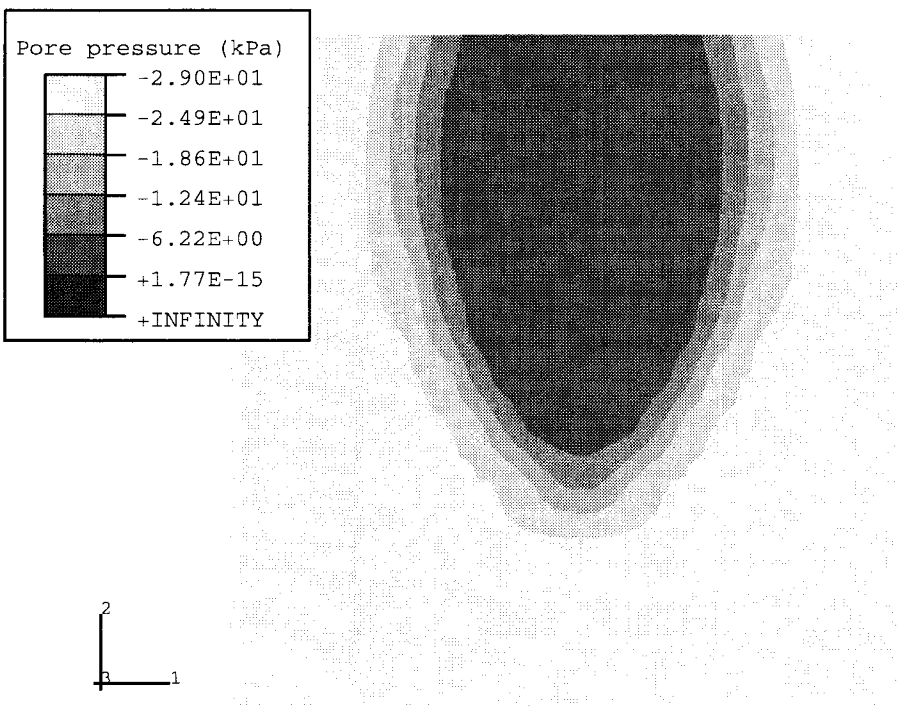

Figure 4-27. Pore-pressure distribution at the end of 2 hr, calculated using ABAQUS for FZ4 analysis case. Only the top 2 m section of the model is shown (model width = 2 m).

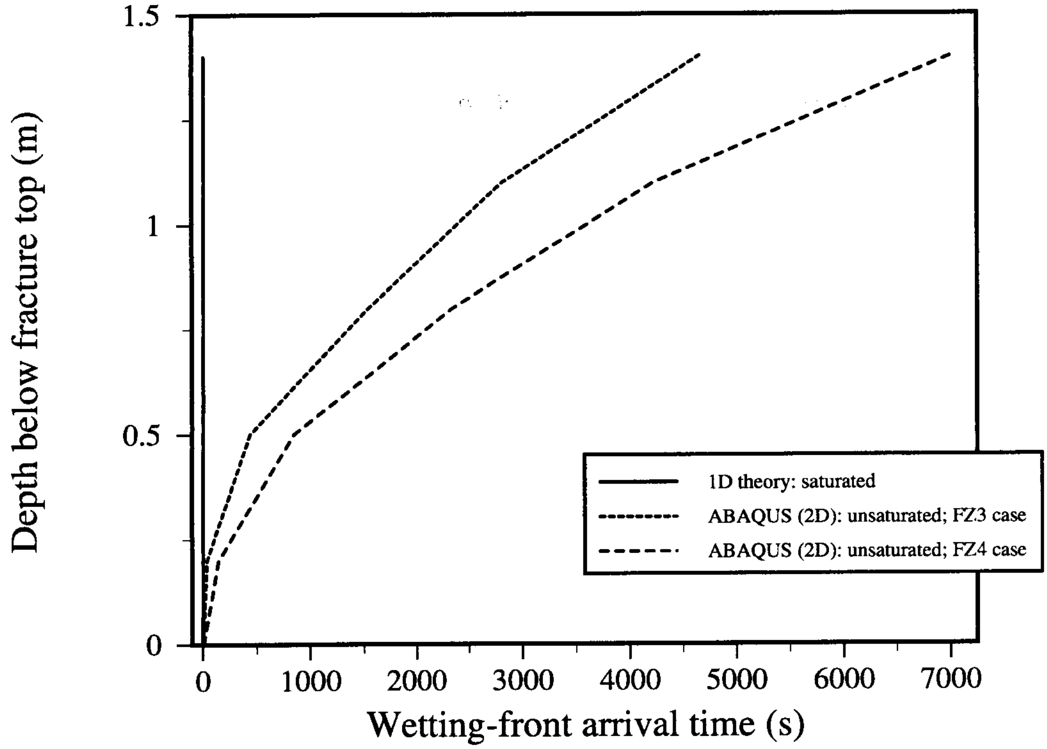

Figure 4-28. Histories of wetting-front advance along a vertical fracture in material #2, calculated using ABAQUS

(ii) Long-term transient solutions obtained using ABAQUS were compared with the steady-state analytical solution for the same problem

(iii) The general response predicted by ABAQUS was compared with the expected response based on theoretical considerations

The problems were solved for a low-permeability and low-porosity material similar to the Topopah Spring welded tuff, as well as for a high-permeability and high-porosity material referred to as material #2, which has a value of permeability similar to that of silty to clean sand (cf. Freeze and Cherry, 1979), thus covering a wide range of hydrological response.

The performance of ABAQUS was found to be satisfactory for the problems examined. Fractures were modeled using thin solid elements, because the interface elements did not give satisfactory predictions. The interface elements, as currently implemented in the code, are not satisfactory for modeling unsaturated fracture flow. It is believed that their unsatisfactory performance is caused by the fact that they are not assigned any moisture-retention characteristics. The changes required to implement such characteristics for the elements cannot be accomplished through any of the user-subroutine interfaces currently available in ABAQUS. Therefore, such changes require access to the ABAQUS source code.

5 THERMAL-MECHANICAL PROBLEMS: HEATED DRIFT IN FRACTURED ROCK MASS

The problems solved under this category were selected to examine the capabilities of ABAQUS in modeling both excavation- and thermally induced stresses and deformations in a fractured rock mass. One of the concerns in evaluating the performance of a proposed nuclear waste repository at YM is the effect of thermal and mechanical loads on the hydraulic conductivity of fractures. Mechanical effects on the flow of water through fractures arise from changes in fracture aperture. It is expected that the magnitude of such effects will vary, depending on such factors as the fracture orientations and surface properties, the distribution and connectivity of fractures, the initial stress state, and the distribution of water in the rock mass. Therefore, the decision regarding the extent to which thermal and mechanical loads may affect the deformation of fractures and, consequently, their contribution to the rock-mass hydraulic conductivity, is likely to be made on the basis of the analyses of specific cases. The heated-drift problems were chosen to determine the extent to which ABAQUS may be suitable for calculating stresses and deformations in a fractured rock mass, including fracture deformations due to thermal and mechanical loads.

Two cases of a heated drift in a fractured rock mass are examined. In one case the drift is intersected by four sets of fractures and is considered to lie in the interior of a rectangular array of horizontal drifts. In the other case, the drift is intersected at its crown by a single vertical fracture; it is considered to lie in the middle of a linear array of horizontal drifts, so its interaction with the ground surface was included in the analyses. In both cases, the drift-wall was subjected to a prescribed temperature history to simulate the thermal load due to emplaced waste, and the distributions of stresses and fracture aperture were monitored. The first problem was solved in two dimensions, whereas the second was solved in both two and three dimensions.

5.1 PROBLEM GEOMETRY AND MATERIAL PROPERTIES: CASE OF DRIFT INTERSECTED BY FOUR FRACTURE SETS

The problem considers a horizontal drift in a rock mass containing four sets of fractures as follows: a vertical set, a horizontal set, and two orthogonal sets dipping at 45° into the drift. All the fractures were assumed to be infinitely persistent and initially closed. All the fracture planes were assigned a strike parallel to the drift axis. The drift was assumed to be infinitely long, and the directions of the three *in situ* principal stress components were assumed to be vertical, horizontal and coincident with the drift axis, and horizontal and normal to the drift axis. These assumptions for the strike direction of the fracture planes and the orientations of the principal stress components permit the problem to be analyzed using plane strain.

The analyses considered only two fractures from the vertical set, two from the horizontal set, and one from each of the inclined sets, in order to simplify the problem geometry. Furthermore, the selected fractures were assumed to intersect the drift wall at the locations shown in Figure 5-1, which permits the problem to be symmetrical about the horizontal and vertical planes that intersect along the drift axis. Therefore, only one-quarter of the problem domain needs to be analyzed, and the quadrant selected for analyses (any of the four could have been selected) is shown in Figure 5-2.

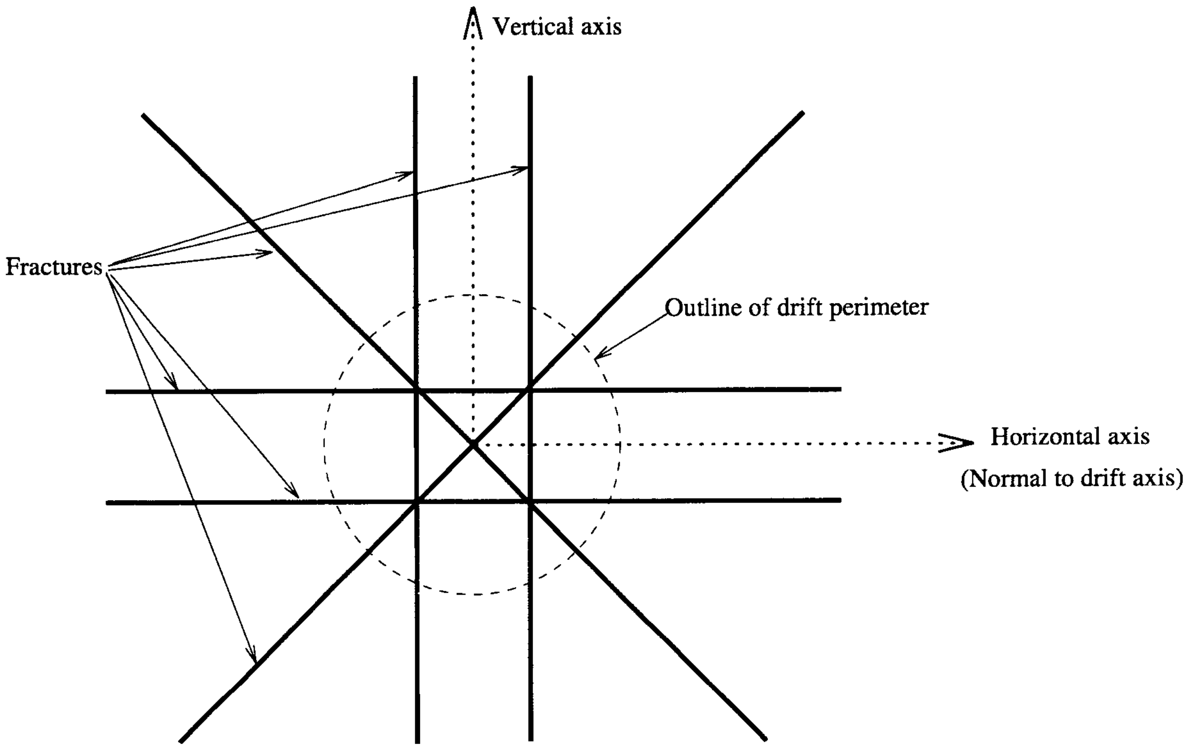

Figure 5-1. Problem geometry for heated drift in fractured rock (case of four fracture sets): A vertical section through the drift showing the fractures selected for analyses

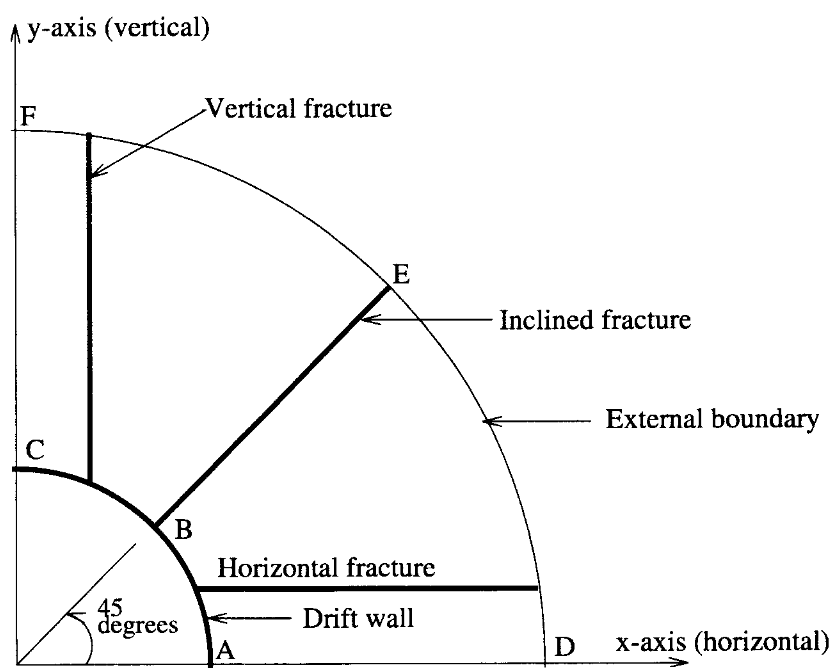

Figure 5-2. Problem domain discretized for the analyses of heated drift in fractured rock (case of four fracture sets)

The drift was assigned a circular cross-section with a diameter of 9 m. The horizontal, inclined, and vertical fractures intersect the drift wall at $\theta = 22.5°$, 45°, and 67.5°, respectively, where θ is the angle measured counterclockwise from the x-axis (Figure 5-2). The initial temperature (i.e., at the zero-strain state) was 25 °C, and the initial principal compressive stress components were 10 MPa (vertical) and 2 MPa (horizontal). The problems in this set were also to be solved for the case of a hydrostatic initial stress state, but the results of an initial scoping analysis indicated that this case does not add any information on the performance of the code. Therefore, the hydrostatic case was dropped from the study. The intact rock was assumed to be similar to the Topopah Spring welded tuff; the values for material parameters were assigned from the RIB (Version 4.4) and are given in Table 5-1. The simulated sequence

Table 5-1. Material property specifications for the heated-drift problem sets

Property, Symbol, and Unit	Value
Young's modulus, E (MPa)	3.27×10^4
Poisson's ratio, ν	0.25
Friction angle for fracture surfaces, ϕ	40°
Cohesion for fracture surfaces (MPa)	0.0
Coefficient of linear expansion, α (K^{-1})	8.5×10^{-6}
Thermal conductivity, k_θ [MJ/(m·s·K)]	2.1×10^{-6}
Specific heat capacity, C_v [MJ/(m^3·K)]	2.2
Density, ρ (kg/m^3)	2.24×10^3

of events consisted of drift excavation under constant temperature, followed by heating. The thermal history of emplaced waste was simulated by subjecting the drift wall to the temperature history shown in Figure 5-3 (Manteufel et al., 1993). As this figure shows, the wall temperature attained a maximum of 230 °C after 9 yr; thereafter it decreased, reaching 120 °C in 1,000 yr. The entire 1,000-yr temperature history was applied. The calculated responses are presented for 9, 300, and 1,000 yr, representing the time of maximum input temperature, a time near the middle of the temperature-time history, and a long time.

5.1.1 Boundary Conditions

The boundaries of the problem domain can be classified as internal and external boundaries. The internal boundaries are the drift wall (represented by curve ABC in Figure 5-2) and the symmetry planes (represented in the same figure by the horizontal line AD and vertical line CF) that were established as a result of the assumptions presented in Section 5.1. The external boundary is represented in Figure 5-2 by curve DEF; the shape of the external boundary may vary depending on the method chosen to model the problem domain.

The conditions at the internal boundary were specified as follows: (i) values of temperature were specified at the drift wall, according to the temperature history described in Section 5.1; (also, the condition of zero normal stress was specified for this boundary after the drift was excavated); (ii) symmetry boundary conditions (i.e., zero heat flux and displacement perpendicular to the boundary) were specified on AD and CF.

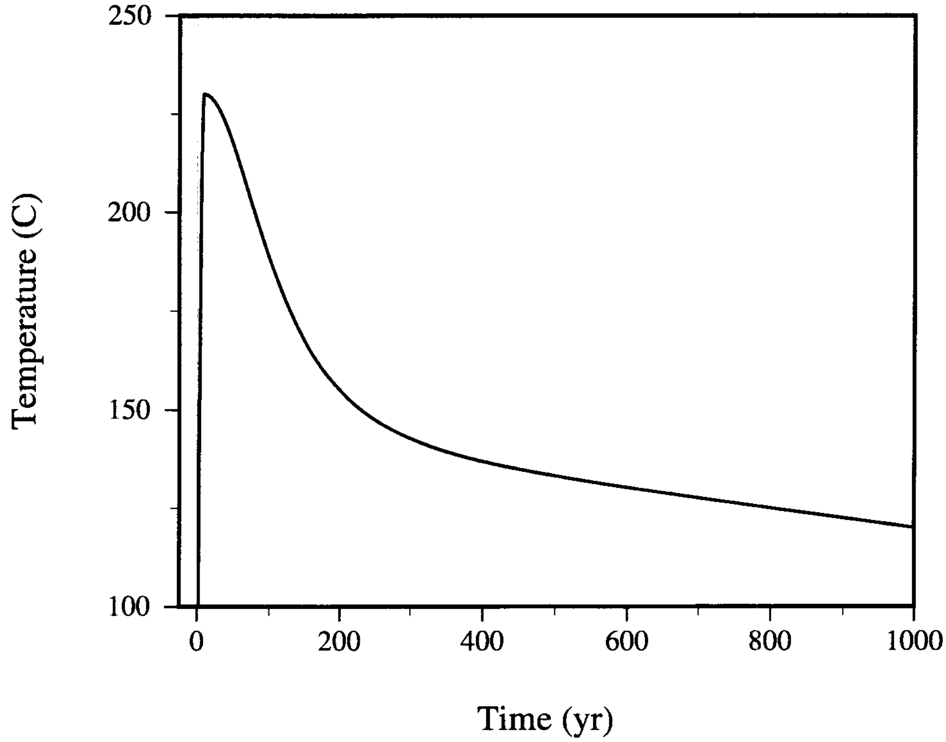

Figure 5-3. Temperature history applied to the drift wall to simulate the thermal history of emplaced waste

The appropriate external boundary conditions for a drift depend on its location relative to other drifts, such as is shown in Figure 5-4. Each interior drift interacts with its neighbors, such that symmetry conditions exist on a part or all of its external boundary. On the other hand, zero-perturbation conditions need to be enforced on at least some part of the external boundary of each exterior drift; that is, the part of its boundary that coincides with the boundary between the perturbed and unperturbed regions of the rock mass surrounding the drift array. These variations of the external boundary conditions can be considered to lie between two extremes; namely, (i) a pure interior problem, for which symmetry conditions exist on the entire external boundary, and (ii) a pure exterior problem, for which the entire external boundary is assigned zero-perturbation conditions.

The boundary conditions for the interior problem were used for this problem set. The external boundary for the problem was established along the lines x=50 m (vertical external boundary) and y=50 m (horizontal external boundary); symmetry conditions were applied on the boundary. Such an external boundary implies the assumption that the drift is surrounded by other drifts located at a distance of 100 m center-to-center, both in the vertical and horizontal directions, such as in Figure 5-4.

5.1.2 Evaluation Strategy

The problems in this set cannot be solved analytically, because of (i) the complexity of the driftwall temperature history, and (ii) the possibility of inelastic response on parts of the fractures. Therefore, it was decided to evaluate the performance of ABAQUS by comparing the ABAQUS-calculated responses with those calculated using the distinct element code UDEC (ITASCA Consulting Group, 1993).

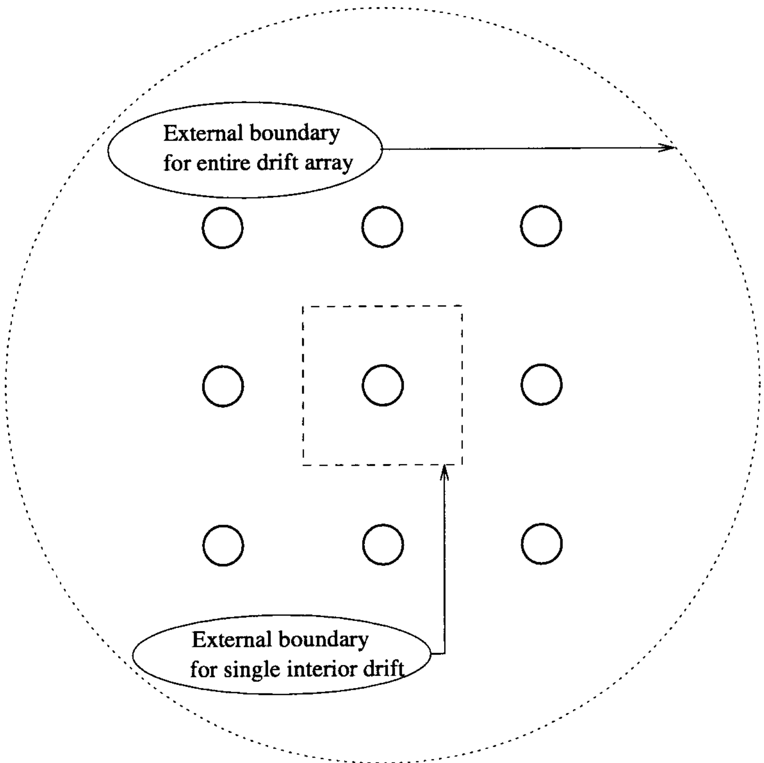

Figure 5-4. A vertical section through a hypothetical array of horizontal drifts showing one interior drift surrounded by eight exterior ones

The responses calculated using the two codes are compared through plots of the shear stress, τ, and normal stress, σ_n, on the three fractures shown in Figure 5-2. In addition, contours of the principal stress components, σ_1 (maximum principal compressive stress) and σ_3 (minimum principal compressive stress), are presented. Some of the comparisons are semiquantitative, whereas others are purely qualitative; attempts are made to explain any differences that are observed between the responses calculated using the two codes.

5.1.3 ABAQUS Model

The ABAQUS model was based on the sequential-coupling approach that was described briefly in Section 3.4. This approach was chosen because a decision was made to ignore the effect of fractures on heat transfer (by conduction), in order to avoid further complication of the comparison of ABAQUS- and UDEC-calculated responses. Changes in fracture aperture may occur during the simulation period, which may change the contribution of fractures to the effective thermal conductivity, as was demonstrated in Chapter 3. Although the effect of fracture aperture on thermal conductivity can be incorporated in the ABAQUS model using the procedure described in Section 3.4.1.2, it cannot be incorporated in the UDEC model. Therefore, this effect was ignored in the analyses and, as a result, the sequential-coupling approach could be used.

The finite-element discretization of the problem domain is shown in Figure 5-5. The mesh consists of 1,028 four-noded solid quadrilateral elements for the intact rock, and 80 four-noded interface quadrilateral elements for the fractures. The mesh was generated using PATRAN (PDA Engineering, 1994).

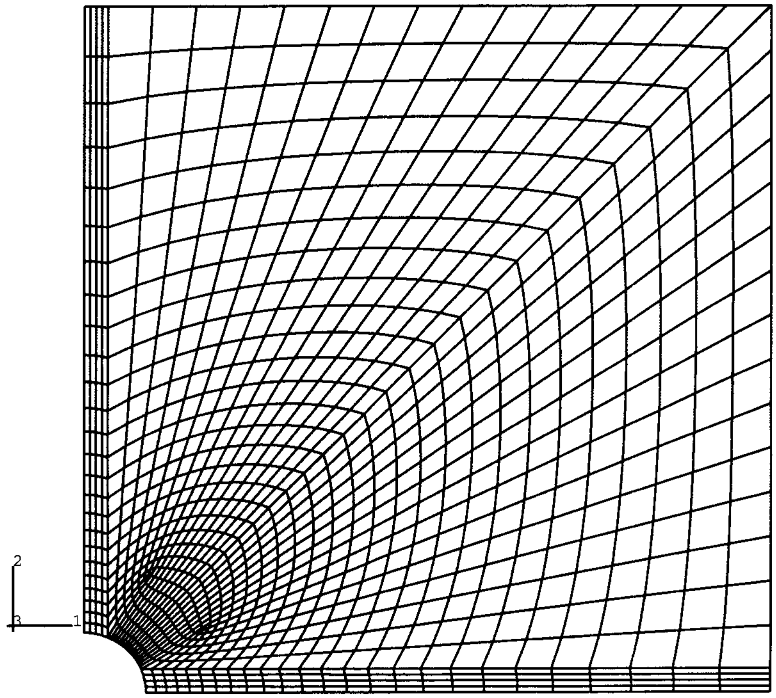

Figure 5-5. Finite-element discretization of the interior-drift problem

5.1.3.1 Thermal Analysis Model

The elements used for the heat transfer analyses are the DC2D4 (solid elements) and DINTER2 (interface elements). The material properties required for the solid elements are the thermal conductivity, density, and heat capacity per unit mass (equal to C_v/ρ); these properties were defined as specified in Table 5-1. The unit of time was changed from seconds to days, in order to reduce the size of numbers required to specify time. As a result, the thermal conductivity, k_θ, was specified as 0.1814 MJ/(m·d·K). The value of gap conductance, μ, obtained using Eq. (3-9) would be infinite for zero fracture aperture. Therefore, μ was set to 1,000 times k_θ, and was held constant at that value throughout the heat transfer simulation period.

Definition of Thermal Boundary Conditions

The temperature history shown in Figure 5-3 was defined in the model using the *AMPLITUDE command, as follows:

```
*AMPLITUDE,NAME=TEMPHIST,DEFINITION=TABULAR,TIME=TOTAL TIME
0.000,25.000,1.000,25.000,132.400,41.072,263.800,56.488
395.200,71.248,526.600,85.352,658.000,98.800,789.400,111.592
920.800,123.728,1052.200,135.208,1183.600,146.032,1315.000,156.200
etc.
```

where the numbers are given in the sequence t_i, θ_i, t_{i+1}, θ_{i+1}, etc., and θ_i is the temperature (°C) at the time t_i (d). The temperature was kept constant at 25 °C from time of 0 through 1 d to synchronize the thermal and mechanical analyses; the excavation phase of the mechanical analysis, which was conducted under constant temperature (as is discussed later), was completed from time of 0 through 1 d. The above *AMPLITUDE command essentially established the temperature-time function (Figure 5-3) under the name TEMPHIST. Thereafter, the drift-wall temperature was assigned a value in each thermal-analysis step using the command:

```
*BOUNDARY,AMPLITUDE=TEMPHIST
WALL,11, ,1.0
```

where the node set named WALL consists of the nodal points on the drift wall. This statement causes ABAQUS to calculate the temperature at such nodal points at any time by multiplying the value of temperature given for that time by the function TEMPHIST with the number 1.0 (given in the *BOUNDARY command).

The condition of zero heat flux perpendicular to the remaining part of the internal boundary (i.e., lines AD and CF in Figure 5-2) was specified using the *DFLUX command. The *DFLUX command was also used to specify the zero normal heat flux condition for the external boundary (i.e., the lines x=50 m and y=50 m).

Thermal Analysis Steps

Each of the heat transfer analyses was accomplished in nine steps, as shown in Table 5-2. All zero-flux and fixed-temperature boundary conditions were defined during the first step, which lasted until the end of 1 d. The *BOUNDARY command for the drift-wall temperature was invoked during each step. The values of temperature at all nodal points were saved at the end of each step using the "*NODE FILE" command. The saved file constitutes the interface between the thermal and mechanical analyses.

Table 5-2. Thermal analysis steps for the ABAQUS model

Step Number	Total Time at End of Step		Remarks
	d	Yr	
1	1.0	1/365	Initial temperature; zero boundary flux established.
2	1,643.5	4.5	Drift-wall heating started in this step.
3	3,286	9.0	Drift-wall heating continues in this and subsequent steps.
4	36,501	100	
5	73,001	200	
6	109,501	300	
7	146,001	400	
8	182,501	500	
9	365,001	1,000	

5.1.3.2 Mechanical Analysis Model

The elements used for the mechanical analyses were CPE4 (solid elements) and INTER2 (interface elements). The material parameters required for the solid elements are the Young's modulus, Poisson's ratio, and coefficient of linear expansion. The only parameter required for the interface elements is the friction coefficient for the fracture surfaces. The shear resistance of the fracture surfaces was modeled using the Coulomb failure criterion. These parameters were assigned the values specified in Table 5-1.

Definition of Mechanical Boundary and Initial Conditions

The condition of zero normal displacement was prescribed at all times for the horizontal and vertical internal boundaries (lines AD and CF in Figure 5-2), as well as for the external boundaries x=50 m (vertical) and y=50 m (horizontal). The boundary conditions for the drift wall (the remaining part of the internal boundary) required special treatment, as is explained in the next section.

The initial conditions (i.e., for the state of zero strain) were specified using the "*INITIAL CONDITIONS" command, as follows:

```
*INITIAL CONDITIONS,TYPE=STRESS
BODY,-2.0,-10.0,-2.0,0.0
*INITIAL CONDITIONS,TYPE=TEMPERATURE
ALLN,25.0
```

where the element set named BODY includes only all the nodal points. the solid elements, and the node set named ALLN includes every nodal point in the model. The first use of the command (first two lines in the above paragraph) assigned initial values to the stress components σ_{xx}, σ_{yy}, σ_{zz}, and σ_{xy}, for all elements in the set BODY; the values are negative because ABAQUS uses the tension-positive sign convention. The second use of the command assigned an initial temperature of 25 °C at every nodal point.

Mechanical Analysis Steps

Each mechanical analysis was accomplished in 10 steps, as described in Table 5-3. During the first step, the drift-wall part of the internal boundary was fixed using the following command:

```
*BOUNDARY,FIXED
WALL,1,2
```

where the node set named WALL consists of the nodal points on the drift wall. This command causes ABAQUS to hold the x- and y-displacements at all such nodes at their current value, which in this case is zero. This value is held constant until a new boundary-condition definition is entered for the same nodes. Having fixed the drift wall, the only thing accomplished in this step was to establish the initial stress state in the rock mass under zero strain.

Thereafter, the excavation of the drift was simulated during the second step by redefining all boundary conditions as follows:

```
*BOUNDARY,OP=NEW
LEFT,1
BASE,2
RIGHT,1
TOP,2
```

where the node sets named LEFT and BASE consist of nodes on the vertical and horizontal internal boundaries, respectively; those node sets named RIGHT and TOP consist of nodes on the vertical and horizontal external boundaries, respectively. The nodes in the named sets were fixed in the specified directions (direction 1 is the x-direction, whereas 2 is the y-direction). The modifier "OP=NEW" in the command causes ABAQUS to fix the named nodes in the specified directions and free all nodes as follows: (i) all nodes not named in the command are freed in every direction, and (ii) all the directions not specified for the named nodes are freed. Because the node set WALL was not named, all the member nodes of this set were freed in accordance with this prescription. Therefore, the drift wall was free to move as it would in this and subsequent steps.

Table 5-3. Mechanical analysis steps for the ABAQUS model

Step Number	Total Time at End of Step		Remarks
	d	Yr	
1	0.5	0.5/365	Initial temperature, initial stress, perimeter of proposed drift fixed.
2	1.0	1/365	Initial temperature, drift excavation completed, excavation-induced displacements and stress change.
3	1,643.5	4.5	Temperature change due to drift-wall heating introduced at the beginning of this and subsequent steps.
4	3,286	9.0	
5	36,501	100	
6	73,001	200	
7	109,501	300	
8	146,001	400	
9	182,501	500	
10	365,001	1,000	

5.1.4 UDEC Model

The approach used in UDEC for thermal-mechanical coupled analyses is similar to the sequential-coupling scheme described in Section 5.1.3. After specifying the problem geometry, appropriate mechanical and thermal material properties, and both thermal and mechanical boundary and initial conditions, the problem is cycled (CYCLE command) to bring it to mechanical equilibrium. A small net unbalanced force in this explicit mechanical formulation is taken as the mechanical equilibrium. Once the mechanical state was ready for thermal analysis after the drift was excavated, thermal time steps were taken, using the RUN command, until the desired time (0.36 yr in this simulation) was reached. At this point, the mechanical cycling was carried out to bring the problem domain to mechanical equilibrium. Thermal cycling using explicit logic was repeated at an increment of 0.36 yr followed by mechanical cycling to bring the problem back to mechanical equilibrium until the desired simulation time of 9 yr was reached.

The mechanical properties for intact rock needed for UDEC analysis are: density $2{,}240\times10^{-6}$ in unit of 10^6 kg/m^3, bulk modulus K equal to 21,800 MPa, and shear modulus G equal to 13,080 MPa. The values of basic friction angle and cohesion for the fracture surfaces were assumed to be 40° and 0 MPa, respectively. The normal and shear stiffnesses were 3.5×10^4 MPa/m and 0.5×10^4 MPa/m respectively. The Mohr-Coulomb joint constitutive model (ITASCA Consulting Group, Inc., 1993) was used to model the load-deformation response of all the fractures. A dilation angle ψ equal to 2.9° and a critical shear displacement of 0.037 m were assumed for all three joints. These values were within the measured ranges for natural joints in Apache Leap tuff (Hsiung et al., 1994b). Domain boundaries in UDEC models, such as the boundary between the fine- and coarse-mesh regions in Figure 5-6, are defined using fractures. If the corresponding boundaries in the physical problem are not formed by fractures, then the fractures used to represent them in the model should be assigned values of properties that would preclude their contributing to the response of the model. Such fictitious fractures used in the study were assigned property values as follows: tensile strength of 10^{20} MPa, cohesion of 20 MPa, normal stiffness of 4×10^5 MPa/m, and shear stiffness of 2×10^4 MPa/m.

The thermal properties required by UDEC in consistent units are specific heat [9.82×10^8 in units of 10^{-6} J/(kg·K)], thermal conductivity [2.13 W/(m·K)], and coefficient of linear thermal expansion (8.5×10^{-6} K^{-1}). These values are consistent with the values given in Table 5-1.

5.1.4.1 Discretization

The discretization of the problem domain is shown in Figure 5-6. The region up to 10 m from the drift center was discretized into triangular finite difference grid with maximum edge length of 1 m. Outside this region, the mesh size was increased to 2 m.

5.1.4.2 Initial and Boundary Conditions

The initial conditions for both problems include an ambient temperature of 25 °C (298 K), and *in situ* vertical and horizontal stresses of 10 and 2 MPa, respectively. The INSITU command was used to apply these initial conditions.

All the horizontal and vertical boundaries of the problem domain were symmetry planes. Both horizontal symmetry lines were assigned a zero-vertical-velocity condition. Horizontal velocity was restricted to zero for both vertical symmetry lines.

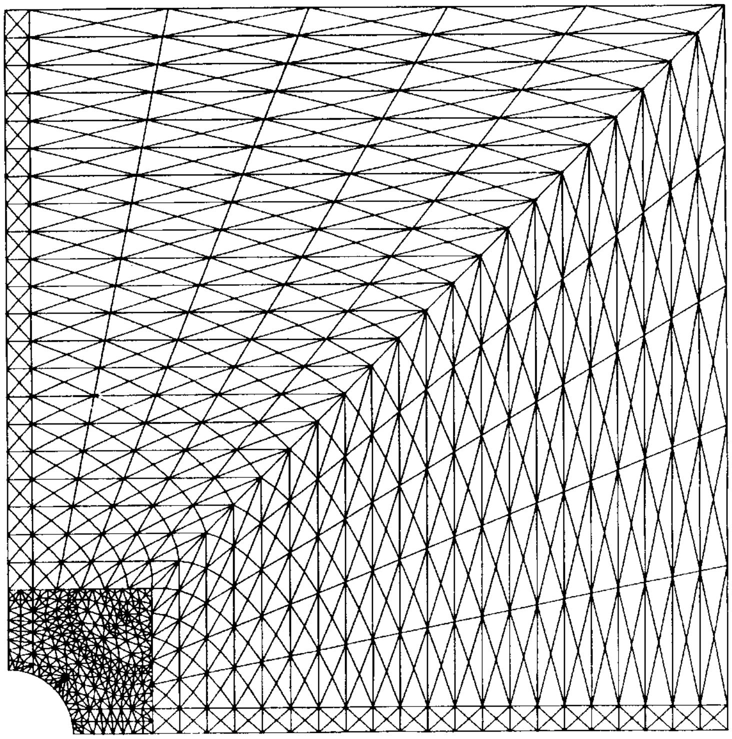

Figure 5-6. Distinct element discretization used for UDEC analyses

5.1.4.3 Loading Procedure

For all the problems a temperature time history was applied at the drift wall at a constant time interval of 0.36 yr. Temperature data at the specific time intervals were obtained from the equation describing the temperature history in Figure 5-3.

5.1.5 Results

It should be recalled that the interior problem, as modeled in this code-evaluation study, represents an infinitely long horizontal drift surrounded by other such drifts, each at a center-to-center distance of 100 m. A vertical section normal to the axial direction of such drifts is shown in Figure 5-4. The drifts are excavated in a fractured rock mass; the intact rock is homogeneous, linear-elastic, and isotropic; and the fractures intersect each of the drifts as shown in Figures 5-1 and 5-2.

The responses calculated for the interior problem are presented in two parts as follows: (i) ABAQUS results, and (ii) comparison of ABAQUS and UDEC results.

5.1.5.1 ABAQUS Results

The temperature distributions around the drift are given in Figures 5-7 through 5-9, for the conditions after 9, 300, and 1,000 yr, respectively. The figures suggest that, for the specific conditions of the interior problem and the specific thermal-output history used in this study, long-term temperatures approach the same value everywhere within the region around the interior drifts. Because of this uniform-temperature condition, the stress state within the region would tend to be hydrostatic (equal

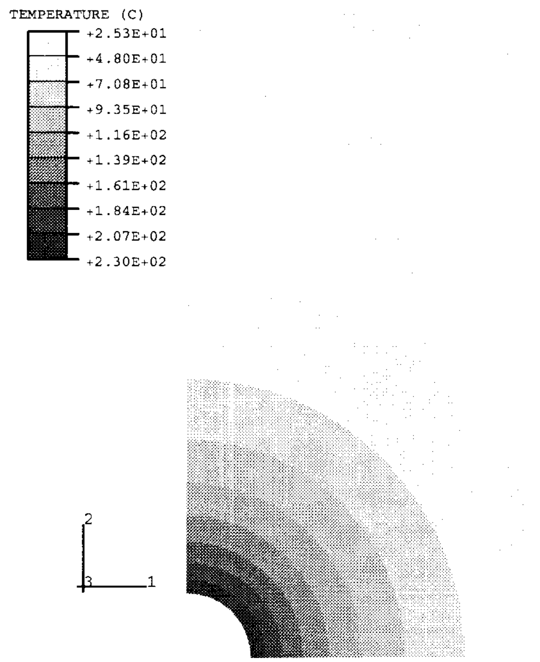

Figure 5-7. Temperature distribution around an interior drift, 9 yr after waste emplacement, based on ABAQUS-calculated response

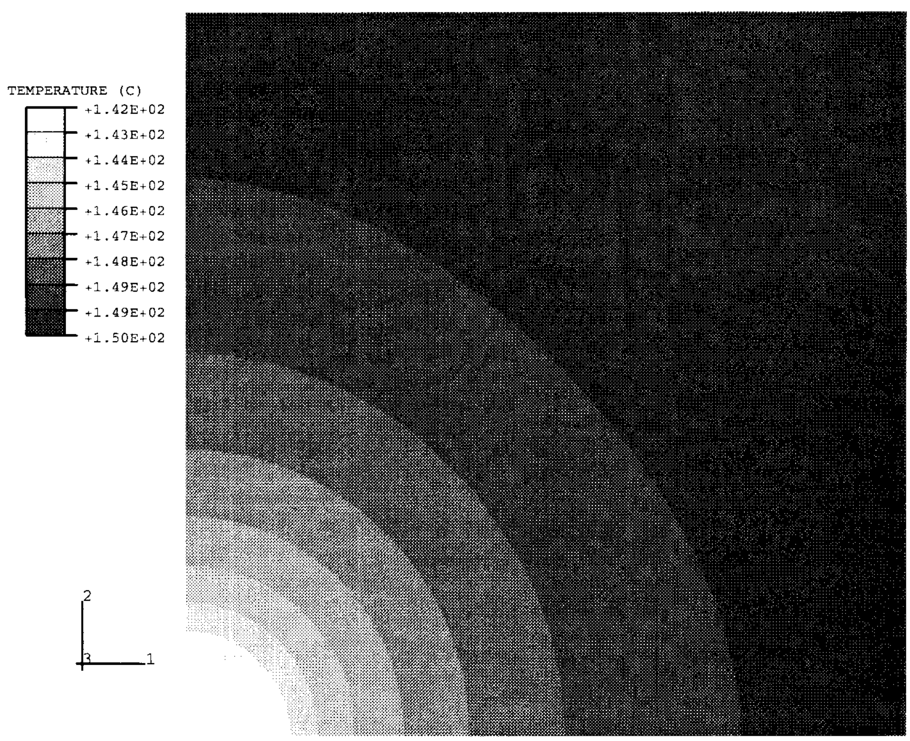

Figure 5-8. Temperature distribution around an interior drift, 300 yr after waste emplacement, based on ABAQUS-calculated response

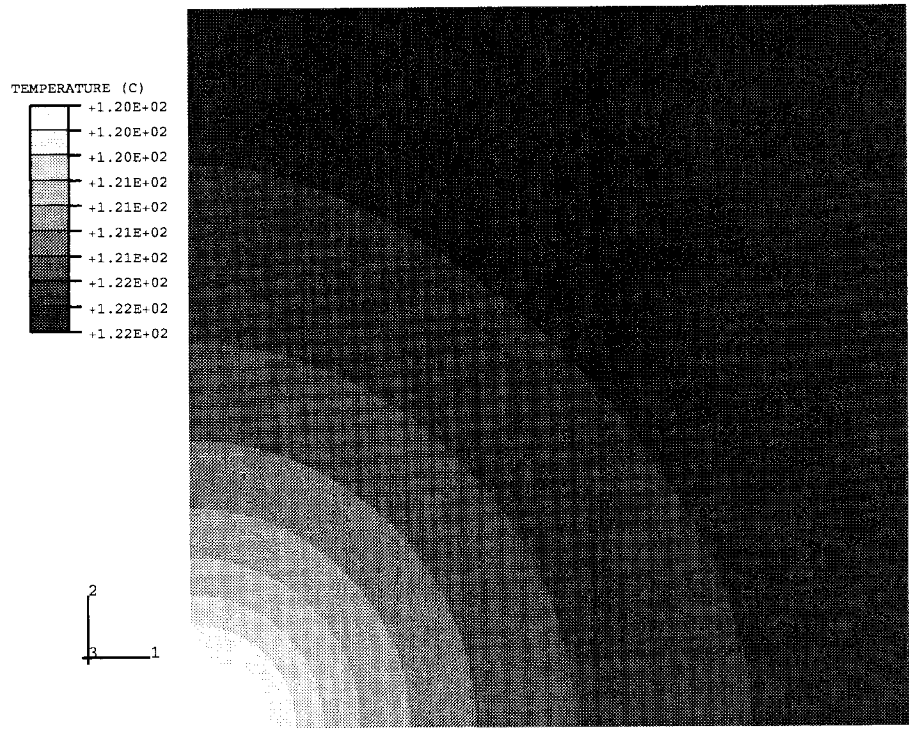

Figure 5-9. Temperature distribution around an interior drift, 1,000 yr after waste emplacement, based on ABAQUS-calculated response

magnitude in every direction) and compressive everywhere, except very close to the drift, where the mechanical effects of the opening hinder the development of hydrostatic stress states. Furthermore, the symmetry condition on the external boundaries will tend to increase the degree of confinement within the region, thereby reinforcing the effect of the uniform-temperature condition in causing the development of hydrostatic compressive stress states. Most fractures within the region are likely to close (i.e., attain minimum aperture) under this stress condition.

The distributions of the horizontal and vertical stress components (σ_{xx} and σ_{yy}, respectively) are plotted in Figures 5-10 through 5-15. The values of stress in the figures are negative because ABAQUS uses the tension-positive sign convention. The observation (illustrated in Table 5-4) that the difference between σ_{xx} and σ_{yy} decreases with time in a large area of the problem domain is consistent with the expected development of nearly hydrostatic stress states. The same conclusion can be reached by examining the distributions of the maximum and minimum principal stress components (σ_{max} and σ_{min}, respectively), which are summarized in Table 5-5.

Table 5-4. Values of compressive stress within most of the region around the drift

Year	Values of Compressive Stress Components within Most of the Problem Domain		Figure Number
	σ_{xx} (MPa)	σ_{yy} (MPa)	
9	49 – 72	58 – 85	5-10 and 5-11
300	63 – 82	52 – 76	5-12 and 5-13
1000	52 – 68	45 – 66	5-14 and 5-15

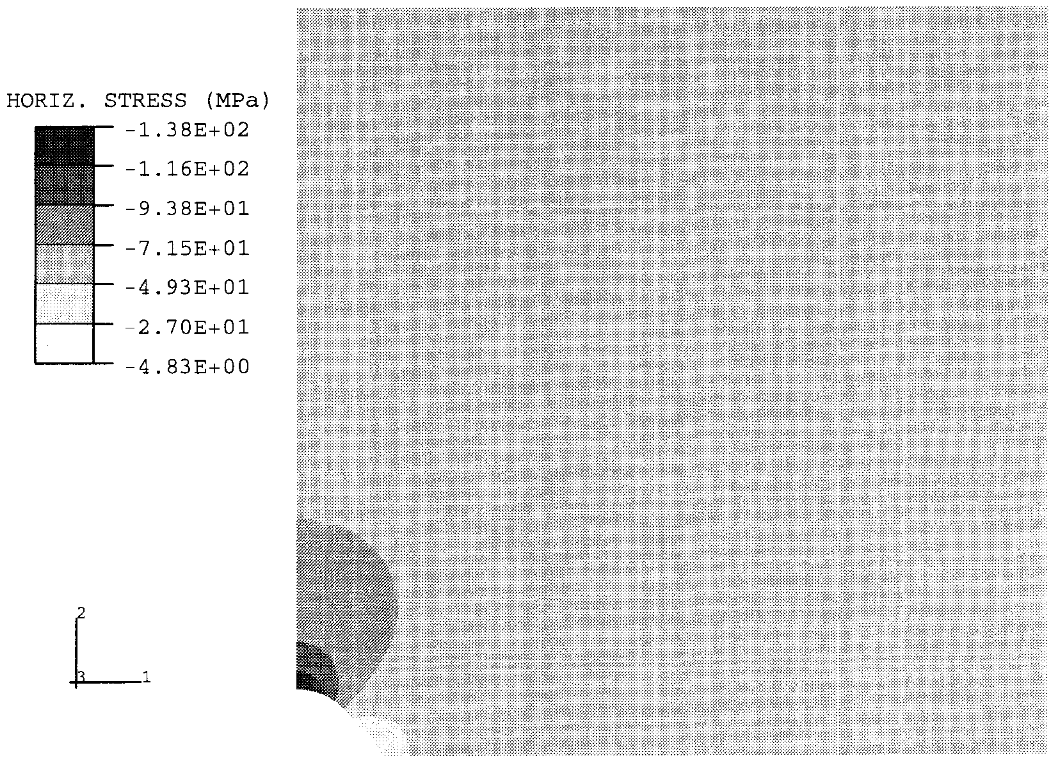

Figure 5-10. The distribution of horizontal stress, σ_{xx}, around an interior drift, 9 yr after waste emplacement, based on ABAQUS-calculated response

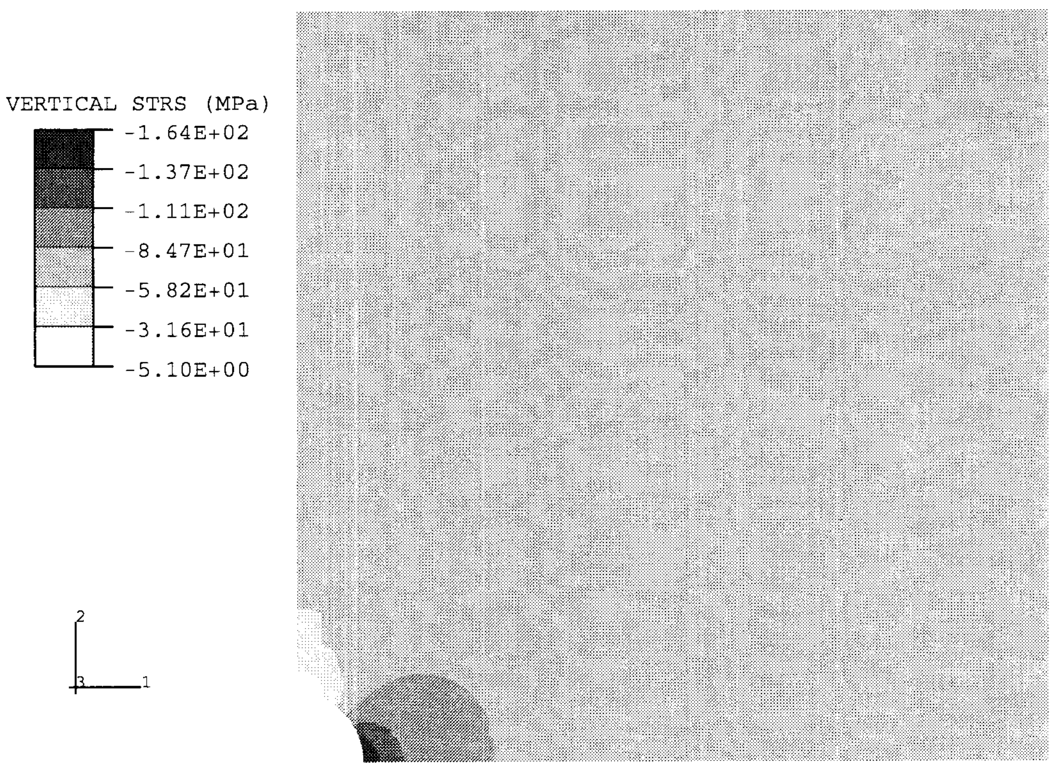

Figure 5-11. The distribution of vertical stress, σ_{yy}, around an interior drift, 9 yr after waste emplacement, based on ABAQUS-calculated response

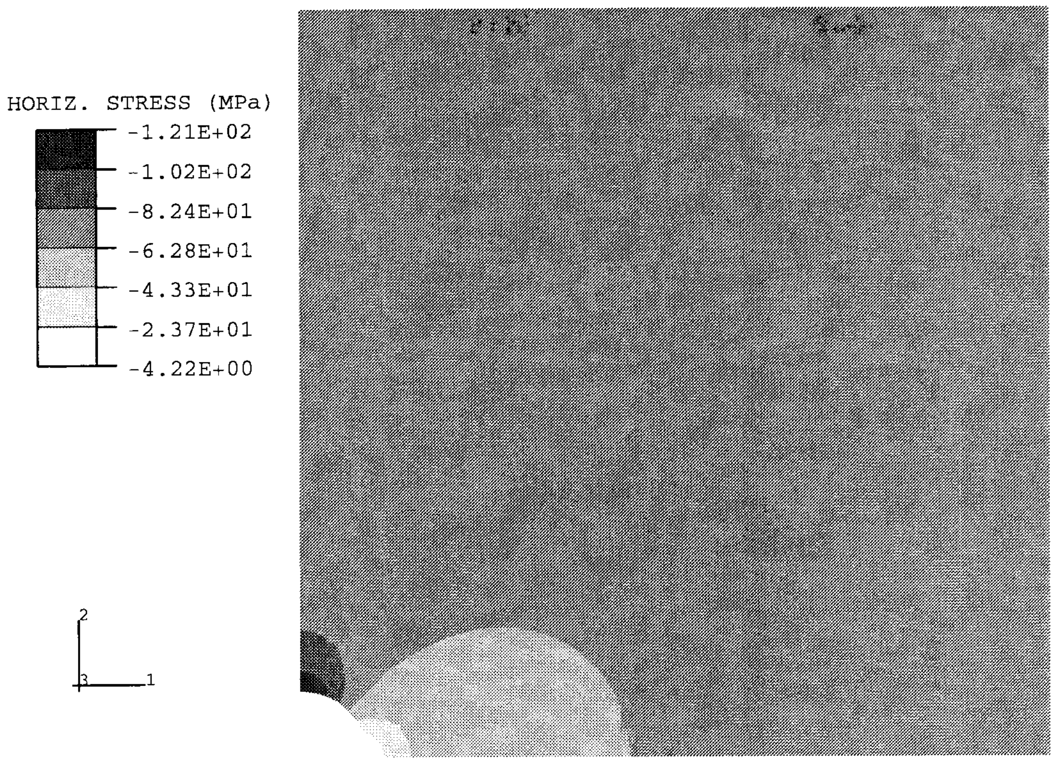

Figure 5-12. The distribution of horizontal stress, σ_{xx}, around an interior drift, 300 yr after waste emplacement, based on ABAQUS-calculated response

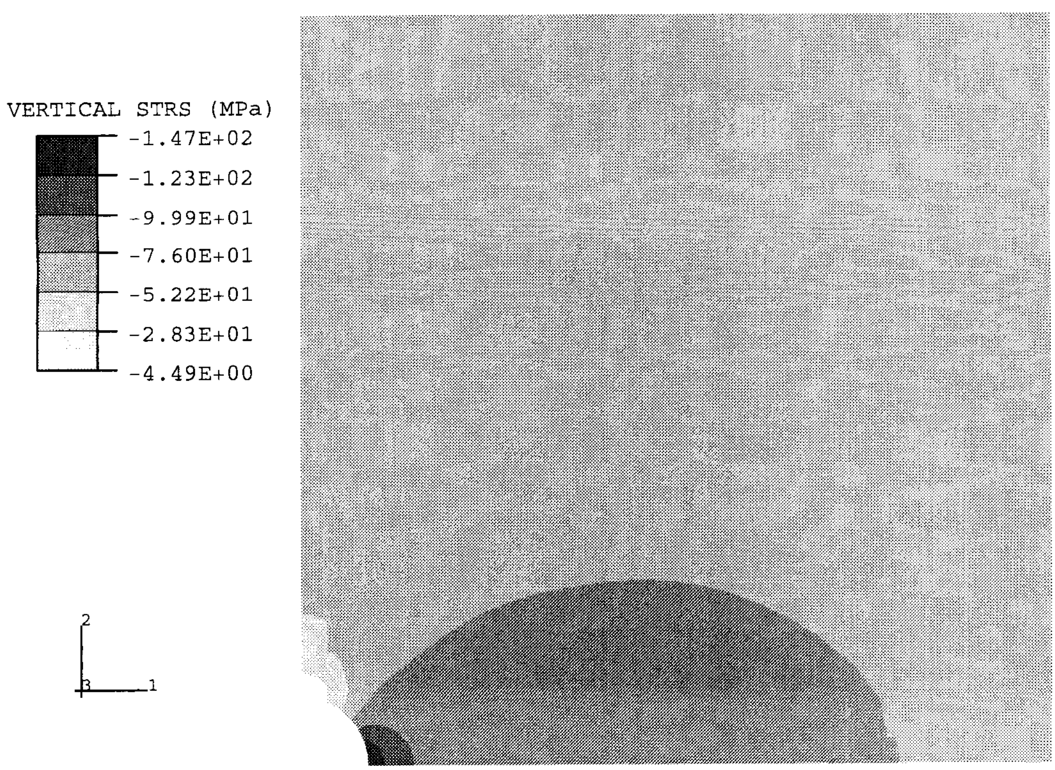

Figure 5-13. The distribution of vertical stress, σ_{yy}, around an interior drift, 300 yr after waste emplacement, based on ABAQUS-calculated response

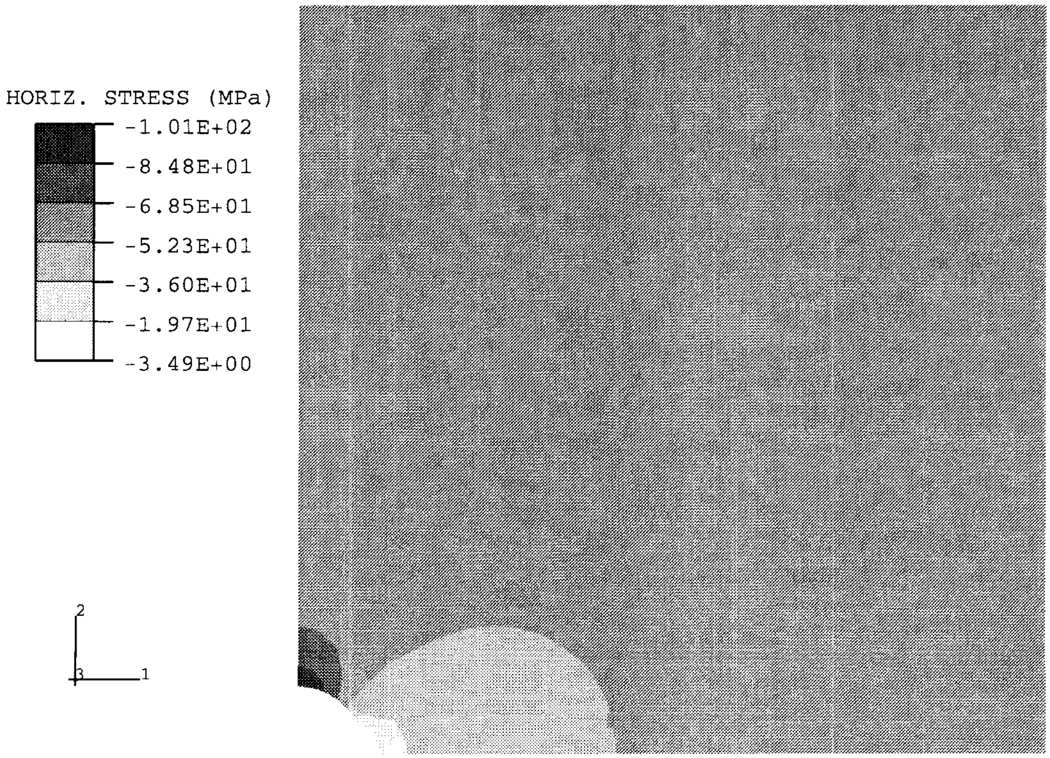

Figure 5-14. The distribution of horizontal stress, σ_{xx}, around an interior drift, 1000 yr after waste emplacement, based on ABAQUS-calculated response

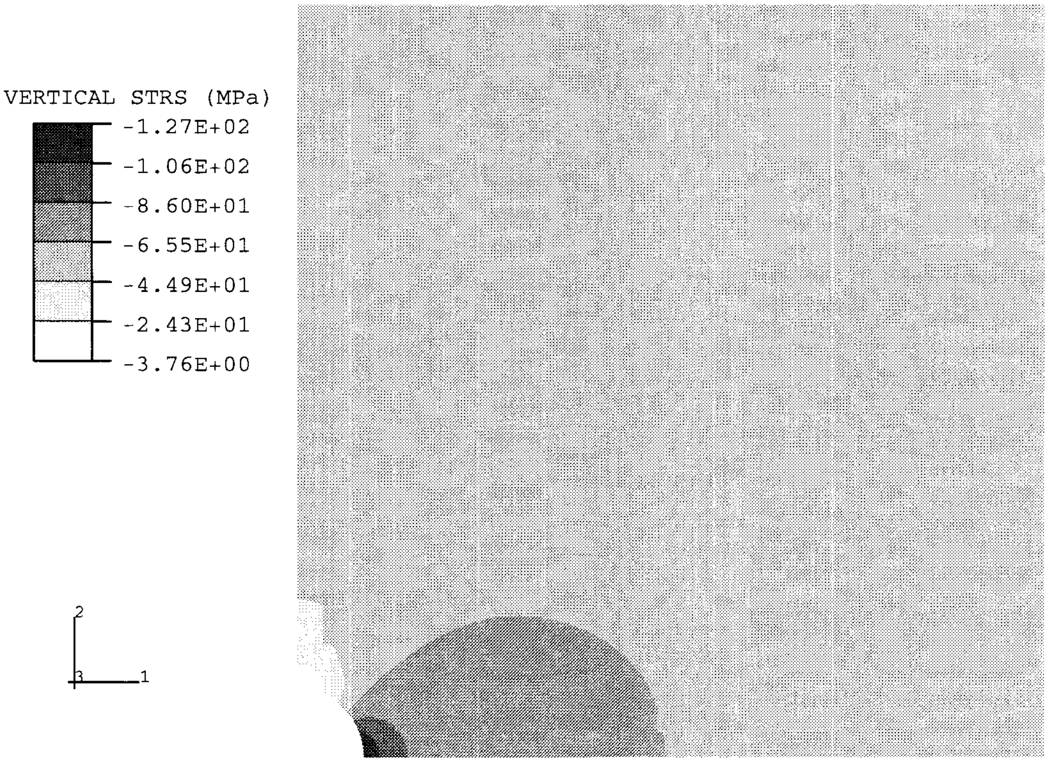

Figure 5-15. The distribution of vertical stress, σ_{yy}, around an interior drift, 1000 yr after waste emplacement, based on ABAQUS-calculated response

Table 5-5. Values of principal compressive stress within most of the region around the drift

Year	Values of Principal Compressive Stress Components within Most of the Problem Domain	
	σ_{max} (MPa)	σ_{min} (MPa)
9	70 – 81	56 – 70
300	69 – 78	59 – 66
1000	57 – 65	49 – 55

These stresses caused the fractures to close, as would be expected. The stress conditions on the fractures are presented in Figures 5-16 through 5-21, in terms of the profiles of normal and shear stresses (σ_n and τ, respectively) on the fracture surfaces. The figures show the values of σ_n and τ at the end of excavation (i.e., prior to waste emplacement) and at the end of 9, 300, and 1,000 yr following waste emplacement. Based on these figures, the effect of heating on the fracture-surface stress, for the case of the interior drift, can be summarized as follows:

(i) The magnitude of the normal compressive stress increased by about 70 MPa for the vertical, horizontal and inclined fractures. The magnitude of the increase is largest at the drift wall, and it decreases rapidly to a constant value as the distance from the wall increases. All open fractures close as a result. For example, as Figure 5-18 shows, the vertical fracture was open to a depth of about 2 m at the end of excavation (σ_n=0 on open fractures), but closed up thereafter as a result of heating. The discontinuity in the σ_{yy} contours in the vicinity of the vertical fracture (which is shown in Figures 5-11, 5-13, and 5-15) is believed to have been caused by the fracture being open during the early part of the simulation period.

(ii) The magnitude of shear stress increased on horizontal and vertical fractures. The increase in shear stress is limited to about a 10-m length of the fracture closest to the opening; furthermore, the amount of the increase is not sufficient to cause slip on the fractures, because of the large increase in normal stress. The inclined fractures experienced no change in shear stress. The change in shear stress on fractures dipping at 45° is equal to $(\Delta\sigma_{yy} - \Delta\sigma_{xx})/2$, where Δ stands for "change in". In this case, $\Delta\sigma_{yy} \approx \Delta\sigma_{xx}$. Hence there was essentially no change in the shear stress on the inclined fractures, as Figure 5-21 shows.

The drop in the values of σ_n and τ at the external end of the inclined fracture (see Figures 5-20 and 5-21) is believed to have been caused by a numerical problem that may occur when the displacement at an interface-element node is restricted in a direction normal to the interface element. But, as the figures show, the effect of the problem is limited to a short distance from the boundary.

Based on the results presented in Figures 5-10 through 5-21, it can be concluded that the stresses calculated using ABAQUS are consistent with the expected mechanical response within the region that surrounds an interior drift. This conclusion arises from a qualitative examination of the calculated stresses, considering, as stated at the beginning of this section, that the mechanical response within such a region is influenced most by two factors: (i) the existence of almost-uniform temperature conditions within the region, which causes the stress components to approach equal magnitudes; and (ii) the existence of symmetry conditions on the external boundary, which causes increased confinement within the region. In the next section, the stresses calculated using ABAQUS will be compared with those calculated using UDEC.

5.1.5.2 Comparison of ABAQUS and UDEC Results for the Interior Drift

The profiles of σ_n and τ calculated for the three fractures using ABAQUS and UDEC are compared in this section for the condition at the end of 9 yr following waste emplacement. The 9-yr condition was selected for two reasons: (i) as Figures 5-16 through 5-21 show, the long-term stress profiles are similar to the 9-yr profile, such that conclusions based on the examination of the 9-yr data regarding the relative performance of the two codes are likely to hold for the long term; and (ii) the conditions at the end of excavation arise from purely mechanical effects, and the performance of the two codes for such effects has been examined previously (Ghosh et al., 1994).

The comparative profiles are presented in Figures 5-22 through 5-27, which show significant differences between the magnitudes of fracture-surface stresses calculated using the two codes. The two codes agree in the shapes of the profiles, but disagree on the magnitudes of the stresses. The values of shear stress calculated using the two codes compare better than the values of normal stress. The apparent disagreement is caused by differences in the elastic stiffness assigned to the fracture surfaces in the two codes. Because the fractures are under pre-slip stress states, the magnitude of stress developed on each fracture surface depends on its elastic stiffness.

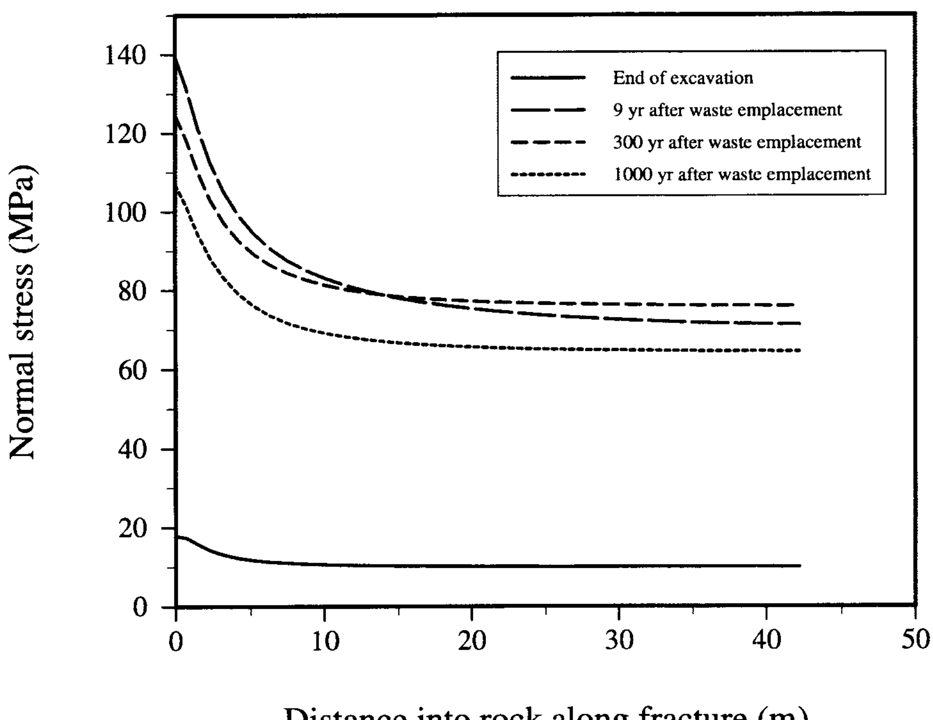

Figure 5-16. Profiles of normal stress on the horizontal fracture for the case of the interior drift, based on ABAQUS-calculated response

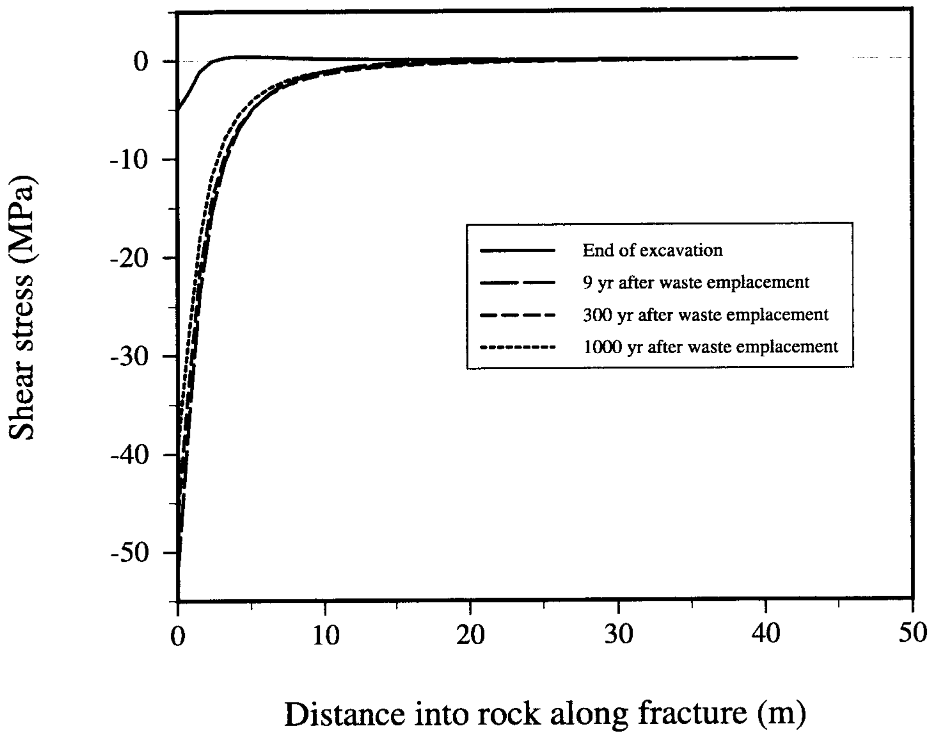

Figure 5-17. Profiles of shear stress on the horizontal fracture for the case of the interior drift, based on ABAQUS-calculated response

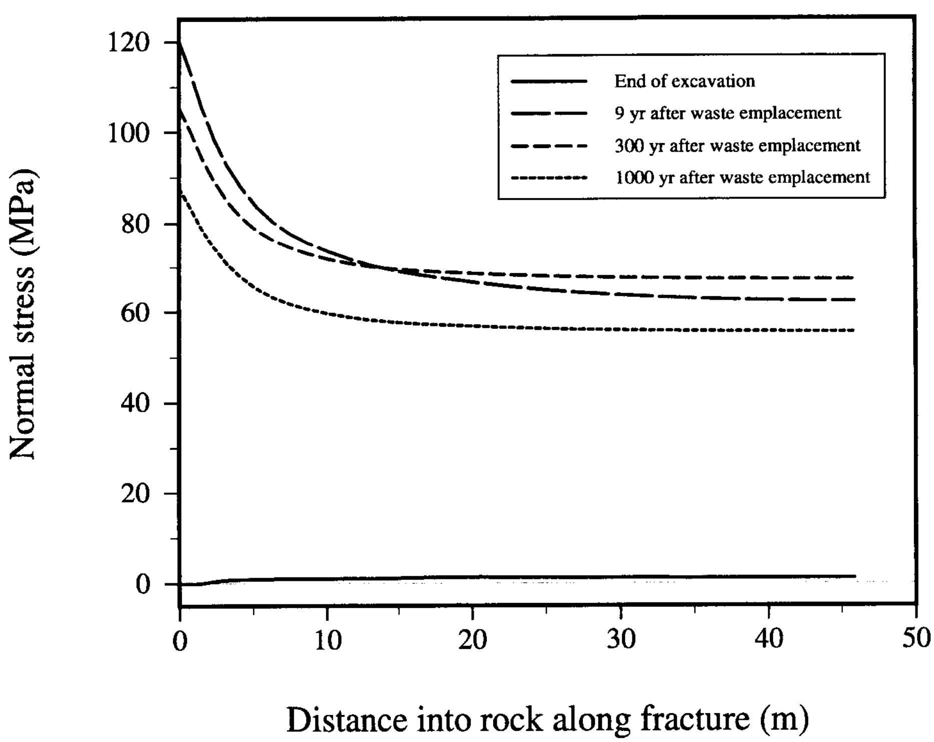

Figure 5-18. Profiles of normal stress on the vertical fracture for the case of the interior drift, based on ABAQUS-calculated response

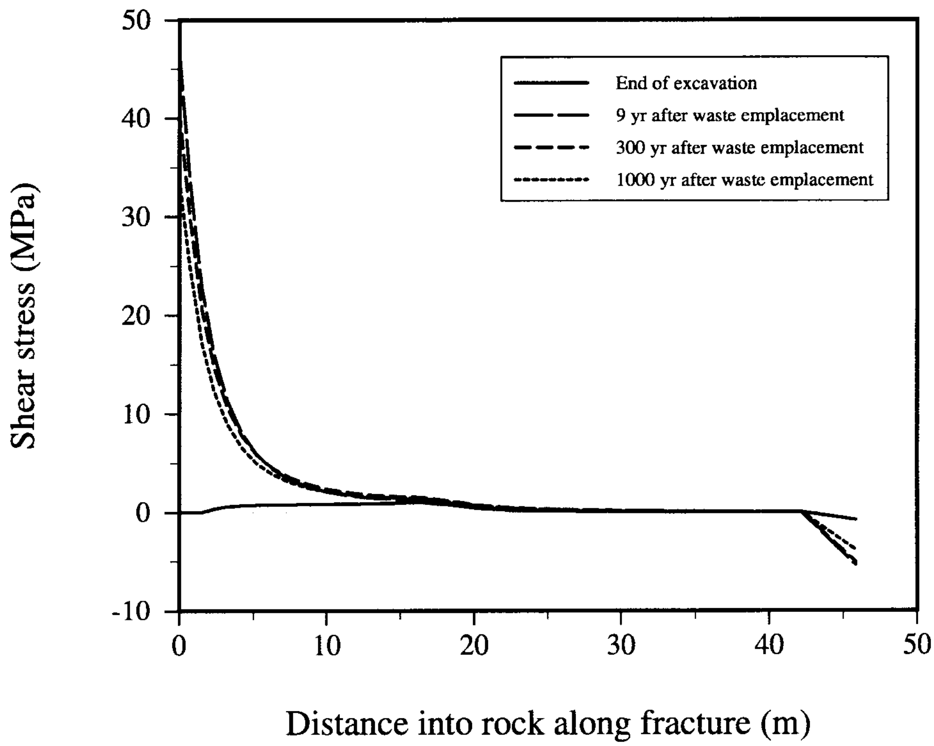

Figure 5-19. Profiles of shear stress on the vertical fracture for the case of the interior drift, based on ABAQUS-calculated response

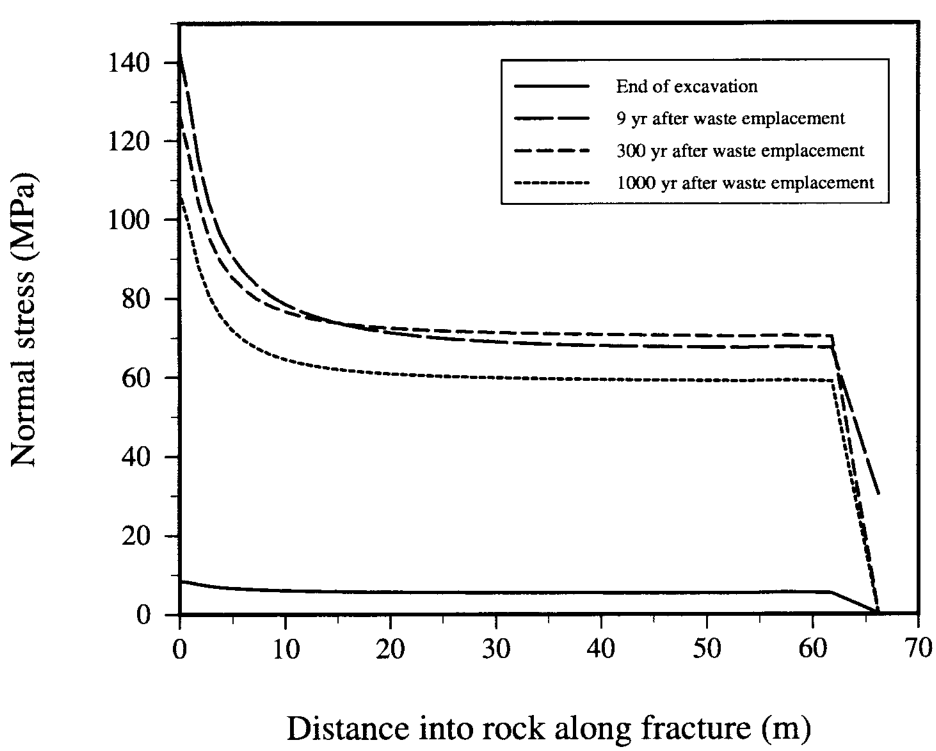

Figure 5-20. Profiles of normal stress on the 45°-inclined fracture for the case of the interior drift, based on ABAQUS-calculated response

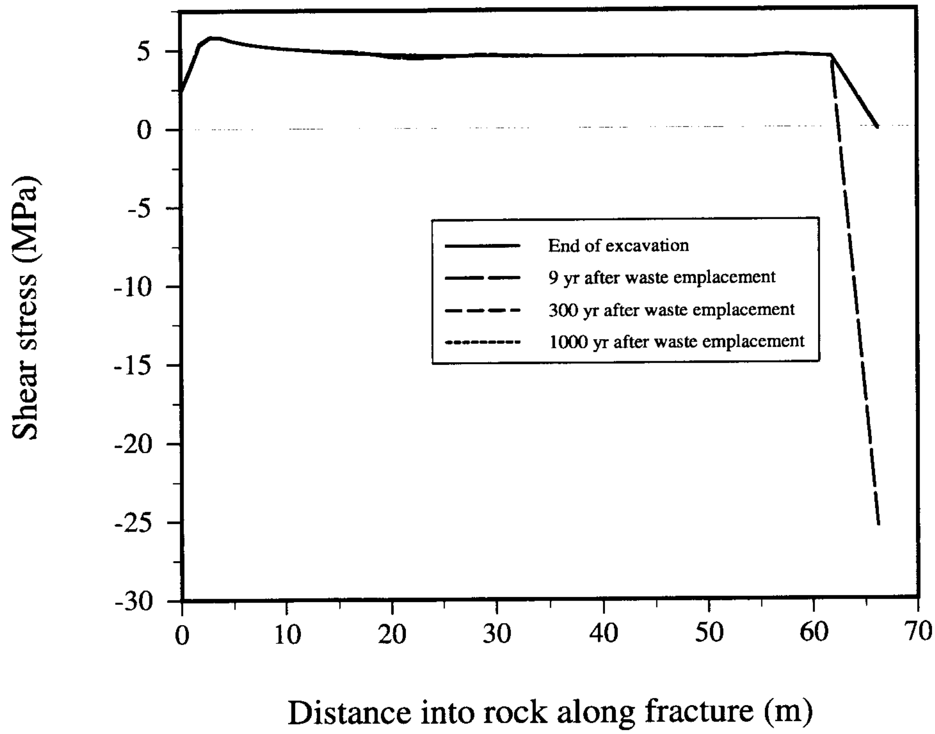

Figure 5-21. Profiles of shear stress on the 45°-inclined fracture for the case of the interior drift, based on ABAQUS-calculated response

In UDEC, the elastic stiffness of fracture surfaces is defined through the user-supplied values for K_s (shear stiffness) and K_n (normal stiffness). The use of finite values for these two parameters implies that relative movement of the two adjacent blocks that define the fracture surface can occur under pre-slip stress states. In that case, the effective stiffness of the rock mass is smaller than the stiffness of the intact rock, even if the fractures have zero aperture and are under pre-slip stress states. On the other hand, the elastic stiffness of rock fractures vary with stress in ABAQUS, and the values of K_s and K_n are not specified directly by the user. The magnitude of elastic stiffness applied to a fracture surface may be controlled by the user as follows:

(i) If a fracture has zero aperture, then its normal stiffness is the same as the stiffness of the adjacent rock blocks in the direction normal to the fracture surface; in that case, the fracture does not contribute to the elastic stiffness of the rock mass in that direction. There is no user control for this case.

(ii) If a fracture has nonzero aperture, its normal stiffness can be controlled by the user through the "*SURFACE BEHAVIOR, SOFTENED" command. This command causes ABAQUS to permit such open fractures to transmit compressive stress. The normal stiffness of the fracture is controlled by the user through two parameters: one denoted e_{max}, which is the largest value of aperture that permits the transmission of compressive stress across the fracture; and another denoted p_{max}, which is the value of normal pressure at which the fracture aperture decreases to zero. This model was not applied in the interior-drift problem, because the fractures were closed most of the time along most of their length.

(iii) The pre-slip shear stiffness of a rock fracture may be assigned an infinite value using the command "*FRICTION, LAGRANGE". In that case, the fracture does not contribute to the shear stiffness of the rock mass unless the stress state on the fracture surface attains the user-specified slip condition. The analysis results already presented in this chapter were obtained using this approach.

(iv) Alternatively, a user may specify the amount of relative displacement that may occur on a fracture surface under pre-slip stress states. The amount of such relative displacement can be specified as a fraction of the length of the interface elements using the command "*FRICTION, SLIP TOLERANCE=f"; in that case the interface element (representing a part of a fracture) for which this property is specified may undergo pre-slip shear displacement, up to a maximum of $f\lambda$, where λ is the length of the element. The exact magnitude of K_s implied by a given value of f depends on λ and on the stress state of the fracture surface. As a result, it is not possible to determine the value of f that would be equivalent to a given value of K_s, which would be necessary in order to use equivalent models of the elastic shear stiffness of a fracture in both UDEC and ABAQUS.

Therefore, the observed difference between the magnitudes of fracture-surface stresses calculated using the two codes does not reflect a difference in the performance of the codes; instead, it is caused by differences in the effective value of elastic stiffness applied to the fracture surfaces. The validity of this statement was investigated using the results of three sets of ABAQUS analyses of the interior-drift problem. The three sets differ with respect to the amount of pre-slip shear displacement permitted on the fracture surfaces, as follows:

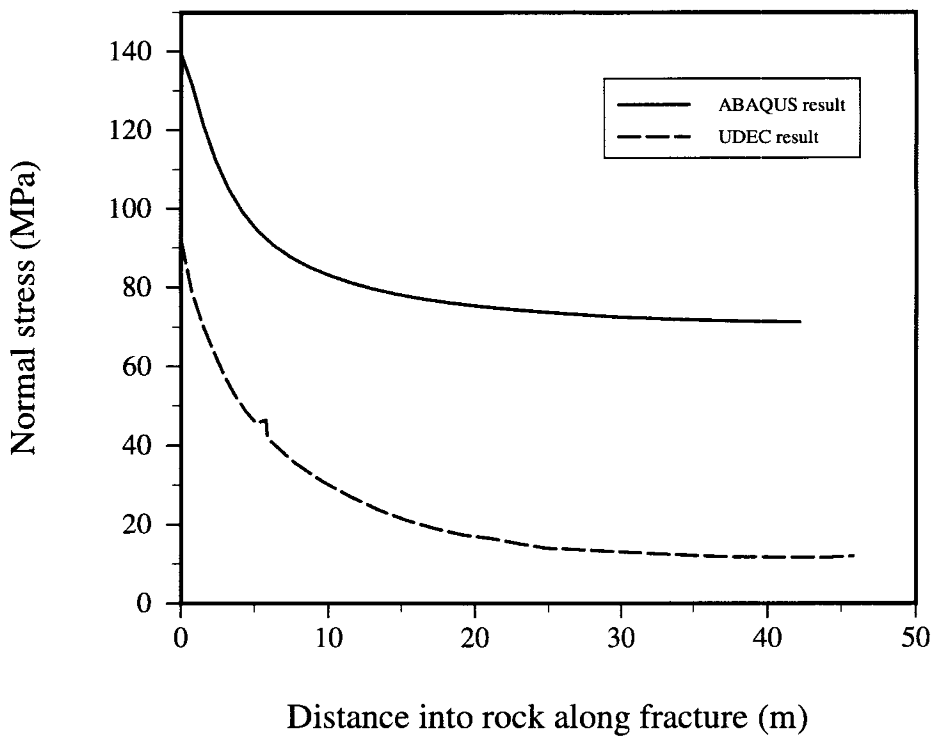

Figure 5-22. Comparison of 9-yr profiles of normal stress on the horizontal fracture for the case of the interior drift

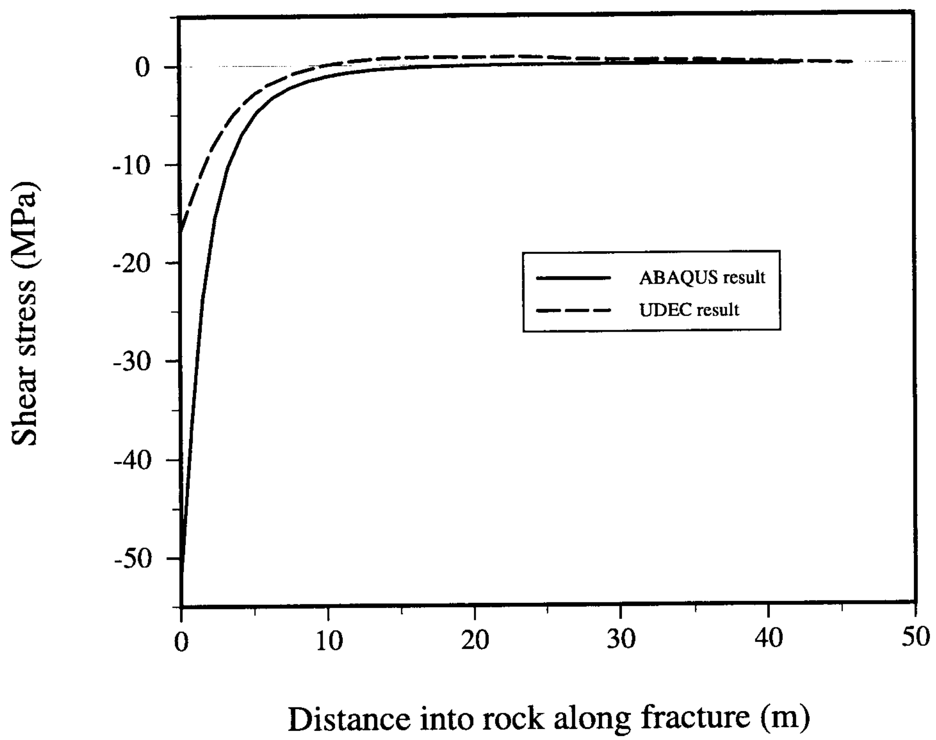

Figure 5-23. Comparison of 9-yr profiles of shear stress on the horizontal fracture for the case of the interior drift

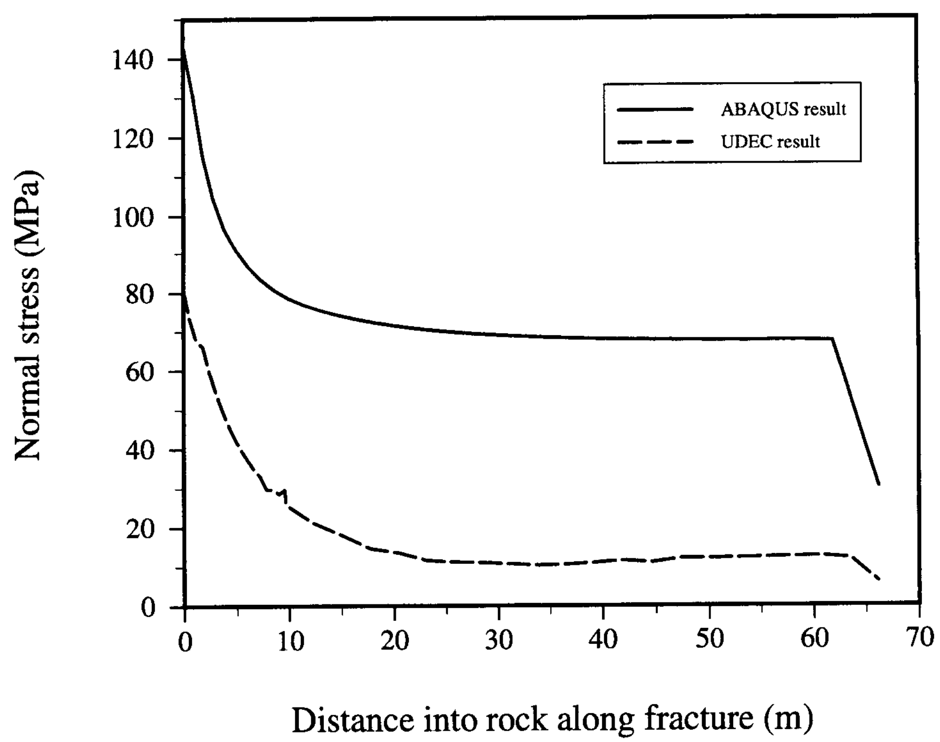

Figure 5-24. Comparison of 9-yr profiles of normal stress on the 45°-inclined fracture for the case of the interior drift

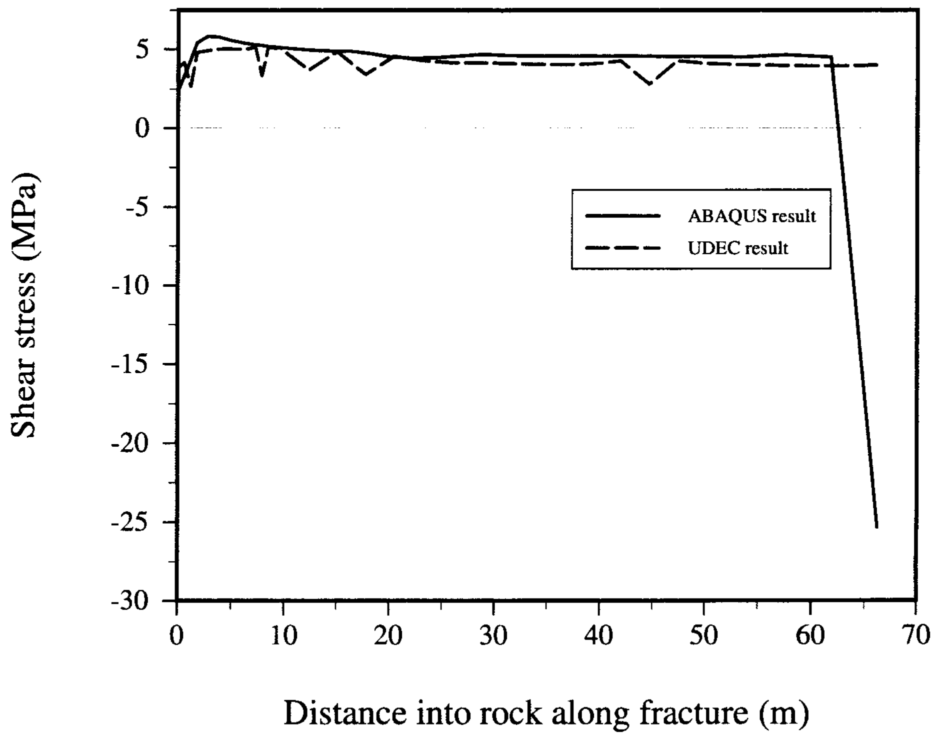

Figure 5-25. Comparison of 9-yr profiles of shear stress on the 45°-inclined fracture for the case of the interior drift

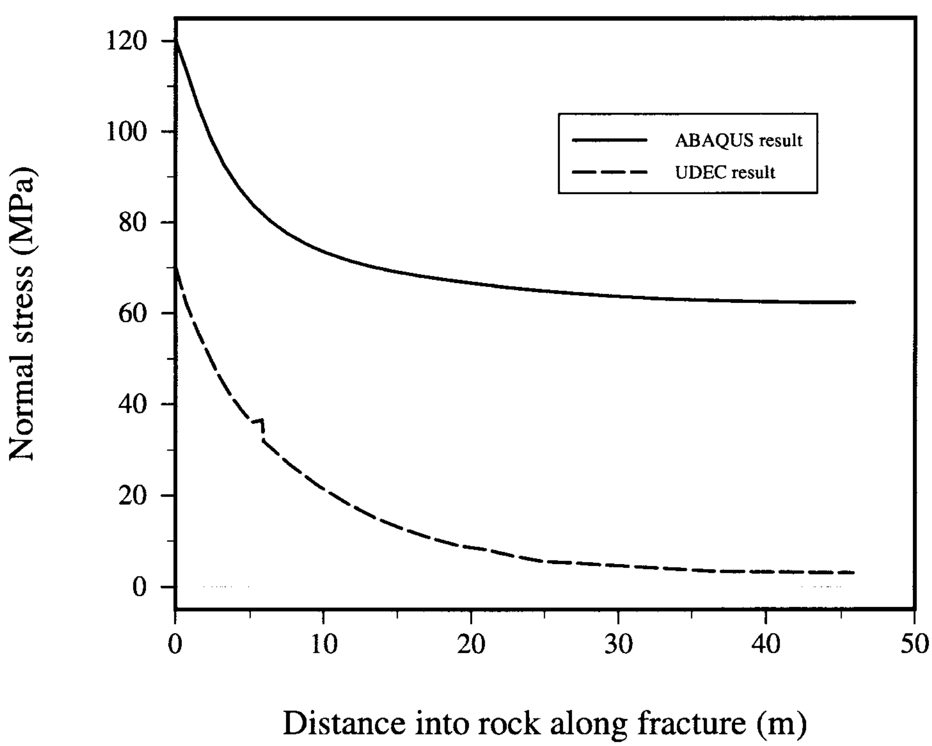

Figure 5-26. Comparison of 9-yr profiles of normal stress on the vertical fracture for the case of the interior drift

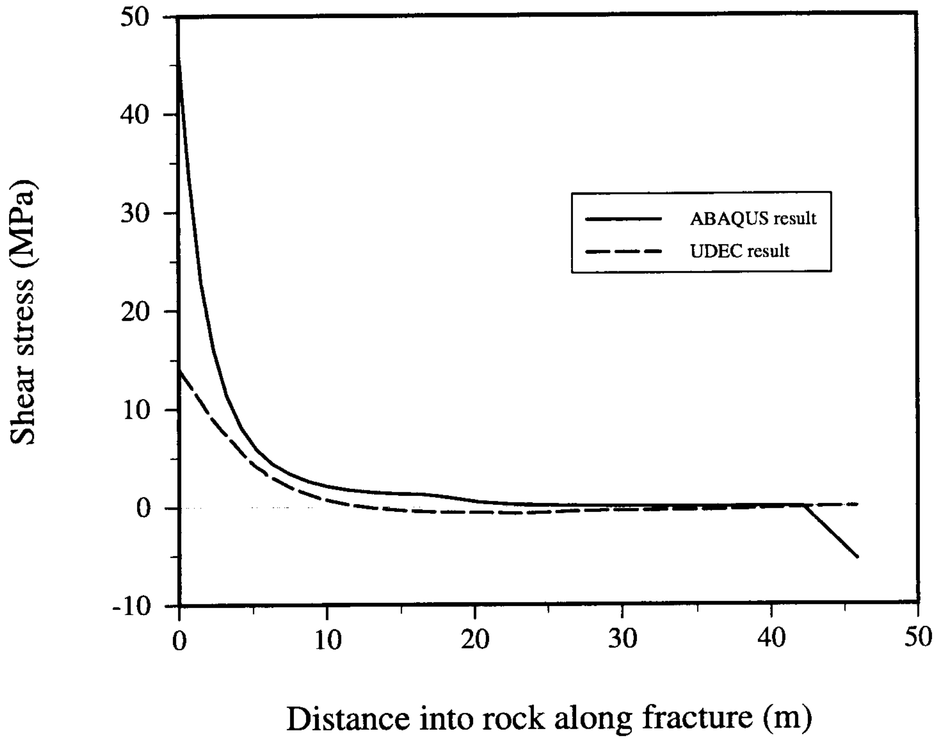

Figure 5-27. Comparison of 9-yr profiles of shear stress on the vertical fracture for the case of the interior drift

(i) The "*FRICTION, LAGRANGE" command was applied, thereby prohibiting the occurrence of pre-slip shear displacement in the first set of analyses. The results of this set have already been presented (Figures 5-16 through 5-21).

(ii) The "*FRICTION, SLIP TOLERANCE=0.005" command was applied in the second set, thereby permitting up to 0.005λ of pre-slip shear displacement.

(iii) The "*FRICTION, SLIP TOLERANCE=0.05" command was applied in the third analyses set.

The results of the three analyses sets are compared in Figures 5-28 through 5-30 using the profiles of shear stress on the fracture surfaces. The "*FRICTION, LAGRANGE" analysis is identified in the figures as a "SLIP TOLERANCE=0.0" case. The figures confirm that the value of the parameter f has a strong effect on the magnitude of shear stress. For the vertical and horizontal fractures, the magnitude of shear stress close to the drift wall decreased from about 50 MPa to about 17 MPa as the value of f increased from 0 to 0.05. An increase in the value of f implies a decrease in the value of K_s. In fact, the shear stress profiles obtained with f=0.05 would closely match the corresponding UDEC-calculated shear stress profiles in Figures 5-23, 5-25, and 5-27. The effect of K_s on the UDEC-calculated values of fracture-surface shear stress was also investigated. The values of shear stress increased as the value of K_s increased.

The value of f does not affect the normal stress profile as strongly. Figure 5-31 shows its effect on the normal stress profile for the inclined fracture. As the figure shows, its effect on normal stress is limited to a short length of the fracture close to the drift wall. In order to reduce the magnitude of normal stress on the fractures, each fracture would have to be assigned a non-zero initial aperture, and the

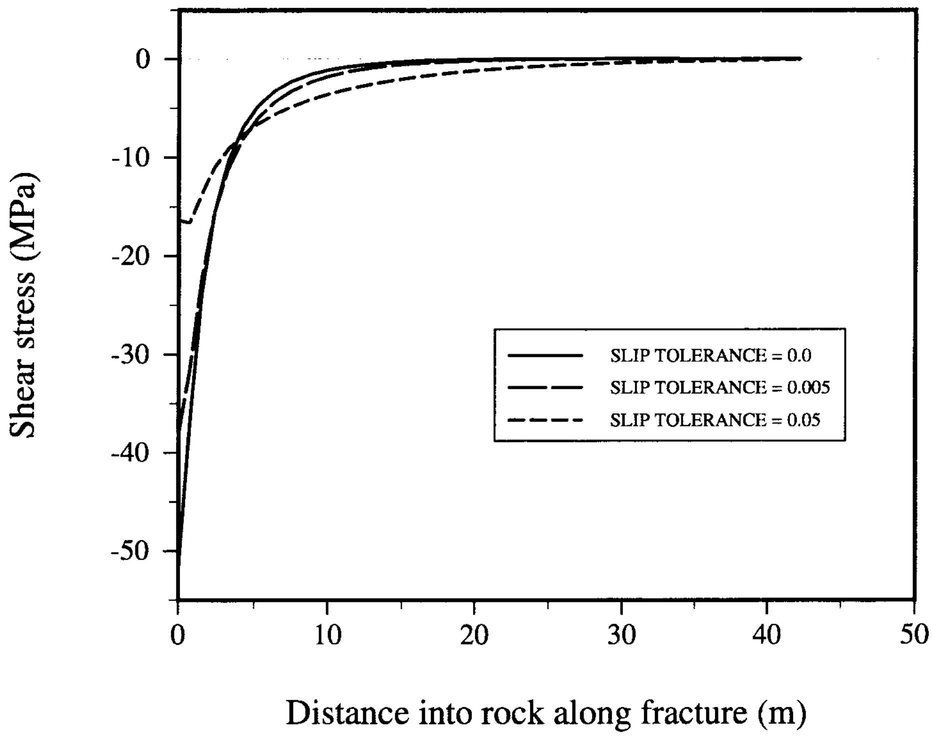

Figure 5-28. The effect of pre-slip shear stiffness on the 9-yr profile of shear stress on the horizontal fracture: Case of the interior drift, based on ABAQUS-calculated response

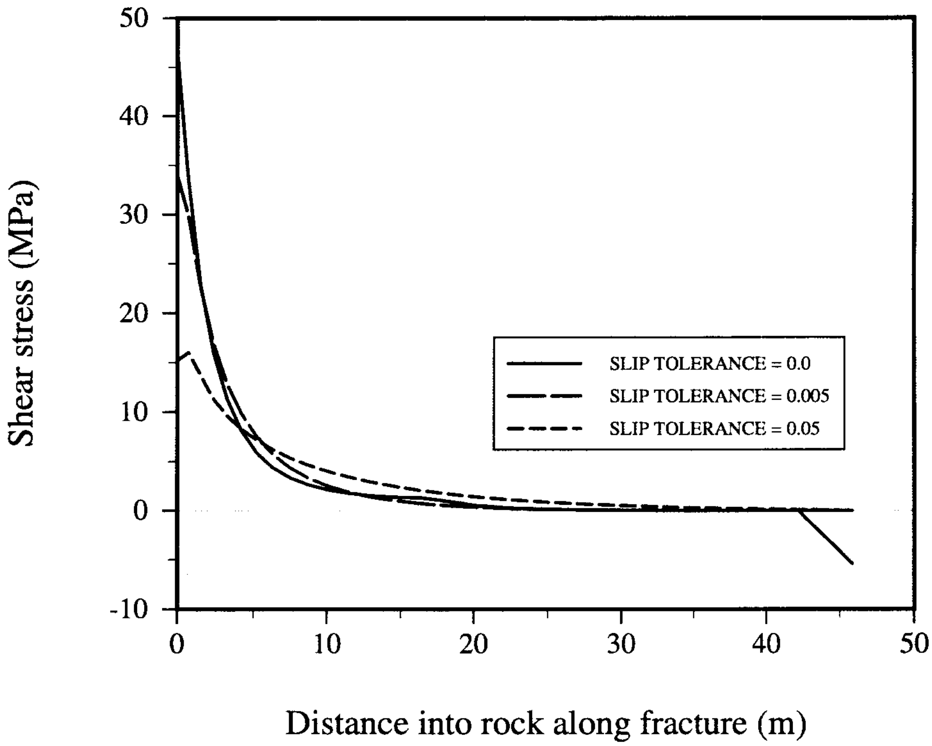

Figure 5-29. The effect of pre-slip shear stiffness on the 9-yr profile of shear stress on the vertical fracture: Case of the interior drift, based on ABAQUS-calculated response

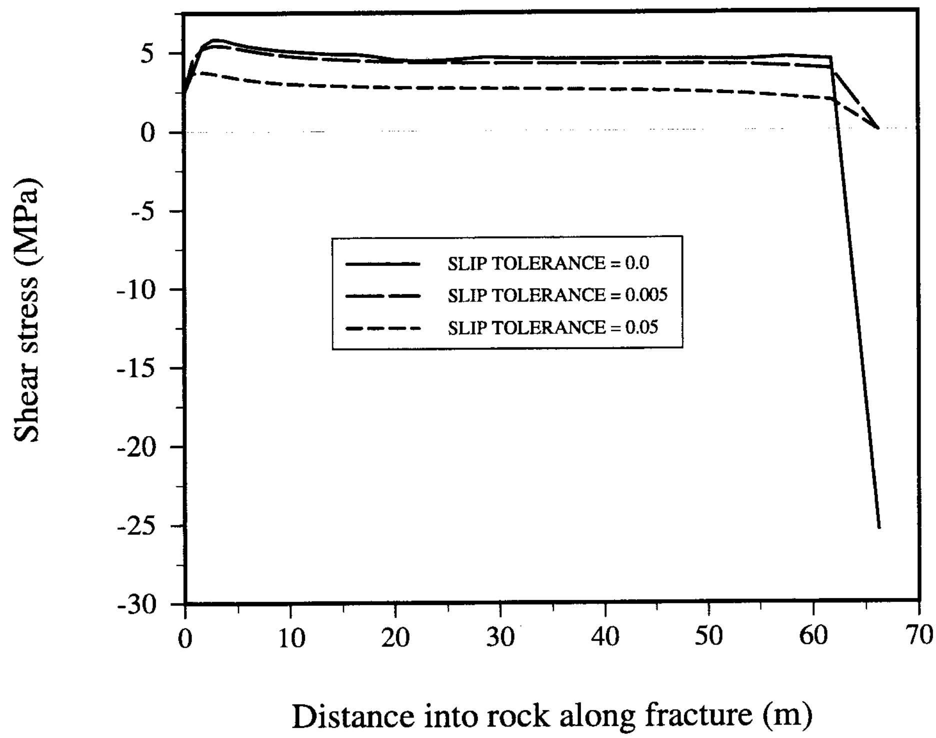

Figure 5-30. The effect of pre-slip shear stiffness on the 9-yr profile of shear stress on the 45°-inclined fracture: Case of the interior drift, based on ABAQUS-calculated response

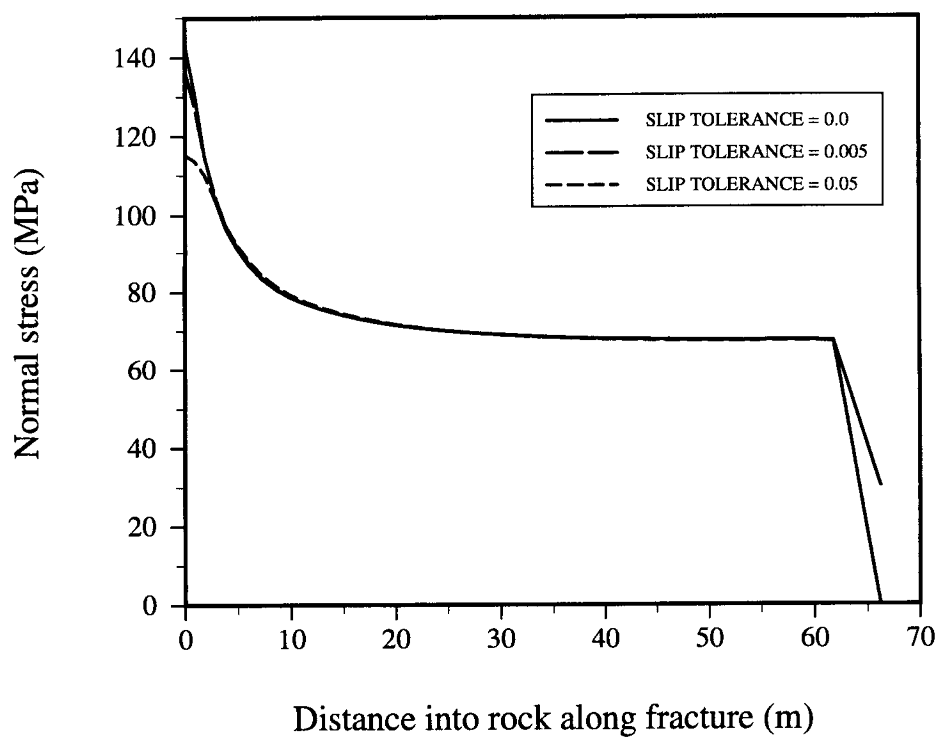

Figure 5-31. The effect of pre-slip shear stiffness on the 9-yr profile of normal stress on the 45°-inclined fracture: Case of the interior drift, based on ABAQUS-calculated response

"*SURFACE BEHAVIOR, SOFTENED" command would have to be applied to enable the open fractures to transmit compressive stress, with a value of normal stiffness that varies with the normal stress, according to a user-specified rule. The use of the "*SURFACE BEHAVIOR" command was not examined for the interior-drift problem because a different discretization of the domain would be required in order to assign non-zero initial aperture to the fractures.

The following conclusions can be reached regarding the interior-drift problem, considering the results presented in Figures 5-22 through 5-31, along with the foregoing discussion of these results:

(i) The shapes of corresponding profiles of fracture-surface stresses calculated using ABAQUS and UDEC match each other satisfactorily;

(ii) The two codes would predict satisfactorily similar magnitudes for fracture-surface shear stress if the values of pre-slip shear stiffness used in both codes were matched.

(iii) ABAQUS allows the user the flexibility of assigning a wide range of values of pre-slip shear stiffness to fractures, including infinite stiffness. The specific values used within this range are a modeling decision that would have to be made for each given case.

The ABAQUS model for open fractures, which permits user-control of the normal stiffness through the "*SURFACE BEHAVIOR" command, is examined in the next set of thermomechanical problems.

5.2 PROBLEM GEOMETRY AND MATERIAL PROPERTIES: CASE OF DRIFT INTERSECTED BY SINGLE OPEN VERTICAL FRACTURE

The second set of thermomechanical problems consists of a horizontal drift intersected at its crown and floor by a single vertical fracture. The fracture is infinitely continuous, with an initial aperture of 1 mm everywhere; its aperture may decrease to a minimum value of 0.1 mm. The geometry of the problems is illustrated in Figures 5-32 and 5-33, which show two schematic vertical sections normal to and along the drift axis, respectively. The drift axis coincides with the z-axis in Figure 5-33; the x-axis is horizontal and normal to the drift axis, and the y-axis is vertical, as shown in Figure 5-32. The drift is considered to lie in the interior of a linear horizontal array of drifts, with a diameter of 5 m and a center-to-center distance of 22.5 m in the x direction. A 2D solution of the problem was obtained based on the section in Figure 5-32; a 3D solution was also obtained.

The material-property values are the same as were specified in Table 5-1. The normal stiffness of the fracture was modeled using an ABAQUS-generated exponential pressure-vs-aperture function based on the parameters p_{max}=180 MPa and e_{max}=1.11 mm, as shown in Figure 5-34. The values of p_{max} and e_{max} were chosen by trial to give an exponential function that maintains the specified initial and minimum aperture values for the fracture.

The boundary conditions are: (i) no vertical displacement and no change in temperature at the base of the model (i.e., at y=−1000 m); (ii) no z-displacement and no temperature change on the vertical plane z=50 m; (iii) symmetry boundary conditions on the vertical planes x=±11.25 m; and (iv) free-surface conditions and no temperature change on the ground surface. An initial temperature of 25 °C was applied everywhere. The initial stress state was set using a vertical stress gradient of 0.025 MPa/m and a horizontal-to-vertical stress ratio of 0.2. The initial principal stress directions are vertical, horizontal along the drift axis, and horizontal normal to the drift axis. As in the heated-drift problem described in

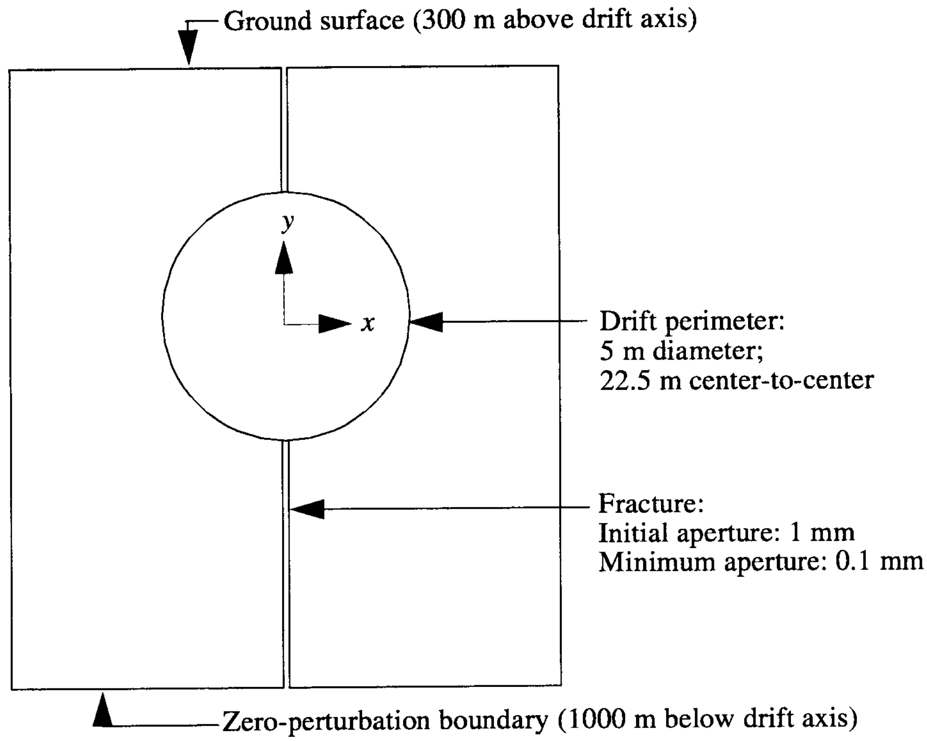

Figure 5-32. Problem geometry for heated drift intersected by single open vertical fracture: Vertical section normal to drift axis at z=0

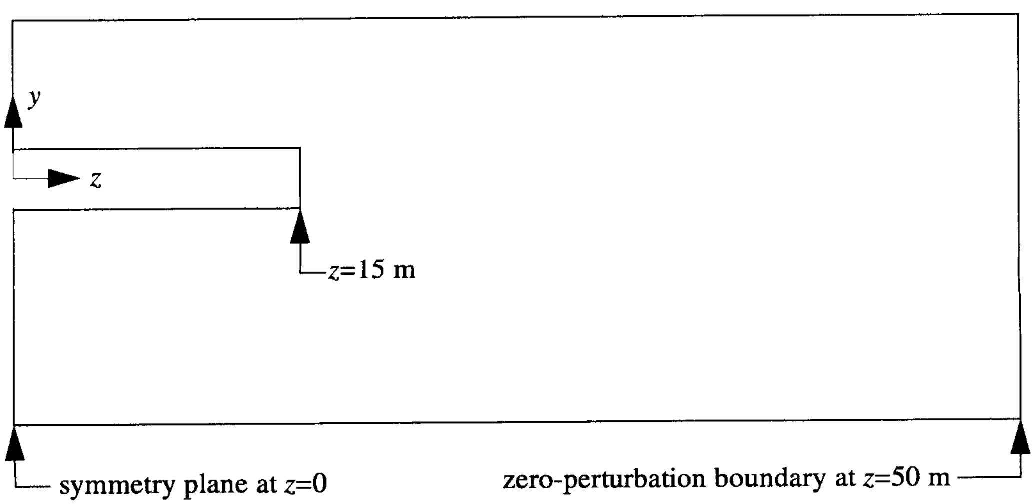

Figure 5-33. Problem geometry for heated drift intersected by single open vertical fracture: Vertical section along drift axis at x=0

Section 5.1, the simulated sequence of events consists of drift excavation under constant temperature, followed by heating. The thermal history of emplaced waste was simulated using the temperature history shown in Figure 5-3 that was applied to the drift wall between z=0 and z=5 m. In the 3D model, the entire length of the drift was assumed to be excavated at the same time; that is, the z-direction sequence of excavation was not modeled.

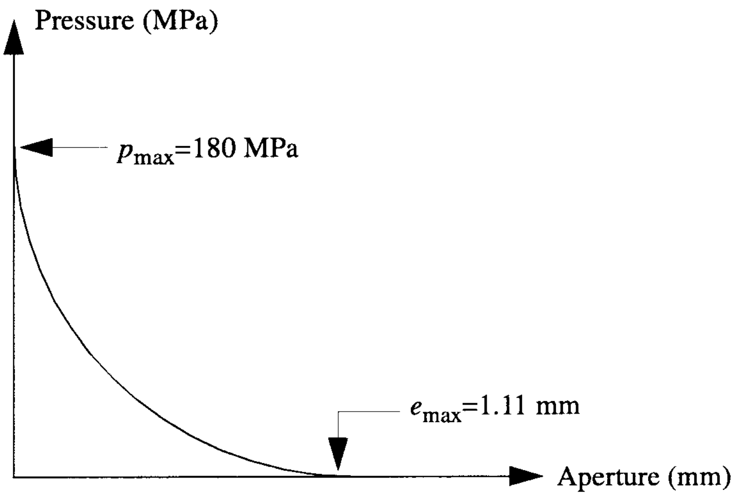

Figure 5-34. Pressure-vs-aperture relationship used to simulate the normal stiffness of open fracture

5.2.1 ABAQUS Model

The sequential coupling of heat-flow and mechanical-deformation analyses described in Chapter 3 was applied. In the 2D model, heat-flow analyses were performed using DC2D4 and DINTER2 elements for the solid rock and fracture, respectively. The corresponding elements for the mechanical analyses are the CPE4 and INTER2 elements. In the 3D model, heat flow analyses were performed using DC3D8, DC3D6, and DINTER4 elements; the elements used in the mechanical analyses are C3D8, C3D6, and INTER4. The C3D8 and DC3D8 elements are 8-noded bricks (3D equivalents of the 4-noded quadrilaterals used in the 2D analyses). On the other hand, the C3D6 and DC3D6 elements are 6-noded triangular prisms that were used to form the transition between the drift centerline and the brick elements in the region between z=15 and z=50 m (Figure 5-33).

The SUBMODEL provision in ABAQUS was used in the 2D model. First, a coarse mesh of the entire domain (hereafter referred to as the global model) was used to compute the histories of temperature and z-displacement on the lines y=±50 m; the computed temperatures and displacements were stored in an ABAQUS interface file. Thereafter, the region within y=±50 m was discretized into a finer mesh that has twice as many elements as the global model in the circumferential direction of the drift wall (referred to hereafter as the local model). The problem was re-analyzed using the local model with the boundary temperature and z-displacement histories stored in the interface file. The SUBMODEL approach was not applied in the 3D model because a comparison of the results obtained using the 2D global and local models showed no significant difference between the two. Although the SUBMODEL approach did not yield significant benefits for this particular problem, it is likely to be of considerable benefit in problems with complicated geometries and a region of interest limited to a small fraction of the entire spatial domain. Therefore, it was applied in the 2D model in order to examine its performance as a modeling tool.

The initial stress state for the 3D model was implemented using the user-interface subroutine SIGINI. The use of this subroutine, instead of the direct specification of the initial stresses in the input file, was necessary because the orientations of the coordinate axes (Figures 5-32 and 5-33) are inconsistent with the orientations assumed by ABAQUS for the interpretation of the initial-stress input data for 3D solid elements. ABAQUS assumes that the z-axis (i.e., coordinate direction 3) of the 3D solid elements is vertical. At the time this inconsistency was discovered, modifying the finite element models was considered more expensive than developing the user-subroutine SIGINI.

5.2.2 Results: Two-Dimensional Model

The profiles of fracture pressure (i.e., normal stress) and aperture calculated using the 2D model are presented in Figures 5-35 and 5-36, respectively. The profiles are for the section of the fracture above the drift. A 2D analysis of the problem was also performed using UDEC, and the UDEC-calculated pressure profile is also shown in Figure 5-35.

The level of agrement between the ABAQUS and UDEC results in Figure 5-35 is satisfactory. In Section 5.1.5.2, differences between ABAQUS- and UDEC-calculated fracture normal stresses were attributed to the differences between the normal stiffness models applied in the two codes. It was argued that user-control of the fracture normal stiffness in ABAQUS can be exercised through the parameters p_{max} and e_{max} (Figure 5-34), using the "*SURFACE BEHAVIOR" command. This approach for controlling the normal stiffness was tested in the current problem. The values p_{max}=180 MPa and e_{max}=1.11 mm used in the ABAQUS model imply an average normal stiffness of about 7.2×10^4 MPa/m. A constant normal stiffness of 3.5×10^4 MPa/m was used in the UDEC model. Therefore, the fact that the calculated normal stress profiles agree satisfactorily, except near the wall, as shown in Figure 5-35,

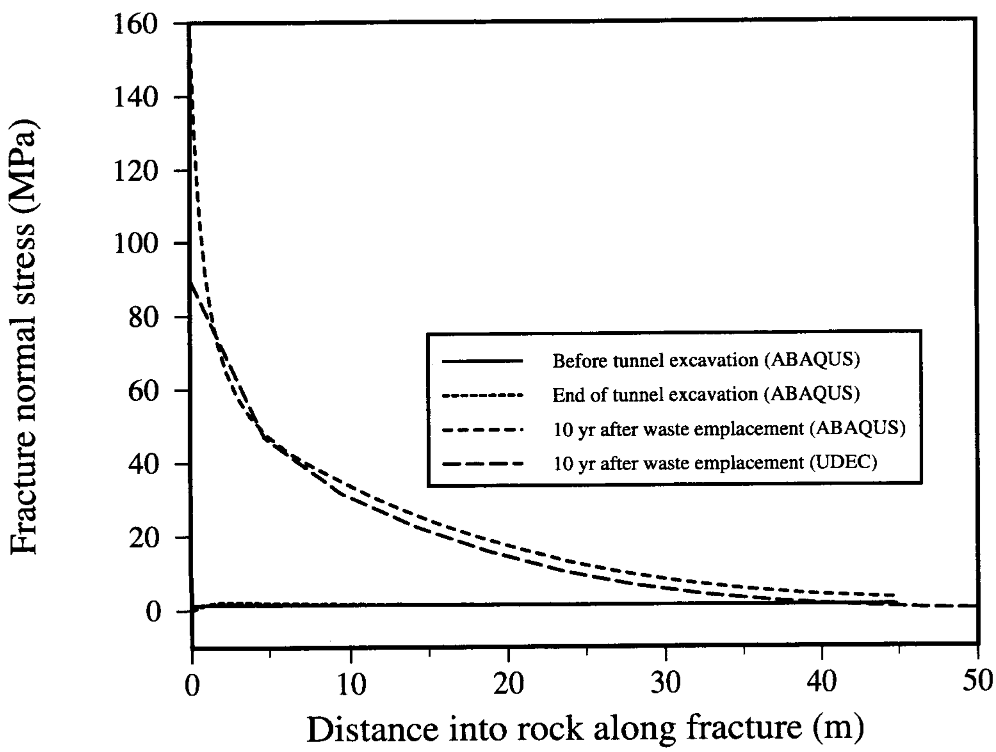

Figure 5-35. Profiles of fracture normal stress calculated using the 2D models for the case of drift with open vertical fracture

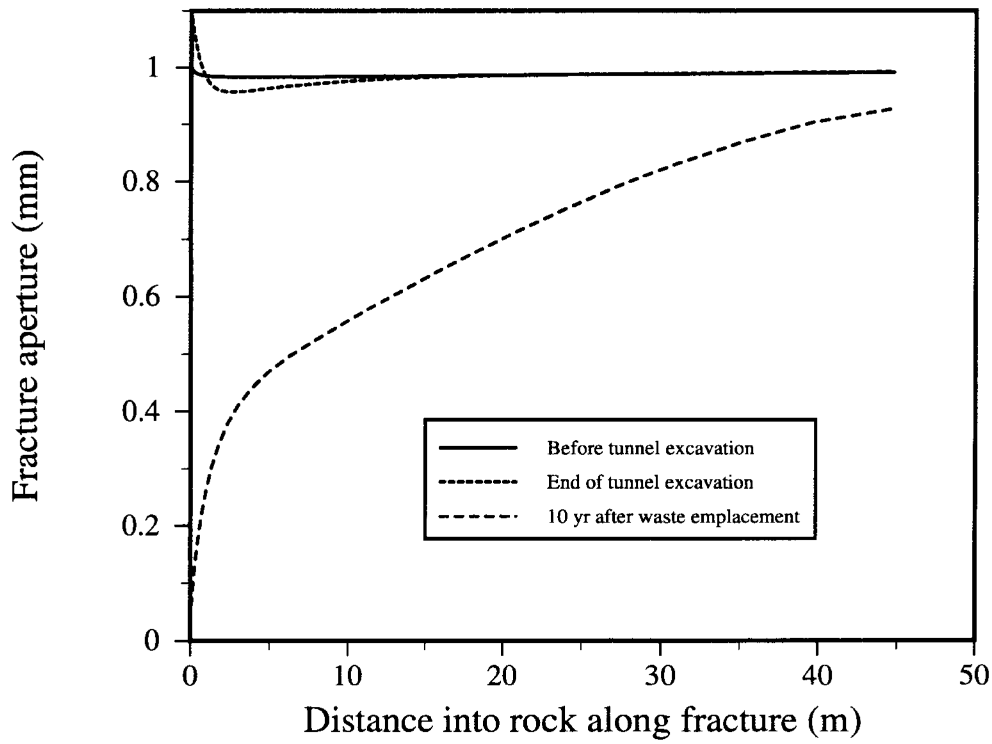

Figure 5-36. Profiles of fracture aperture calculated using the 2D ABAQUS model, for the case of drift with open vertical fracture

and e_{max} (Figure 5-34), using the "*SURFACE BEHAVIOR" command. This approach for controlling the normal stiffness was tested in the current problem. The values p_{max}=180 MPa and e_{max}=1.11 mm used in the ABAQUS model imply an average normal stiffness of about 7.2×10^4 MPa/m. A constant normal stiffness of 3.5×10^4 MPa/m was used in the UDEC model. Therefore, the fact that the calculated normal stress profiles agree satisfactorily, except near the wall, as shown in Figure 5-35, confirms that the differences observed earlier are caused by the specification of normal stiffness. It also confirms that the "*SURFACE BEHAVIOR" command in ABAQUS constitutes an appropriate provision for user-control of the normal stiffness of fractures. The use of this provision can be simplified by letting the user specify the pressure-vs-aperture relationship through a table, instead of through an ABAQUS-generated exponential function based on two user-supplied parameters.

The results in Figures 5-35 and 5-36 show that the changes in fracture stress and aperture caused by excavation are very small compared to the thermally induced changes. Also, whereas the excavation-induced changes are limited to a distance of about 2 drift-diameters from the opening, the thermally induced changes extend much farther. These results suggest that it would not be correct to estimate the spatial dimensions of the zone of influence of a potential repository based on current underground rock engineering rules-of-thumb which are valid only for excavation-induced zone of influence. Such rules would predict a zone of influence of no more than three drift-diameters, which would be too small for the case illustrated in Figures 5-35 and 5-36.

5.2.3 Results: Three-Dimensional Model

The main objective of the 3D model is to examine the performance of the 3D interface elements (such as the INTER4 elements) that are used for the 3D modeling of fractures. The performance of the 3D interface elements is evaluated by comparing the solutions obtained using the 2D and 3D models. In order for such comparison to be valid, the initial stress state for the problem was chosen such that one of the principal stress directions coincides with the drift axis; furthermore, the *z*-dimension of the drift was chosen to be sufficiently long such that the conditions on the middle vertical plane normal to the drift axis (i.e., the plane z=0 in Figure 5-33) are close to the plane-strain conditions assumed in the 2D model. The profiles of fracture normal stress and aperture calculated using the 2D and 3D models are compared in Figures 5-37 and 5-38.

One implication of the plane-strain assumption is that the gradients of quantities such as stress and temperature are zero in the normal direction of the analysis plane. In reality, such normal gradients are nonzero. For example, contour plots of temperature, principal stresses, and fracture normal stress and aperture are presented in Figures 5-39 through 5-47, which show that the values of these quantities vary in the axial direction of the drift. As the figures show, the axial gradients of both temperature and stress may be small, but they are nonzero; in general, the magnitude of stress (or temperature) decreases as distance from the middle plane (*z*=0 plane) increases. Therefore, because the 3D solution involves the averaging of response over a small but finite axial thickness, the magnitudes of stresses should be smaller in the 3D model than in the equivalent plane strain model. On the other hand, because the conditions (e.g., temperature- and stress-gradient conditions) on the *z*=0 plane of the 3D model are close to those of plane-strain, the 3D- and 2D-calculated stresses on this plane should be closely similar.

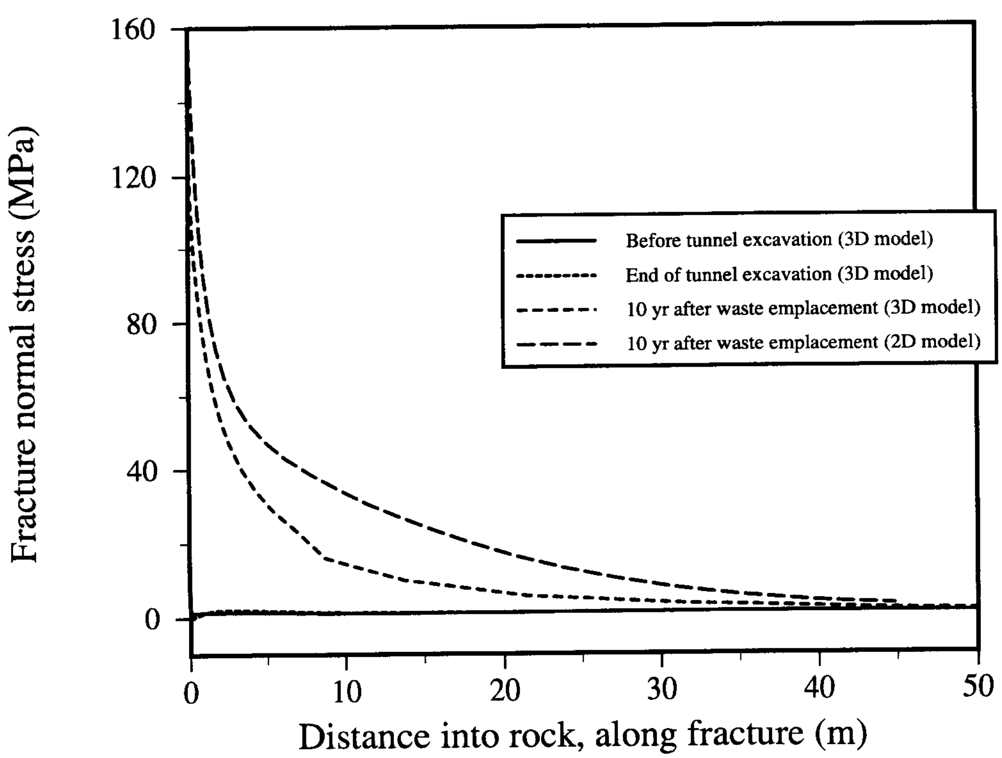

Figure 5-37. Profiles of fracture normal stress calculated using the 2D and 3D models for the case of drift with open vertical fracture

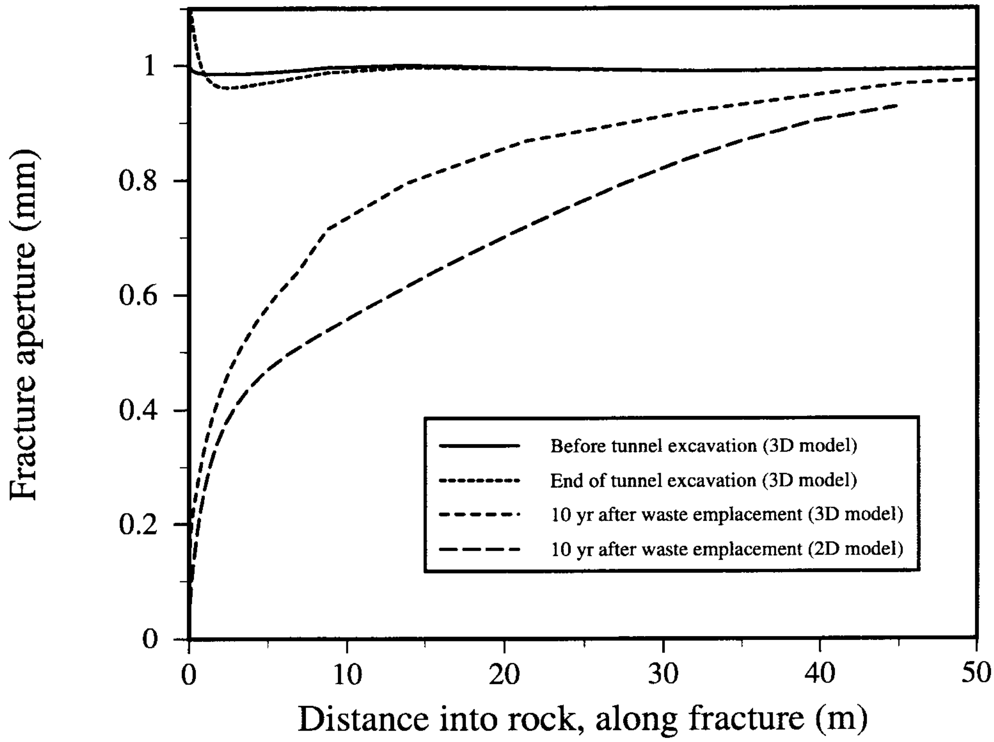

Figure 5-38. Profiles of fracture aperture calculated using the 2D and 3D models for the case of drift with open vertical fracture

The relationship between the 2D- and 3D-predicted fracture normal stress and aperture in Figures 5-37 and 5-38 is consistent with the response expected from plane strain models and their 3D equivalents, explained in the foregoing paragraph. The profiles of normal stress and aperture computed in the 2D model are closely similar to those computed in the 3D model; the 2D-computed values of normal stress are slightly larger, and the corresponding values of fracture aperture slightly smaller, than their 3D equivalents. The fracture normal stress profiles shown in Figure 5-37 for the before- and after-excavation conditions also agree satisfactorily with stresses calculated for the same conditions using the distinct element code 3DEC.

An examination of the analysis results presented in Figures 5-39 through 5-47 leads to an important observation regarding the effect of the ground surface on the distributions of stresses and deformations within the near-field of the drift. It should be recalled that the region above the drift is bounded by the ground surface at an elevation of 300 m above the drift axis, whereas the region below the drift is bounded by a zero-perturbation boundary at a depth of 1000 m. This difference does not have any noticeable effect on the temperature distributions, as Figure 5-39 through 5-41 show. On the other hand, as Figures 5-42 through 5-47 show, the distributions of stresses and fracture aperture above the drift axis are different from the corresponding distributions below the axis. This difference between the calculated responses above and below the drift axis is caused by the ground surface, and it suggests that the presence of the ground surface should be included in the mechanical analyses of drifts such as this. It may also indicate that the material-property variabilities that occur between the drift and the ground surface should also be considered.

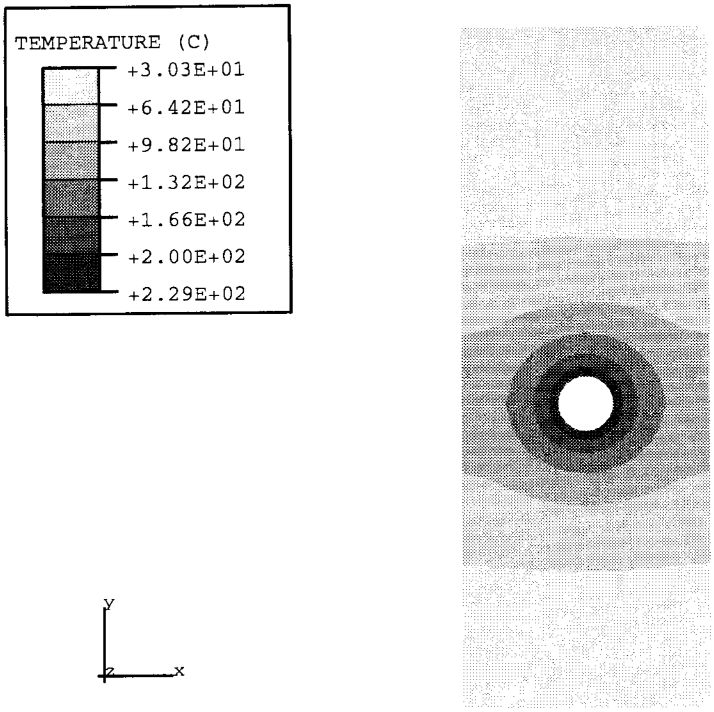

Figure 5-39. Temperature distributions on z=0 plane, based on results calculated using the 3D ABAQUS model: From (*x*=–11.25, *y*=–25 m) to (*x*=11.25, *y*=25 m)

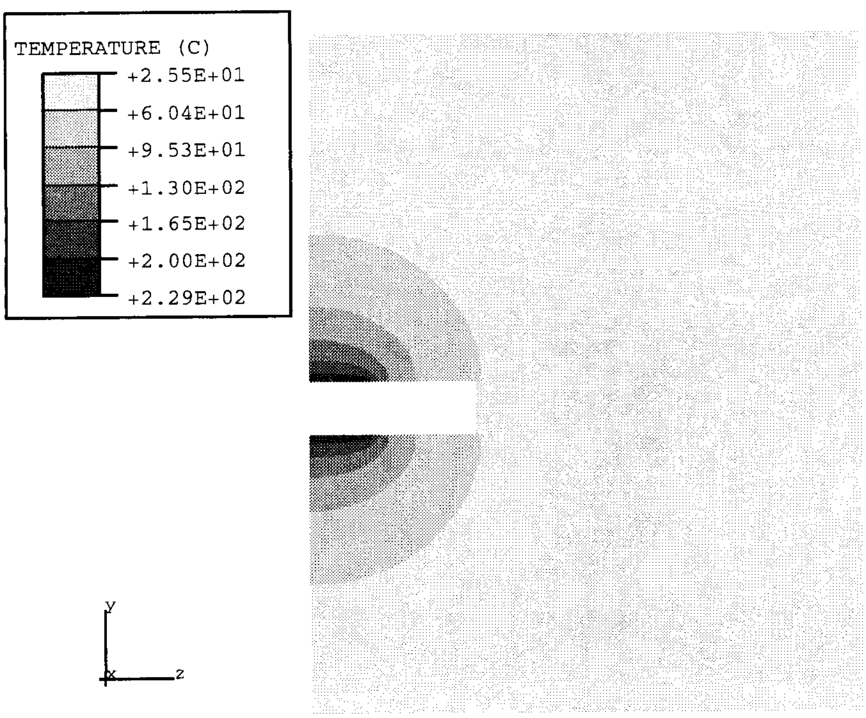

Figure 5-40. Temperature distributions on x=0 plane, based on results calculated using the 3D ABAQUS model: From (*z*=0, *y*=–25 m) to (*z*=50, *y*=25 m)

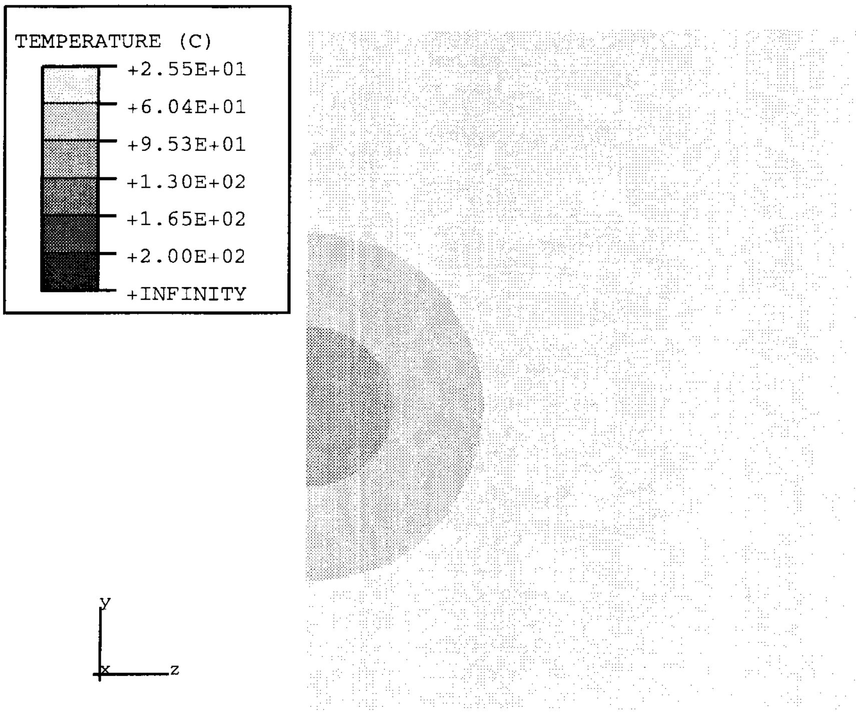

Figure 5-41. Temperature distributions on x=11.25-m plane, based on results calculated using the 3D ABAQUS model: From (*z*=0, *y*=–25 m) to (*z*=50, *y*=25 m)

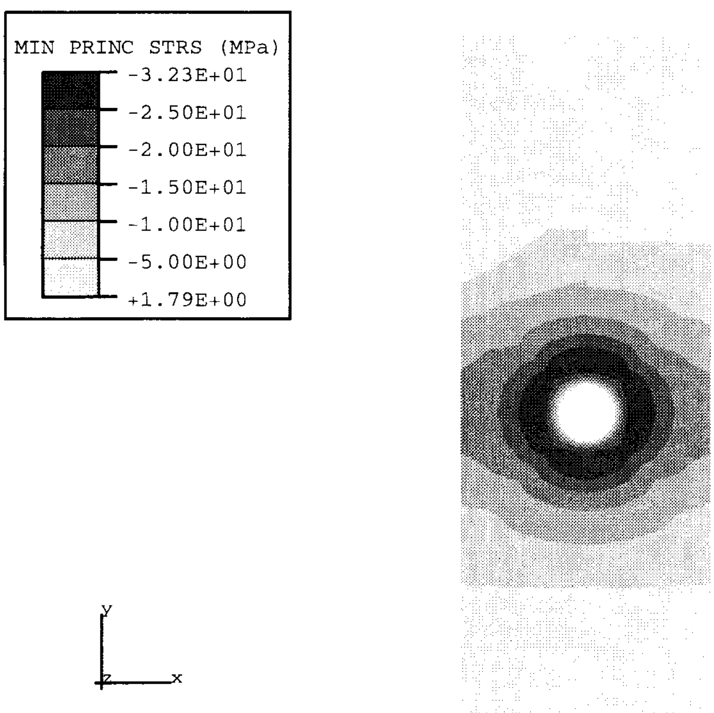

Figure 5-42. Distributions of the minimum principal compressive stress on z=0 plane, based on results calculated using the 3D ABAQUS model: From (*x*=–11.25, *y*=–25 m) to (*x*=11.25, *y*=25 m)

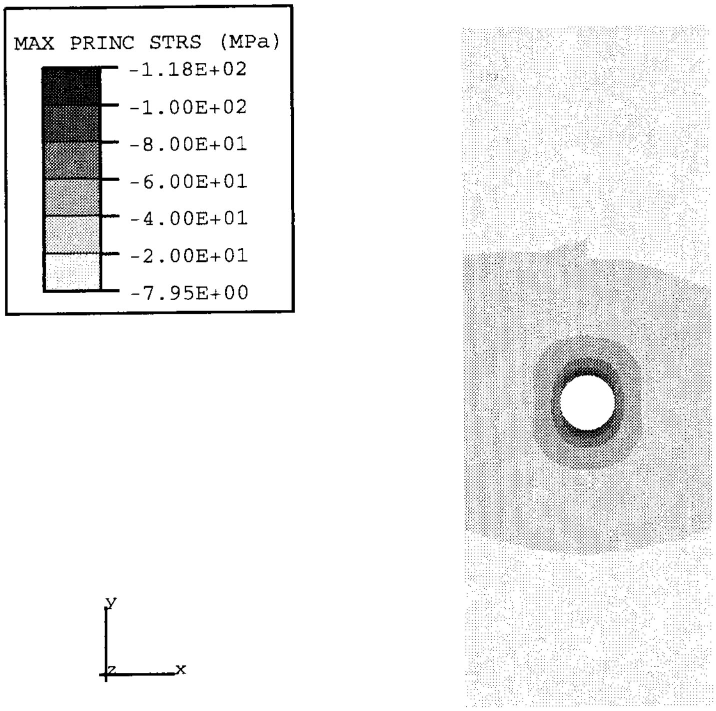

Figure 5-43. Distributions of the maximum principal compressive stress on z=0 plane, based on results calculated using the 3D ABAQUS model: From (*x*=–11.25, *y*=–25 m) to (*x*=11.25, *y*=25 m)

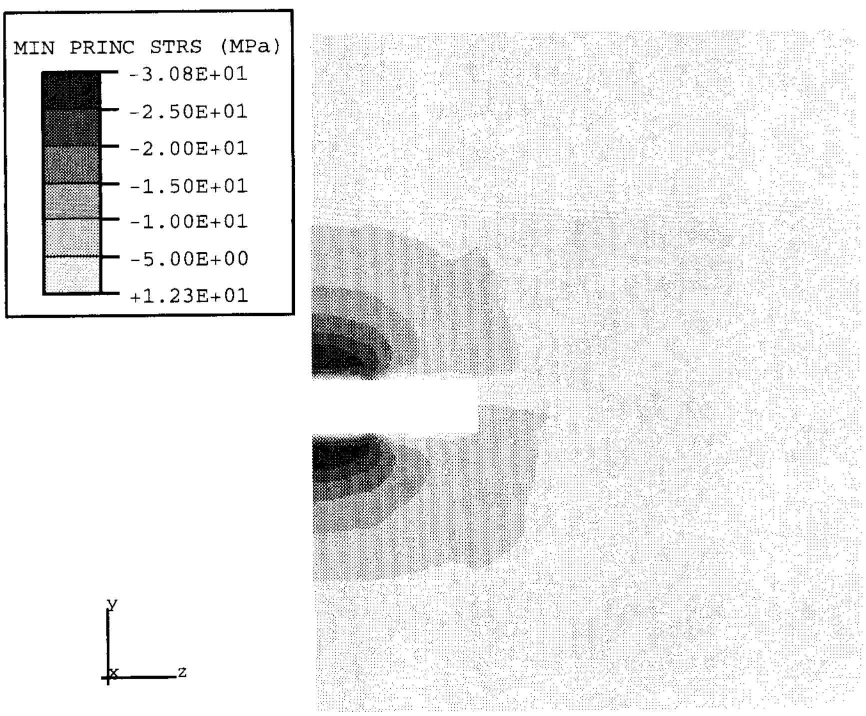

Figure 5-44. Distributions of the minimum principal compressive stress on x=0 plane, based on results calculated using the 3D ABAQUS model: From (*z*=0, *y*=–25 m) to (*z*=50, *y*=25 m)

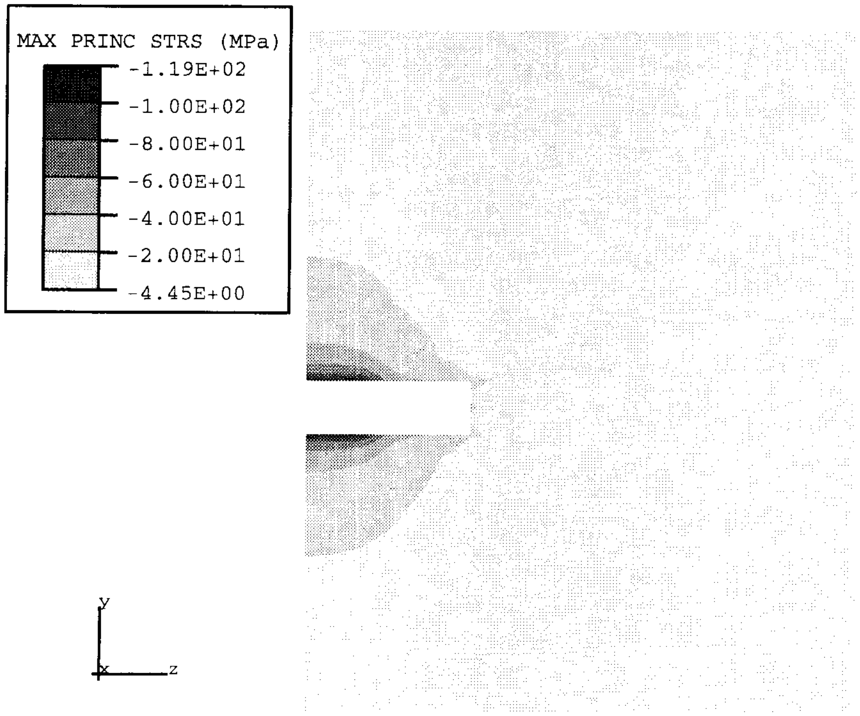

Figure 5-45. Distributions of the maximum principal compressive stress on x=0 plane, based on results calculated using the 3D ABAQUS model: From (*z*=0, *y*=–25 m) to (*z*=50, *y*=25 m)

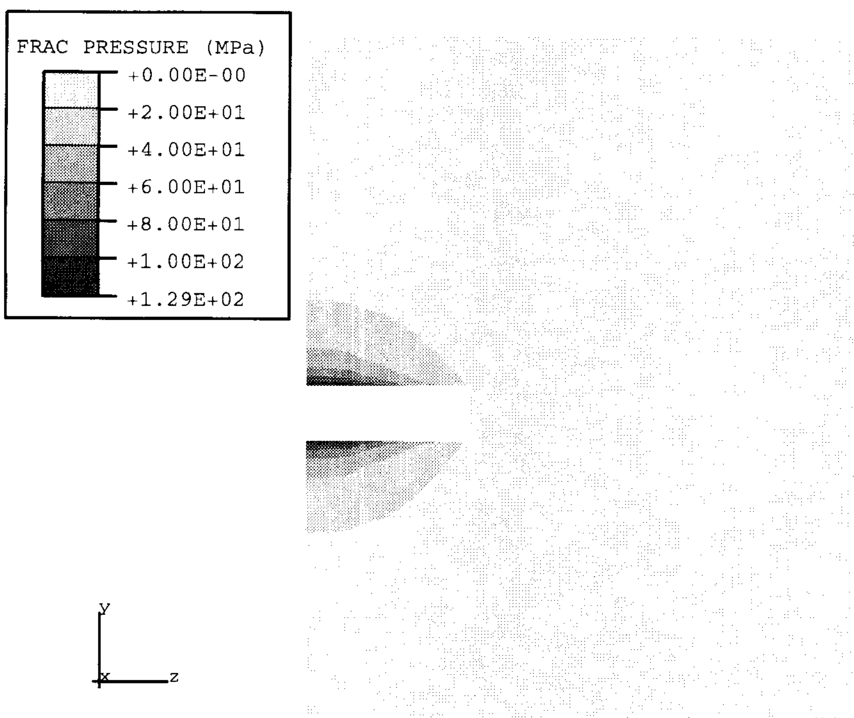

Figure 5-46. Distributions of fracture normal stress on x=0 plane, based on results calculated using the 3D ABAQUS model: From (*z*=0, *y*=–25 m) to (*z*=50, *y*=25 m)

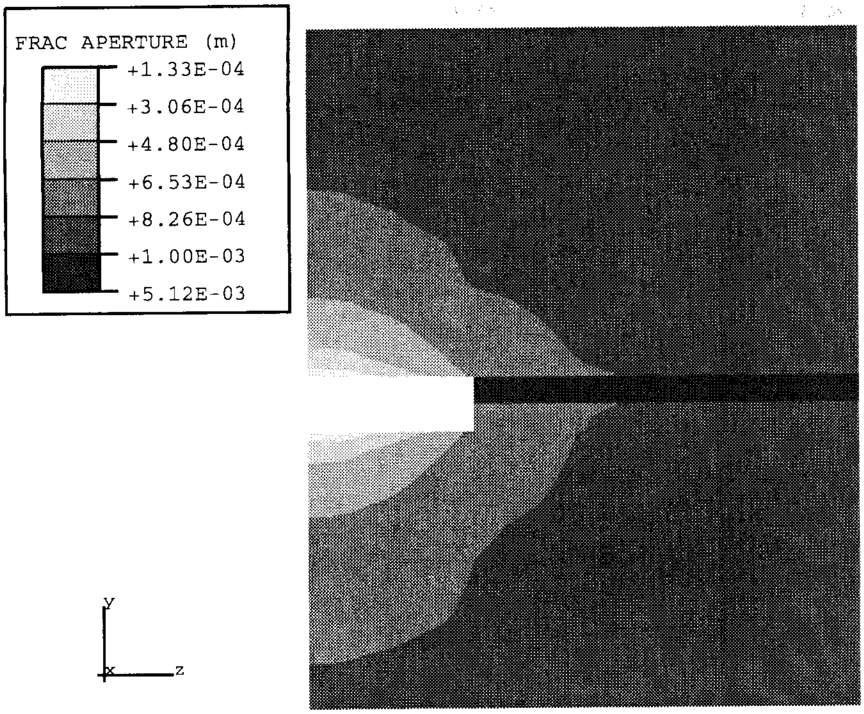

Figure 5-47. Distributions of fracture aperture on x=0 plane, based on results calculated using the 3D ABAQUS model: From (*z*=0, *y*=–25 m) to (*z*=50, *y*=25 m)

5.3 CONCLUSIONS

The computer code ABAQUS was evaluated in this chapter with respect to its capabilities to model the thermal-mechanical processes that may occur in a heated fractured rock mass. The performance of the code was evaluated as follows:

(i) The general response calculated using ABAQUS was compared with the theoretically expected response of the rock mass

(ii) The ABAQUS-calculated fracture-surface stresses were compared with those calculated using the distinct element code UDEC

(iii) The values of fracture pressure and aperture calculated using an ABAQUS plane-strain model were compared with those calculated using a closely equivalent 3D ABAQUS model

Based on the problems solved, the code is judged to possess the capabilities for modeling the thermal-mechanical response of fractured rock. The values of fracture-surface stress and aperture were found to be sensitive to the normal stiffness and pre-slip shear stiffness of the fracture. The user-control of the pre-slip shear stiffness of fractures is exercised in ABAQUS through the SLIP TOLERANCE parameter. This parameter enables the user to assign a wide range of values of pre-slip shear stiffness, including infinite stiffness (through the "*FRICTION, LAGRANGE" command). The code simulates the normal stiffness through an internally generated exponential pressure-vs-aperture function based on two user-supplied parameters. Because such an exponential function may not always be appropriate, it would be better to provide for user-specification of the pressure-vs-aperture relationship through a table. The change required in ABAQUS to provide for such a table is likely to be feasible (considering that similar tables are used in several places in the code), but such a change requires access to the ABAQUS source code.

6 THERMAL-HYDROLOGICAL PROBLEMS: CYLINDRICAL HEAT SOURCE IN INFINITE MEDIUM

The problems solved under this category were selected to evaluate the capabilities of ABAQUS in modeling the coupled flow of heat and fluids through geologic media. Thermal-hydrological (TH) coupled processes under saturated conditions involve the expansion of water and consequent development of water pressure, the flow of water and the associated dissipation of excess water pressure, as well as conductive and convective heat flow. The TH processes under unsaturated conditions are more complicated since they include the following: the flow of water and gas (including water vapor), evaporation and condensation of water, and convective and conductive heat flow. Because ABAQUS does not have specific provisions for modeling the simultaneous flow of two fluid phases, it is likely to run into difficulty with TH processes under unsaturated conditions. On the other hand, the code should handle the saturated-medium TH processes satisfactorily, except under conditions for which the effects of convective heat flow cannot be ignored. The objectives of the selected TH problem are to: (i) determine whether the code solves the problem satisfactorily under saturated conditions, (ii) identify the extent to which the solutions given by the code for unsaturated conditions might be inadequate, and (iii) identify possible ways of improving the capabilities of the code for modeling TH processes under unsaturated conditions.

6.1 PROBLEM DEFINITION

The geometry of the problem is illustrated in Figure 6-1. It consists of a cylindrical heat source of height $2h$ and radius r_o buried in an infinite rock mass. The axis of the cylindrical source, that is the z-axis in Figure 6-1, is vertical. The rock mass is assumed to be homogeneous and isotropic. The heat source consists of the same material as the rock mass, but it differs from the surrounding rock by being impregnated with heat-producing material. The dimensions of the cylindrical source are h=0.5 m and r_o=0.25 m; heat was generated at the rate of 600 W/m^3 within the cylinder.

The thermal, mechanical, and hydrological properties of the rock are given in Table 6-1. The value of gravitational acceleration was set to 10 m/s^2 (vertically downward). The initial temperature was set at 25°C everywhere in the rock mass. The problem was solved for two cases of initial pore pressure: (i) the saturated case, with an initial pore pressure of 0 everywhere; and (ii) the unsaturated case, with an initial pore pressure of −3.75 kPa (corresponding to a saturation of 0.741) everywhere. The infinite-boundary condition of zero perturbation (i.e., no change in temperature or pore pressure, and no displacement) was applied at r=50 m and at z=50 m; this location for the external boundary was found to be sufficiently far for the simulation time of 1000 d. The problem was solved only for the top half of the domain ($z \geq 0$), to take advantage of symmetry.

6.2 EVALUATION STRATEGY

Booker and Savvidou (1985) developed a set of analytical solutions for the temperature and pore-pressure distributions caused by a point heat source in an infinite water-saturated rock mass. The solutions for a cylindrical source of the type described in Section 6.1 can be obtained by integrating the point-source solutions over the cylindrical volume. A FORTRAN code of such a numerical integration, developed by Nguyen and Selvadurai (1995) was made available to the CNWRA through the DECOVALEX secretariat. The saturated case of the cylindrical-source problem was solved using this code, as well as using ABAQUS and CTOUGH. The unsaturated case of the problem was also solved using ABAQUS and CTOUGH. There is no analytical solution available for the unsaturated case.

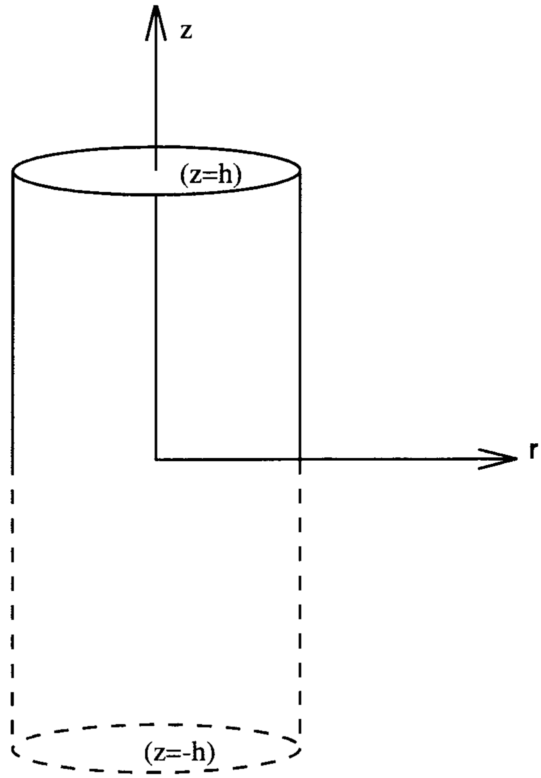

Figure 6-1. Problem geometry for the analysis of the thermal-hydrological effects of a cylindrical heat source

The evaluation of ABAQUS with respect to this problem consists of comparing the ABAQUS solutions with the corresponding analytical and CTOUGH solutions. The histories of temperature, pore pressure, and, for the unsaturated case, saturation are examined at radial distances of 0, r_o, $2r_o$, and $5r_o$, on the planes z=0 (middle plane) and z=h (end plane).

Table 6-1. Material and model parameter specifications for the cylindrical source problem

Material and Model Parameters	Value
Young's modulus (Pa)	10^8
Poisson's ratio	0.4
Density of solid particles (kg/m^3)	2,700
Density of water (kg/m^3)	1,000
Porosity	0.3
Volumetric thermal expansivity of solid particles (K^{-1})	5×10^{-5}
Volumetric thermal expansivity of water (K^{-1})	5.5×10^{-4}
Specific heat capacity of solid particles [J/(kg·K)]	710

Table 6-1. (Cont'd)Material and model parameter specifications for the cylindrical source problem

Material and Model Parameters	Value
Specific heat capacity of water [J/(kg·K)]	4,189
Bulk thermal conductivity [W/(m·K)]	1.6
Saturated hydraulic conductivity (m/s)	1.017×10^{-10}
van Genuchten moisture-retention parameter, β (m^{-1})	2.9227
van Genuchten moisture-retention parameter, *n*	2.0304
Residual saturation	0.1833

6.3 ABAQUS MODEL

Each of the problems consisted of two separate ABAQUS analyses: a heat-conduction analysis to obtain the temperature histories at nodal points, and a soils-consolidation analysis in which ABAQUS read the temperature histories from an interface file and applied them as user-supplied input. The same finite element mesh was used for both analyses, as is required by ABAQUS. The heat-conduction analysis was performed using DCAX8 elements (eight-noded axisymmetric quadrilaterals that monitor the value of temperature at every node); the corresponding elements for the soils-consolidation analyses are the CAX8RP (8-noded axisymmetric quadrilaterals that monitor the values of pore pressure, *r*-displacement and *z*-displacement at every node).

6.4 RESULTS

The temperature histories at the monitored points are presented in Figures 6-2 through 6-5. The ABAQUS-calculated results are compared with the analytical solutions in Figures 6-2 and 6-3, and with the CTOUGH solutions in Figures 6-4 and 6-5. The level of agreement between the three sets of solutions is satisfactory. Both the analytical solution and the model used in the ABAQUS solution assume heat flow by conduction only. On the other hand, the CTOUGH solution may include possible effects of convection (i.e., flow of variably heated water). Therefore, the agreement between the three sets of solutions implies that heat flow is dominated by conduction for the specific conditions described in Section 6.1.

The calculated pore-pressure histories for the saturated case are presented in Figures 6-6 through 6-9. As Figures 6-6 and 6-7 show, the results calculated using ABAQUS agree satisfactorily with the analytical solutions. On the other hand, as Figures 6-8 and 6-9 show, there are significant differences between the ABAQUS and CTOUGH results. The shapes of the pore-pressure history curves predicted by the two codes are similar, which implies that the processes that cause the pore-pressure changes (i.e., pressure build-up due to the expansion of water, and pressure dissipation due to fluid flow) are appropriately represented in both codes. However, there are subtle differences between the ABAQUS and analytical models of the problem on the one hand, and the model implemented in CTOUGH on the other:

(i) In the analytical and ABAQUS models, thermal expansion of water is calculated using a constant, user-supplied thermal expansivity; on the other hand, thermal expansion of water in the CTOUGH model is based on changes in water density with temperature derived from thermodynamics tables.

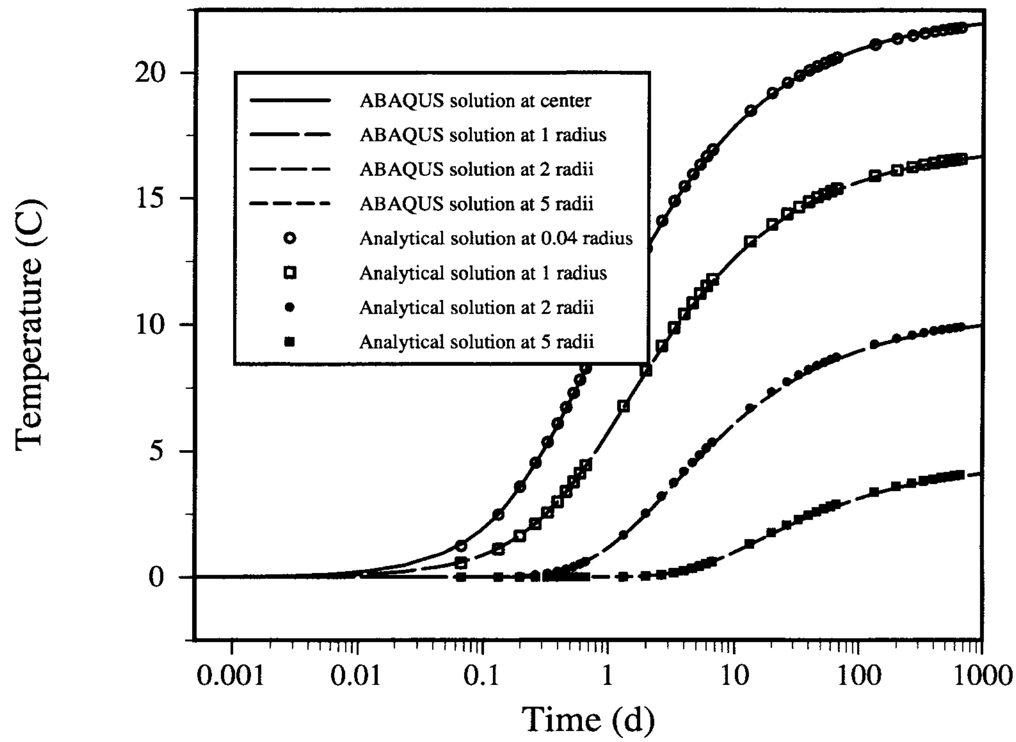

Figure 6-2. Histories of temperature-change on the middle plane comparing ABAQUS-calculated results with the analytical solutions

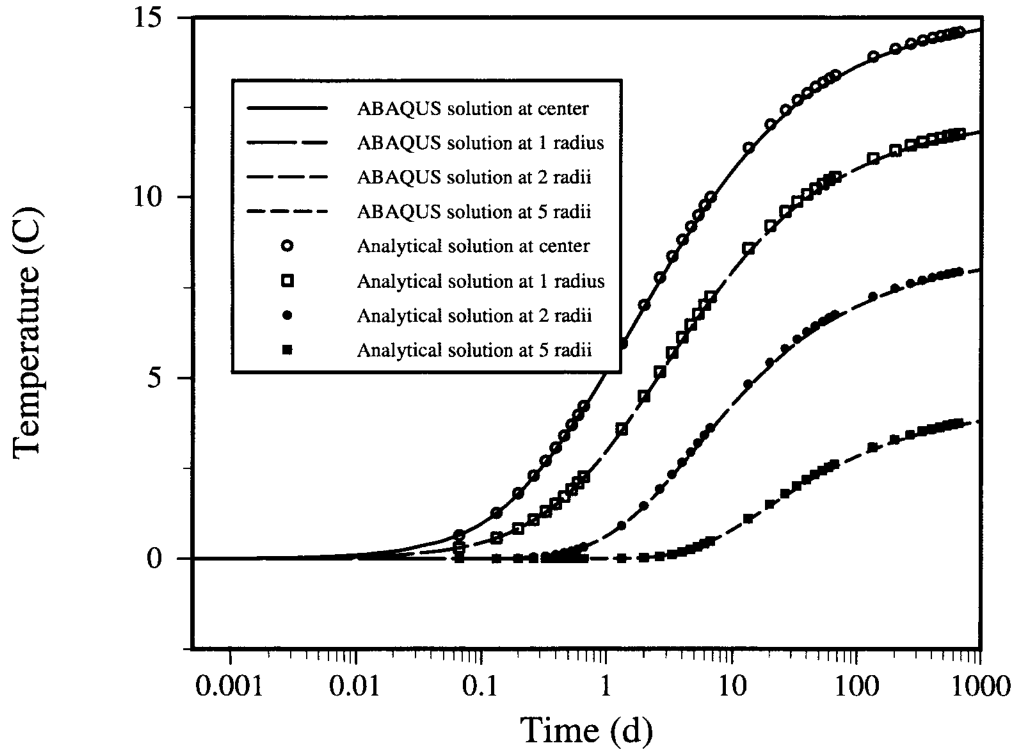

Figure 6-3. Histories of temperature-change on the end plane comparing ABAQUS-calculated results with the analytical solutions

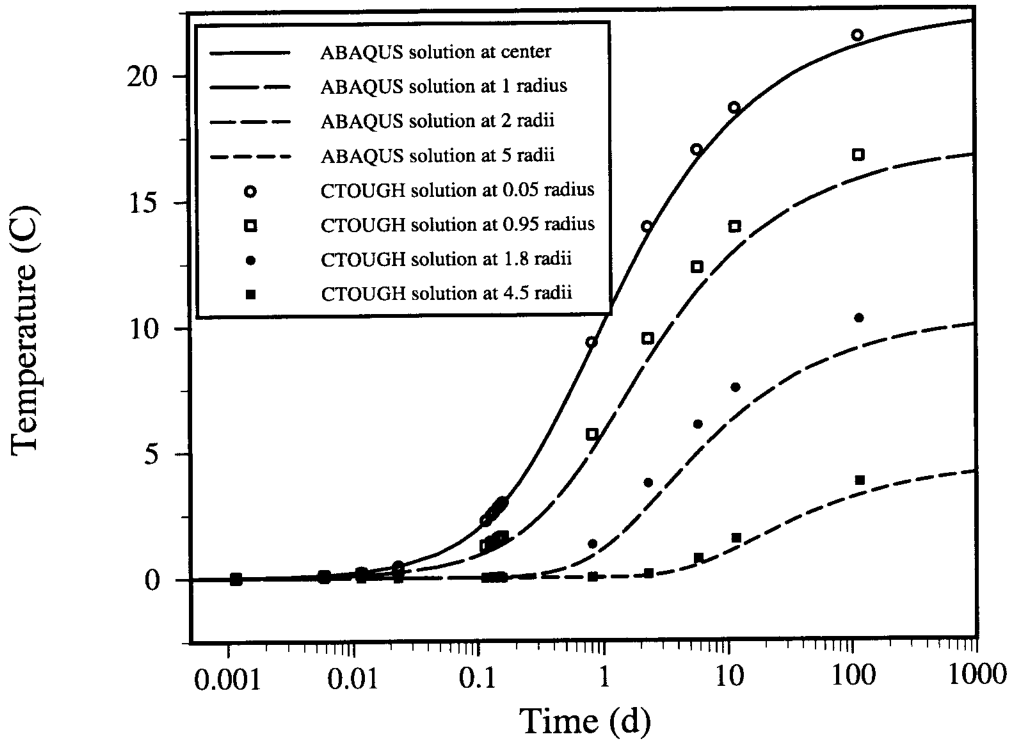

Figure 6-4. Histories of temperature-change on the middle plane comparing results calculated using ABAQUS and CTOUGH

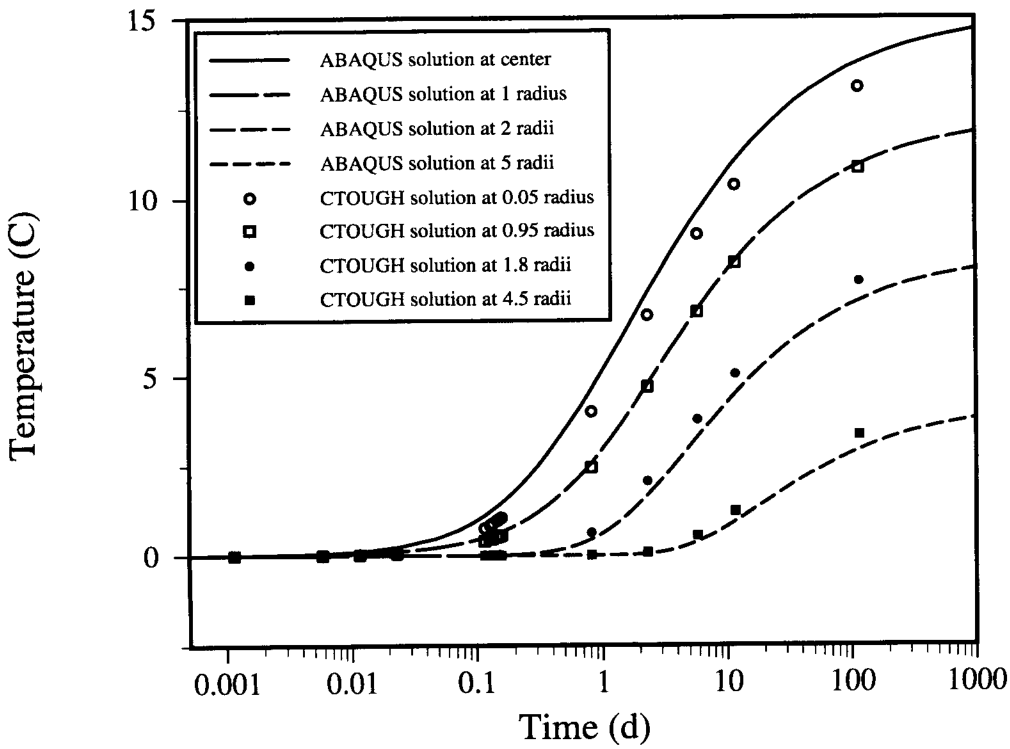

Figure 6-5. Histories of temperature-change on the end plane comparing results calculated using ABAQUS and CTOUGH

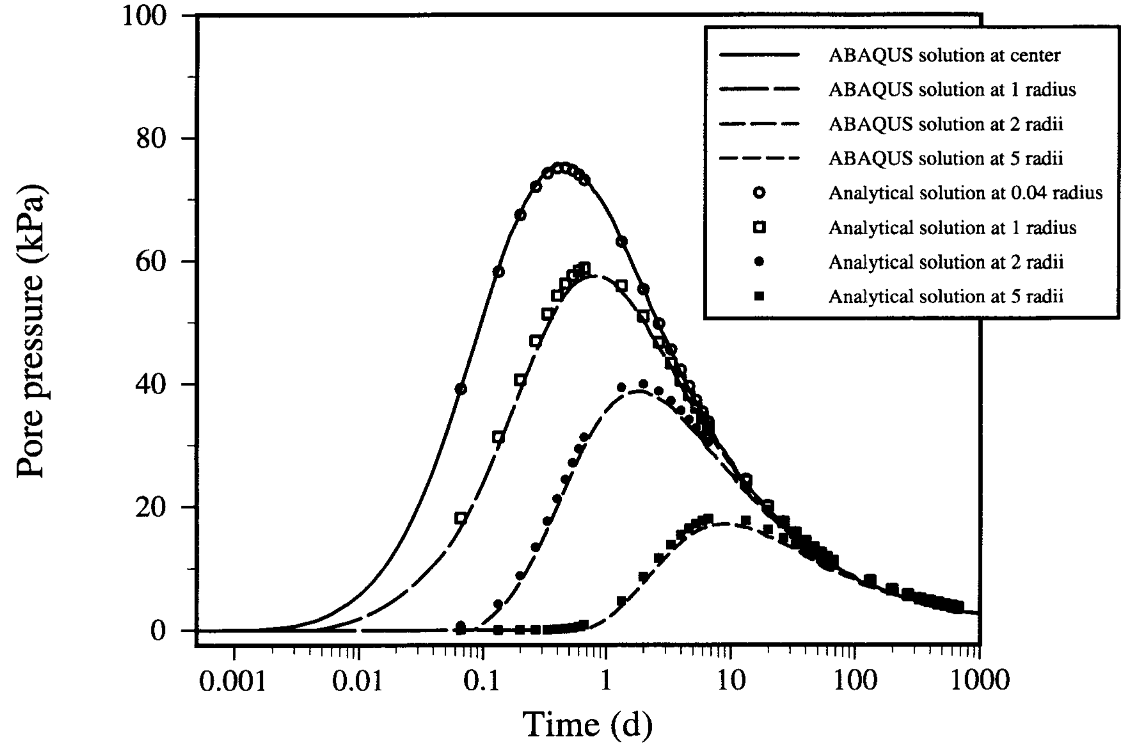

Figure 6-6. Histories of pore pressure on the middle plane for the saturated case (comparing ABAQUS-calculated results with the analytical solution)

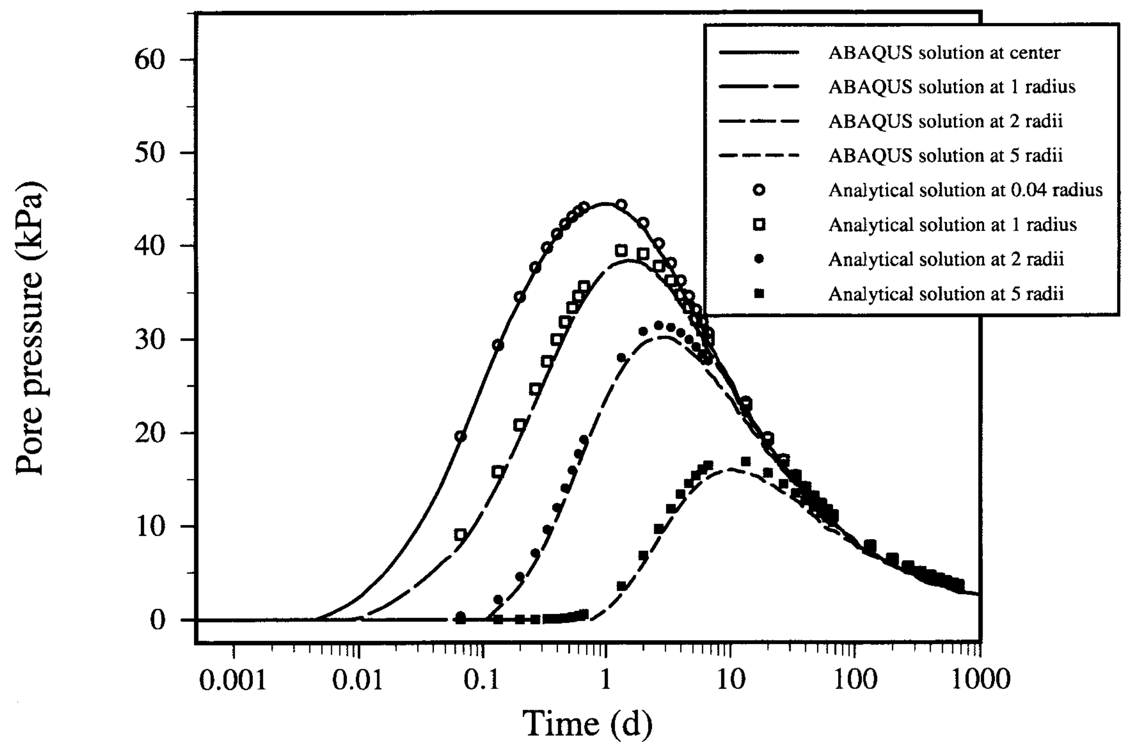

Figure 6-7. Histories of pore pressure on the end plane for the saturated case comparing ABAQUS-calculated results with the analytical solution

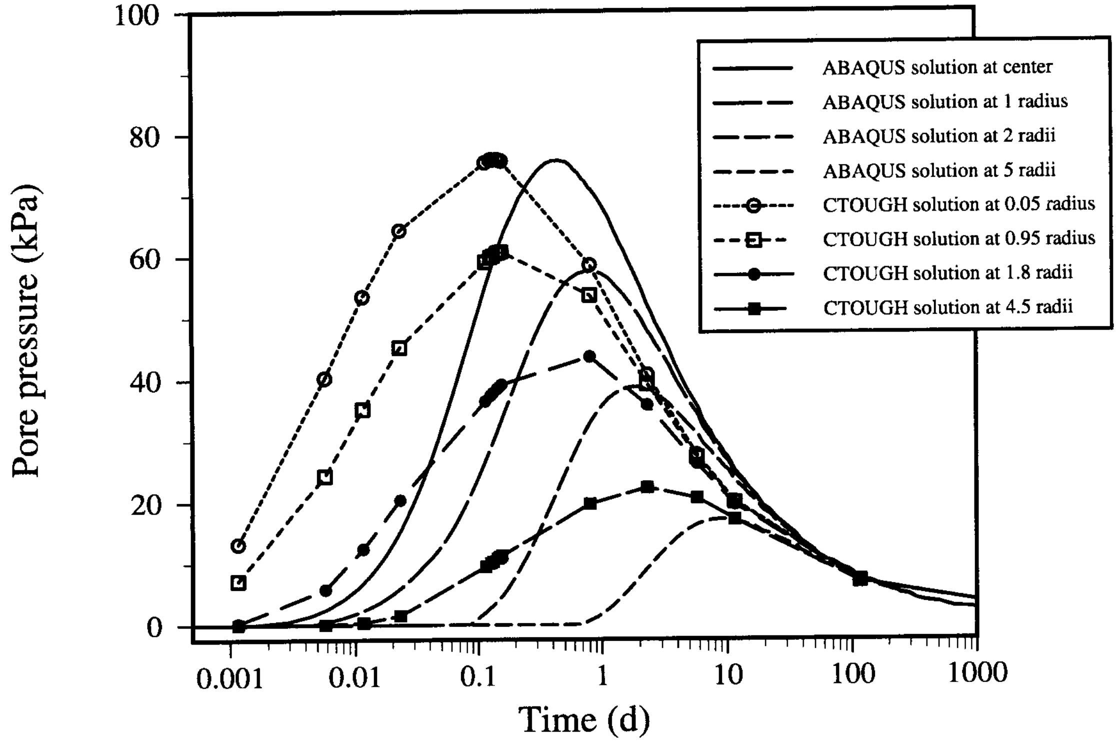

Figure 6-8. Histories of pore pressure on the middle plane for the saturated case comparing results calculated using ABAQUS and CTOUGH

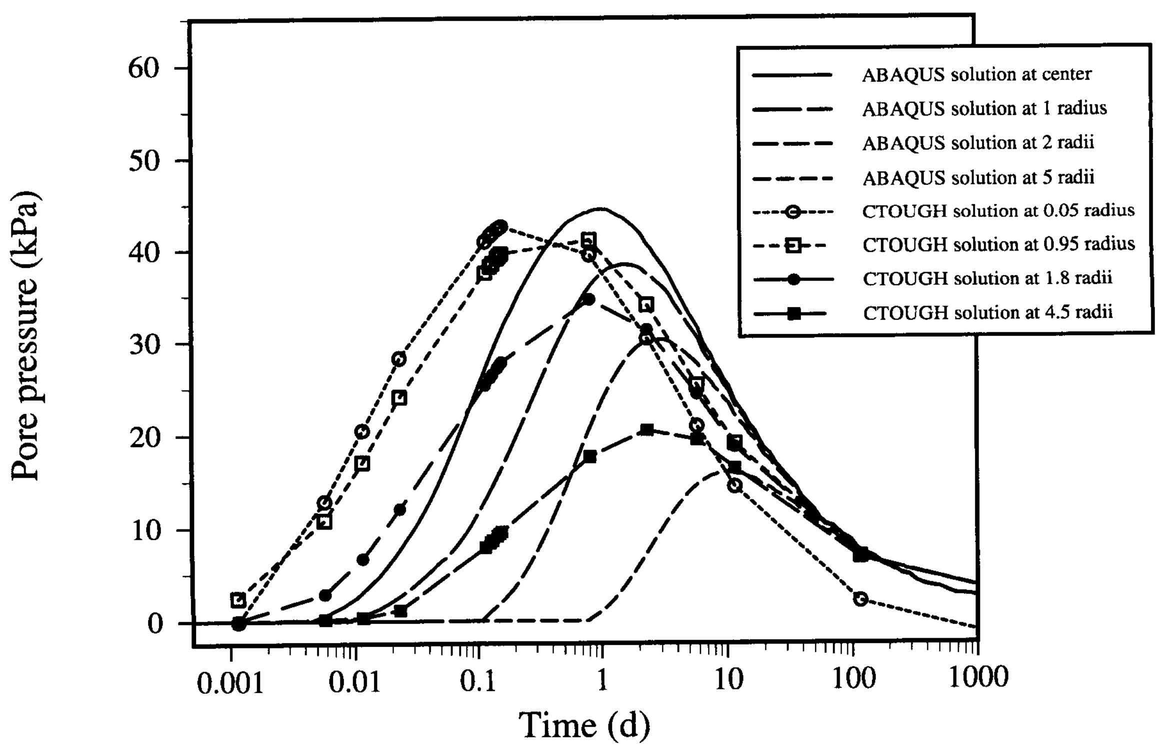

Figure 6-9. Histories of pore pressure on the end plane for the saturated case comparing results calculated using ABAQUS and CTOUGH

(ii) The hydraulic conductivity of the medium varies with temperature in the CTOUGH model because of temperature-dependent changes in the values of density and viscosity for water. On the other hand, the value of hydraulic conductivity is fixed in the analytical model. A fixed value of hydraulic conductivity was also used in the ABAQUS model, although the code makes provisions for temperature-dependent hydraulic conductivity.

(iii) The CTOUGH model includes both conductive and convective heat flow, whereas the analytical and ABAQUS models are based on heat conduction alone. Although this difference has no noticeable effect on the calculated temperature histories, as was shown earlier, it may still have an effect on the pore-pressure histories.

A second ABAQUS analysis of the saturated case was conducted with temperature-dependent hydraulic conductivity values calculated using the same viscosity-vs-temperature relation that is implemented in CTOUGH. The results of the second analysis are the same as those presented in Figures 6-6 and 6-7, which suggests that temperature-dependent hydraulic conductivity alone cannot account for the observed differences between the ABAQUS and CTOUGH results. Although the difference between the CTOUGH and other solutions could not be resolved, the fact that the ABAQUS solution agrees satisfactorily with the analytical solutions indicates that the ABAQUS simulation of the saturated-medium TH processes is satisfactory for situations in which the effects of convective heat flow can be ignored.

The histories of pore pressure and saturation for the unsaturated case are presented in Figures 6-10 through 6-13. The ABAQUS calculated results are given in Figures 6-10 and 6-11, whereas those of CTOUGH are in Figures 6-12 and 6-13. Results are presented for the middle plane only; the end-plane results are similar to the corresponding middle-plane results. The ABAQUS results show a progressive increase in both pore pressure and saturation that is caused by the thermal expansion of water. On the other hand, the CTOUGH results show a decrease in saturation within the perimeter of the heat source and increase in saturation outside. The decrease in saturation within the heat-source perimeter may have been caused by the thermal expansion of gas (i.e., water being driven away by the expanding gas) or by evaporation (cf. Green et al., 1995).

Although the specific values of saturation and pore pressure calculated using CTOUGH have not been validated, the CTOUGH results are generally consistent with the expected processes associated with the introduction of heat in an unsaturated rock mass. To simulate such processes satisfactorily, it is necessary to model, as a minimum, the simultaneous flow of gas and water under the influence of heat. The evaporation and condensation of water may also be important, depending on the level of heating (cf. Green et al., 1995). The current implementation of unsaturated fluid flow in ABAQUS does not recognize the mobility of the non-wetting phase, which is assumed to be air under atmospheric pressure.

In order to model the unsaturated-medium TH processes satisfactorily, ABAQUS needs to be modified to account for the coupled flow of gas and water. The required modification is considered feasible because the elements currently equipped with the capability to calculate pore-water pressure can be modified to also calculate pore-gas pressure. The code will have to solve a mass-conservation equation for gas similar to the one solved for water, and a relative-permeability-vs-saturation table for gas will have to be supplied by the user, in addition to the table supplied for water. Because such changes are fundamental to the code, they cannot be effected through a user-subroutine interface. Access to the source code would be needed to effect the required changes.

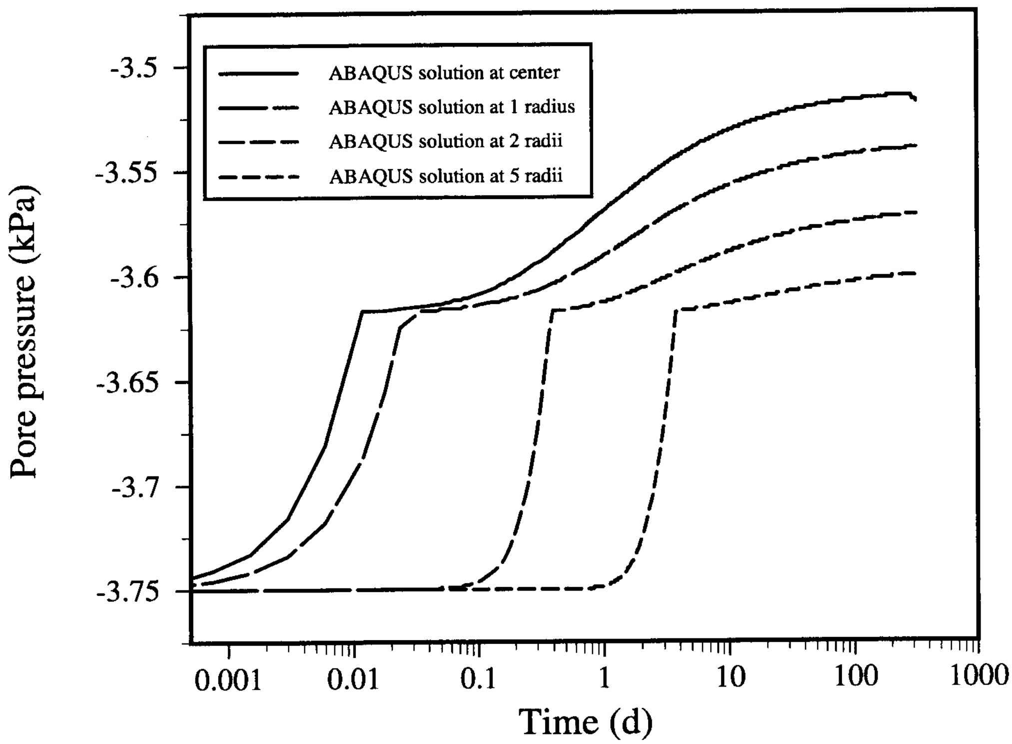

Figure 6-10. Histories of pore pressure on the middle plane for the unsaturated case based on results calculated using ABAQUS

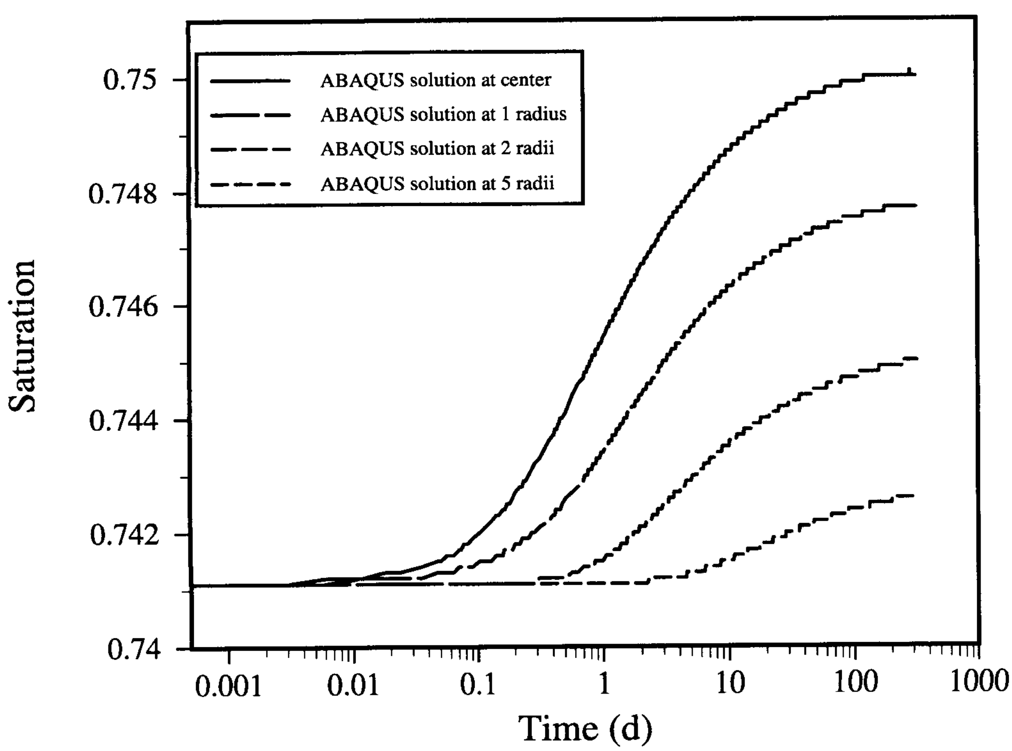

Figure 6-11. Histories of saturation on the middle plane for the unsaturated case based on results calculated using ABAQUS

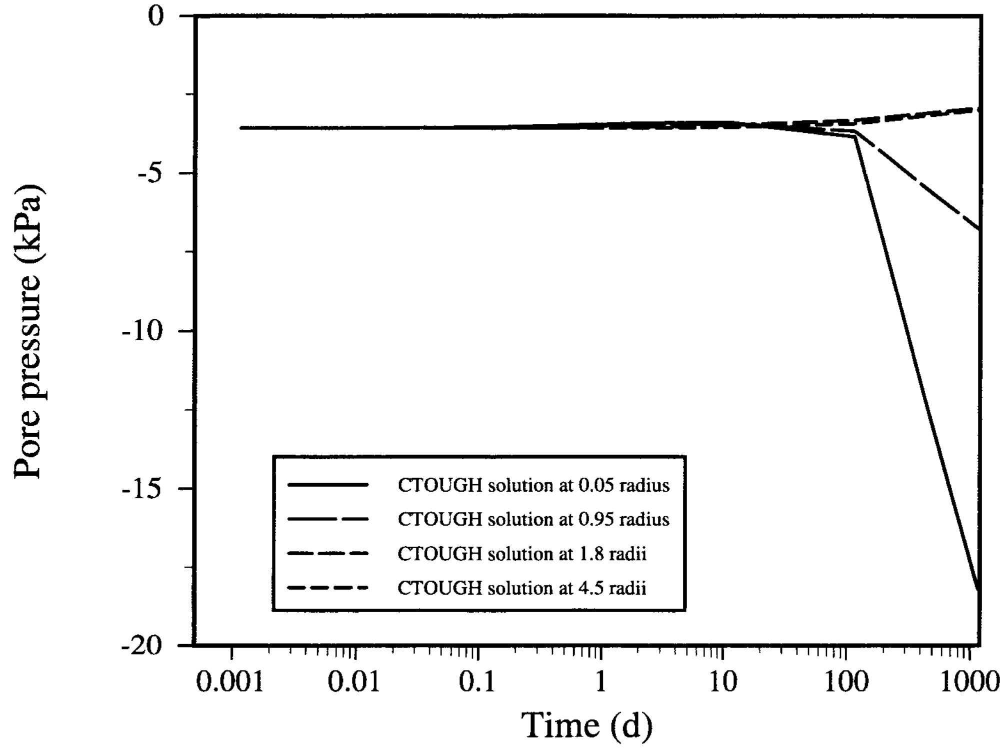

Figure 6-12. Histories of pore pressure on the middle plane for the unsaturated case based on results calculated using CTOUGH

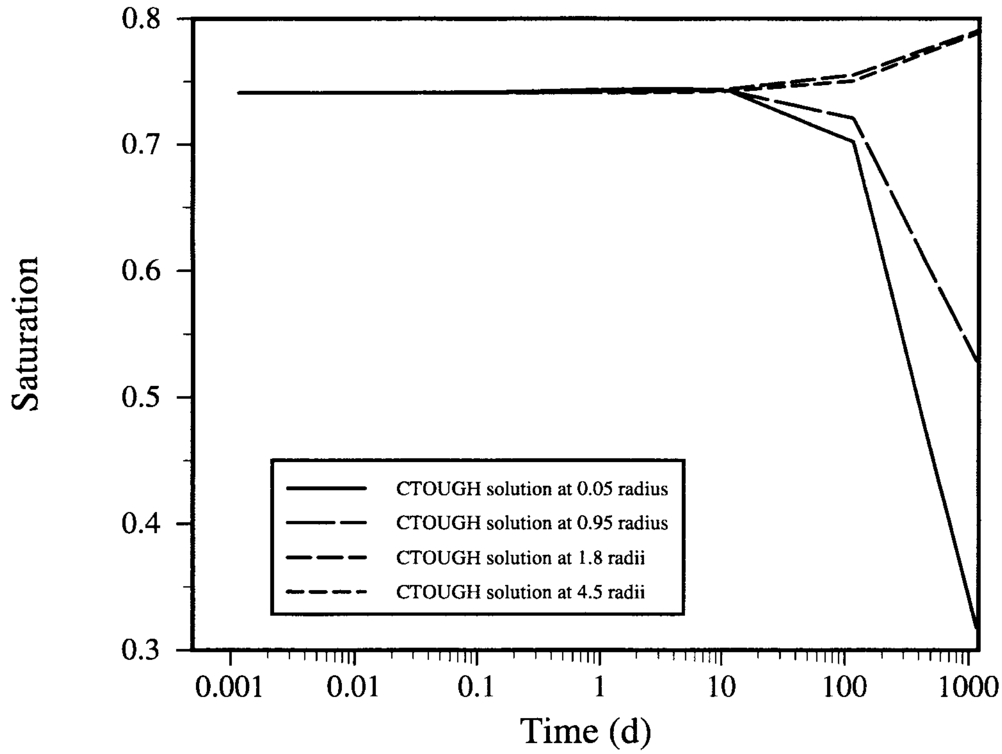

Figure 6-13. Histories of saturation on the middle plane for the unsaturated case based on results calculated using CTOUGH

6.5 CONCLUSIONS

The computer code ABAQUS was evaluated in this chapter with respect to its capabilities to model the coupled thermal-hydrological processes that may occur in a heated water-saturated or unsaturated medium. The performance of the code was evaluated as follows:

(i) The solutions calculated using ABAQUS for the saturated conditions were compared with analytical solutions developed by Booker and Savvidou (1985) and with solutions obtained using CTOUGH.

(ii) The ABAQUS solutions for the unsaturated conditions were compared with those obtained using CTOUGH.

The performance of ABAQUS for the analysis of conductive heat flow under saturated conditions was found to be satisfactory. On the other hand, in order to model the unsaturated-medium TH processes satisfactorily, including the simulation of drying (i.e., decrease in saturation) ABAQUS needs to be modified to account for the coupled flow of gas and water, including the effect of heat on such flow. With such modifications, the code would likely model the TH processes satisfactorily for situations in which the effects of evaporation and condensation can be ignored.

7 MECHANICAL-HYDROLOGICAL PROBLEM: EFFECTS OF MECHANICAL LOADING ON FRACTURE PERMEABILITY

The effects of mechanical deformation on rock-mass permeability are associated with changes in fracture aperture and connectivity and with microcracking of intact rock. The objective of the mechanical-hydrological (MH) problem is to examine the tools available in ABAQUS for modeling the effects of mechanical loading on the permeability of rock fractures. The mechanical response of fractures may be modeled in ABAQUS using either the interface elements or thin solid elements. However, results presented in Chapter 2 show that the interface elements are not suitable for modeling networks of intersecting fractures. Because the constitutive behavior currently provided for the interface elements does not account for shear-induced dilation, the elements are also not suitable for modeling the effects of mechanical loading on single-fracture permeability under situations for which shear-induced dilation is important. Furthermore, results presented in Chapter 4 show that the interface elements are not suitable for modeling the flow of water through fractures in unsaturated rock. On the other hand, the examination of thin solid elements presented in Chapter 4 suggests that they are likely to be satisfactory for modeling the hydrological (including unsaturated flow) responses of single fractures and fracture networks. Also, because the thin solid elements can use any of the several constitutive models available in ABAQUS, it is likely that they can be adapted to model both shear- and normal-load-induced changes in fracture aperture. Consequently, only the thin solid elements were examined as possible tools for modeling the effects of mechanical loading on fracture permeability.

7.1 MECHANICAL-HYDROLOGICAL MODEL OF FRACTURES BASED ON THIN SOLID ELEMENTS

The use of thin solid elements to model the MH responses of rock fractures requires the resolution of two problems. First, it is necessary to define a procedure for relating changes in fracture permeability to the mechanical deformation of the thin solid. Second, it is necessary to identify the values of aspect ratio of the thin solid, for which its mechanical responses adequately simulate those of the fracture.

7.1.1 Relationship Between Fracture Permeability and Mechanical Deformation of Thin Solid Elements

One advantage of modeling fractures with interface elements is that the changes in fracture aperture can be computed directly from the geometry of the element. On the other hand, in order to model the MH responses of a fracture using thin solid elements, it is necessary to develop a procedure for relating the fracture-aperture changes to the mechanical deformation of the thin solid. Suppose that a fracture segment of given length, aperture, and width is modeled using a thin solid element of the same length and width as the fracture. If it is assumed that the pore volume of the thin solid is equal to the volume of the fracture segment, and that inelastic volume changes in the solid arise entirely from changes in pore volume, then it can be shown that the fracture aperture e is related to the inelastic volumetric strain of the solid through the equation:

$$e = e_o \, (1 + \Delta\varepsilon_p) \tag{7-1}$$

where e_o is the fracture aperture at the beginning of a time increment during which the thin solid undergoes an inelastic volumetric strain increment of $\Delta\varepsilon_p$. The fracture permeability can be related to the fracture aperture through the cubic law, which gives the following equation for the hydraulic conductivity, K:

$$K = \frac{\gamma_w e^2}{12\mu} \tag{7-2}$$

where γ_w is the unit weight of water (10 kN/m^3) and μ is its dynamic viscosity (10^{-6} kPa·s).

These two equations [(7-1) and (7-2)] were implemented in ABAQUS through the user-subroutine interface UVARM, which makes provisions for the computation of user-defined output variables. The output variables so computed are not available for additional computations in the same analysis, but they may be used as input for separate analyses. For example, the values of hydraulic conductivity computed using this implementation of the two equations cannot be used in the same analysis to solve for fluid-flow responses, but they may be used as input in a subsequent hydrologic or thermal-hydrologic analysis.

A different implementation of the equations would be required in order to apply the thin-solid model to a fully coupled MH or TMH analysis of fracture flow. Such implementation requires a user-subroutine interface that makes provisions for the computation of the hydraulic conductivity of solid elements as a function of their inelastic strain. Such a user-subroutine interface is currently not available in ABAQUS. Therefore, an implementation of the equations through the UVARM interface was developed; it allows only for the computation of hydraulic conductivities as output from mechanical analyses, which is sufficient to examine the use of thin solid elements to model the effects of mechanical loading on fracture permeability.

7.1.2 The Effects of Aspect Ratio on the Thin Solid Element Model of Fractures

The aspect ratio of thin solid elements has an effect on their performance in modeling the mechanical response of rock fractures. Sharma and Desai (1992) investigated this effect through a series of numerical experiments, and suggested that the mechanical responses of thin solid elements are sufficiently close to those of interface elements when both of the following conditions are satisfied:

$$\frac{L}{t^2}\sqrt{\frac{E_r G_r}{k_n k_s}} \geq 10^4 \tag{7-3}$$

and

$$\frac{L}{t} \geq 100 \tag{7-4}$$

where L is the length of the thin solid element, t its thickness, E_r and G_r are the Young's and shear moduli,

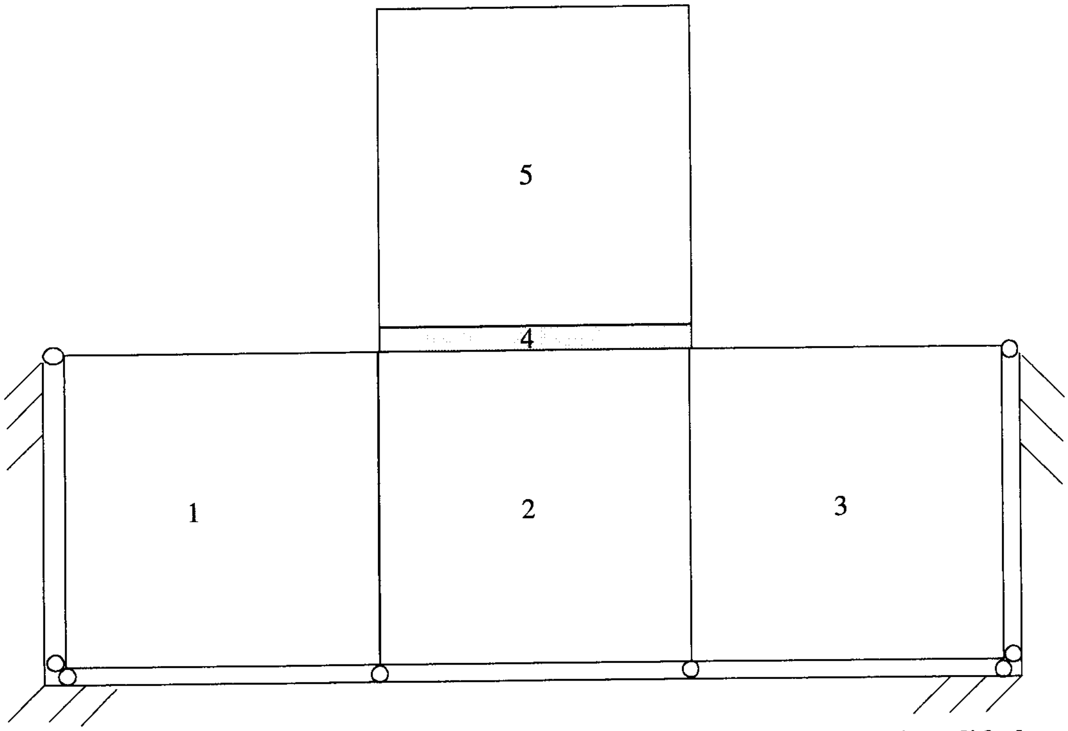

Figure 7-1. Finite element mesh used to study the mechanical response of thin solid elements as a tool for modeling the MH responses of a rock fracture

respectively, of the surrounding rock, and k_n and k_s are the normal and shear stiffnesses, respectively, of the fracture.

Because the ratio $E_r G_r / k_n k_s$ is likely to be a constant for most situations, both (7-3) and (7-4) imply a restriction on the aspect ratio L/t of the thin solid element. A numerical experiment was conducted to examine the effects of the aspect ratio of solid elements on two aspects of their mechanical response: that is, (i) their strength, and (ii) their inelastic-volumetric-strain response. The design and results of the experiment are presented in the next section.

7.2 FINITE ELEMENT MODEL

The finite element model used for the study is shown in Figure 7-1. It consists of a movable rock block, represented by element number 5, which is caused to slide on a fixed block, represented by element numbers 1, 2, and 3. The interface between the blocks is modeled using a thin solid element (element number 4). Each element is 1 m long (horizontal dimension); elements 1, 2, 3, and 5 have a vertical dimension of 1 m each. The vertical dimension (i.e., thickness) of element 4 was varied in the experiment.

All elements in the model are CPE8R elements (eight-noded solid quadrilateral plane-strain elements with reduced order of integration); the rock blocks (elements 1, 2, 3, and 5) were modeled as a linear-elastic material; the thin element, which represents the contact between the sliding blocks, was modeled as an elastic-plastic material. Its elastic-plastic behavior was modeled using the Drucker-Prager failure criterion (Drucker and Prager, 1952), modified to suppress the effect of the intermediate principal stress (cf. Hibbitt, Karlsson, and Sorensen, Inc., 1994). This form of the Drucker-Prager criterion is comparable to the Mohr-Coulomb failure criterion that is usually applied to rock interfaces (cf. Hsiung et al., 1994b). Its implementation in ABAQUS requires four user-supplied parameters: the friction angle, β, the dilation angle, ψ, the unconfined compressive strength, q_u, and a ratio, κ, that controls the role of the intermediate principal stress. Values of κ may lie in the range $0.778 \leq \kappa \leq 1.0$. The classical Drucker-Prager criterion corresponds to κ=1, for which condition the effect of the intermediate principal stress on the yield strength is maximum. For κ=0.778, the Drucker-Prager failure criterion is closely similar to the Mohr-Coulomb criterion, for which the intermediate principal stress has no effect. The value of κ was set to 0.78 in this study, to give a yield behavior for the solid elements that is similar to the yield behavior of rock interfaces (cf. Hsiung et al., 1994b).

The relationship between the Drucker-Prager friction angle, β, for a solid and the Mohr-Coulomb friction angle, ϕ, for the equivalent interface depends on the value of the ratio ψ/β (cf. Hibbitt, Karlsson, and Sorensen, Inc., 1994). For $\psi=\beta$ (i.e., so-called associative flow condition),

$$\tan\beta = \frac{\sqrt{3}\sin\phi}{\sqrt{1 + \frac{1}{3}\sin^2\phi}} \tag{7-5}$$

On the other hand, for the condition of non-dilatant flow, that is for ψ=0, the relationship is

$$\tan\beta = \sqrt{3}\sin\phi \tag{7-6}$$

These equations [(7-5) and (7-6)] apply to the condition of plane strain. The corresponding equations for other conditions are given in the ABAQUS manual (Hibbitt, Karlsson, and Sorensen, Inc., 1994).

The values of the material parameters were set as follows for the numerical experiment: β=50°, ψ=40°, q_u=1 MPa, and κ=0.78. These values of β, ψ, and q_u imply a Mohr-Coulomb friction angle ϕ=47.6° and cohesion of about 0.2 MPa.

Each test was conducted in two analysis steps: first, a vertical pressure of 2 MPa was applied on the top surface of element number 5 (Figure 7-1); next, a prescribed horizontal (rightward) displacement was applied to the left boundary of the same element. The magnitude of the applied displacement (i.e., the shear displacement) was varied with the thickness (t) of the thin solid element (element 4) as shown in Table 7-1, in order to control the magnitude of shear strain applied to the element. The maximum average shear strain applied to the element is equal to $u_{\max}/t$, where $u_{\max}$ is the prescribed horizontal displacement. The inelastic volumetric strain calculated for the thin solid element using the plasticity theory is proportional to the inelastic shear strain. Therefore, because one of the objectives of the experiment is to examine the effect of aspect ratio on the inelastic volumetric strain, it is necessary that the element be subjected to the same amount of inelastic shear strain in each test. The magnitudes of shear displacement shown in Table 7-1 were adjusted by adding the shear displacement at the yield point, that is, the amount of shear displacement that occurred up to the beginning of the horizontal section of the stress-strain curve (e.g., Figure 7-2). The purpose of the adjustment was to ensure that the element was subjected to the same amount of inelastic shear strain in each test.

Table 7-1. Effects of aspect ratio on the shear strength and dilation of thin solid elements based on analyses conducted under average normal stress of 2 MPa

Element thickness (mm)	Aspect ratio	Shear displacement (mm)	Inelastic volumetric strain	Shear strength (MPa)
40	25	40	0.351	1.741
20	50	20	0.350	1.781
13.33	75	13.33	0.350	1.796
10	100	10	0.350	1.804
4.0	250	4.0	0.352	1.820
2.0	500	2.0	0.355	1.825
1.333	750	1.333	0.358	1.827
1.0	1000	1.0	0.362	1.828

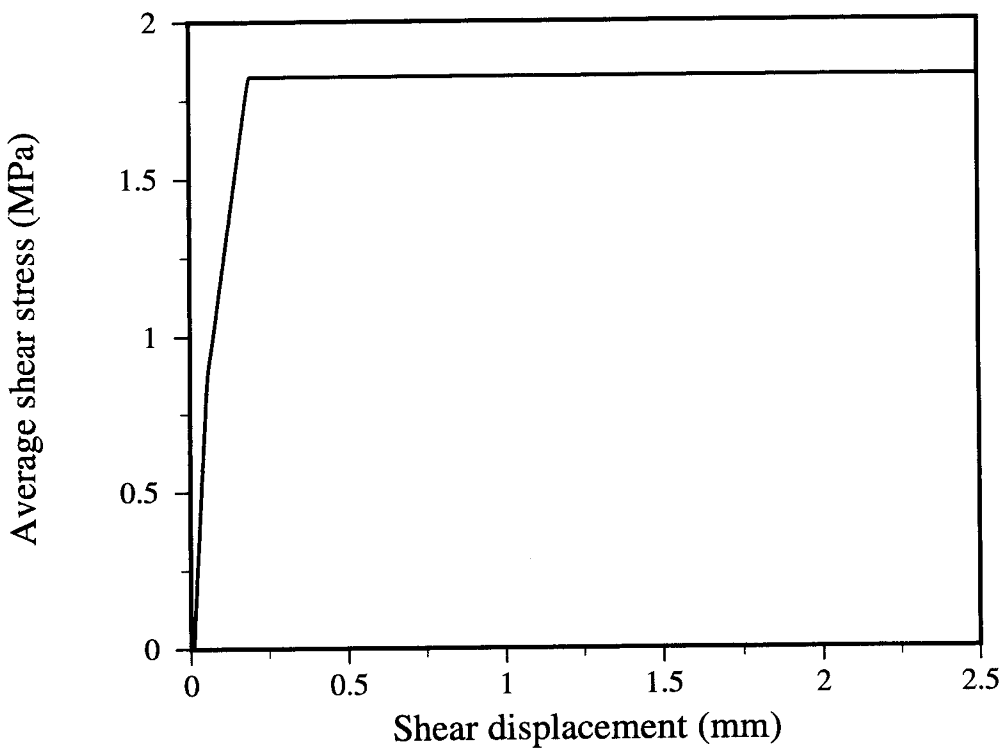

Figure 7-2. Shear stress versus shear displacement for the case of aspect ratio of 500 under average normal stress of 2 MPa

7.3 RESULTS OF THE NUMERICAL EXPERIMENT

The results of the experiment are shown in Table 7-1. The shear strength of the thin element (shear strength of the modeled interface) was calculated as the maximum average shear stress, where the average shear stress is the sum of the reaction force on the left boundary of the sliding block (element 5) divided by the length of the interface (equal to 1 m in the experiment). A plot of shear strength versus aspect ratio is shown in Figure 7-3, which shows that the calculated shear strength is essentially independent of the aspect ratio for values of aspect ratio larger than about 250. The data in Table 7-1 also shows that the calculated inelastic volumetric strain is essentially independent of the aspect ratio.

The effect of aspect ratio was investigated further through another analysis in which the 1-m long fracture (interface between the sliding and stationary blocks) was modeled using 10 thin solid elements connected end to end. The thin elements were each 10 cm long and 0.2 cm thick, which gave an aspect ratio of 50 for each element. Therefore, the zone of weakness representing the fracture (i.e., the array of 10 thin solid elements) had an aspect ratio of 500. The mesh for the sliding and stationary blocks was also modified to be consistent with the mesh for the zone of weakness. The results obtained using this model were the same as those obtained using a single 1-m long thin solid element with aspect ratio of 500 to model the fracture. These results lead to the following conclusions:

(i) The response calculated by modeling a fracture using thin solid elements is sensitive to the aspect ratio of the entire weakness zone that represents the fracture, but not necessarily to the aspect ratio of the individual thin elements

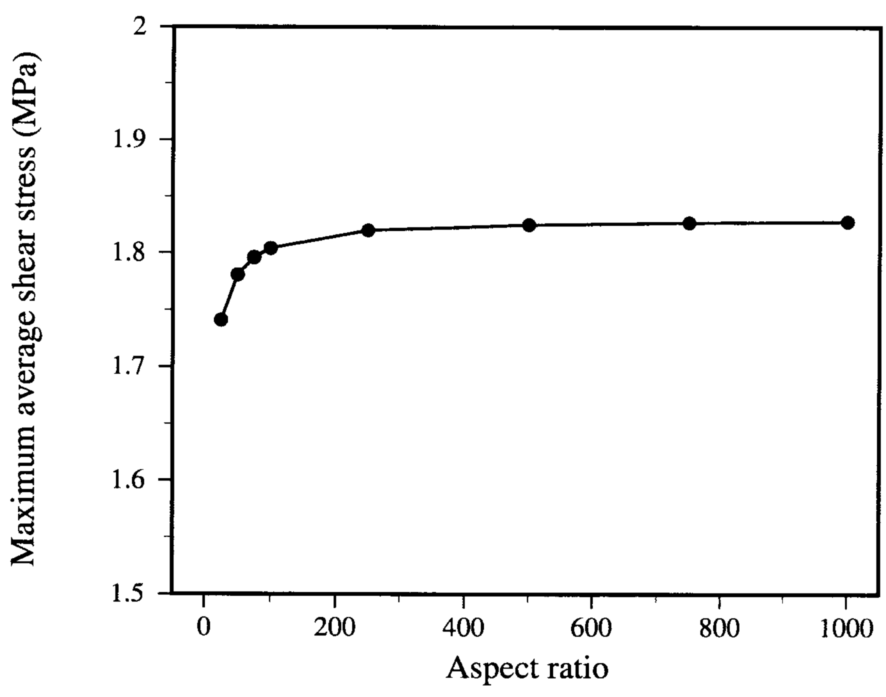

Figure 7-3. The effect of aspect ratio on the calculated shear strength under 2 MPa normal stress

(ii) The performance of the individual thin elements does not appear to be sensitive to their aspect ratio

The shear strength of the interface calculated using the solid elements is about 1.83 MPa. An analysis of the sliding blocks was also conducted using interface elements. That is, the thin solid element (element 4) was deleted from the model and the contact between the sliding and restrained blocks was modeled using an INTER3 interface element, which was assigned the same friction angle (i.e., ϕ=47.6°) as the thin solid elements. The constitutive behavior of the interface element does not account for cohesion; therefore, the element could not be assigned a nonzero value of cohesion. The shear strength calculated using the interface element (based on the definition of shear strength given previously) is 2.19 MPa, which is equal to the value given by the Mohr-Coulomb failure criterion for ϕ=47.6°, zero cohesion, and normal stress of 2 MPa. The fact that the interface shear strength calculated using the thin solid elements is smaller than the Mohr-Coulomb-based shear strength of the interface is likely to have been caused by the difference between the Drucker-Prager failure criterion (applied to the solid elements) and the Mohr-Columb criterion (applied to the interface elements).

The results of this experiment lead to two conclusions. First, the amount of inelastic volumetric strain calculated using thin solid elements is independent of their aspect ratio; therefore, such elements may be used to model the effects of mechanical deformation on fracture permeability, based on the equations [(7-1) and (7-2)] introduced earlier. Second, the interface shear strength calculated using the thin-solid model is essentially independent of the aspect ratio of the thin solid that represents the interface, for values of such ratio larger than about 250. However, the thin-solid model may underestimate the Mohr-Coulomb-based shear strength of the modeled interface.

7.4 NUMERICAL EXAMPLE ON THE CALCULATION OF MECHANICAL EFFECTS ON FRACTURE PERMEABILITY

A numerical-model example was analyzed to illustrate the computation of mechanical effects on fracture permeability, using Eqs. (7-1) and (7-2). The analysis was conducted using the finite element model of sliding blocks presented earlier (Figure 7-1). The thickness of the thin solid element was set to 2 mm, which gives an aspect ratio of 500 for the element. The material parameters were assigned the following values: β=50°, q_u=1 MPa, and κ=0.78. The modeled fracture (i.e., interface between the sliding and restrained blocks) was assigned an initial aperture of 0.2 mm. The dilation angle, ψ, was assigned values from a shear-displacement-dependent function, as shown in Figure 7-4. The curve labeled "Low dilation" in the figure was calculated from a laboratory data set in Hsiung et al. (1994b); each of the other two curves was obtained by increasing the dilation values of the first curve by a constant factor. An analysis was conducted using each of the three curves, in order to examine the effects of dilation angle on the calculated mechanical effects on fracture permeability.

The dilation angle versus shear displacement relations were specified in the ABAQUS input files using the *FIELD command. Using this command, an arbitrary field variable was specified, the value of which varied from 0 to 40 at every interface node during the shear-displacement analysis step; the values of dilation angle for the thin solid element were specified as functions of the field variable, using the curves presented in Figure 7-4. This method of specifying the dilation function would be successful only for situations, such as the example problems, in which the values of shear displacement are known *a priori*. In order to specify dilation functions (such as those in Figure 7-4) in a general analysis, the capability is

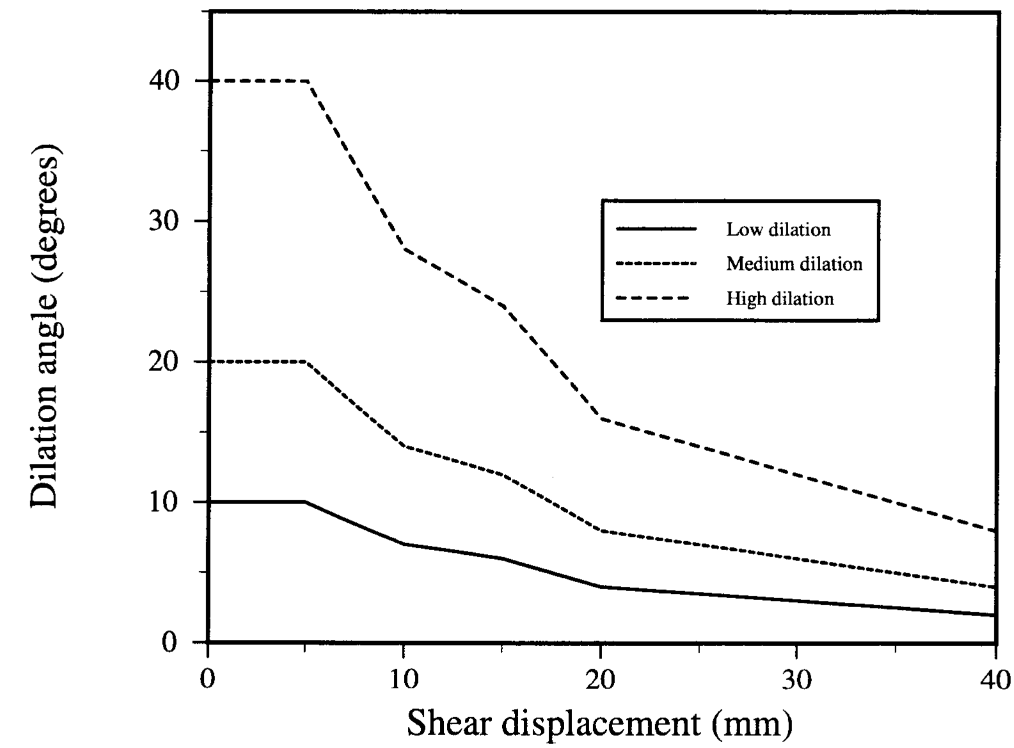

Figure 7-4. Dilation angle versus shear displacement relations used in the example problems

required to relate the values of dilation angles to the magnitudes of shear strain (cf. Ofoegbu and Curran, 1992). Such a capability may be implemented in ABAQUS in one of the following ways:

(i) Through a modification of one or more of the constitutive models that use dilation angle, to make provisions for strain-dependent dilation. Such a modification may be effected only by the developers of the code.

(ii) Through a user-subroutine interface dedicated to the description of dilation. The development of such an interface can be effected only by the developers.

(iii) Through the development of a user-material subroutine, using the UMAT interface that is currently available in ABAQUS. This option would allow the user to exercise complete control of the constitutive behavior of the elements to which it is applied.

The results of the numerical-model example are presented in Figures 7-5 through 7-7. Figure 7-5 shows the calculated average shear stress as a function of the applied shear displacement. The decrease in shear strength with increasing shear displacement was caused by the fact that the β-versus-ϕ relationship varies with dilation angle, as explained earlier (see 7-5 and 7-6). Although β was assigned a constant value of 50°, the values of ψ and, hence, ψ/β, decreased during each analysis as shown in Figure 7-4. Therefore, the values of ϕ decreased accordingly, which caused the shear strength to decrease as shown in Figure 7-5, the effect being more pronounced at larger values of the dilation angle.

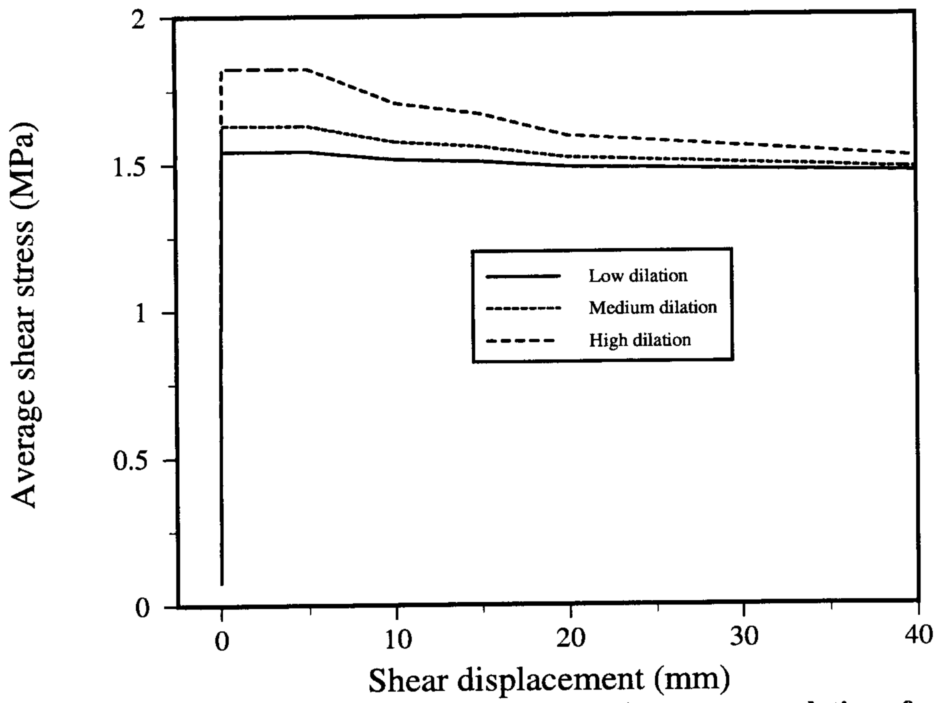

Figure 7-5. Calculated shear stress versus shear displacement relations for a rock interface under normal stress of 2 MPa based on a thin solid model

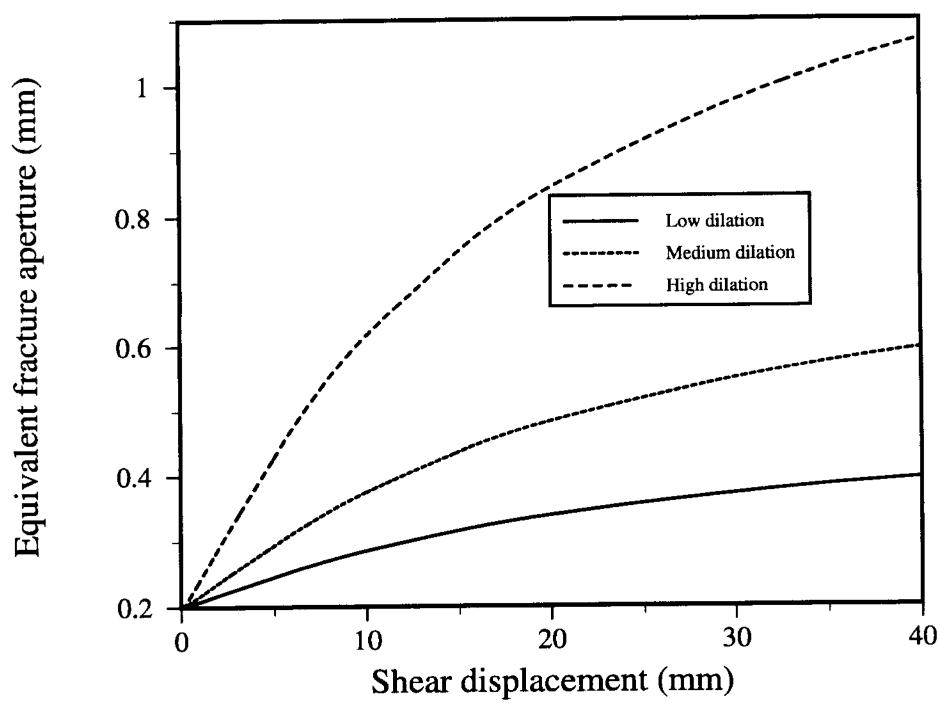

Figure 7-6. Calculated aperture versus shear displacement relations for a rock interface under normal stress of 2 MPa based on a thin solid model

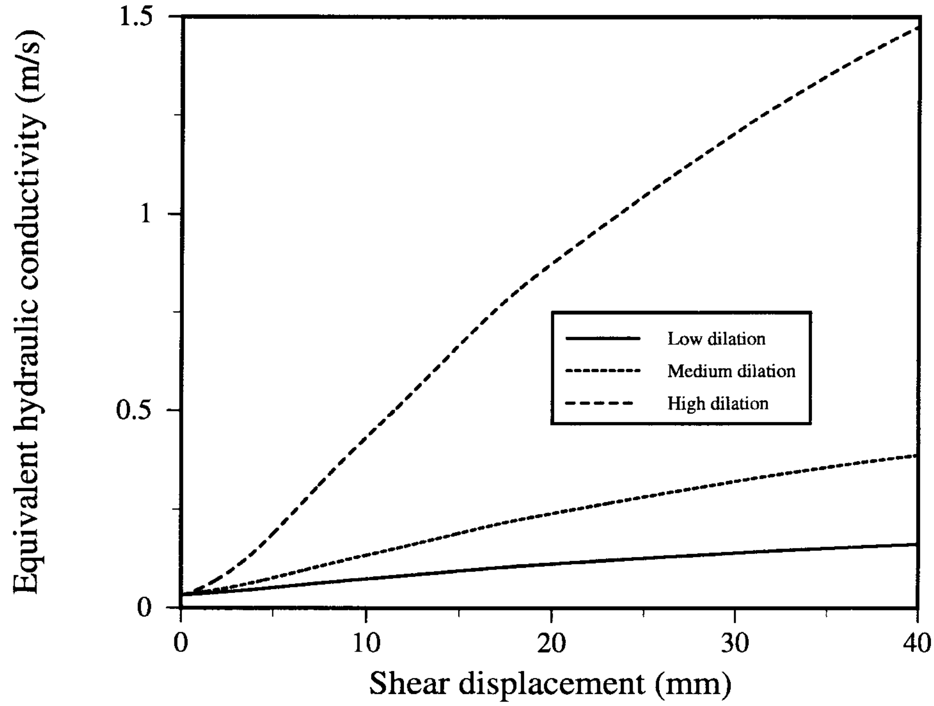

Figure 7-7. Calculated hydraulic conductivity versus shear displacement relations for a rock interface under normal stress of 2 MPa based on a thin solid model

Figures 7-6 and 7-7, show the values of fracture aperture and hydraulic conductivity, respectively, calculated using (7-1) and (7-2). The figures show that the calculated mechanical effects on fracture permeability vary with the dilation angle. The specific values of hydraulic conductivity presented in Figure 7-7 depend on the specified initial aperture of 0.2 mm, as well as on the magnitude of shear displacement applied to the modeled interface.

7.5 INTERSECTING JOINTS

The problem of intersecting joints (Section 2.5) was modeled again, to examine the performance of the thin solid elements for modeling joint intersections. The geometry of the problem is illustrated in Figure 2-12; also, Figure 2-13 illustrates the response calculated by modeling the joints (contact between the blocks) using interface elements. Figure 7-8 illustrates the finite element mesh used to model the problem, with the joints modeled using thin solid elements. Blocks B1, B2, B3, and B4, each 1 m by 1 m, were modeled as linear elastic materials (Young's modulus of 3.25×10^4 MPa, and Poisson's ratio of 0.25). The (1-m long) contact between each pair of blocks was modeled using 10 thin solid elements, each 10 cm long and 0.2 cm thick, connected end to end. Therefore, each of the thin solid elements has an aspect ratio of 50; on the other hand, each of the thin-solid zones (array of 10 thin solid elements) representing the block-to-block contacts has an aspect ratio of 500. The corner-to-corner contact of the blocks is represented by the intersection of the 4 thin-solid zones, which consists of a 0.2 cm by 0.2 cm element. The thin-solid zones were modeled as elastic-plastic materials, using the Drucker-Prager material model (with constant Drucker-Prager friction and dilation angles of 50° and 40°, respectively).

Blocks B1, B2, and B3 were restrained as illustrated in Figure 2-12, and equal magnitudes of rightward and upward displacements were applied on the left and bottom boundaries, respectively, of block B4. The analysis terminated after 0.26 mm of such boundary displacements (which corresponds to a diagonally upward displacement of about 0.37 mm at the bottom-left corner of block B4). The distributions of maximum and minimum principal compressive stresses developed in the model are shown in Figures 7-9 and 7-10. The nature of the stress distributions is consistent with compression in the direction of the applied displacement (i.e., along the right-upward diagonals of B4 and B2), and extension in the perpendicular direction (i.e., along the left-upward diagonals of B1 and B3). Such distributions of extension and compression indicate that the corner-to-corner contact of blocks B4 and B2 was being compressed in the model. The deformed shape of the corner-to-corner contact of the two blocks is shown in Figure 7-11, which was obtained by enlarging the center of the model (see Figures 7-9 and 7-10). Such a deformed shape is consistent with the compression of the contacting block corners in the direction of the applied displacement, and extension of the contact in the perpendicular direction.

7.6 CONCLUSIONS

The use of thin solid continuum elements to model the MH responses of rock fractures was examined in this chapter, with special attention on the effects of the aspect ratio of such elements on their mechanical response. It was determined that the amount of inelastic volumetric strain experienced by the thin solid elements is essentially unaffected by their aspect ratio. As a result, it is possible to relate mechanically induced changes in fracture permeability to the deformation of the thin solid elements through their inelastic volumetric strain. It was also determined that the shear strength of rock interfaces calculated using thin solid elements is independent of the aspect ratio of the individual elements; on the other hand, the calculated strength is sensitive to the aspect ratio of the entire weakness zone representing the fracture, for values of such ratio smaller than about 250. However, such elements are likely to underestimate the shear strength because of differences between the Drucker-Prager failure criterion (applied to the solid elements) and the Mohr-Coulomb failure criterion (applied to the interface).

Based on this examination of the thin solid elements, it was determined that the following changes would be necessary in ABAQUS in order to improve the capabilities of such elements for modeling the MH responses of rock fractures:

(i) It is necessary to implement a constitutive model for the elements based on the Mohr-Coulomb failure criterion (cf. Zienkiewicz and Humpheson, 1977). The problem of the interface shear strength being underestimated by the solid elements is likely to be corrected by using such a constitutive model. An implementation of the model can be effected through the UMAT user-subroutine interface currently available in ABAQUS (cf. Ofoegbu and Curran, 1992).

(ii) It is also necessary to implement a constitutive model for the solid elements to provide for the description of their friction and dilation angles as functions of inelastic shear strain. Such a model would best be implemented through the UMAT interface.

(iii) In order to conduct fully coupled MH analyses using the solid elements, it would be necessary to implement a model that enables the specification of their permeability as a function of their inelastic strain. The user-interface required for the implementation of such a model is currently not available in ABAQUS.

(iv) A model is also required to enable the solid elements to simulate the response of fractures under normal loading.

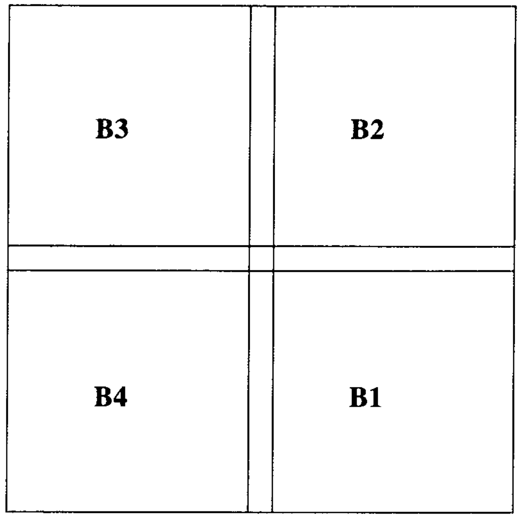

Figure 7-8. Schematic illustration of finite element mesh used to model the intersecting-joints problem (Section 2.5, Figure 2-12), with joints modeled as thin solids

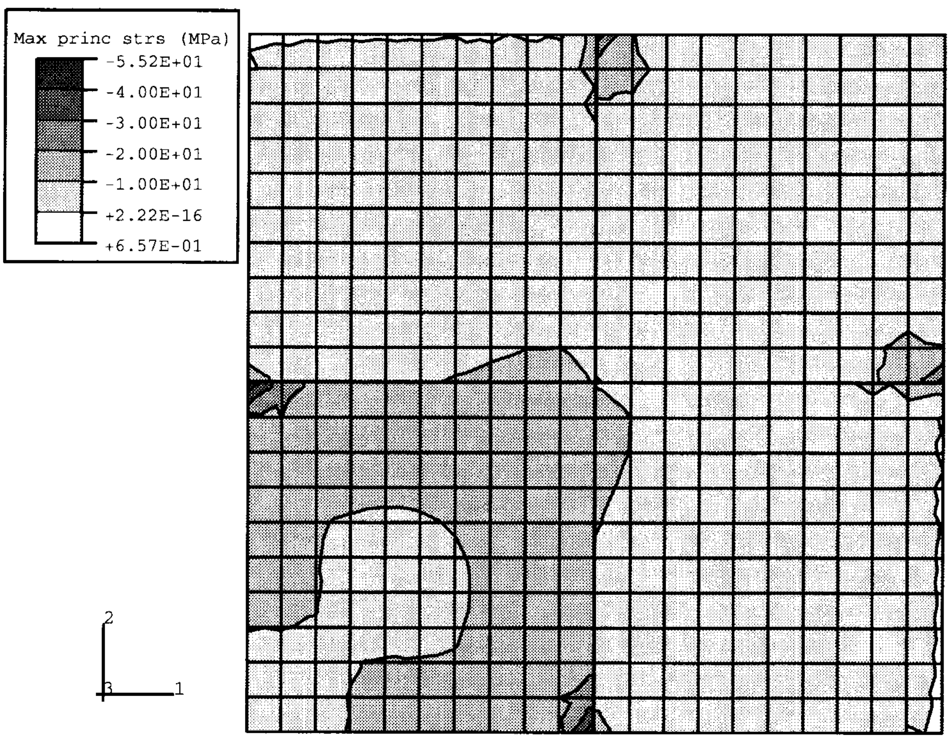

Figure 7-9. Distribution of maximum principal compressive stress calculated for the contacting blocks, with contacts modeled as thin solids

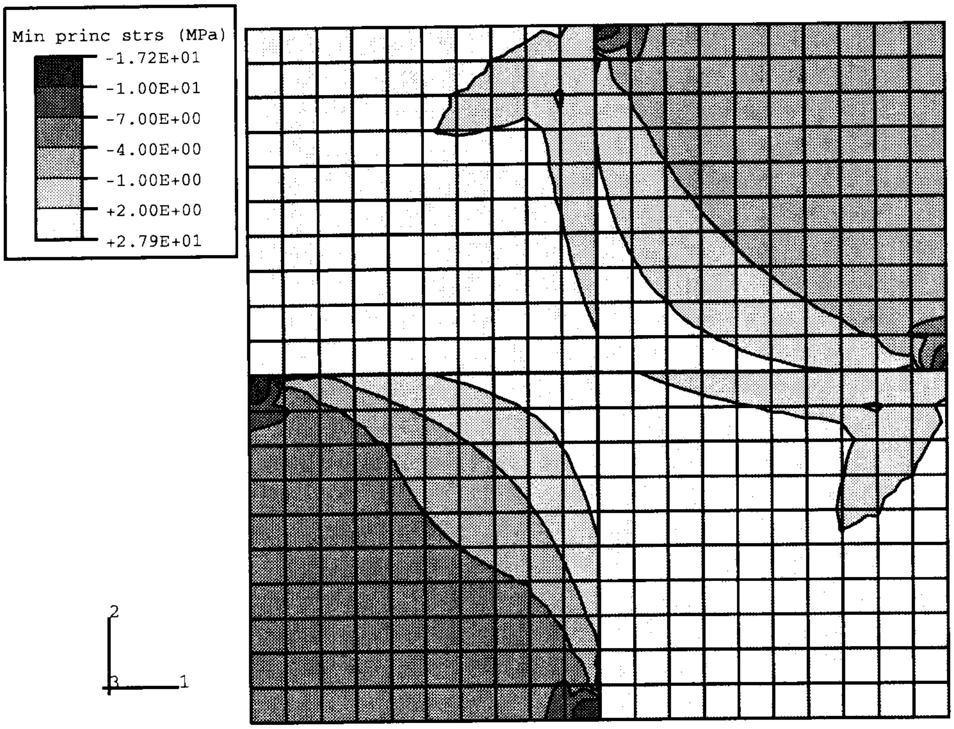

Figure 7-10. Distribution of minimum principal compressive stress calculated for the contacting blocks, with contacts modeled as thin solids

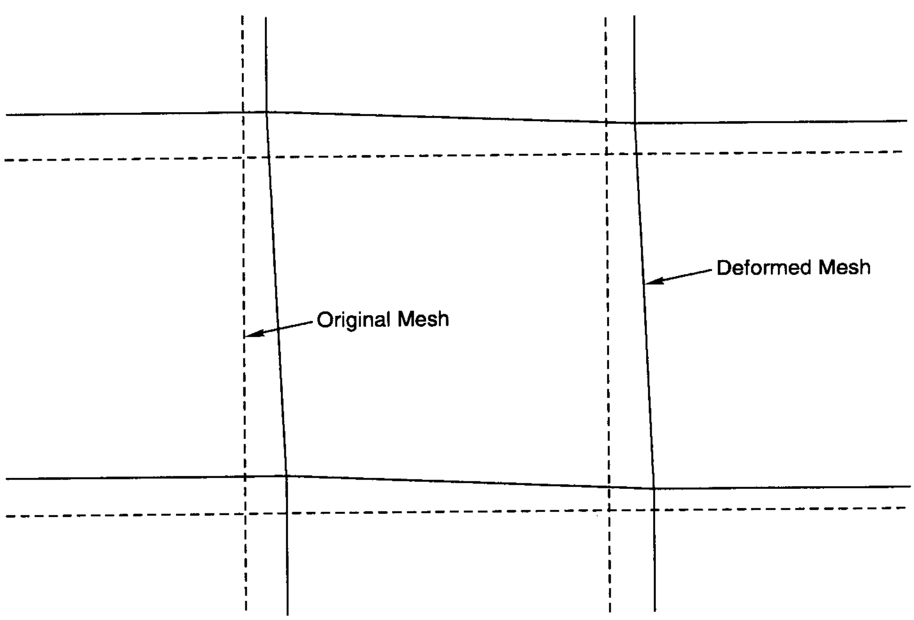

Figure 7-11. Deformed shape of the contacting block corners calculated using thin solid elements for the interfaces

8 THERMAL-MECHANICAL-HYDROLOGICAL PROBLEM: BIG-BEN EXPERIMENT

The Big-Ben Experiment was designed to evaluate the EBS for the current Japanese radioactive waste disposal concept. The experiment was conducted under the auspices of DECOVALEX by the Japanese team. Its objectives were to develop better understanding of the heat transfer, water absorption, and swelling behavior in an EBS for underground disposal of HLW, and to evaluate the capability of mathematical models to predict the observed phenomena. In addition to the experimental measurements conducted by the Japanese, the Big-Ben Experiment was modeled numerically by three separate DECOVALEX research teams. These teams included the NRC-funded research team (CNWRA), the Japanese Power Reactor and Nuclear Fuel Development Corporation-funded research team from Kyoto University (KPH), and the Swedish Nuclear Fuel and Waste Management Company-funded research team (Clay Technology AB). Both the CNWRA and Clay Technology teams used ABAQUS for the modeling exercise. The Japanese KPH team used its 3D finite element code THAMES (Ohnishi et al., 1985). A detailed description of the problem and comparison of the experimental and numerical-model results have been provided in a separate report (Ahola et al., 1994).

8.1 PROBLEM DESCRIPTION

The experimental EBS is composed of an electric heater, carbon steel overpack, buffer material, and concrete containment simulating the surrounding host rock. The reinforced concrete containment has an outside diameter of 6 m and is 5 m in height. A borehole, approximately 1.7 m in diameter and 4.5 m in depth, is located in the center of the concrete. An electric heater with several cartridge heaters, all set in a carbon steel overpack, which is about 1 m in diameter and about 2 m in height, was placed in the borehole. A buffer material was packed between the overpack and concrete containment. This particular experiment consisted of uniform heating as well as water injection under constant pressure into the partially saturated buffer.

Figure 8-1 shows a view of the buffer material region. The buffer itself is composed of a mixture of 70 percent bentonite and 30 percent quartz sand. It is partially saturated, having an initial saturation of approximately 0.63 (i.e., 63 percent). Around the inner and outer edges of the bentonite lie two thin, highly permeable quartz sand layers a few centimeters thick. During the experiment, water was injected through a tube directly into the outer quartz sand layer at a constant pressure of 50 kPa throughout a 5-mo period to simulate water flowing in from the surface of the borehole through a fracture. Over this same 5-mo period, the heater was operated at a constant power output of 0.8 kW. The TMH coupling effects thus consisted of water being imbibed into the buffer material, creating an increase in saturation and swelling of the buffer material. In addition, the heating caused thermal expansion within the different engineered materials, and created some vapor-driven moisture flow outward, thus desaturating the inner portions of the buffer material. During the experiment, periodic measurements of temperatures, strains, water content, and swelling pressures were taken.

8.2 RESULTS

Figure 8-2 shows the temperature distribution at three different elevations within the buffer as measured experimentally and calculated numerically by the different modeling teams after a period of 5 mo (i.e., end of the experiment). The figure shows that both the CNWRA and Clay Technology results obtained using ABAQUS agree very well with the experimental measurements. The KPH research team

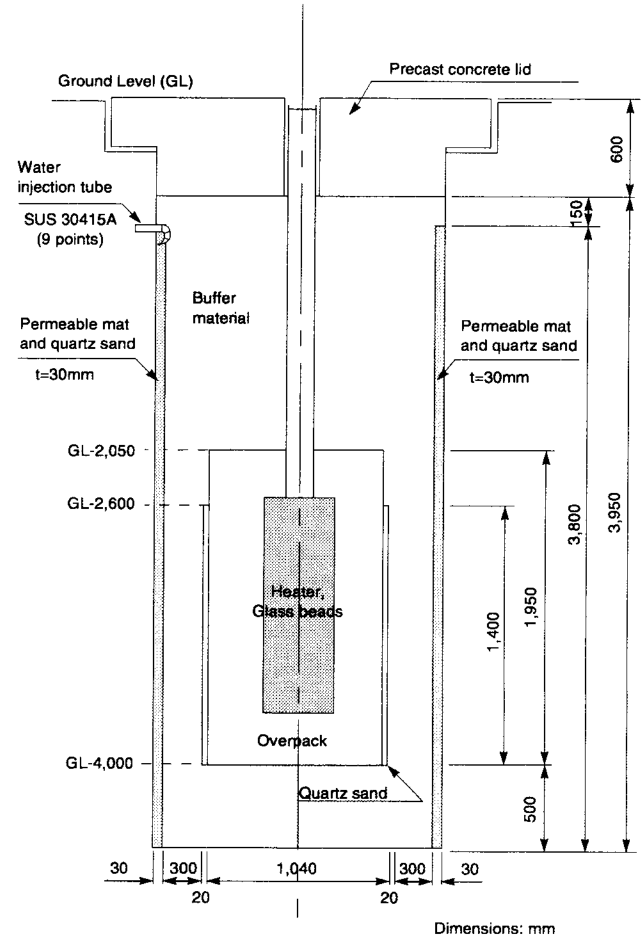

Figure 8-1. Schematic view of the buffer region of the Big-Ben experiment (Ahola et al., 1994)

results using THAMES somewhat underestimated the experimental measurements of temperature throughout the buffer. Some slight discrepancies in the calculated results are likely because certain boundary condition and material property uncertainties required varying assumptions to be made by the different teams.

The distribution of water content after 5 mo is shown in Figure 8-3 at the same three elevations within the buffer. In portions of the buffer, for example above the heater and to some extent along the heater midplane, the computed results agree well with the experimental measurements of water content. Near the base of the heater, all three computed results underestimate the water content, especially toward the outer region of the buffer. The experimental measurements along the midplane and base profiles (G.L.–3.0 m and G.L.–4.0 m, respectively, where G.L. stands for ground level) show that the water content of the buffer decreased below the initial value of 16 percent near the heater. This decrease in water content is believed to be associated with either the gas-phase transport of water vapor or the expansion of air, or both. Because thermal expansion of water is the only thermal effect on water transport accounted for by the ABAQUS model, the code is currently unable to predict such a decrease in water content. The Clay Technology team developed a vapor-phase transport model specifically for this problem, which they used to modify results computed using ABAQUS (Börgesson and Hernelind, 1994). Consequently, the results calculated by the CNWRA deviate from those calculated by Clay Technology near the innermost portion

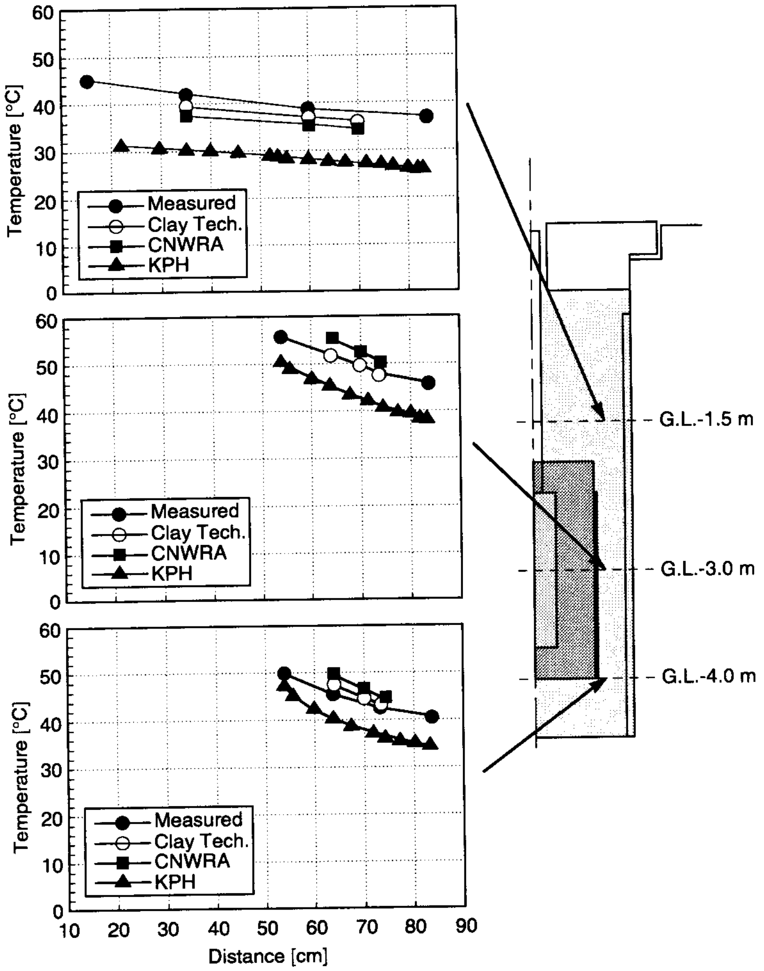

Figure 8-2. Distributions of temperature after 5 months (Ahola et al., 1994)

of the buffer. The Clay Technology results appear to account for the effects of vapor-phase transport, which are not accounted for in the CNWRA results. The values of water content obtained by Clay Technology along these two lower elevations in the buffer track the experimentally measured values better than the CNWRA results. The THAMES code is also able to account for the heat and moisture flow in the vapor, and the results obtained by the KPH team agree well with the Clay Technology results. However, the water content at the innermost calculation point near the heater is somewhat underestimated.

The calculated distributions of radial (total) stress within the bentonite are shown in Figure 8-4. There is a considerable discrepancy between the CNWRA results and those obtained by both KPH and Clay Technology. This discrepancy is related to the calculation of effective stresses in unsatured soil or rock media. The method used in ABAQUS is described in the ABAQUS theory manual (Hibbit, Karlsson, and Sorensen, Inc., 1994), and is based on the following equation, originally proposed by Bishop (1960):

$$\sigma' = \sigma + \chi u_w + (1 - \chi) u_a \tag{8-1}$$

where σ' is the effective stress, σ is the total stress, u_w is the water pressure, u_a is the air pressure, and χ is a parameter that depends on the degree of saturation (tensile stress is positive in this equation). There is little experimental data available for the parameter χ and, as a result, its value is assumed to be equal to the degree of saturation in the ABAQUS code. This assumption is likely to be justified for values of saturation

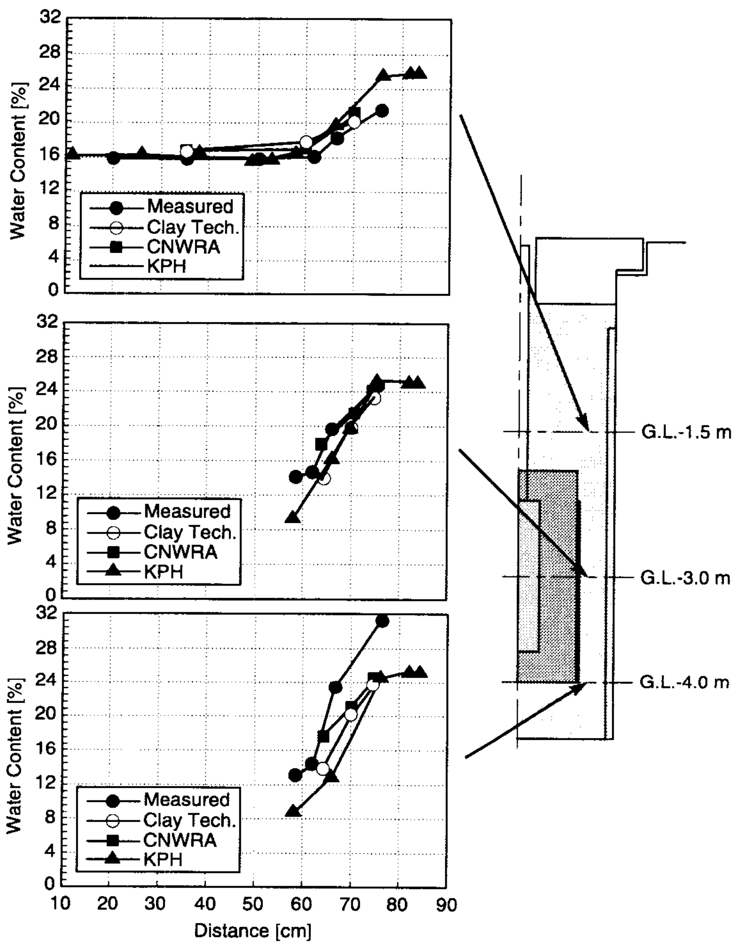

Figure 8-3. Distributions of water content after 5 months (Ahola et al., 1994)

close to 1, but is likely to cause overestimation of the contributions of pore-fluid pressure to stress for most unsaturated conditions. Although it is clear that χ=1 for saturated conditions and χ=0 for dry conditions, their is unresolved uncertainty regarding the values of χ for intermediate values of saturation (cf. Mitchell, 1976).

The large (and most probably unrealistic) values of stress calculated by the CNWRA were caused by the assumption in ABAQUS that χ is equal to the degree of saturation. The values of suction (negative water pressure) provided by the Japanese team for the saturation conditions of the buffer material were very high. These high values of suction, applied in Eq. (8-1), lead to high values of stress in the buffer, as the CNWRA results show (Figure 8-4). On the other hand, the version of THAMES used for the analysis does not account for the contributions of fluid suction in the mechanical equilibrium equations; as a result, the maximum stress calculated using the THAMES code is only a few tenths of a megapascal. Although the Clay Technology team used ABAQUS, they opted to use much smaller values of fluid suction in the moisture-retention curve for the buffer than those provided to the CNWRA team. Their choice of the smaller values was based on their own laboratory measurements for the buffer material.

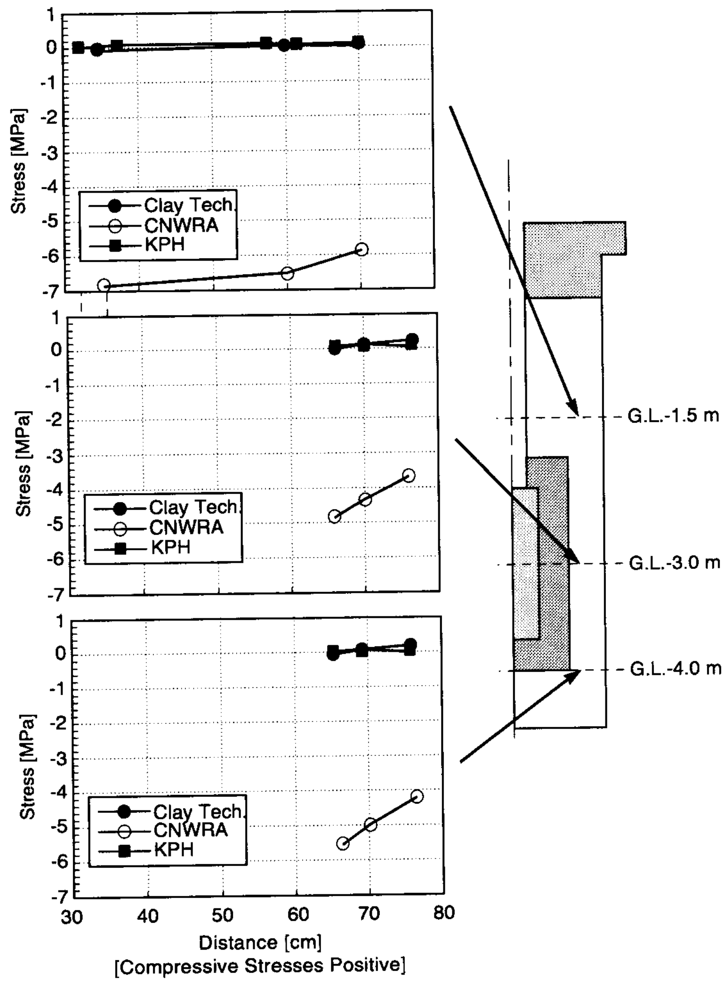

Figure 8-4. Distributions of radial stress after 5 months (Ahola et al., 1994)

Experimental measurements of stress were only available from a few pressure cells attached to the concrete on the outermost edge of the buffer. The pressure cell mounted to the concrete along the midplane elevation of the heater (i.e., G.L.-3.0 m in Figure 8-4) measured approximately 0.4 MPa radial stress at the end of 5 mo. The KPH and Clay Technology results in the center plot in Figure 8-4 appear to agree more closely with the experimentally measured stress than the CNWRA results.

8.3 CONCLUSIONS

The capabilities of ABAQUS to model a coupled TMH problem was examined in this chapter. The histories of temperature, water content, and stress calculated using ABAQUS were compared with those calculated using other codes, as well as with laboratory data. The code was able to predict water-content increases due to the thermal expansion of water, but was unable to predict decreases of water content that may have been caused by evaporation or gas expansion or both. It is believed that the inability of ABAQUS to predict these drying effects is because the fluid flow model in the code does not recognize the simultaneous flow of water and gas (such as water vapor) and evaporation and condensation.

9 CONCLUSIONS

The finite element code ABAQUS was evaluated to assess its suitability for conducting analyses related to the evaluation of DOE compliance with NRC regulations on the design of the proposed YM nuclear waste repository. Specifically, the code was evaluated to determine its capabilities to conduct analyses related to the assessment of thermal-mechanical effects on near-field fluid flow. If the code is found suitable, it may be used to conduct analyses to determine the following:

(i) Effects of thermally induced mechanical deformation on rock-mass permeability, including changes in both matrix and fracture permeability and fracture connectivity

(ii) Effects of matrix imbibition, vapor flow, including evaporation and condensation, on fluid flow through fracture network, especially through preferential flow path(s)

(iii) Effects of deterioration of rock strength due to creep, chemical alterations of fracture-wall rock, or both

(iv) The cumulative effects of repetitive episodes of seismic disturbance on near-field fluid flow

(v) Thermal-hydrological effects on rock supports

A number of pertinent benchmark problems were developed to facilitate the evaluation of ABAQUS. In all the benchmark problems, major focus was given to modeling rock fractures as distinct entities. In many problems, two different approaches were taken to simulate a joint or a rough fracture: (i) using interface elements and (ii) using thin solid elements (regular quadrilateral elements with an aspect ratio greater than 250). The benchmark problems that dealt with individual and coupled thermal, mechanical, and hydrological processes included: (i) simulation of mechanical response of a single fracture under pseudostatic and dynamic loads, (ii) simulation of the response of intersecting fractures under mechanical load, (iii) simulation of thermally-induced stress field in fractured rock, (iv) simulation of fluid flow through matrix and fractures under saturated and partially saturated conditions (saturated case was treated as the first step before undertaking analysis of partially saturated case), (v) simulation of thermal and mechanically induced stress and deformation fields, (vi) simulation of thermal and hydrological responses from a cylindrical heat source in a saturated and a partially saturated media, (vii) simulation of the effects on fluid flow through fractures by the change in fracture aperture due to mechanical stress field, and (viii) simulation of the Big-Ben experiment involving coupled TMH processes. The performance of ABAQUS was evaluated by comparing its computed responses with the analytical solutions for the same problems. Where there is no known analytical solution available, results computed using ABAQUS were compared with those computed using other codes. For one problem set, the ABAQUS results were compared with field-test results.

9.1 SUMMARY OF OBSERVATIONS

The performance of ABAQUS was judged to be satisfactory for many of the problems solved, but unsatisfactory for others. The following observations regarding the performance of the code are based on the results of the evaluation exercise.

(i) Interface elements of ABAQUS could simulate the response of a single fracture under pseudostatic and dynamic loads (Chapter 2). However, these elements cannot model intersecting fractures. Both single and intersecting fractures may be modeled using solid elements provided that the zone of weakness that represents each fracture has an aspect ratio of 250 or more.

(ii) ABAQUS simulates the normal stiffness of a fracture in the interface elements through an internally generated exponential pressure versus aperture function based on two user-supplied parameters: (a) maximum aperture at zero normal stress and (b) maximum normal stress necessary to close the fracture completely. However, this exponential function may not always be appropriate.

(iii) Interface elements of ABAQUS cannot simulate the dilation of a fracture undergoing shear displacement since the only rock joint model available is the Coulomb law, which lacks the mechanism to simulate shear-induced dilation.

(iv) ABAQUS could simulate conductive heat flow in a fractured rock mass. Results of the benchmark problem (Chapter 3) show that ABAQUS produced acceptable results in terms of the distribution of temperature, stresses, and deformations, including areas surrounding rock fractures. ABAQUS has a provision to specify thermal conductivities of fractures correlating with the change of aperture or normal stress.

(v) ABAQUS could simulate the isothermal flow of water through rock matrix in both saturated and partially saturated cases. Both the interface and thin solid elements could model water flow through a fracture under saturated conditions. Flow through fractures in partially saturated media can only be modeled using thin solid elements. Because the fluid-flow constitutive model for the interface elements does not incorporate the moisture-retention behavior of fractures, such elements do not simulate fracture-flow satisfactorily under unsaturated conditions. On the other hand, significant differences were observed between the rates of fracture flow calculated using ABAQUS and CTOUGH. This difference in the calculated rates of fracture flow appears to be caused by differences in the effects of matrix imbibition based on the simulations in the two codes. That is, fracture flow is slowed down by matrix imbibition more in CTOUGH than in ABAQUS.

(vi) ABAQUS could simulate thermally induced water flow in a saturated medium for situations in which the contribution of convective heat flow can be ignored. Results calculated using ABAQUS compared well with the analytical solution for a cylindrical heat source embedded in a saturated medium. However, only conductive heat flow was considered in the analytical solution.

(vii) Results calculated using ABAQUS for the problem of a cylindrical heat source in a partially saturated medium differ significantly from those calculated using CTOUGH. The ABAQUS results showed progressive increase in both pore pressure and saturation from the center of the heat source due to thermal expansion of water. On the other hand, the CTOUGH results showed a decrease in saturation within the boundary of the heat source and an increase in saturation in the outside region. The decrease in saturation within the boundary of the heat source was attributed to the thermal expansion of gas (water driven away by the expanding gas) or evaporation. A similar drying effect was observed in the Big-Ben experiment (Chapter 8). ABAQUS is unable to simulate such drying effects because the fluid-flow model in the code does not account for the simultaneous flow of two fluid phases, such as water and gas.

9.2 POTENTIAL OPTIONS FOR MODIFICATION OF ABAQUS CODE

As discussed in Chapter 1, the purpose for the evaluation of ABAQUS is to identify its capabilities and modifications necessary to model thermal-mechanical effects on the hydrological response of a fractured rock mass. The capabilities to model rock fractures as distinct entities are of particular interest. The following options to modifying the ABAQUS code have been identified, based on the current examination of its TMH modeling capabilities.

9.2.1 Modeling of Discrete Fractures

In this study, two different approaches were investigated to model the response of a joint or fracture: (i) using interface elements and (ii) using thin solid elements. Both approaches need some modifications to the ABAQUS code in order to model satisfactorily the thermal-mechanical effects on near-field fluid flow.

9.2.1.1 Fractures Modeled Using Interface Elements

When the fractures are modeled using interface elements, the code simulates the normal stiffness of fractures through an internally generated exponential pressure versus aperture function based on two user-supplied parameters. Such an exponential function may not always be appropriate. Therefore, it would be better to provide for a user-specified pressure versus aperture relationship through a table. Alternatively, a provision should be developed to input the normal stiffness directly, including its variation with the applied normal stress (e.g., similar to the provision available in UDEC).

A new constitutive model for simulating the shear response of rock joints is required for the interface elements in order to simulate shear-induced dilation. The currently available constitutive model for the interface elements does not model the dilation behavior of rough joints.

It is not feasible[1] to modify the interface elements to incorporate capabilities to model intersecting fractures.

The fluid-flow constitutive model for the interface elements needs to be modified to account for the moisture-retention behavior of fractures, in order to use such elements to simulate fracture-flow under unsaturated conditions.

---

[1] Personal communication with a representative of Hibbitt, Karlsson & Sorensen, Inc., Pawtucket, Rhode Island, 1993.

9.2.1.2 Fractures Modeled Using Thin Solid Elements

It is necessary to develop the capability to specify the friction and dilation angles for solid elements as a function of their inelastic strain. This capability is required in the computation of mechanical effects on fracture permeability using thin solid elements. Currently the friction and dilation angles for such elements may be specified either as constants or as functions of temperature or a user-defined field variable. For example, for the problems solved in Chapter 7, the dilation angle was specified as a function of a field variable that was set equal to the applied shear displacement. This procedure of specifying the dilation angle was successful for the problem because the inelastic shear strain developed in the thin solid element was proportional to the applied shear displacement, which was known *a priori*. The same procedure would be difficult to apply in a general problem, for which the values of inelastic strain are not known prior to conducting the analysis. For such problems, the use of thin solid elements to compute mechanical effects on fracture permeability requires the capability to update the value of their friction and dilation angles internally (i.e., within the code) as functions of the inelastic strain developed in the elements.

Such a capability may be implemented in ABAQUS through: (i) a modification of one of the existing constitutive models that use friction and dilation angles, (ii) the development of a user-subroutine interface for the specification of friction and dilation angles, or (iii) the development of a user-material subroutine (using the UMAT interface). The first two approaches require access to the ABAQUS source code, but the third does not. Furthermore, the development of a user-material subroutine for thin solid elements has the added advantage that it would enable the implementation of a Mohr-Coulomb-based strength criterion for such elements. Based on results presented in Chapter 7, it is suggested that a Mohr-Coulomb-based failure criterion for such elements would be more appropriate than the Drucker-Prager criterion for the simulation of the shear strength of rock interfaces. An additional benefit of implementing a new material subroutine for solid elements is that it would enable the implementation of a model for simulating the normal-load response of joints using such elements.

The modifications proposed in the foregoing paragraphs would be sufficient to use the thin solid elements for the computation of thermal-mechanical effects on permeability, to generate permeability histories that may be applied as input into separate thermal-hydrological analyses.

To use thin solid elements for coupled MH analyses in which possible mechanical effects on permeability are accounted for internally (within the code), it would be necessary to develop the capability to update the permeability of such elements as a function of their deformation history. At the present time, the permeability history computed in a given analysis, using the procedure described in Chapter 7 for example, cannot be used to compute hydrological response in the same analysis. It may, however, be used as input for a separate hydrological analysis. There is currently no user-interface in ABAQUS that would enable user-implementation of the internal updating of the permeability of solid elements as a function of their deformation history.

9.3 RECOMMENDED CHANGES TO THE ABAQUS CODE

Two alternative approaches for the use of ABAQUS in TMH modeling were considered. The first approach is based on modeling fractures with interface elements. This approach was rejected because of the following reasons:

(i) The ABAQUS interface elements cannot model intersecting fractures, and it is not feasible to modify the code to correct this deficiency.

(ii) In order to evaluate mechanical effects on permeability using the interface elements, the constitutive model for such elements would have to be modified to account for shear-induced dilation. The current formulation of the interface elements does not make any provision for such a modification.

(iii) Furthermore, a modification of the fluid-flow constitutive model for the interface elements to account for the moisture-retention behavior of fractures would be required in order to use the elements for modeling unsaturated fracture flow. Such a modification is also not feasible.

The recommended approach for the use of ABAQUS in TMH analyses is based on the thin-solid model of fractures. Such a model may be used to simulate the thermal, mechanical, and hydrologic responses of individual fractures, as well as a limited number of intersecting fractures. The approach for using the thin-solid model in coupled TMH analyses will be developed in up to three steps, as follows:

- The first step is to develop an ABAQUS implementation (through the UMAT user-subroutine interface) of a Mohr-Coulomb-based material model for solid elements, with provisions for strain-dependent dilation and friction angles. The resulting model would be used to conduct a study on the effects of thermally induced mechanical deformations on fracture permeability. If such a study should lead to the conclusion that thermally induced mechanical effects on fluid flow can be simulated satisfactorily through separate TM and TH analyses, then the use of ABAQUS in TMH modeling would be limited to the computation of permeabilities. In that case, a separate code would be used for TH modeling, using the ABAQUS-computed permeabilities as input.

- A second step would be necessary if the investigations of thermally induced mechanical effects on rock mass permeability lead to the conclusion that TH analyses need to be fully coupled with mechanical analyses in order to account satisfactorily for the mechanical effects on fluid flow. In that case, ABAQUS would be recommended as a stand-alone code for coupled TMH analyses. For situations in which the effects of vapor flow may be ignored, it would be sufficient to develop a code that provides for the specification of the permeability of solid elements as a function of their mechanical deformation. Such a code would be linked with ABAQUS through a user-subroutine interface that the ABAQUS developer would be requested to provide.

- A third step would be required to enable the use of ABAQUS for TMH modeling under situations in which the contributions of vapor flow cannot be ignored. The use of ABAQUS in this capacity would require the development of a separate code that would provide for the effects of vapor flow to be expressed in terms of distributions of volumetric source strengths. The results of such a code would be applied to provide input of temperature-dependent water sources and sinks for ABAQUS fluid-flow analyses. This use of ABAQUS would require a modification of its fluid-flow model to account for volumetric sources, as well as the modification of the DFLOW user-subroutine interface to enable the specification of temperature-dependent source strength.

10 REFERENCES

Ababou, R., and A.C. Bagtzoglou. 1993. *BIGFLOW: A Numerical Code for Simulating Flow in Variably Saturated, Heterogeneous Geologic Media.* CNWRA 92-026. San Antonio, TX: Center for Nuclear Waste Regulatory Analyses.

Ahola, M.P., S.M. Hsiung, L.J. Lorig, and A.H. Chowdhury. 1992. *Thermo-Hydro-Mechanical Coupled Modeling: Multiple Fracture Model, BMT2; Coupled Stress-Flow Model, TC1. DECOVALEX — Phase I.* CNWRA 92-005. San Antonio, TX: Center for Nuclear Waste Regulatory Analyses.

Ahola, M.P., L.J. Lorig, A.H. Chowdhury, and S.M. Hsiung. 1993. *Thermo-Hydro-Mechanical Coupled Modeling: Near-Field Repository Model, BMT3. DECOVALEX — Phase II.* CNWRA 93-002. San Antonio, TX: Center for Nuclear Waste Regulatory Analyses.

Ahola, M.P., G.I. Ofoegbu, A.H. Chowdhury, and S.M. Hsiung. 1994. *Thermo-Hydro-Mechanical Coupled Modeling: Big-Ben Experiment, TC3. DECOVALEX — Phase III.* CNWRA 94-021. San Antonio, TX: Center for Nuclear Waste Regulatory Analyses.

Althaus, E., A. Friz-Topfer, C. Lempp, and O. Natau. 1994. Effects of water on strength and failure mode of coarse-grained granites at 300°C. *Rock Mechanics and Rock Engineering* 27: 1–21.

Bagtzoglou, A.C., and M. Muller. 1994. *Stochastic Analysis of Large-Scale Unsaturated Flow and Transport in Layered, Heterogeneous Media.* CNWRA 94–012. San Antonio, TX: Center For Nuclear Waste Regulatory Analyses.

Bishop, A.W. 1960. *The Principle of Effective Stress.* Publication No. 32. Oslo, Norway: Norwegian Geotechnical Institute.

Boley, B.A., and J.H. Weiner. 1960. *Theory of Thermal Stresses.* London, UK: John Wiley and Sons.

Booker, J.R., and C. Savvidou. 1985. Consolidation around a point heat source. *International Journal for Numerical and Analytical Methods in Geomechanics* 9: 173–184.

Börgesson, L., and J. Hernelind. 1994. *Calculation of Test Case 3—Big Ben Experiment.* DECOVALEX Phase III. Draft Report. Lund, Sweden: Clay Technology AB.

Brady, B.H.G., M.L. Cramer, and R.D. Hart. 1985. Preliminary analysis of a loading test on a large basalt block. *International Journal of Rock Mechanics and Mining Sciences & Geomechanics Abstracts* 22: 345–348.

Brady, B.H.G., and E.T. Brown. 1985. *Rock Mechanics for Underground Mining.* London, UK: George Allen & Unwin Ltd.

Brady, B.H.G., S.M. Hsiung, and A.H. Chowdhury. 1990. *Qualification Studies on the Distinct Element Code UDEC Against Some Benchmark Analytical Problems.* CNWRA 90-004. San Antonio, TX: Center for Nuclear Waste Regulatory Analyses.

Buscheck, T.A., and J.J. Nitao. 1993. Repository-heat-driven hydrothermal flow at Yucca Mountain, Part I: Modeling and analysis. *Nuclear Technology* 104: 481–448.

Carslaw, H.S., and J.C. Jaeger. 1959. *Conduction of Heat in Solids.* Oxford, UK: Oxford University Press.

Day, S.M. 1985. Test Problem for Plane Strain Block Motion Codes. S-Cubed Inc. Memorandum to ITASCA Consulting Group, Inc.

de Marsily, G. 1987. An overview of coupled processes with emphasis on geohydrology. *Coupled Processes Associated with Nuclear Waste Repositories.* C.F. Tsang, ed. San Diego, CA: Academic Press: 27–37.

Drucker, D.C., and W. Prager. 1952. Soil mechanics and plastic analysis of limit design. *Quarterly of Applied Mathematics* 10(2): 157–172.

Freeze, R.A., and J.A. Cherry. 1979. *Groundwater.* Englewood Cliffs, NJ: Prentice-Hall, Inc.

Gardner, W.R. 1958. Some steady state solutions of the unsaturated moisture flow equation with application to evaporation from a water table. *Soil Science* 85(4): 228–232.

Ghosh, A., S.M. Hsiung, M.P. Ahola, and A.H. Chowdhury. 1993. *Evaluation of Coupled Computer Codes for Compliance Determination.* CNWRA 93-005. San Antonio, TX: Center for Nuclear Waste Regulatory Analyses.

Ghosh, A., S.M. Hsiung, G.I. Ofoegbu, and A.H. Chowdhury. 1994. *Evaluation of Computer Codes for Compliance Determination–Phase II.* CNWRA 94-001. San Antonio, TX: Center for Nuclear Waste Regulatory Analyses.

Ghosh, A., S.M. Hsiung, and A.H. Chowdhury. 1995. *Seismic Response of Rock Joints and Jointed Rock Mass.* CNWRA 95-013. San Antonio, TX: Center for Nuclear Waste Regulatory Analyses.

Gilman, J.R. 1986. An efficient finite-difference method for simulating phase segregation in the matrix blocks in double-porosity reservoirs. *Society of Petroleum Engineers, Reservoir Engineering* 1: 403–413.

Green, R.T., F.T. Dodge, S.J. Svedeman, R.D. Manteufel, G. Rice, K.A. Meyer, and R.G. Baca. 1995. *Thermally Driven Moisture Redistribution in Partially Saturated Porous Media.* CNWRA 95-005. San Antonio, TX: Center for Nuclear Waste Regulatory Analyses.

Hardy, M.P., M. Bai, R.R. Goodrich, M. Lin, and S. Carlisle. 1993. *New Three-Dimensional Far-Field Potential Repository Thermomechanical Calculations.* SAND-92-0589. UC-814. Albuquerque, NM: Sandia National Laboratories.

Hibbitt, Karlsson, and Sorensen, Inc. 1994. *ABAQUS Users' Manual, Version 5.4.* Pawtucket, RI: Hibbit, Karlsson and Sorensen, Inc.

Hoek, E., and E.T. Brown. 1980. *Underground Excavations in Rock*. London, UK: Institution of Mining and Metallurgy.

Hsiung, S.M., and A.H. Chowdhury. 1991. Seismic rock mechanics. *Report on Research Activities for Calendar Year 1990*. NUREG/CR-5817. W.C. Patrick, ed. Washington, DC: Nuclear Regulatory Commission.

Hsiung, S.M., W. Blake, A.H. Chowdhury, and T.J. Williams. 1992. Effects of mining-induced seismic events on a deep underground mine. *Pure and Applied Geophysics* 139: 741–762.

Hsiung, S.M., A. Ghosh, A.H. Chowdhury, and M.P. Ahola. 1994a. *Evaluation of Rock Joint Models and Computer Code UDEC Against Experimental Results*. NUREG/CR-6216. Washington, DC: Nuclear Regulatory Commission.

Hsiung, S.M., D.D. Kana, M.P. Ahola, A.H. Chowdhury, and A. Ghosh. 1994b. *Laboratory Characterization of Rock Joints*. NUREG/CR-6178. Washington, DC: Nuclear Regulatory Commission.

ITASCA Consulting Group, Inc. 1993. *UDEC Universal Distinct Element Code Version 2.0 Volume I: User's Manual*. Minneapolis, MN: ITASCA Consulting Group, Inc.

Kapoor, V. 1994. *Water Film Flow in a Fracture in Unsaturated Porous Medium*. CNWRA 94-009. San Antonio, TX: Center for Nuclear Waste Regulatory Analyses.

Kana, D.D., B.H.G. Brady, B.W. Vanzant, and P.K. Nair. 1991. *Critical Assessment of Seismic and Geomechanics Literature Related to a High-Level Nuclear Waste Underground Repository*. NUREG/CR-5440. Washington, DC: Nuclear Regulatory Commission.

Klavetter, E.A., and R.R. Peters. 1986. *Estimation of Hydrologic Properties of an Unsaturated Fracture Rock Mass*. SAND84-2642. Albuquerque, NM: Sandia National Laboratories.

Lichtner, P.C. 1994. *Engineered Barrier System Performance Assessment Codes (EBSPAC) Progress Report: October 1, 1993, Through September 25, 1994*. CNWRA 94-026. San Antonio, TX: Center for Nuclear Waste Regulatory Analyses.

Lichtner, P.C. 1995. *Multi-Phase Reactive Transport Theory*. NUREG/CR-6347. Washington, DC: Nuclear Regulatory Commission.

Lin, W.A., and W.D. Daily. 1989. Laboratory study of fracture healing in Topopah Spring tuff — Implications for near field hydrology. *Nuclear Waste Isolation in Unsaturated Zone Focus 89 Proceedings*. La Grange Park, IL: American Nuclear Society: 443–449.

Lin, W.A., A. Ramirez, and D. Watwood. 1991. *Temperature Measurements from a Horizontal Heater Test in G-Tunnel*. UCRL-JC-106693. Livermore, CA: Lawrence Livermore National Laboratory.

Manteufel, R.D., M.P. Ahola, D.R. Turner, and A.H. Chowdhury. 1993. *A Literature Review of Coupled Thermal-Hydrologic-Mechanical-Chemical Processes Pertinent to the Proposed High-Level Nuclear Waste Repository at Yucca Mountain.* NUREG/CR-6021. Washington, DC: Nuclear Regulatory Commission.

Mitchell, J.K. 1976. *Fundamentals of Soil Behavior.* New York, NY: John Wiley & Sons, Inc.

Nguyen, T.S., and A.P.S. Selvadurai. 1995. Coupled thermo-mechanical-hydrological behavior of sparsely fractured rock—Implications on nuclear waste disposal. *International Journal of Rock Mechanics and Mining Sciences & Geomechanics Abstracts* 32(5): 465–479.

Nitao, J.J. 1989. *V-TOUGH — An Enhanced Version of the TOUGH Code for the Thermal and Hydrologic Simulation of Large-Scale Problems in Nuclear Waste Isolation.* UCID-21954. Livermore, CA: Lawrence Livermore National Laboratory.

Nitao, J.J. 1991. Theory of matrix and fracture flow regimes in unsaturated, fractured porous media. *Second Annual International High-Level Radioactive Waste Management Conference Proceedings.* La Grange Park, IL: American Nuclear Society: 845–852.

Ofoegbu, G.I., and J.H. Curran. 1992. Deformability of intact rock. *International Journal of Rock Mechanics and Mining Sciences & Geomechanics Abstracts* 29(1): 35–48.

Ofoegbu, G.I., S.M. Hsiung, A.H. Chowdhury, and J. Philip. 1994. *Field Site Investigation: Effect of Mine Seismicity on Groundwater Hydrology.* CNWRA 94-017. San Antonio, TX: Center for Nuclear Waste Regulatory Analyses.

Ohnishi, Y., H. Shibata, and A. Kobayashi. 1985. Development of finite element code for the analysis of coupled thermo-hydro-mechanical behavior of saturated-unsaturated medium. *Proceedings of the International Symposium on Coupled Processes Affecting the Performance of a Nuclear Waste Repository.* Berkeley, CA: 263–268

Olsson, W.A. 1982. Experiments on a slipping crack. *Geophysical Research Letters* 9(8): 797–800.

PDA Engineering. 1994. *PAT3/ABAQUS Interface Guide.* Costa Mesa, CA: PDA Engineering. PATRAN Division.

Rojstaczer, S., and S. Wolf. 1992. Permeability changes associated with large earthquakes: An example from Loma Prieta, California. *Geology* 20: 211–214.

Salvado, C., and J.B. Minster. 1980. Slipping interfaces: A possible source of S radiation from explosive sources. *Bulletin of the Seismological Society of America* 70: 659–670.

Saterlie, S.F., and B.H. Thomson. 1994. *FY93 Thermal Loading Systems Study Final Report.* B00000000-01717-5705-00013 Rev 1. Las Vegas, NV: TRW Environmental Safety Systems Inc.

Scott, R.B. 1990. Tectonic setting of Yucca Mountain, southwestern Nevada. *Basin and Range Extensional Tectonics Near the Latitude of Las Vegas, Nevada*. B.P. Wernicke, ed. Geological Society of America Memoir 176: 251–282.

Sharma, K.G., and C.S. Desai. 1992. Analysis and implementation of thin-layer element for interfaces and joints. *Journal of Engineering Mechanics* 118(12): 2,442–2,462.

Spengler, R.W., C.A. Braun, L.G. Martin, and C.W. Weisenberg. 1994. *The Sundance Fault: A Newly Recognized Shear Zone At Yucca Mountain, Nevada*. Open-File Report 94-49. Denver, CO: U.S. Geological Survey.

Stothoff, S. 1995. *BREATH Version 1.1—Coupled Flow and Energy Transport in Porous Media: Simulator Description and User Guide*. NUREG/CR-6333. Washington, DC: Nuclear Regulatory Commission.

U.S. Department of Energy. 1988. *Site Characterization Plan: Yucca Mountain Site, Nevada Research and Development Area*. DOE/RW-0199. Washington, DC: U.S. Department of Energy.

van Genuchten, M.Th. 1980. A closed-form equation for predicting the hydraulic conductivity of unsaturated soils. *Soil Science Society of America Journal* 44: 892–898.

van Genuchten, M.Th., F.J. Leij, and S.R. Yates. 1991. *The RETC Code for Quantifying the Hydraulic Functions of Unsaturated Soils*. EPA/600/2–91/065. Ada, OK: U. S. Environmental Protection Agency.

Wolfram, S. 1991. *Mathematica — A System for Doing Mathematics by Computer.* New York, NY: Addison-Wesley Publishing Company, Inc.

Young, S.R., G.L. Stirewalt, and A.P. Morris. 1992. *Geometric Models of Faulting at Yucca Mountain*. CNWRA 92-008. San Antonio, TX: Center for Nuclear Waste Regulatory Analyses.

Zienkiewicz, O.C., and C. Humpheson. 1977. Viscoplasticity: A generalized model of soil behavior. *Numerical Methods in Geotechnical Engineering*. C.S. Desai and J.T. Christian, eds. New York, NY: McGraw-Hill Book Company: Chapter 3.